MULTIVALENT IONS IN POLYMER ELECTROLYTES

Mary Anne Mehta

A Thesis Submitted for the Degree of PhD
at the
University of St Andrews

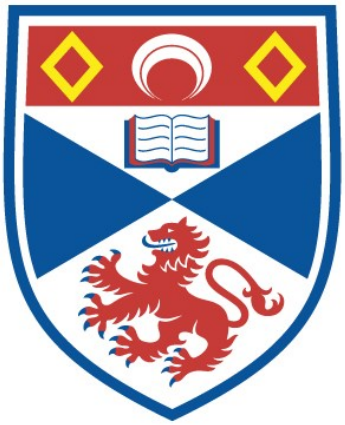

1993

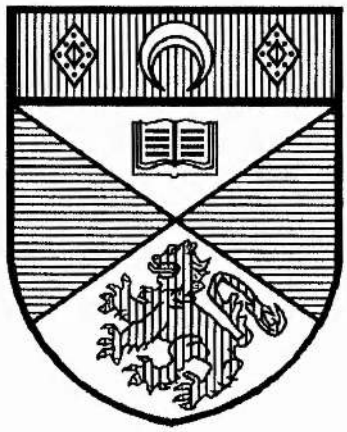

MULTIVALENT IONS

IN

POLYMER ELECTROLYTES

A thesis presented for the degree of

Doctor of Philosophy

in the Faculty of Science of the University of St. Andrews

by Mary Anne Mehta, B.A.

December 1992

Centre for Electrochemical

and Materials Science,

Department of Chemistry,

St.Andrews

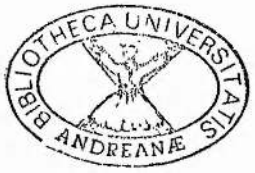

ProQuest LLC.
789 East Eisenhower Parkway
P.O. Box 1346
Ann Arbor, MI 48106 – 1346

DECLARATION

I, Mary Anne Mehta hereby certify that this thesis has been composed by myself, that it is a record of my own work, and that it has not been accepted in partial or complete fulfilment of any other degree or professional qualification.

Signed: Date: 11/12/92

I was admitted to the Faculty of Science of the University of St.Andrews under Ordinance General No. 12 on 1st January 1991 and as a candidate for the degree of PhD on 1st January 1991.

Signed: Date: 11/12/92

CERTIFICATION

I hereby certify that Mary Anne Mehta has spent twelve terms of research work under my supervision and that she has fulfilled the conditions of the Resolution and Regulations appropriate to the degree of Doctor of Philosophy.

December 1992 Signed:

P.G.Bruce

LIBRARY DECLARATION

In submitting this thesis to the University of St.Andrews I understand that I am giving permission for it to be made available for use in accordance with the regulations of the University Library for the time being in force, subject to any copyright vested in the work not being affected thereby. I also understand that the title and abstract will be published, and that a copy of the work may be supplied to any *bona fide* library or research worker.

Signed:

TABLE OF CONTENTS

ACKNOWLEDGEMENTS

Thanks are due to:-

my supervisor, Dr. Peter Bruce, for his advice and support over the years. In particular for the time that he gave up from his busy schedule in order to proof read this thesis.

Dr. Stephen Campbell for many helpful discussions and advice with the electrochemical aspects of the project.

Dr. Philip Lightfoot for assistance with the x-ray diffraction.

Dr. Jan Nowinski for getting me started in the laboratory.

I am also grateful to Jie Shi, Professor Colin Vincent and the members of C.E.M.S. for many helpful discussions, my family for supporting me throughout my 'extended' career as a student and the S.E.R.C. for financial support.

ABSTRACT

The electrochemical, thermal and structural properties of polyethylene oxide (PEO) based polymer electrolytes containing multivalent ions were investigated.

The phase diagram for the PEO:$Ca(CF_3SO_3)_2$ system was determined by x-ray diffraction and differential scanning calorimetry techniques. Precipitation of the salt from the system at high temperatures was directly observed by variable temperature x-ray diffraction. This was ascribed to a negative entropy of dissolution of the salt in the polymer. A new crystalline complex $PEO_6Ca(CF_3SO_3)_2$, which exhibits a phase transition between two polymorphic forms was observed. The temperature dependence of ionic conductivity was related to the phase diagram.

Redox behaviour of the PEO:NiI_2 system was probed. Motion of the Ni(II) species through the system was extremely slow as evidenced by the low effective diffusion coefficient (1.82×10^{-11} cm^2s^{-1}) and cationic current fraction ($F_+ < 0.1$). Deposition of nickel from the polymer was characterised by instantaneous nucleation followed by three dimensional diffusion controlled growth.

Investigation of the redox behaviour of the PEO:$Eu(CF_3SO_3)_3$ system indicated that reduction of Eu^{3+} followed an ec mechanism. Evidence was obtained for extremely slow diffusion of Eu^{3+} containing species ($D_{eff} \sim 3.66 \times 10^{-16} cm^2s^{-1}$) through the system and slow kinetics of electron transfer.

Thermal studies of the PEO:$Co(SCN)_2$ system indicated that the glass transition temperature (Tg) was grossly elevated by the presence of $Co(SCN)_2$ in the polymer. The absence of a crystalline PEO:$Co(SCN)_2$ complex was ascribed to the high Tg which leads to slow crystallisation kinetics. UV-visible spectra indicated that the Co^{2+} ion was tetrahedrally coordinated in the system at low salt concentrations.

The structure of the PEO_3NaClO_4 crystalline complex was reported as a subsiduary study.

CHAPTER 1

AN INTRODUCTION TO POLYMER ELECTROLYTES

1.1 Introduction

A polymer electrolyte is an ionic conductor formed by the dissolution of a salt in a high molecular weight polymer host. Interest in the field was generated when it was demonstrated[1,2,3] that dissolution of alkali metal salts in polyethylene oxide (PEO) produced materials with quite significant conductivities. The earliest work concentrated on developing lithium ion conductors with a view to producing thin film rechargeable lithium batteries. This is still the main technological focus of the work.

Under certain conditions, polymer electrolytes formed from high molecular weight polymer hosts have many of the macroscopic properties of a solid with some of the microscopic properties of a liquid. This gives them several advantages over classical liquid electrolytes.

i) There are not the leakage problems associated with liquid electrolytes.

ii) The materials are often soft and form a good interfacial contact with the electrodes.They can often accomodate the volume changes associated with the ion-electrode exchange processes.

iii) The materials can be produced in a variety of geometries including thin films.

iv) The manufacturing technology for a polymer electrolyte battery is very different from that of conventional liquid electrolyte cells. Polymer electrolyte batteries can be manufactured by highly automated multi-layer processes.

Increased activity in the field of polymer electrolytes quickly led to a greater understanding of the properties of the systems under investigation. It was a natural progression to turn to the study of systems containing multivalent ions.

Conductivity is one of the most important properties of a polymer electrolyte. The most general expression for the conductivity at a given temperature is given by expresssion 1-i)

$$\sigma(T) = \sum_i n_i q_i \mu_i \qquad 1 - i)$$

Where n_i is the number of charge carriers i, q_i is their charge and μ_i their mobility. Interest in the study of multivalent ions in polymer electrolytes was stimulated by the possibility that these materials, containing highly charged species, might have slightly enhanced conductivities. It came as no surprise to discover that many multivalent cations were essentially immobile in polymer electrolyte systems[4]. These findings however sparked off new interest in the possibility of developing systems that were purely anionic conductors.

The frontiers of polymer electrolyte chemistry continue to be pushed back today. Current work in the field is progressing in a variety of different directions of which a few examples follow. The most recent developments in powder X-ray diffraction have made it possible for the structure of polymer electrolyte crystalline complexes to be determined for the first time using this method. This gives valuable insight into the nature of the bonding and coordination in the crystalline state. Many questions however remain unanswered as to the type of charge carriers responsible for conduction in the amorphous phase. The nature of these ions, which may be single ions, triples or other multiples, has been probed by NMR[5], IR[6], and Raman spectroscopy[7,8]. Detailed mechanisms for ion transport in many systems have yet to be determined. In particular, work in this laboratory has been carried out to investigate how ion transport processes change with molecular weight of the host polymer[9].

The particular emphasis of the work of this thesis was to look at the properties of multivalent ions in polymer electrolytes. Electrochemical studies of systems containing Eu^{3+} and Ni^{2+} were carried out with a view to probing their characteristic

redox and mass transport properties. The phase diagram for the PEO-calcium trifluoromethane sulphonate system was investigated and correlated with conductivity measurements for a variety of compositions at different temperatures. These in turn were compared to conductivity data obtained from systems containing Ni^{2+} and Co^{2+}. Finally, the structures of some complexes formed between PEO and alkali metal salts were investigated by powder X-ray diffraction.

The following sections contain a brief treatment of the background and theory behind the work carried out in this investigation.

1.2 The morphology and structure of simple polymers

The term 'morphology' refers to the structure, arrangement and physical form of polymer molecules in the system. In general there are two types of morphology that are characteristic of polymer systems; the amorphous state and the crystalline state.

1.2.1 *The amorphous state*

This is characterised by an almost complete lack of ordering of the molecules. It occurs in crystalline polymeric systems above their melting temperature. However some polymers, due to their structure , show no tendency to become crystalline. This gives rise to systems that have both a liquid and solid amorphous state. In a solid amorphous state, molecular motion is restricted to very short range vibrations and rotations. The liquid or molten amorphous state is characterised by considerable conformational freedom which arises from rotation about chemical bonds as well as significant segmental motion of the polymer chains. If a molten polymer remains amorphous upon cooling to the solid state, the process is called vitrification, so called because of the resemblance of the solid amorphous polymer to a glass.

1.2.2 *The glass transition*

When a solid amorphous polymer or glass is heated, the kinetic energy of the molecules increases. As mentioned above, motion of the molecules is restricted to short range vibration and rotation. The system thus retains its glass like structure. Above a certain temperature, the glass transition temperature (T_g), longer range motion becomes possible. There is greater rotational freedom and segmental motion of the polymer chains . For segmental motion to occur, it is necessary for approximately 20 to 50 atoms to move. The space between the molecules (free volume) is observed to increase above the glass transition temperature. At the glass transition temperature, no discontinuities are observed if the entropy or volume of the system is measured as a function of temperature. A change is however observed in the first derivative of this function i.e. there is a change in the rate of change of entropy with temperature. The glass transition is thus termed a 2nd order transition and is accompanied by a change in the heat capacity of the system.

1.2.3 *The crystalline state*

One of the requirements for crystallinity is that the polymer chains must be capable of packing closely together in a regular array e.g. as stacks of planar zig-zags or helices. Thus, in such systems, there may be regions in the polymer matrix where the molecules have arranged themselves into a thermodynamically favourable alignment. This can be described by the fringed micelle model in which the regions of crystallinity are much smaller than the length of the polymer chains. Thus, one particular polymer chain may extend through a number of crystalline regions. The crystalline regions or micelles are themselves surrounded by an amorphous network.

Crystallization may be induced in a number of ways e.g. cooling of the molten polymer, evaporation of a polymer solution or annealing of the polymer in an inert atmosphere or under vacuum. Each method allows the polymer molecules the vibrational and rotational freedom to reorient themselves into a crystalline morphology.

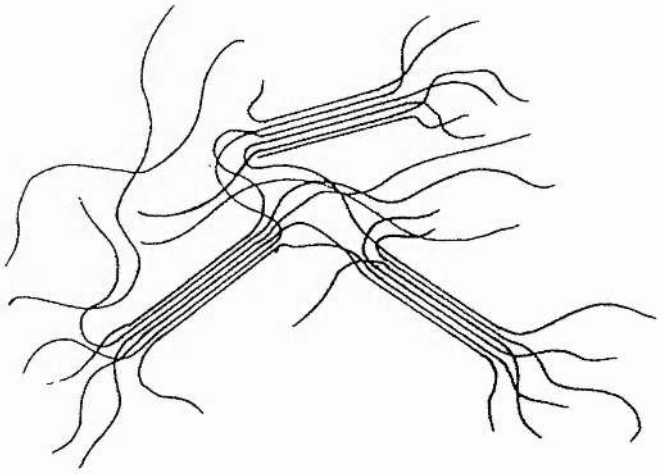

Figure 1 - 1 The fringed micelle model

The crystalline regions have been shown to have a plate-like or lamella structure composed of polymer chains folded back upon themselves. The chain axis or (c-axis) of the molecules is oriented perpendicular to the lamella.This is called the folded chain lamella model where the thickness of the lamellae is very much less than the length of the polymer chains. Each fold in the lamella may be connected either adjacently or non-adjacently. The size of the 'loops' in the folds may be of either uniform or non-uniform length.

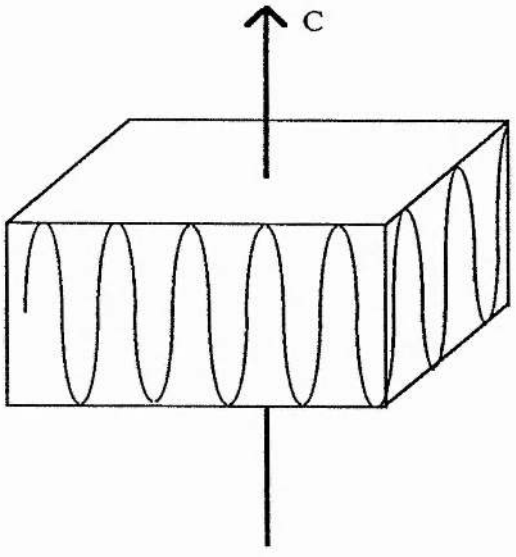

Figure 1 - 2 The folded chain lamella model.

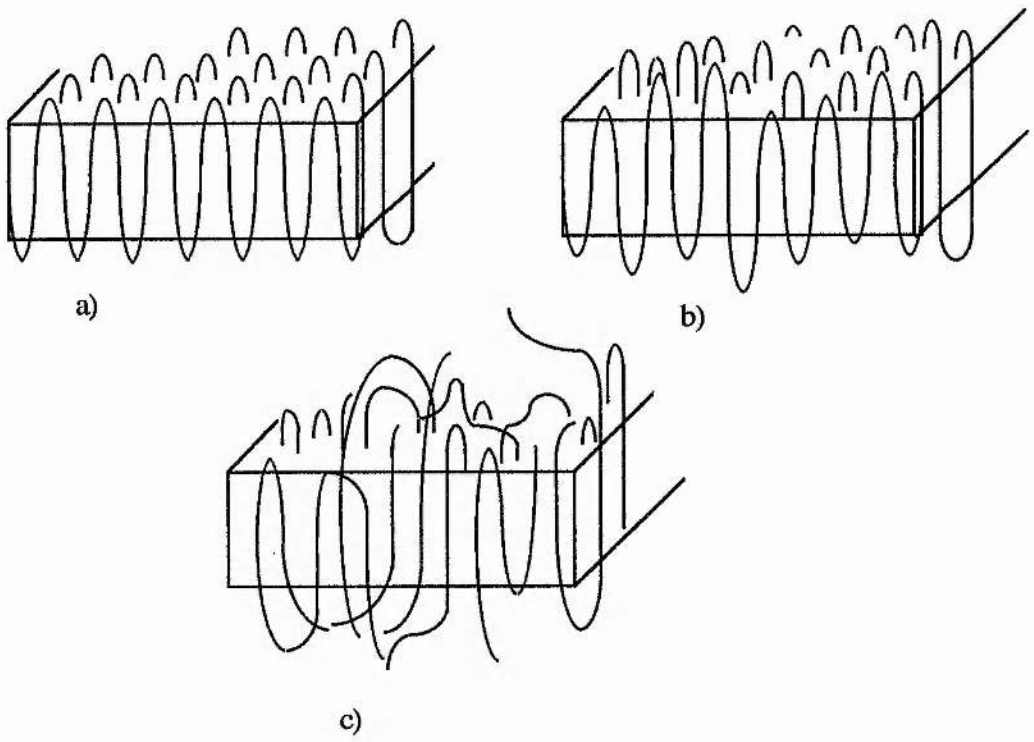

Figure 1 - 3 Fold connections in the folded chain lamella model. a) adjacent uniform folds, b) adjacent non-uniform folds and c) non-adjacent non-uniform folds.

It can be seen from figure 1 - 3 that an increasing amount of amorphous material is associated with the lamellae upon proceeding from a) to b) to c).

The onset of crystallisation is called nucleation and may occur either randomly in the polymer matrix (homogeneous nucleation), or at the interface with an 'impurity'. 'Impurities' are sometimes purposely added to act as nucleating agents.

1.2.4 *Spherulites*

A variety of crystalline morphologies have been identified by X-ray diffraction studies. By far the most common morphology is the spherulite. These are often found in systems where crystallization has occurred in the absence of applied stress. Spherulites are aggregates of small hairlike strands called fibrils arranged as clusters in

a radial pattern. The fibrils in the spherulites consist of chain folded lamellae, the polymer chain axes being perpendicular to the radial direction. Branching in the lamellae causes splaying out of the fibrils. This gives the spherulite its 3-dimensional nature. A spherulite will continue to grow until it impinges on other spherulites.

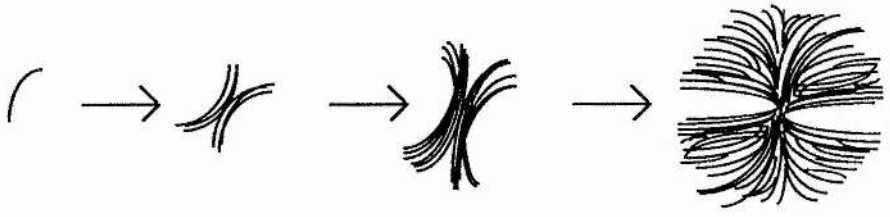

Figure 1 - 4 Stages in the formation of a spherulite

It is found that crystalline polymers containing spherulites are tough and can be deformed under stress. This results from the fact that neighbouring lamellae are bound together by molecules which may be embedded in more than one crystalline region. There are thus layers of amorphous material between the lamellae which remain uncrystallised or crystallise only very slowly. This amorphous material is reproducibly present in systems that are regarded as 'crystalline'. For most situations, such systems can be considered as consisting of a single phase if the time-scale for any measurements is short with respect to any changes in crystallinity. It should however be appreciated that such polymer systems never achieve true thermodynamic equilibrium.

Other crystalline morphologies not considered in detail here include the drawn fibrillar morphology and the shish-kebab or epitaxial morphology. The former may occur when drawing polymer fibres and the latter occurs during crystallisation of stirred solutions or melts.

	Li^+	Na^+	K^+	Rb^+	Cs^+	NH_4^+	Ag^+	Be^{2+}	Mg^{2+}	Ca^{2+}	Sr^{2+}	Ba^{2+}	Co^{2+}	Ni^{2+}	Cu^{2+}	Zn^{2+}	Hg^{2+}
Cl^-	+	-	-	-	-	-	-		+	+	-	-	+	+	+	+	+
Br^-	+	+	-	-	-	-	-		+	+	+	+	+	+	+	+	+
I^-	+	+	+	-	-	+	-	+	+	+			+	+	+	+	+
SCN^-	+	+	+	+	+	+	+		+	+		+			+	+	
ClO_4^-	+	+	+	+	+	+	+		+	+	+	+	+	+	+	+	+
$CF_3SO_3^-$	+	+	+	+	+	+	+		+	+	+		+	+	+	+	
NO_3^-		+															
BF_4^-	+	+															
BPh_4^-	+	+	+	+	+	+	+				+						
AsF_6^-	+	+															
PF_6^-	+																
$H_2PO_4^-$	+																

+ complex formed, - no solubility

Table 1.1 : Solubility of some salts in PEO[10]

	$V^{2+/3+}$	Mn^{2+}	$Cr^{2+/3+}$	$Fe^{2+/3+}$	Al^{3+}	Ga^{3+}	Sc^{3+}	Y^{3+}	La^{3+}	Hf^{3+}	Ta^{3+}	W^{5+}	Ir^{3+}	Pt^{4+}	Th^{4+}	Zr^{4+}	Mo^{5+}
Cl^-	+/+	+	+/+	+/+	+	+	+	+	+	+	+	+	+	+	+	+	+
Br^-	+/+	+	+	+			+	+	+		+						
I^-	+	+	+	+				+	+								
ClO_4^-	+	+		+				+	+								
$CF_3SO_3^-$	+	+		+					+								

	Cd^{2+}	In^{3+}	Sn^{2+}	Bi^{3+}	Ce^{3+}	Pr^{3+}	Nd^{3+}	Sm^{3+}	$Eu^{2+/3}$	Gd^{3+}	Tb^{3+}	Dy^{3+}	Ho^{3+}	Er^{3+}	Tm^{3+}	Yb^{3+}	Lu^{3+}
Cl^-	+	+	+	+	+	+	+	+	+	+	+	+	+	+	+	+	+
Br^-	+		+	+	+	+	+	+	+	+	+	+	+	+	+	+	+
I^-	+		+		+	+	+	+	+	+	+	+	+	+	+	+	+
ClO_4^-	+		+		+	+	+	+	+	+	+	+	+	+	+	+	+
$CF_3SO_3^-$	+		+		+	+	+	+	+	+	+	+	+	+	+	+	+

Table 1.1 cont.

1.3 Polymer electrolyte formation, morphology and structure

1.3.1 *Notation*

The polymer electrolyte systems which are the subject of the current investigation are all formed by the dissolution of a salt in high molecular weight (MW = $5x10^6$) PEO. The notation adopted in this work is to express the composition as a ratio of the PEO repeat units, (CH_2CH_2O), to salt. Thus, the formula PEO_4NiI_2 represents the composition where there are four PEO repeat units for each salt unit, i.e (CH_2CH_2O)$_4NiI_2$. Occasionally, it is necessary to express the composition in terms of a mol fraction or a mass fraction (X_{Salt}). The mol fraction of salt is given by the following expression:-

$$\text{Mol fraction of salt} = \frac{\text{No. of mols of salt}}{(\text{No. mols of polymer} + \text{No. mols of salt})}$$

The mass fraction of salt in a polymer electrolyte, PEO_nSalt, is given by:-

$$X_{Salt} = \frac{RMM_{Salt}}{RMM_{Salt} + (n \times 44)}$$

where RMM_{salt} is the relative molecular mass of the salt and 44 is the 'relative molecular mass' of the ethylene oxide unit.

1.3.2 *Polymer electrolyte formation*

A wide variety of salts will dissolve in PEO (and other polymer hosts) to form a polymer electrolyte as shown in table 1 - 1. For dissolution to occur, the free energy change for the process must be favourable. Thus, the polymer-salt interaction must be significant enough to compensate for the loss of lattice energy of the salt and the polymer-polymer interaction. When a salt dissolves in a solvent, anion stabilisation arises principally from hydrogen bonding and/or ion pairing. The stabilisation of anions in aprotic, non polar solvents is therefore generally negligible, especially if the anion is a weak base with low charge density. Most polymer hosts (and PEO in

particular) have no hydrogen bonding capabilities and thus the primary polymer-salt interaction arises from interaction between the polymer and the cation. This may be viewed as an electrostatic interaction between the cation and the negative end of dipolar groups on the polymer, or as a covalent bond formed between the cation and the lone pairs of the coordinating donor atom (e.g. N or O) on the polymer.

For a given polymer host, polymer electrolyte formation will be most favourable for salts with low lattice energies. Thus anions should ideally be large with a low charge density. Furthermore, they should preferably be weak bases and have little tendency to form ion pairs to enable the polymer to compete more effectively for the cation. The most suitable choices of anion on this basis include ClO_4^- , $CF_3SO_3^-$, BF_4^- and AsF_6^-. No polymer electrolytes are observed to form with fluorides due to their high lattice energies. Lithium chloride is the only chloride capable of forming a polymer electrolyte, the high lattice energy being compensated by the large enthalpy of solvation of the strongly solvated lithium ion.

Both Papke et al[11] and Wright[12,13] adopted a more quantitative approach towards predicting the occurrence of complex formation, Wright proposed that formation of a complex PEO_3MX would occur if:-

$$E(\text{complex}) < E(3EO) + E(MX)$$

where E(complex), E(3EO) and E(MX) were the lattice energies of the complex, the appropriate length of crystalline polymer and the salt respectively. Entropy changes upon complexation were however neglected in this treatment. He was able, using computational methods, to determine the contribution to each component in the equation for the formation of the complex PEO_3NaI. Estimates of the corresponding energetic parameters for other systems enabled more quantitative predictions for complex formation to be made.What became clear from the work of both groups was the importance of the magnitude of the salt lattice energy in determining whether complex formation would occur. Shriver et al[14] commented that for a given polyether

and cation, complex formation would only occur for salts with lattice energies below a certain threshold value. This is illustrated in table 1-2 for some alkali metal salts.

	Li^+	Na^+	K^+	Rb^+	Cs^+
F^-	no 1036	no 923	no 823	no 785	no 740
Cl^-	yes 853	no 786	no 715	no 689	no 659
CH_3COO^-	- 881	no 763	- 682	- 656	- (682)
NO_3^-	- 848	no 756	- 687	- 658	no 625
NO_2^-	- -	no 748	- 648	- 765	no (598)
Br^-	yes 807	yes 747	no 682	no 660	no 631
N_3^-	- 818	no 731	- 658	- 632	- 604
BH_4^-	- (778)	yes (703)	- (665)	- (648)	- (628)
I^-	yes 757	yes 704	? 644	no 630	no 604
SCN^-	yes 807	yes 682	yes 616	yes 619	yes 568
ClO_4^-	yes 723	yes 648	- 602	- 582	- 542
$CF_3SO_3^-$	yes (≤725)	yes (≤650)	yes (≤605)	yes (≤585)	yes (≤550)
BF_4^-	yes (699)	yes 619	- 631	- 605	- 556
BPh_4^-	yes (≤700)	yes (≤630)	yes (≤630)	yes (≤630)	yes (≤550)

Table 1-2. A comparison of PEO / Salt complex formation with lattice energies (kJ/mol) of the pure salt (Data taken from reference 14)
No = No complex formed, Yes = complex formed, (x) = theoretical or estimated value.

1.3.3 *The hard-soft-acid-base theory*

As the variety of systems under investigation increased an attempt was made to rationalise the theory behind polymer electrolyte complex formation and the efficiency of the material as an electrolyte. Many workers[15] turned to the hard-soft-acid-base (HSAB) principal devised by Pearson[16] to predict not only whether a complex was likely to form, but whether the ions were subsequently likely to be mobile. The HSAB theory classified Lewis acids and bases as either hard or soft as follows :-

Hard bases :- Small non-polarisable species with highly electronegative donor atoms.(E.g. ethers, amines and ClO_4^-)

Soft bases :- Highly polarisable species with less electronegative donor atoms.(E.g. SCN^- and I^-)

Hard acids:- Small, non-polarisable species that have no unshared electrons in their valence shell (E.g. Ca^{2+} and Mg^{2+})

Soft acids :- Large, polarisable species with unshared electrons in their valence shell. (E.g. Ag^+ and Hg^{2+})

In general, the most stable complexes are formed between hard acids and bases and between soft acids and bases. PEO can be considered as a regular array of hard bases (the donor atom being the ether oxygen). On this basis, it is likely to form its most stable complexes with hard Lewis acids such as Ca^{2+}, Mg^{2+} and Li^+. Soft Lewis acids such as Ag^+ and Hg^{2+} are likely to interact only weakly with PEO and form relatively unstable complexes. It should be noted however, that although complex formation (i.e. salt dissolution) may be very favourable between PEO and hard Lewis acids, the complex may be so stable that the cations may subsequently be immobile. Reference to equation 1-i) indicates that this will give rise to a poor electrolyte. Bruce et al.[15] have postulated that hard-soft interactions between the polymer and salt favour more rapid cation exchange between ligand sites, thus enhancing mobility.

In summary it can be seen that to form a good polymer electrolyte, there must be a compromise between two factors:-

a) A strong cation-polymer interaction to compensate for the loss of salt lattice energy.

b) Cation-polymer bond lability to facilitate ion transport.

1.3.4 *The nature of the polymer host*

There are three important criteria governing the suitability of a polymer to act as a host.

a) The polymer molecules must have polar groups or donor atoms capable of forming coordinate bonds with the cation.

b) The distance between coordinating groups must be such as to maximise polymer-cation interaction.

c) The polymer must be capable of adopting low energy conformations to allow multiple inter- and intra- molecular coordination.

These factors are discussed with reference to specific polymer hosts.

Initially, the choice of potentially effective polar groups for polymer electrolytes would appear to be limitless, however, many of those initially proposed are found to be too electrochemically active e.g. sulphoxides, ketones, nitriles etc. It is for this reason that so much emphasis has been put into the study of polyethers. Of these, polyethylene oxide (PEO) and polypropylene oxide (PPO) have been the most comprehensively studied. The low glass transition temperature for PEO (-60 °C) is indicative of a flexible polymer backbone that is capable of adopting the conformations necessary to complex the salt with ease. Despite the increased donor power of oxygen linked to a secondary carbon atom, Armand et al[3] demonstrated the greatly reduced solvating power of PPO compared to PEO. This was partly ascribed to the steric hindrance of the CH_3 group interfering with the close approach of two polymer chains to the same cation. In the same work, Armand commented on the fact that neither Polymethylene oxide, (PMO), $(CH_2O)n$, nor polytrimethylene oxide, (PTO),

$(CH_2CH_2CH_2O)_n$, form polymer electrolytes. Mark[17] has in fact discussed the highly constrained nature of the PMO molecule. The reluctance of PTO and PMO to form polymer electrolytes is thus ascribed to their inability to form low energy conformations that would maximise polymer-salt interaction. Watanabe et al[18] investigated polymer electrolyte formation of the host polymers polyethylene succinate and polyethylene sebacetate with alkali metal thiocyanates. They postulated that for intra-molecular coordination of the cation to occur, it was necessary for there to be a cooperative interaction of neighbouring polar groups in the polymer backbone with the ion. This was thought to be entropically unfavourable for polyethylene sebacetate where the coordinating groups were separated by octamethylene units. The salts had a greater tendency to dissolve in polyethylene succinate where there was a higher density of polar groups to maximise polymer-salt interaction.

It might be expected that because of the high donor number of the amine group (N=60, O=22) that linear polyimines would form stronger bonds with cations than their oxygen analogues. The first report of polymer electrolyte formation with polyethylene imine, (PEI), $(CH_2CH_2NH)_n$, was from Chiang et al[19] in 1985. They showed that NaI dissolved in linear PEI (MW 2000) to form a high melting point crystalline complex at high salt concentrations. Strong polymer-salt interaction was evidenced by the loss of crystallinity of the polymer at low concentrations. The reduced conductivity of the system ($5x10^{-6}\ \Omega^{-1}cm^{-1}$ at 75°C, $PEO_{10}NaI$) compared to values obtained for systems with PEO could also be ascribed to a stronger polymer-salt interaction, thereby reducing the lability of the bond. A labile bond being a necessity for ion migration. In a later study[20], the same workers investigated polymer electrolyte formation with a wide variety of lithium salts. Evidence for salt dissolution was obtained from the loss of crystallinity of the polymer as evidenced by the reduction of the enthalpy of fusion of the crystalline phase. This was observed to a greater or lesser extent for all the salts studied, even the fluoride. The glass transition temperature was also observed to increase for all systems except the fluoride. They

concluded that the loss of crystallinity of the polymer was due to the formation of cross links resulting from the interaction of Li^+ with lone pairs on N atoms of neighbouring polymer chains. This would have the affect of disrupting the order of the system (and therefore the crystallinity) as well as raising the Tg as observed. They also concluded that if the fluoride did dissolve, it was to a very much lesser extent than the other lithium salts.

Harris et al[21] investigated the complexing ability of higher molecular weight PEI (MW 10000) with sodium triflate ($NaCF_3SO_3$) and observed similar behaviour to the earlier study. Highly amorphous materials were produced but there was evidence for crystalline complex formation at higher concentrations. Preliminary investigations also indicated that complex formation occurred with transition metal salts although these materials were amorphous with Tg > 25°C.

The conductivity of polymer electrolyte systems has been ascribed to the motion of ions through the amorphous regions of the polymer. Takahashi et al[22] chemically modified linear PEI in an attempt to prevent crystalline complex formation without affecting the ability of the polymer to dissolve salts and conduct ions. They investigated systems containing poly(N-acetyl ethylene imine), partially quaternized PEI with ethyl or butyl groups and crosslinked PEI with diepoxyoctane. All of these modifications, although disrupting the crystallinity of the system, resulted in a large rise in Tg with subsequent reduction of the mobilty of the charge carriers.

Clancy et al[23] prepared and characterised some polymer electrolytes formed from polyalkylene sulphides and some silver salts. It was observed that although polypentamethylene sulphide $[(CH_2)_5S]_n$, (P5S), and polyethylene sulphide, $(CH_2CH_2S)_n$, (PES),both formed polymer electrolytes, it was the P5S that formed the most highly conducting system. This was initially surprising in view of the lower density of polar groups on P5S. P5S was however, observed to have a low Tg (-25°C) and melting point (65°C), factors indicative of a flexible polymer backbone. At most compositions, the complexes formed with P5S were observed to

be highly amorphous although at the highest concentrations evidence for a semi-crystalline complex was obtained.

1.3.5 *The morphology of polymer electrolytes*

The detailed morphology of polymer electrolytes is highly complex and dependent not only on the system and its composition but on the method of preparation used. Currently, the two most common methods of preparation are the solvent casting method and the cryogrinding / hot pressing method (described in more detail in sections 4.1.1 and 4.2.2). It is found that the morphology of a system can be affected by the characteristics of the solvent casting process, e.g. the nature of the solvent and rate of removal, as well as by the temperature and thermal history of the sample.

As for the simple polymers, described in section 1.2.4, most polymer electrolyte systems which crystallise, form spherulites of well defined stoichiomery. It is often found that the interlamella amorphous regions contain small amounts of dissolved salt. Spherulites of more than one composition may be observed in any given system, the proportion of each type of spherulite depends on the overall composition of the system. Thus Neat et al [24] observed three types of spherulite in the PEO (MW $4x10^6$) : $LiClO_4$ system cast from acetonitrile. Each type of spherulite was characterised by a different melting point and salt content. No more than two types of spherulite were observed for any one composition. The same authors[25] also observed similar behaviour in the PEO : $LiCF_3SO_3$ system.

The affect of the nature of the solvent on the morphology of polymer electrolytes has been investigated by Payne and Wright [26] for the PEO (MW $5x10^6$) : $LiBF_4$ system. Films cast from methanol were observed to be semi-crystalline with low melting points. Those cast from a chloroform /acetone mixture were highly crystalline with well defined spherulites melting at much higher temperatures. X-ray diffraction studies however, indicated that the short range structure was similar for both cases. It was postulated that the morphology of the film was affected by the extent of pre-

association of the ions and the polymer in solution prior to removal of the solvent. For example, in dilute solutions where the salt is only weakly solvated, it is possible for 'precursor complexes' to be formed with the ether. Very little reordering is subsequently required to form the final crystalline structure. In such instances, a highly crystalline material containing high melting point spherulites is expected to form as exhibited by the acetone/chloroform mixture. For solutions where the salt is highly solvated, complex formation with the ether is not initiated until the bulk of the solvent has been removed. For such concentrated solutions, there is a high degree of polymer chain entanglement thus reducing the long range order of the resulting complex, as seen from the methanolic solution.

Wendsjo and Yang [27] in their study of factors affecting the degree of crystallinity of PEO based electrolytes containing PbI_2 observed that different complexes formed when the solvents dimethyl sulphoxide (DMSO) and dimethyl formamide (DMF) were used to dissolve the lead iodide. Furthermore, it was found that the use of DMF inhibited the formation of crystalline PEO. The importance of specifying the solvents used in the preparation procedure is thus emphasised.

The affect of water on the morphology and electrical properties of polymer electrolytes has been the subject of several studies. Wendsjo and Yang[27] observed that the degree of water uptake varies greatly with the nature of the ions in the electrolyte. Their X-ray diffraction studies of PEO_4ZnCl_2 and PEO_8NiBr_2 clearly indicated that the uptake of water destroys the crystalline complex phase. Upon subsequent dehydration of PEO_8NiBr_2, peaks due to the crystalline complex reappeared.

Farrington et al[28,4] observed that upon controlled hydration / dehydration of PEO_xNiBr_2 electrolytes, the conductivities and Ni^{2+} transport numbers were greatly enhanced. Spectroscopic studies indicated that upon exposure to moisture, the water preferentially coordinated with Ni(II) to form the hexa-aquo ion. The increased mobility of the hydrated Ni^{2+} ion was ascribed to the fact that it was no longer 'anchored' by coordination to the polymer. Farrington postulated that the increased

conductivity of the electrolyte upon dehydration could be due to a significant change in structure and noted that TGA data indicated that all of the Ni(II) forms a complex with the PEO. The X-ray diffraction patterns of Wendsjo et al do not indicate a significant change in structure upon controlled hydration / dehydration. The explanation for the concommitant enhanced conductivity is thus still the subject of debate.

Gray[10] has cautioned that it is difficult to generalise as to the effect of solvent type and its rate of removal since this will be highly dependent on the individual polymer electrolyte system. In some cases, spherulite growth may not be initiated until after removal of the solvent, in which case, the morphology will not be affected by its rate of removal.

It is difficult to make generalisations as to the effect of heat treatment and thermal history on polymer electrolyte morphology. This is also observed to vary with the individual system and composition. Lee and Wright[29,13] have investigated the effect of heat treatment on the morphology of some PEO (MW 10,000) : NaSCN and PEO (MW 10,000) : NaI complexes. They observed that the solution deposited materials all contained crystalline lamellae of thickness 150 - 200 Å (1Å = 10^{-10}m). Annealing at temperatures just below the melting point gave rise to significant lamella thickening which increased with time. If the same material was heated to above its melting point and subsequently cooled, a lower melting point material was produced for the PEO:NaI system. This process was irreversible and not observed for the PEO : NaSCN system.

1.4 The structure of crystalline complexes

To date, very little structural work has been reported on any crystalline complexes formed with PEO. Indeed, until 1992, only three complete structure determinations had been presented, namely PEO_3NaI, PEO_3NaSCN and PEONaSCN[30,31]. Limited two dimensional information was available for the PEO_4KSCN complex[32].

Much of the earlier work probing the structure and bonding in polymer electrolyte crystalline complexes was obtained from vibrational spectroscopic and the X-ray diffraction studies of oriented fibres listed above. A common characteristic of all the structures studied was that they contained chains of PEO which adopted similar conformations to those observed in the pure polymer. Two crystalline modifications of PEO have been reported by Tadokoro et al[33,34,35]. The first modification has a helical structure which contains seven ethylene oxide units with two turns in the fibre identity period of 19.3Å. The internal conformations of the PEO chains were assigned by IR and Raman studies as follows :-

$-CH_2-O-$	trans
$-O-CH_2-$	trans
$-CH_2-CH_2-$	gauche

This is commonly abbreviated as TTG or T_2G.

In the second modification of PEO, the molecule adopts a planar zig-zag conformation containing two ethylene oxide units in the fibre identity period of 7.12Å. It should be noted however, that this conformation is only adopted when the polymer is under stress.

The earliest structural study of a polymer electrolyte crystalline complex was carried out by Fenton et al[1] who reported crystalline complex formation between PEO and some sodium and potassium salts. It was not until 1981 however, that detailed models for the nature of the coordination of the salt by the polymer were proposed. Papke et al[6] undertook a detailed study of the complexes formed with alkali metal salts using vibrational spectroscopic techniques. They determined that the PEO chains formed compressed helices in which the ether oxygen atoms were directed towards the centre of the channel. They proposed that small cations with ionic radii up to ~ 1.3Å could be accomodated in the channel, coordinated by the ether oxygens.

The complexes formed by rubidium and cesium salts were observed to be amorphous. This was ascribed to the inability of the helices to accomodate the large ions which thus formed random bridges between the ether oxygens on neighbouring

chains. The conformation of the polymer backbone in the sodium complexes was determined to be:-

$-CH_2 - O -$	trans	$CH_2 - O -$	trans
$- O - CH_2 -$	trans	$- O - CH_2 -$	trans
$- CH_2 - CH_2 -$	gauche	$- CH_2 - CH_2 -$	gauche minus

i.e T_2GT_2G

The repeat distance of the helix in the complexes was observed to be approximately 9 - 11 Å, which showed a marked reduction compared to the 19.3Å in pure (helical) PEO. In the sodium salt complexes, the Na^+ ion was observed to be coordinated by four ether oxygens in a highly distorted tetrahedron. This structure appeared to maximise polymer - Na^+ interactions whilst avoiding energetically unfavourable conformations for the polymer; namely, consecutive gauche bonds. No evidence for cation-anion interaction was observed in these complexes. Subsequent work by Parker et al[36] proposed a double helical model for the PEO_4KSCN and PEO_3NaSCN complexes. Shriver et al[37] however commented that this was unlikely since the proposed structure resulted in an unfavourable interaction between non-bonding groups due to the almost eclipsed conformation of some $OCH_2 - CH_2O$ groups.

Papke et al[38,11] subsequently carried out a vibrational spectroscopic study of complexes formed with a variety of lithium salts. A model similar to that for the sodium complexes was proposed, where the polymer host adopted the T_2GT_2G conformation. Some distortion of the conformation was necessary however to enable the polyether helix to 'wrap' round and coordinate the small lithium ion. Some evidence for ion pairing was observed for the PEO : $LiNO_3$ complex.

The first partial X-ray structure determination was performed by Hibma[32] in 1983 for the PEO_4KSCN complex. The most important feature of his proposed structure was that the potassium ions were not enclosed in the polymer helices as had previously been believed. It was not until 1987 however that a complete structural refinement of a polymer electrolyte complex was achieved by Chatani and Okamura for PEO_3NaI [30]. They determined that the crystals belonged to the monoclinic system

with space group $P2_1/a$. Na^+ and I^- ions were linked alternatively to form a zig-zag chain along the c-(chain) axis forming a 2_1 helix. (i.e. two Na^+I^- units to each zig-zag). The PEO backbone was determined to consist of six ethylene oxide units per fibre repeat period (7.98 Å) which assumed a 2_1 helix. Each symmetric unit containing three ethylene oxide units.(i.e. there were six ethylene oxide units for each complete turn of the helix). The polymer helix, which coiled around the Na^+I^- chain, was observed to have the following conformation:-

$$\underset{T}{-O-}\underset{T}{C-}\underset{G}{C-}\underset{T}{O-}\underset{T}{C-}\underset{G}{C-}\underset{T}{O-}\underset{T}{C-}\underset{\overline{G}}{C-}$$

Each Na+ ion was coordinated by three ether oxygen atoms and two I^- ions. The structure of the complex is shown in figure 1 - 5.

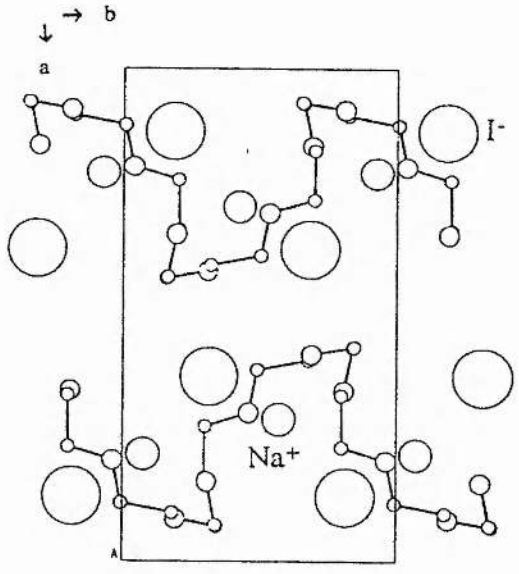

Figure 1 - 5 View of the PEO_3NaI structure along c

In 1990, Chatani et al[31] determined the structures of two PEO:NaSCN complexes, PEO_3NaSCN and PEONaSCN. The structure of PEO_3NaSCN was observed to be similar to PEO_3NaI with the exception that there was six-fold coordination of the ions instead of five-fold coordination. Each Na^+ ion was coordinated by four ether oxygen atoms and two N atoms from SCN^-. No Na^+ - S interactions were reported. It was

postulated that the different cation coordination resulted from the slightly larger fibre repeat distance (7.98Å) in the PEO : NaI complex.

The PEONaSCN complex was only observed to exist when the polymer was under tension. The polymer adopted a zig-zag structure with conformation :-

$$\underset{T}{-O-}\underset{G}{C-}\underset{G}{C-}\underset{T}{O-}\underset{\bar{G}}{C-}\underset{\bar{G}}{C-O-}$$

Each Na^+ ion was coordinated by two N atoms and two S atoms from the SCN^- ions as well as two ether oxygen atoms from the same chain. The instability of the TG_2TG_2 conformation of the PEO chain was further illustrated by the fact that when the tension was released, the PEO_3NaSCN complex was observed to form. No appreciable free NaSCN was observed after this transformation and it was postulated that the excess salt dissolved in the amorphous regions of the polymer.

Recent developments in powder X-ray diffraction techniques have enabled the structure of the PEO_3NaClO_4 complex to be elucidated in this laboratory[39]. This is described in more detail in appendix 1.

1.5 Phase diagrams

Much of the early work in the field of polymer electrolytes concentrated on determining the factors affecting the conductivities of each system. In particular, the interdependence of ionic conductivity and the nature and proportion of the different phases present was of great interest. It was established quite early on[40] that the motion of ions through the amorphous regions of the polymer was responsible for the significant conductivities of these systems.

As mentioned in section 1.2, many PEO based polymer electrolytes contain at least three phases; crystalline PEO, a crystalline complex formed between the polymer and the salt and inter- and intra- crystalline amorphous phases. To explain the variations in

conductivity of the polymer electrolyte systems as a function of composition and temperature, it was of vital importance to establish which phases were present in the system at any given time. This information is most clearly presented in the form of a phase diagram.

Vincent[41] has commented that phase diagrams for polymer electrolyte systems should be approached with great caution. The sluggish nature of the transport processes and crystallisation kinetics in polymers at low temperatures in particular, mean that it is only generally possible to *approach* conditions of thermodynamic equilibrium. It is well established that even polymers regarded as 'crystalline' contain amorphous regions that are not in thermodynamic equilibrium. Lee and Crist[42] have discussed the fact that in polymer electrolyte systems, these regions may often contain salts dissolved up to a certain saturation limit. Because they appear to occur reproducibly, these regions are often treated as single phases for the purposes of phases diagram construction.

The emphasis of much of the earlier work in polymer electrolytes was on systems containing salts of alkali metals dissolved in PEO. It is for this reason that most of the phase diagrams that have been determined today are for those systems containing salts of monovalent ions. The growth of interest in polymer electrolytes containing salts of multivalent cations has led to recent determination of the phase diagrams for some of these systems. It would be fair to comment however, that as a general rule, these systems are less well understood than their monovalent counterparts.

The most commonly used techniques for determining phases diagrams are differential scanning calorimetry (DSC), X-ray diffraction and hot stage polarising microscopy. Some workers [40,43,44] have used NMR to determine the fractions of ions in the amorphous and crystalline regions of the polymer. The most recent developments in the technology of X-ray diffraction have enabled patterns to be

recorded at elevated temperatures. This powerful technique, at present in use in this laboratory, greatly simplifies the identification of the crystalline phases present and helps in the assignment of DSC thermal events to processes occurring in the electrolyte.

It is found that the phase diagrams for polymer electrolyte systems often have many features in common. These are illustrated with reference to some specific systems below.

1.5.1 *The PEO : $LiCF_3SO_3$ system*

The earliest studies [40,43,44] of the PEO : $LiCF_3SO_3$ system using DSC and X-ray diffraction techniques established the existence of two crystalline phases. Phase I, which was PEO rich, was observed to have a melting point close to that for pure PEO. It was proposed that phase II, which was richer in salt and had a higher melting point, was the result of stoichiometric complexation of the salt by the polymer. It was originally believed that this complex had a composition of $PEO_4LiCF_3SO_3$, but later studies[40,44] using NMR techniques established that the complex composition was in fact $PEO_{3.5}LiCF_3SO_3$. Neat et al [24,25] determined that both crystalline phases were spherulitic in nature and suggested that phase I consisted of a pure PEO crystalline skeleton with salt dissolved in the interlamellar amorphous regions. Sorensen and Jacobsen[46] proposed a schematic phase diagram for polymer electrolyte systems containing both crystalline and amorphous phases (figure 1 - 6). They produced a phase diagram for the PEO : $LiCF_3SO_3$ system that was in agreement with this. Although they proposed the existence of a eutectic in the region of $PEO_{50}LiCF_3SO_3$, a later study by Minier et al[44] argued against its existence. The argument was to continue when Robitaille and Fateux [47] produced evidence for a eutectic in the region of $PEO_{100}LiCF_3SO_3$ from optical microscopy experiments. The most recent study by Zahurak et al[48] suggested that these observations could be explained by the presence of a second complex. Having obtained X-ray diffraction

evidence for a complex of composition $PEO_7LiCF_3SO_3$, they argued against the existance of a eutectic. Two schools of thought still exist regarding the presence of a eutectic in this system. This further illustrates the difficulty in unambiguous interpretation of the data necessary for phase diagram construction.

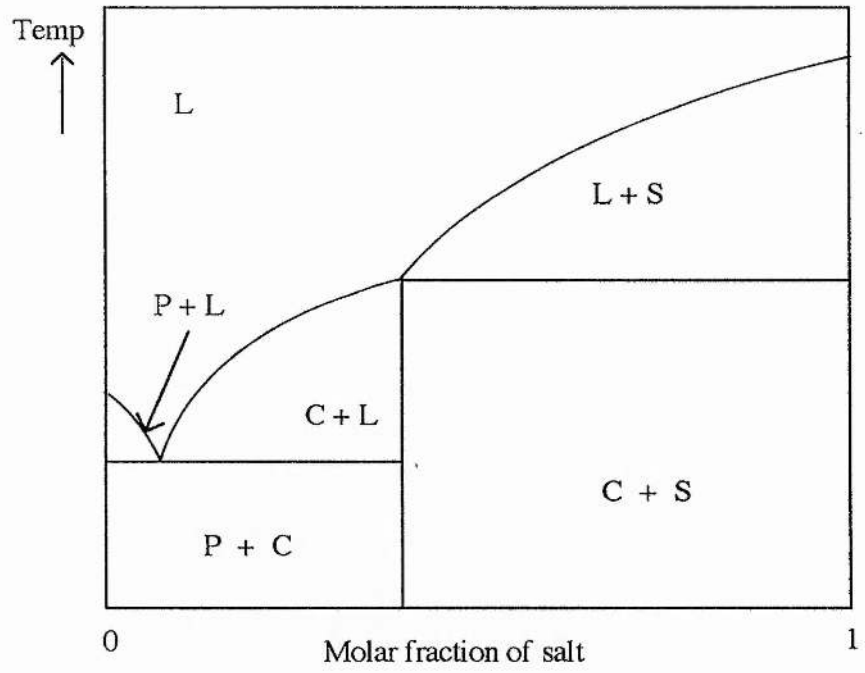

Figure 1 - 6 A schematic phase diagram [46] for a polymer electrolyte system containing PEO (P), crystalline complex(C), salt (S) and an amorphous phase (L)

The form of the phase diagram in figure 1 - 7 ,which can be considered as being made up of two subsystems, each with a eutectic, is adopted by a variety of other polymer electrolyte systems including PEO : NH_4SCN, PEO : $LiAsF_6$ and PEO : $LiBF_4$[10].

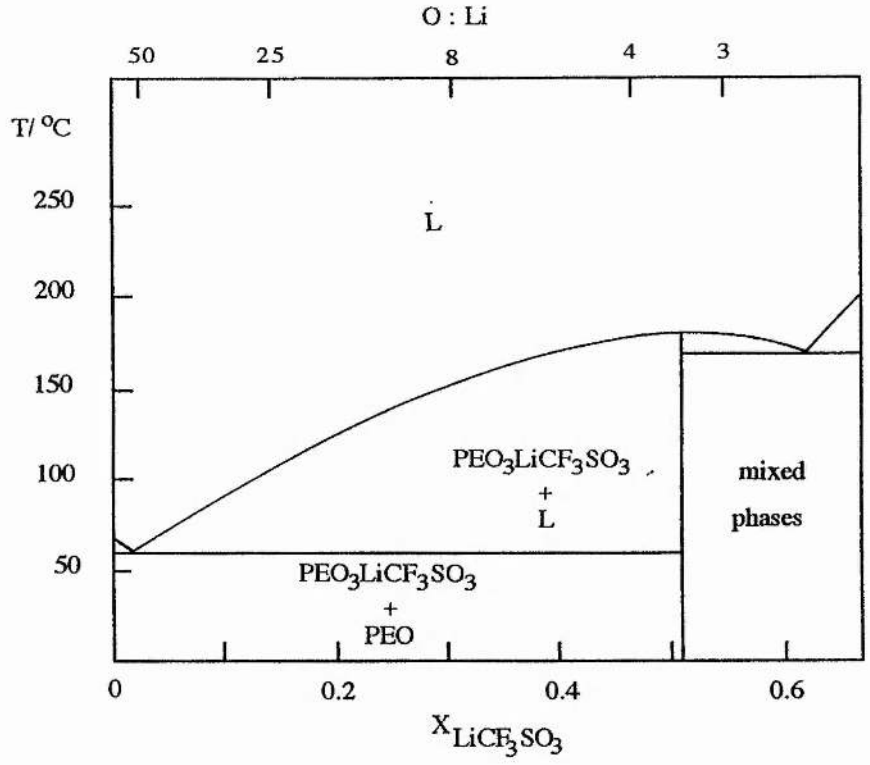

Figure 1 - 7 The phase diagram for the PEO : $LiCF_3SO_3$ system [10]

1.5.2 *The PEO : NaSCN system*

The earliest study of PEO : NaSCN mixtures was carried out by Lee and Crist[42] using DSC, optical microscopy and X-ray diffraction techniques. They proposed that a complex of composition $PEO_{3.5}NaSCN$ was formed and obtained evidence for a eutectic of composition $PEO_{37.5}NaSCN$. In their experiments however, no precautions were taken to avoid contamination of the samples with water vapour.

A subsequent study by Robitaille et al[49] produced a phase diagram (figure 1 - 8) with many similar features to that proposed by Lee and Crist. They proposed a complex of composition PEO_3NaSCN and a eutectic of composition $PEO_{25}NaSCN$. A high temperature feature of the system was the incongruent melting of the crystalline complex above 182°C to produce the pure solid salt and a liquid, the peritectic liquid.

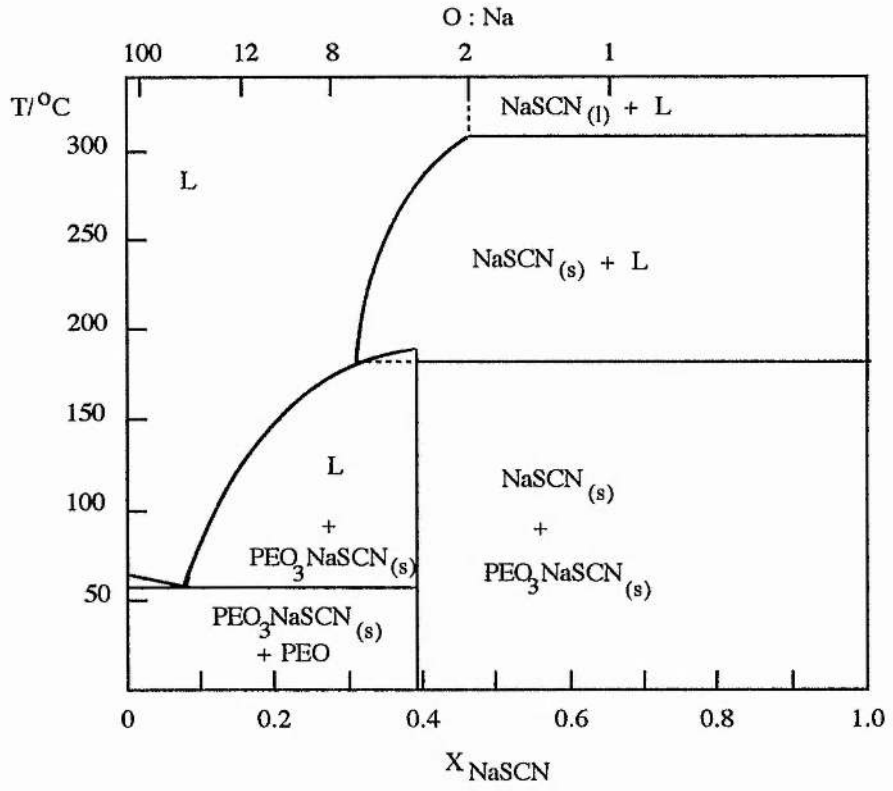

Figure 1 - 8 The phase diagram for the PEO : NaSCN system [49]

Analysis of DSC endotherms enabled them to determine that the composition of the peritectic liquid was PEO_4NaSCN. The peritectic reaction could thus be represented by the following equation:-

$$4\ PEO_3NaSCN_{(s)} \rightleftharpoons 3\ PEO_4NaSCN_{(l)} + NaSCN_{(s)}$$

They observed that the solubility of the salt remained essentially invariant with ether oxygen:Na^+ ratio of 4:1, over a large temperature range above the peritectic equilibrium. This was interpreted[50] as indicating that well defined solvates formed in liquid PEO.

$$Salt_{(s)} \rightleftharpoons Salt_{(l)} \qquad (a)$$

$$nPEO_{(l)} + Salt_{(l)} \rightleftharpoons PEO_nSalt_{(l)} \qquad (b)$$

Thus, below ~240°C, salt dissolution (a) is controlled by the solvation reaction (b), the solution concentration at saturation being equal to the solvate composition.

The phase diagram for the PEO : NaSCN system closely resembles those for the PEO : KSCN[49] and PEO : NaI[51] systems. Both of these systems form a single stoichiometric crystalline complex (PEO_4KSCN and PEO_3NaI) and undergo a peritectic reaction at elevated temperatures. The PEO : KSCN system differs slightly in that a crystallinity gap is observed between the 8:1 and 12:1 ether oxygen : K^+ compositions; i.e in this composition range, there is an absence of crystalline phases at any temperature. It is not therefore possible to determine whether a eutectic mixture is formed.

1.5.3 *The PEO : $ZnCl_2$ system*

Bermudez et al [52] used DSC and X-ray diffraction techniques to determine the phase diagram for the PEO : $ZnCl_2$ system. Two complexes were observed to form with composition PEO_xZnCl_2 , x = 22 and x = 4 to 6 as well as two eutectics with composition x = 14 and x = 34 as shown in figure 1 - 9.

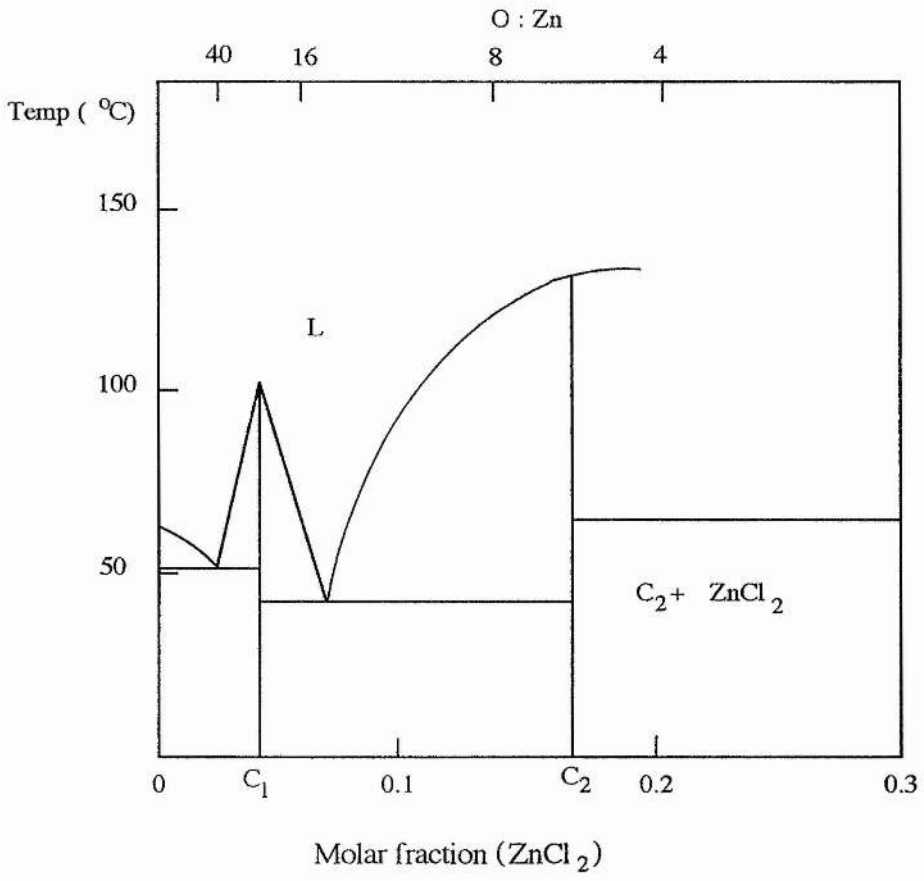

Figure 1 - 9 The phase digram for the PEO / $ZnCl_2$ system[52]

1.5.4 *The PEO : $Cu(CF_3SO_3)_2$ system*

The PEO : $Cu(CF_3SO3)_2$ system shown in figure 1 - 10 is very similar to that for the PEO:$ZnCl_2$ system. Two eutectics are observed in the region of $PEO_xCu(CF_3SO3)_2$ where x = 6 and x = 11. The regions of the phase diagram have been described in terms of the eutectic compositions. Although this is strictly not accurate, the precise compositions of the components were possibly difficult to determine due to the low number of data points. Passerini et al [53] commented on the highly amorphous nature of compositions that are rich in salt. Although crystalline material was present, they did not report the stoichiometry of any specific crystalline complex.

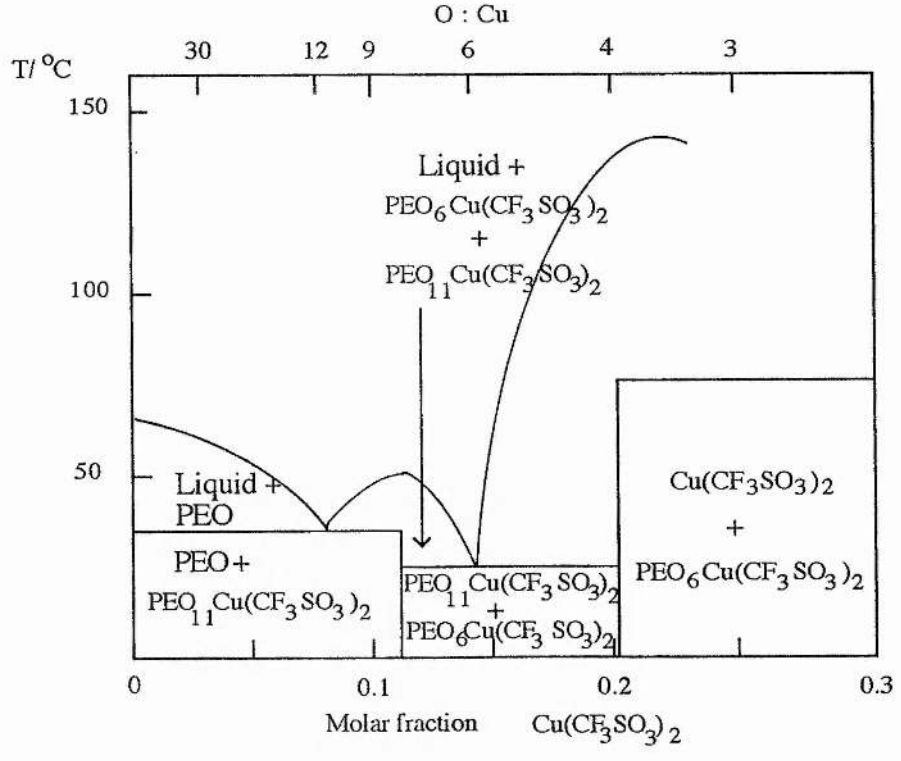

Figure 1 - 10 The phase diagram for the PEO / $Cu(CF_3SO_3)_2$ system [53]

1.5.5 *The PEO : $Eu(CF_3SO_3)_3$ system*

Work has been progressing by Smith et al. to determine the phase digram for the PEO: $Eu(CF_3SO_3)_3$ system. A preliminary phase diagram has been reported[54] as shown in figure 1 - 11.

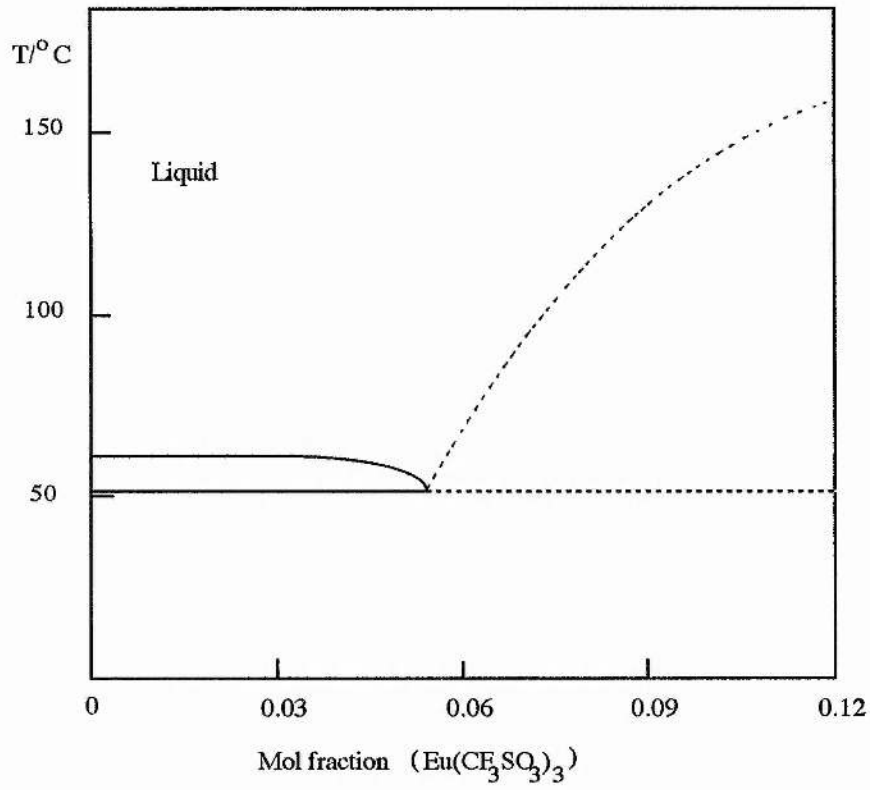

Figure 1 - 11 The phase diagram for the PEO / $Eu(CF_3SO_3)_3$ system[54]

1.6 Aspects of ionic conductivity in polymer electrolytes

1.6.1 *Introduction*

The way in which the ionic conductivity of a polymer electrolyte varies with temperature is very characteristic of such electrolytes. Many studies have focussed on determining $\sigma(T)$, the conductivity as a function of temperature. Several attempts have been made to model and explain the observed temperature dependence. The earliest studies [3] showed that over certain temperature ranges, many $\sigma(T)$ curves followed either Arrhenius behaviour (box 1) or Vogel-Tamman-Fulcher[55] (VTF) behaviour (box2).

Box 1

Arrhenius behaviour :-

$$\sigma = A \exp (-E_a / RT)$$

A is a constant
E_a is the activation energy for the process

Box 2

VTF behaviour :-

$$\sigma = \sigma_o \exp [-B/ (T - T_o)]$$

σ_o is weakly temperature dependent; $\sigma_o \propto T^{-1/2}$
T_o is a reference temperature
B is a constant

It has subsequently been found that most polymer electrolytes show one of four patterns of behaviour:-

a) VTF behaviour over the observable temperature range.

b) Arrhenius behaviour for low temperatures and VTF behaviour at higher temperatures.

c) Arrhenius behaviour over the whole temperature range falling into two regions. One with high activation energy close to the glass transition temperature Tg and the second with a lower activation energy at higher temperatures.

d) VTF behaviour for temperatures just above Tg but Arrhenius behaviour at higher temperatures.

Theoretical models for the conductivity of polymer electrolytes have encompassed the free volume theory of Cohen and Turnbull[57], the configurational entropy theory of Adam, Gibbs and DiMarzio[58,59] and the dynamic bond percolation theory of Ratner, Nitzan and Druger[61,62]. These models,which often expand on the ideas of Williams, Landel and Ferry, are sketched in more detail below.

1.6.2 *Williams, Landel and Ferry (WLF) theory*

Williams, Landel and Ferry[56] investigated the mechanical and electrical relaxation processes characterizing glass forming materials. They observed that the ratio,a_T, of any relaxation time at a temperature T (above Tg) to its value at a reference temperature T_s, determined from a variety of experiments, was identical. Furthermore, by suitable choice of T_s it was found that a_T as a function of $T - T_s$ was identical for a variety of polymers and glass forming materials. This relationship was observed to hold over the range $T \simeq T_s \pm 50$ °C. For the systems studied, it was found that $T_s - Tg = 50 \pm 5$°C. Modification of a VTF type equation for the viscosity:-

$$\log \eta = A + B/(T - T_\infty) \qquad 1 - ii)$$

(where A , B and T_∞ are constants and $T_\infty \ll Tg$) yielded an analytical form for the shift factor a_T:-

$$\log a_T = \frac{-C_1(T - T_s)}{(C_2 + T - T_s)} \qquad 1 - iii)$$

where a fit was obtained for their data with $C_1 = 8.86$ and $C_2 = 101.6$.

The expression was in good agreement with experimental data except where $T < Tg$.

The equation could also be written in terms of Tg as the reference temperature.

$$\log a_T = \frac{-17.44(T-Tg)}{(51.6 + T - Tg)} \qquad 1 - iv)$$

Williams et al commented however that it was less precise.

Using the Doolittle equation , which related viscosity to free volume:-

$$\ln \eta = \ln A + Bv_0 / v_f \qquad 1 - v)$$

(where v_0 and v_f were the occupied and free volume per g), they were able to obtain an expression for the shift factor in terms of the fraction of free volume (f_g) at Tg and the difference in the thermal expansion coefficients above and below Tg (α_2).

$$\log a_T = \left(\frac{-1}{2.303\, f_g}\right)\left(\frac{T - T_g}{f_g/\alpha_2 + T - T_g}\right) \qquad 1 - vi)$$

This was observed to be of the same form as equation 1 - iv). Thus by equating the coefficients in each expression $\alpha = 4.8 \times 10^{-4} K^{-1}$ and $f_g = 0.025$.

1.6.3 *Free volume theory*

Free volume theory was most clearly presented by Cohen and Turnbull in their paper of 1959 [57]. They proposed that molecular transport occurred as the result of the movement of molecules into voids greater than a certain critical size formed by the redistribution of the free volume of the system. They suggested that diffusive motion would occur if another molecule jumped into the hole vacated by the first before it could return. They defined the free volume of the molecule to be equal to the volume of the molecule in its cage less that occupied by the molecule itself. The contribution of each molecule, with gas kinetic velocity u, to the diffusion coefficient was given by :-

$$D(v) = ga(v)u \qquad 1 - vii)$$

where a(v) was the cage diameter and g a geometric factor.

For the contribution to be non-zero, the volume of the void had to be greater than a critical value v*. Cohen and Turnbull determined the total probability of a hole with volume > v* and thus obtained an expression for the diffusion coefficient :-

$$D = ga^*u \exp (-\gamma v^*/v_f) \qquad 1 - viii)$$

where a* is the molecular diameter and γ is a numerical factor to take account of the overlap of free volume. They then considered the temperature dependence of the free volume:-

$$v_f = \alpha \bar{v}_m (T - T_0) \qquad 1 - ix)$$

where $\bar{v}_m$ was the mean molecular volume in the temperature range, T_0 the temperature at which the free volume disappears and α as before. The full expression for the diffusion coefficient derived was thus:-

$$D = ga^*u \exp \left[\frac{-\gamma v^*}{\alpha \bar{v}_m (T - T_0)} \right] \qquad 1 - x)$$

This expression could be related to the conductivity via the Nernst- Einstein relationship:-

$$\sigma = \frac{nq^2D}{kT} \qquad 1 - xi)$$

where n is the carrier concentration and q the carrier charge. Thus :-

$$\sigma = \sigma_0 \exp [-B / (T - T_0)] \qquad 1 - xii)$$

σ_0 can be seen to vary with $T^{-1/2}$ since it contains the term u (where $u = [3kT/m]^{1/2}$). It can thus be seen that the expression for conductivity derived from free volume theory is of the VTF form.

1.6.4 *Configurational entropy theory*

The configurational entropy model was first proposed by Gibbs and DiMarzio in 1958 [58]. They proposed that the total configurational entropy of a system was a linear function of the fraction of bonds flexed out of their low energy orientations. The number of configurations available to the system at a given temperature thus varied with the number of flexed bonds. They were able to show that below a temperature, T_2, there could be no possible further reduction in the configurational energy of the system i.e. the system would remain in one of its lowest energy configurations. If the system could not crystallise, then this 'thermodynamically frozen' state could be identified with the glassy state. They thus predicted that at T_2 (where configurational entropy is zero) , the system would undergo a second order transition. They also suggested that the classically determined glass transition was not a true thermodynamic parameter since to some extent it depends on the timescale of the experiment.

In a subsequent paper[59] they commented that when there were departures from T-Tg = 50 °C by 5 or 10 °C, there were large deviations in the constants $C_1^{'}$= 17.44 and $C_2^{'}$= 51.6 in the WLF equation 1 - iv). They thus suggested that the 'universality' of the WLF expression was poor and searched for a statistical mechanical model. They constructed partition functions for the fractions of the system which could and could not undergo configurational rearrangements. They then used these functions to calculate the overall entropy in terms of the configurational entropy of the polymer subunits. In this way they were able to obtain an expression for the probability of a mass transporting cooperative rearrangement in the system:-

$$\overline{W} = \overline{A} \exp\left(\frac{-\Delta\mu s_c^*}{kTS_c}\right) \qquad 1 - xiii)$$

where s_c^* is the minimum configurational entropy required for rearrangement,

S_c is the configurational entropy of the system at temperature T,

$\Delta\mu$ is the free energy barrier per mol impeding the rearrangement and

A is a prefactor that is only weakly dependent on T.

The equation was derived on the basis that there was only a weak interaction between the cooperatively rearranging region and its environment.

Cohen and Turnbull then turned their attention to obtaining an expression for the WLF shift factor in terms of the transition probabilities derived from configurational entropy arguements. The relaxation time for the system is inversely related to the transition probability, i.e.:-

$$\tau(T) \propto 1/\overline{W}(T) \qquad 1 - xix)$$

Thus they were able to rewrite the logarithmic shift factor as shown in equation 1 - xx)

$$\log a_T = \log [\, \overline{W}(T_s) / \overline{W}(T) \,] \qquad 1 - xx)$$

which gave :-

$$-\log a_T = 2.303 \left(\frac{\Delta\mu s_c^*}{k}\right)\left[\frac{1}{T_s S_c(T_s)} - \frac{1}{TS_c(T)}\right] \qquad 1 - xxi)$$

Using the thermodynamic expression for entropy (1 - xxii), where ΔC_p is the difference in the specific heat capacity of the melt and the glass, they obtained equation 1 - xxiii).

$$S_c(T) - S_c(T_s) = \int_{T_s}^{T} \frac{\Delta C_p}{T} dT \qquad 1 - xxii)$$

$$S_c(T) - S_c(T_s) = \Delta C_p \ln\left(\frac{T}{T_s}\right) \qquad 1 - xxiii)$$

At T_2 the configurational entropy of the system is zero and thus :-

$$S_c(T_s) = \Delta C_p \ln\left(\frac{T_s}{T_2}\right) \qquad 1 - xxiv)$$

It was thus possible for Cohen and Turnbull to derive an expression for the logarithmic shift factor in the WLF form:-

$$-\log a_T = \frac{a_1(T - T_s)}{[a_2 + (T - T_s)]} \qquad 1 - xxv)$$

where

$$a_1 = \frac{2.303\,\Delta\mu s_c^*}{k\Delta C_p T_s \ln(T_s/T_2)}$$

$$a_2 = \frac{T_s \ln(T_s/T_2)}{\ln(T_s/T_2) + [1 + T_s/(T - T_s)]\ln(T/T_s)}$$

Unlike the originally proposed 'universal' WLF expression, one of the coefficients, a_2, was observed to be weakly temperature dependent. If the approximations that $\ln(T/T_2) \simeq (T - T_2)/T_2$ and $T/T_2 \simeq 1$ are made, then equation 1 - xiii) can be rewritten in the VTF form. i.e :-

$$\overline{W} = \overline{A} \exp[-K_\sigma/(T - T_2)] \qquad 1 - xxvi)$$

$$\text{where } K_\sigma = \frac{\Delta\mu s_c^*}{k\Delta C_p}$$

Papke et al [60] also derived an expression of the VTF form for the transition probability by taking $\Delta C_p = B\,T^{-1}$:-

$$\overline{W} = \overline{A} \exp [-K_\sigma / (T - T_2)] \qquad 1 - xxvii)$$

$$\text{where } K_\sigma = \frac{\Delta \mu s_c^* T_2}{kB}$$

The prefactor was slightly different to that derived by Cohen and Turnbull. By redefining the prefactor, Papke et al were able to obtain an expression for the conductivity virtually identical with equation 1 - xii)).

$$\sigma = A_\sigma T^{-1/2} \exp \{ -K_\sigma / (T - T_2) \} \qquad 1 - xxviii)$$

1.6.5 *Dynamic Bond Percolation (DBP) Theory*

The DBP theory of Druger, Ratner and Nitzan is the only microscopic model that has been developed to specifically describe the transport mechanisms in polymer electrolytes. Druger et al [61] have commented that although the free volume theory of Cohen and Turnbull characterises the conductivity of most polymer electrolytes fairly satisfactorily, it does have several drawbacks. It was originally intended to describe thermodynamic data, viscosity and relaxation behaviour of glass forming materials rather than to describe the diffusion of small molecules within polymeric materials. It is instructive to consider the discussion of Druger et al for the breakdown of free volume theory.

Using the arguments of free volume theory, they were able to derive diffusion coefficients for the ions and polymer segments in a material such as a polymer electrolyte.

$$D_{seg} = u_{seg} a_{seg} g \exp\{-\gamma v_{seg}^* / v_f\} \qquad 1 - xxix$$

$$D_{ion} = u_{ion} a_{ion} g \exp \{-\gamma v_{ion}^* / v_f\} \qquad 1 - xxx$$

where v_{seg}^* and v_{ion}^* are the critical void sizes for the polymer segments and ions respectively and the temperature dependence of v_f is given by equation 1 - ix).

At temperatures close to T_0, $v_f << v^*_{seg}$ and the rate of free volume reorganisation is small. At the same time however, $v_f > v_{ion}$. Free volume theory would thus predict that at temperatures where there is little reorganisation of free volume, there is facile ion diffusion. This is clearly a breakdown of the theory for polymer electrolytes.

In DBP theory, Druger et al take account of the fact that ion hopping may occur on timescales faster than the typical reorganisation times of the polymer host. The motion of the ions is described by a percolation model. The probability of an ion hopping between two sites varies between zero (bond closed, site unavailable) and a finite limit (bond open, site accessible). Since the polymer is in continuous motion ($T > T_0$), the complexion of the open or closed bonds is also continuously changing. In DBP theory, the hopping probabilities are allowed to adjust on a timescale corresponding to the motion of the polymer host.

$$P_i = \sum_{j \neq i} \{ P_j(t)\, w_{j \to i} - P_i(t)\, w_{i \to j} \} \qquad 1 - xxxi)$$

where P_i is the probability of occupying a site j at time t and w is the hopping probability. The hopping probabilities (equation 1 - xxxii) assigned as available (w) and unavailable (0) change at a rate $(\tau_{ren})^{-1}$ where τ_{ren} is the time for the 'solvent' motion process.

$$w_{i \to j} \quad \begin{cases} 0 & \text{i,j not neighbours} \\ 0 & \text{bond (i,j) not available} \\ w & \text{bond (i,j) available} \end{cases} \qquad 1 - xxxii)$$

The reassignment of bonds is assumed to be completely random and irrespective of previous assignments.

Full analysis of DBP theory is quite complex but the most important results have been discussed by Ratner[62] and Druger et al[61]. They comment that the system shows diffusive behaviour for observation times (τ_{obs}) where $\tau_{obs} >> \tau_{ren} >> 1/w$. Thus the mean squared displacement is proportional to the observation time. On a one dimensional model, an ion may hop until it is stopped by a closed bond. It then has to wait on a timescale τ_{ren} for the bond assignment to change. The rate of diffusion (and

therefore conductivity) is thus proportional to the renewal rate. For very fast renewal rates, $w^{-1} >> \tau_{ren}$, the motion corresponds to hopping in a homogeneous non-percolating system with an effective hopping rate wf (where f is the fraction of available bonds). For very slow renewal rates, the motion is simply that predicted by the static bond percolation model and is no longer diffusive. The mean squared displacement is then given by:-

$$\langle x^2 \rangle = fa^2 / (1 - f)^2 \qquad 1 - xxxiii)$$

where a is the distance between 'lattice' sites. The model has also shown that the diffusion coefficient (and therefore conductivity) in a system undergoing dynamic percolation (D_{dy}) is related to that undergoing static percolation (D_{st}) in the same lattice:-

$$D_{dy}(\omega) = D_{st}(\omega - j/\tau_{ren}) \qquad 1 - xxxiv)$$

where ω is the frequency. It can thus be seen that the frequency dependent properties of the system can be modelled by DBP theory. Secondly, knowledge of the hopping behaviour in a frozen polymer host together with the value of the renewal time for the host determines the full frequency dependent conductivity of the ions.

1.7 Transference numbers in polymer electrolytes

Having established that many polymer electrolyte systems were characterised by significant ionic conductivities, it became of great importance to identify the charge carrying species. Attention therefore turned to the determination of transport numbers in polymer electrolyte systems. For an electrolyte which dissociates into a single cationic and anionic species, the cationic transport number t_+ is defined as the fraction of total charge carried through a reference plane fixed relative to the solvent.

$$MX \rightleftharpoons M^+ + X^-$$

$$t_+ = i_+ / (i_+ + i_-)$$

$$= i_+ / i \qquad \text{1 - xxxv)}$$

(where i_+ and i_- are the partial currents carried by the cation and anions respectively and i is the total current.)

The experimental parameter often measured however, is the gross transference number T_+. This is due to the fact that the current may not only be carried by simple ions but also by triple and higher aggregate ions. The transference number is thus the fraction of the total current carried across the reference plane by the cation containing species (i.e. M^+, M_2X^+, $M_3X_2^+$....). A range of techniques have been used by different groups for the determination of transference numbers which have been reviewed by Vincent[41] and Gray[10]. Transference numbers determined are found to be affected by the conditions used for the preparation of the electrolyte. Thus measurements obtained for nominally identical compositions may be vastly different. Huq et al[4] observed this for samples containing $ZnCl_2$ where one was prepared from the anhydrous salt and another was prepared from the hydrated salt. A summary of the data obtained from the literature is shown in table 1-3 and 1-4.

For systems containing the Li^+ ion, the cation transference number consistantly falls in the range 0.15 - 0.3. Leveque et al[63] commented that their data indicated that T_{Li}^+ was independent of temperature and the nature of the anion. General agreement on these points has yet to be obtained. Some of the more recent measurements by Evans et al[64] have indicated a slightly higher Li^+ 'transference number' of 0.46 for $PEO_9LiCF_3SO_3$. This may be explained by the fact that the technique used by these workers measured the current fraction rather than T_+. This is the ratio of the final to

initial currents corrected for the formation of a passive layer on the lithium electrode and includes contributions from diffusion of neutral species e.g. Li^+X^-.

Farrington and Linford[13] have indicated that the cation contribution of divalent ions to the total conductivity is of the order:-

$$Cd^{2+} > Pb^{2+} > Cu^{2+} > Zn^{2+} > Ag^{2+},\ Ni^{2+},\ Mg^{2+},\ Ca^{2+},Co^{2+}$$

This order appears to result from a combination of factors including hardness of the ion, ionic radius, water exchange rate and electronegativity. It is clear from table 1-4 that small hard ions e.g Ca^{2+} and Mg^{2+} tend to form materials that are predominantly anionic conductors. It has been proposed that the cations are trapped by the strong electrostatic interaction with the ether oxygen atoms on the polymer chains. Softer cations such as Cd^{2+} and Pb^{2+} form weaker associations with the 'hard' ether oxygen atoms. They thus provide a significant contribution to the ionic conductivity at temperatures greater than 130 °C.

The PEO : $NiBr_2$ system is of considerable interest since it has been demonstrated by Huq et al[4] that cation transport appears to be activated by controlled hydration and dehydration of the electrolyte. The reason for this phenomenon is as yet unclear.

1.8 The electrochemical stability of polymer electrolyte systems

The ether linkage in PEO is extremely unreactive. As well as being chemically inert, the ideal polymer electrolyte should have a wide electrochemical stability window, being tolerant of both oxidizing and reducing conditions.

The formation of a resistive layer at the lithium / polymer electrolyte interface was first reported by Armstrong et al[76] as a result of ac impedance measurements on the PEO:$LiCF_3SO_3$ and PEO:$LiClO_4$ systems. He suggested that a reaction was occurring between the lithium and the polymer rather than with the anion since it was not prevented by the use of the 'non-reducible' Br^-.

Salt	Composition PEO'O':M^{n+}	'T_+'	T(°C)	Comment	Reference
$LiClO_4$	?	~0.3	90		69
	8.2	0.42	132	Low purity solvent	66
	8.0	0.27	112	High purity solvent	66
	8	0.17 - 0.18	80 - 122		43
	6.0	0.23 - 0.29	80 - 122		43
	4.3	0.16 - 0.28	50 - 122		43
	8	0.3	70 - 150		67
	59	0.37	70 - 120	PEO (MW 1000) all	63 & 68
	36	0.30	70 - 120	amorphous polymer	63 & 68
	24	0.19	70 - 120	"	63 & 68
	20	0.23	70 -120	"	63 & 68
	12	0.23	70 - 120	"	63 & 68
	8	0.23	70 - 120	"	63 & 68
	20	0.23	90	"	63 & 68
	20	0.23	90	PEO (MW 3000) all	63 & 68
	30	0.17	90	amorphous polymer	63 & 68
$LiCF_3SO_3$	?	0.7	90		65
	9	0.46	90	Correction made for passivating layer on electrode	64
	24	0.21	70 - 120		63 & 68
Li I	?	~ 0.3	90		65
$NaClO_4$	36	0.17	92	PEO (MW 1000) all	63 & 68
$KClO_4$	36	0.20	90	amorphous polymer	63 & 68
$AgClO_4$	20	0.23	80	"	63 & 68

Table 1 - 3 : Transference numbers for PEO based polymer electrolytes containing monovalent cations

Salt	Composition PEO'O':M^{n+}	'T_+'	T (°C)	Comment	Reference
$MgCl_2$	16	> 0.005	100		69
$MgBr_2$	16	~ 0	100		4
$Mg(ClO_4)_2$	16	~ 0	100		4
$Ca(ClO_4)_2$	50	~ 0	75		70
$ZnCl_2$	8 - 24	0.01	100		4
	12	~ 0.09	20 - 80	Prepared from	71
	8	~ 0.09	20 - 80	hydrated salts	71
	4	~ 0.09	20 - 80	"	71
$ZnBr_2$	12 - 24	0.03	100		4
ZnI_2	12	0.19	100	Hydrated	72 & 73
	12	0.23	120	Hydrated	72 & 73
$CdBr_2$	8	0.4	100		4
	8	0.92	140		4
	8	1	150		4
$Hg(ClO_4)_2$	20	0.25	52		15
$PbBr_2$	20	0.6 - 0.7	140		74 & 75
	20	0.58	140		4
	20	0.70	160		4
$CoBr_2$	8	0	100 - 140		4
	16	0	100 - 140		4
$NiBr_2$	8	0.01 - 0.009	100 - 140	As cast polymer	4
	8	0.24 - 0.62	100 - 140	Hydrated/dehydrated	4
$Cu(CF_3SO_3)_2$	9	0.18 - 0.24	75		53

Table 1 - 4 : Transference numbers for PEO based electrolytes containing multivalent cations

A subsequent study by Fateux[77] on the PEO:$LiCF_3SO_3$ system in rigorously anhydrous conditions indicated that the reaction was not simply the result of residual water in the electrolyte. He proposed that at low salt concentrations, the lithium reacted with catalytic residues in the polymer. At higher salt concentrations, he proposed that an electrochemical reaction occurred with the salt, with the subsequent formation of LiF at the interface.

Some of the earliest systematic studies of the stability domains of polymer electrolytes were carried out by Armand and his co-workers using cyclic voltammetry. The results of these and parallel investigations were reviewed by Armand[78] and are summarised in table 1 - 5

Metal	Anion	Temp (°C)	Cathodic limit (V)	Anodic limit (V)
Li^+	I^-	85	0 (Li^0)	+ 2.8 (ox I^-)
Na^+	I^-	60	0 (Na^0)	+ 3 (ox I^-)
Li^+	ClO_4^-	100	0 (Li^0)	+ 4.3 (*)
Na^+	ClO_4^-	80	0 (Na^0)	+ 4.0 (*)
Li^+	$CF_3SO_3^-$	80	+ 0.5 (red X^-)	+ 4.8 (*)
Li^+	$CF_3SO_3^-$	130	0 (Li^0)	+ 3.5 (*)
Na^+	$CF_3SO_3^-$	80	0 (Na^0)	+ 4.9 (*)
Li^+	NO_3^-	110	+ 1 (red X^-)	+ 4.0 (*)
K^+	SCN^-	80	+ 1.5 (red X^-)	+ 3.5 (*)

Table 1 - 5 The electrochemical stability windows for some polymer electrolyte systems[78] (versus M^+ / M)
(*) Oxidation of the polymer or the anion

For most systems, the stability window appears to be of the order of between 3.0 - 4.5V. In the cathodic domain, the stability is limited by the metal deposition process. This is often not straightforward for lithium ion conductors. Lithium will form alloys with virtually all metal substrates. Bonino et al[79] investigated the plating and stripping of lithium from PEO based polymer electrolytes onto a variety of substrates. Formation of a monolayer of lithium on nickel required an overpotential of 250mV (Figure 1-12). Once this layer was formed, further deposition could occur below zero volts. The subsequent recovery of lithium on the anodic sweep increased in efficiency with faster scan rates. The freshly deposited lithium in this case had less opportunity to react either with the electrolyte to form a passive layer or with the substrate to form an alloy. When a stainless steel substrate was used (Figure 1-13), the overpotential required was less than for the nickel case. A double peak was however observed on the anodic sweep. Armand[78] had previously ascribed similar behaviour to alloy formation with the substrate.

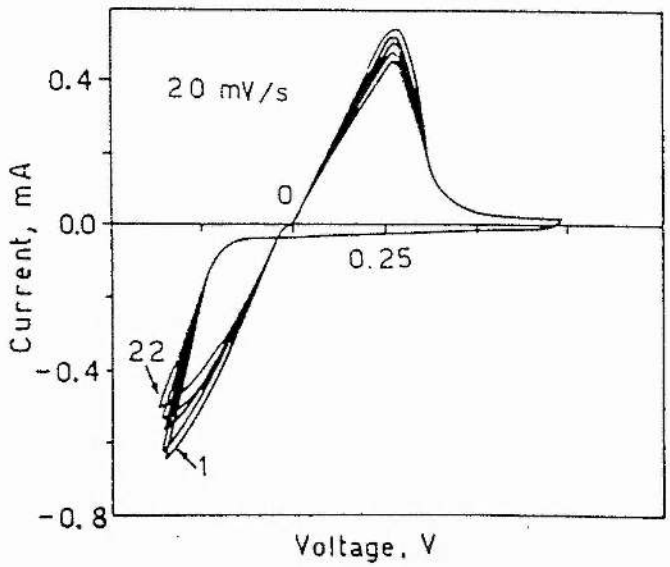

Figure 1-12 Cyclic voltammetry of the lithium plating stripping process. Nickel substrate; $PEO_9LiCF_3SO_3$ electrolyte at 80 °C.From ref [79]

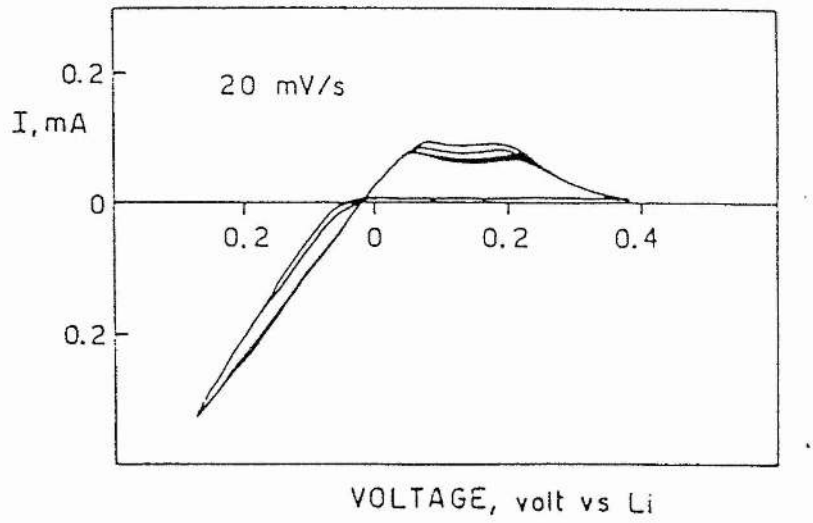

Figure 1-13 Cyclic voltammetry of the lithium plating-stripping process. Stainless steel substrate; $PEO_9LiCF_3SO_3$ electrolyte at 80 °C. From reference[79]

The stability in the anodic domain is limited by the oxidation of the anion. systems containing $LiCF_3SO_3$ and $LiClO_4$ have been observed to show oxidation peaks in the region of 4.0 - 4.5V versus Li / Li^+. It has been proposed that both ions are oxidised to the radical which subsequently reacts to degrade the polymer. The perchlorate and triflate ions are both fairly stable to reduction. Small parasitic reduction peaks have been observed in the PEO : $LiCF_3SO_3$ system in the region of + 0.5V versus Li / Li^+. There is some argument as to whether these are due to the reaction of the salt with the lithium to form the triflate radical and LiF or whether they result from the diffusion controlled reduction of water.

Abrantes et al[71] investigated the stability domain of PEO based polymer electrolytes containing $AgClO_4$, $Zn(ClO_4)_2$, $Cu(ClO_4)_2$ and $CuCl_2$. These were observed to be limited by the discharge of Zn^{2+}, Cu^{2+} and Ag^{+} in the cathodic region and Cl^- and ClO_4^- in the anodic region. The stability window of the $PEO_8Cu(ClO_4)_2$ system was shown to be temperature dependent. The window decreased from 1.80V at 26 ^{0}C to 1.07V at 85 ^{o}C, the change being dominated by a reduction in the anodic limit.

Armand et al[80] have investigated the redox behaviour of $Cu(CF_3SO_3)_2$ in both polyethylene glycol (PEG) and PEO. In PEG, plating and stripping of copper was observed however only a single cathodic and anodic peak were obtained. There was no evidence for multistep electrochemical processes. This was in contrast to the cyclic voltammogram obtained for the same system in PEO. This revealed a double peak response which was attributed to the subsequent reduction-oxidation of copper species in two oxidation states.

The most recent study of a system containing multivalent ions was carried out by Yang and Farrington[81] for the PEO:$ZnCl_2$ system containing LiBr as a supporting electrolyte. A single Zn^{2+}/Zn reduction peak and oxidation peak was observed for slow sweep rates and higher temperatures. At faster sweep rates and lower temperatures however, evidence for a second oxidation peak was obtained. Chronocoulometric studies indicated that the reduction of the Zn(II) species was controlled not only by diffusion but also migration. This was despite the presence of the 'supporting electrolyte'. It was proposed that the LiBr, rather than acting as a supporting electrolyte, formed a variety of complex species with the Zn(II) ions.

For systems containing multivalent ions, it is not an unusual occurrence for a single peak associated with metal deposition to be observed in the cathodic region of the cyclic voltammogram. Due to the complexity of the multistep process, the rate limiting step may be mass transport of species to the electrode, ad-atom formation, two dimensional diffusion of ad-atoms across the electrode surface or incorporation of ad-atoms into the lattice. Indeed the rate limiting behaviour of the the first or last of these

processes is a common phenomenon and thus separate peaks due to reduction of the M(II) and M(I) oxidation states may not be observed. The absence of separate peaks in the anodic domain is also common where one oxidation state is very unstable (e.g. Cu(I) or Zn(I)). The M(I) species may behave much like an activated complex, the kinetics of oxidation being rapid. That two oxidation peaks are observed in the PEO : $Cu(CF_3SO_3)_2$ and the PEO : $ZnCl_2$ systems is indicative of stabilisation of the M(I) state. This might be expected in the presence of the Cl^- ion in the latter system. That it occurs in the PEO : $Cu(CF_3SO_3)_2$ system is possibly indicative of stabilisation of Cu(I) by the PEO.

As yet, there have been relatively few investigations of polymer electrolyte systems containing redox couples e.g. Cu(II)/Cu(I), Co(III)/Co(II) or Eu(III)/Eu(II) due to the problem of preparation. A wealth of information on mass transport mechanisms and electron transfer processes in the electrolyte could be obtained from such systems. They invite investigation.

CHAPTER 2

FUNDAMENTAL PRINCIPLES OF ELECTROCHEMISTRY

2.1 Introduction

As part of this work, a variety of electrochemical studies of polymer electrolyte systems were undertaken. The following section contains a brief overview of the theory behind the electrochemical techniques used. More detailed reviews of the field may be found elsewhere.

In common with the IUPAC convention, in this work, anodic currents are considered positive and cathodic currents negative.

2.2 Mass transport and electron transfer processes

For the generalised cathodic reaction:-

$$\mathbf{O} + ne \rightleftharpoons \mathbf{R}$$

the rate of reduction and therefore the magnitude of the cathodic current may be either kinetically or mass transport controlled. Further complications may arise if there are coupled chemical reactions either preceding or following electron transfer or when a new phase is formed.

In general there are three possible contributions to mass transport; diffusion, convection and migration. The viscosity of high molecular weight polymer electrolytes is so great however, that the effects of convection in these systems is negligible. The use of a supporting electrolyte furthermore means that very little charge will be carried by the electroactive species due to migration. It can thus be seen that diffusion is the most important mechanism for mass transport in high molecular weight polymer electrolyte systems.

For a system in equilibrium where no net current is flowing, the relationship between the potential of the working electrode to the concentration of species at its surface is given by the Nernst equation:-

$$E_e = E_e^{\ominus} + \frac{RT}{nF} \ln \frac{C_O^{\sigma}}{C_R^{\sigma}} \qquad 2 - i)$$

Where $E_e^{\ominus}$ is the standard reduction potential and C_O^{σ} and C_R^{σ} are the concentrations of **O** and **R** at the electrode surface respectively. (It is assumed that the activity coefficients for both species are 1).

Since no net current flows at equilibrium, (and there is therefore no net chemical change), the concentrations of the species at the surface will be the same as those in the bulk . Thus $C_O^{\sigma} = C_O^{\infty}$ and $C_R^{\sigma} = C_R^{\infty}$.

It should be recalled that the partial current densities for the anodic reaction, $\overleftarrow{I}$, and cathodic reaction, $\vec{I}$, are dependent on the concentration of the electroactive species at the electrode and on the rate constant for electron transfer k.

$$\vec{I} = -nF\vec{k}C_O^{\sigma} \qquad 2 - ii)$$

$$\overleftarrow{I} = nF\overleftarrow{k}C_R^{\sigma} \qquad 2 - iii)$$

The rate constants for electron transfer vary with the applied potential E in the following way:-

$$\vec{k} = \vec{k}_o \exp\left(\frac{-\alpha_C nFE}{RT}\right) \qquad 2 - iv)$$

$$\overleftarrow{k} = \overleftarrow{k}_o \exp\left(\frac{\alpha_A nFE}{RT}\right) \qquad 2 - v)$$

(α_C and α_A are the electron transfer coefficients for the cathodic and anodic reactions respectively and k_o is the rate constant for the cathodic or anodic process at 0 V versus the reference electrode. For a simple electron transfer reaction it is usually found that $\alpha_C + \alpha_A = 1$).

The magnitude of the partial current densities at equilibrium is known as the exchange current density (I_0).

$$I_0 = -\vec{I} = \overleftarrow{I} \qquad 2 - vi)$$

2.3 Derivation of the Butler - Volmer Equation

Using the information from the previous section, it is possible to derive an expression relating the net current density to the applied overpotential. The overpotential (η) is simply the deviation of the potential of the working electrode, (E), from the equilibrium value, (E_e).

$$E = E_e + \eta \qquad 2 - vii)$$

Substitution of equations (2 - ii) to (2 - v) into (2 - vi) gives :-

$$I = nFC_R^{\sigma}\overleftarrow{k_o}\exp\left[\frac{\alpha_A nF(\eta + E_e)}{RT}\right] - nFC_O^{\sigma}\vec{k_o}\exp\left[\frac{-\alpha_C nF(\eta+E_e)}{RT}\right] \qquad 2 - viii)$$

At equilibrium :-

$$I_0 = nFC_R^{\sigma}\overleftarrow{k_o}\exp\left[\frac{\alpha_A nFE_e}{RT}\right] \qquad 2 - ix - a)$$

$$= nFC_O^{\sigma} \vec{k}_o \exp\left[\frac{-\alpha_C nFE_e}{RT}\right] \qquad 2 - ix - b)$$

Manipulation of equations 2 - viii) and 2 - ix) using the relationship exp(x) exp(y) = exp(x+y) then leads to the Butler-Volmer equation.

$$I = I_0 \left[\exp\left(\frac{\alpha_A nF\eta}{RT}\right) - \exp\left(\frac{-\alpha_C nF\eta}{RT}\right) \right] \qquad 2 - x)$$

Three limiting forms of the Butler-Volmer equation are commonly used.

2.3.1 *High positive overpotentials*

At high positive overpotentials, the rate of the anodic reaction is very much greater than the rate of the cathodic reaction. The second term in the Butler-Volmer equation then becomes negligible. The net current density is thus approximated by the anodic current density:-

$$\log I = \log I_0 + \left(\frac{\alpha_A nF\eta}{2.3RT}\right) \qquad 2 - xi)$$

2.3.2 *High negative overpotentials*

By a similar argument, the cathodic current density is given by :-

$$\log(-I) = \log I_0 - \left(\frac{\alpha_C nF\eta}{2.3RT}\right) \qquad 2 - xii)$$

2.3.3 *Small overpotentials*

For situations where the overpotential is very small, ($\eta \ll \frac{RT}{\alpha nF}$), the exponential terms in the Butler-Volmer equation may be expanded as a series. Since the quadratic and higher order terms are negligible, the net current density is given as:-

$$I = I_0\left[\frac{\alpha_A nF\eta}{RT} + \frac{\alpha_C nF\eta}{RT}\right] \qquad 2 - xiii)$$

This can be further simplified using the relationship $\alpha_A + \alpha_C = 1$.

$$I = \frac{I_0 nF\eta}{RT} \qquad 2 - xiv)$$

2.4 The Tafel Equations

The limiting forms of the Butler-Volmer equation for high overpotentials given by equations 2 - xi) and 2 - xii) are known as the Tafel equations and provide a simple method for determining the exchange current density, I_o, and the transfer coefficients α_A and α_C. A graph of log I against overpotential, obtained for example from cyclic voltammetry, will be of the form shown in figure 2-1.

At large positive and negative overpotentials, the Tafel equations are valid and the graph of log I against overpotential is linear. The transfer coefficients may thus be obtained from the gradients of the graph in these regions. Extrapolation of the linear regions back to zero overpotential yields the exchange current density.

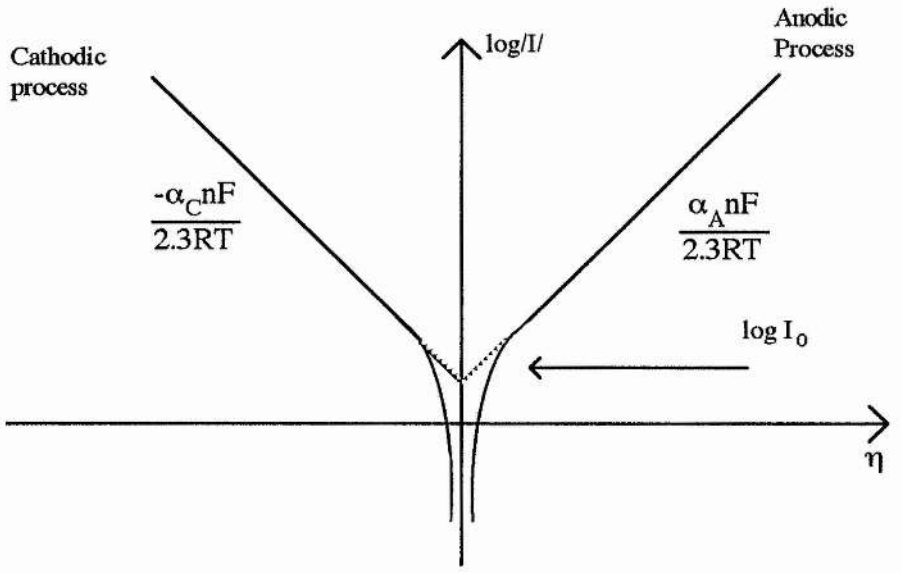

Figure 2-1 Determination of the exchange current density and transfer coefficients using the Tafel equations.

The exchange current density varies with the concentrations of **O** and **R** at the *surface* of the electrode. Manipulation of equations 2 -i) and 2 - ix) to at equilibrium leads to the following expression:-

$$I_0 = nFk_0^{\ominus}(C_O^{\infty})^{\alpha_A}(C_R^{\infty})^{\alpha_C} \qquad 2 - xv)$$

where $k_O^{\ominus}$ is the standard rate constant for electron transfer (both oxidation and reduction) at the standard potential , $E_O^{\ominus}$. In this way, the exchange current density is specified for all potentials in terms of determinable quantities.

2.5 Linear diffusion to a planar electrode

As mentioned earlier, diffusion is one of the most important mechanisms for mass transport in polymer electrolyte systems containing a supporting electrolyte. A more quantitative understanding of diffusion comes from a consideration of Fick's laws. A simple model for the treatment of diffusion in the systems under investigation is commonly used. It is assumed that concentration gradients exist only in a direction perpendicular to the electrode surface and that the electrode itself is completely flat and of infinite dimensions. The regime is thus one of linear diffusion to a planar electrode and can be characterised by Fick's laws in one dimension.

Ficks first law states that the rate of diffusion (or flux) of a species i through a plane parallel to the electrode surface is proportional to the concentration gradient:-

$$\text{Flux} = -D_i \frac{dc_i(x)}{dx} \qquad 2 - \text{xvi})$$

Fick's first law can be used to relate the current density to the flux of species **O** and **R** at the electrode surface (x=0). By the laws of conservation of mass, the flux of **O** must be equal (and opposite) to the flux of **R**. Interconversion of **O** and **R** requires I/nF electrons. From Fick's first law, the net current density at the electrode can be found (Figure 2.2).

$$\frac{I}{nF} = -D_O \left(\frac{\partial C_O(x)}{\partial x} \right)_{x=0} \qquad 2 - \text{xvii} - \text{a})$$

$$= D_R \left(\frac{\partial C_R(x)}{\partial x} \right)_{x=0} \qquad 2 - \text{xvii} - \text{b})$$

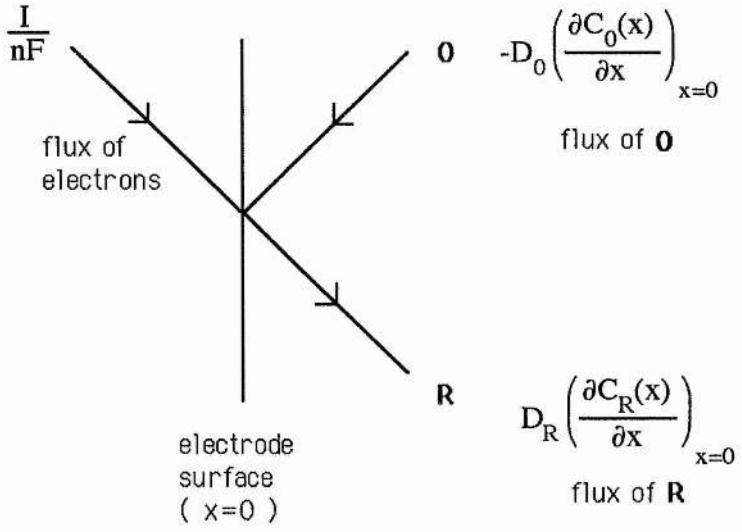

Figure 2-2 The relationship between the flux of electrons and the flux of species **O** and **R** at the electrode surface for the reaction $\mathbf{O} + ne \rightarrow \mathbf{R}$.

2.6 The potential step experiment

In a potential step experiment, the potential of the working electrode is stepped instantaneously from one potential to a different potential. The current - time response (chronoamperometry) or the charge - time response (chronocoulometry) of the system is recorded. Analysis of the response of the system can give an insight into the kinetic and / or mass transport processes occurring.

If for example, a system, initially containing **O** but no **R** is stepped from a potential well positive of the equilibrium potential, E_e, to one well negative, the surface concentration of **O** will change from C_O^{∞}, the bulk value, to zero. Diffusion will then occur to minimise the resulting concentration gradients which become less steep and extend further into the solution with time. Figure 2-3 shows how the concentration profiles for species **O** and **R** develop with time.

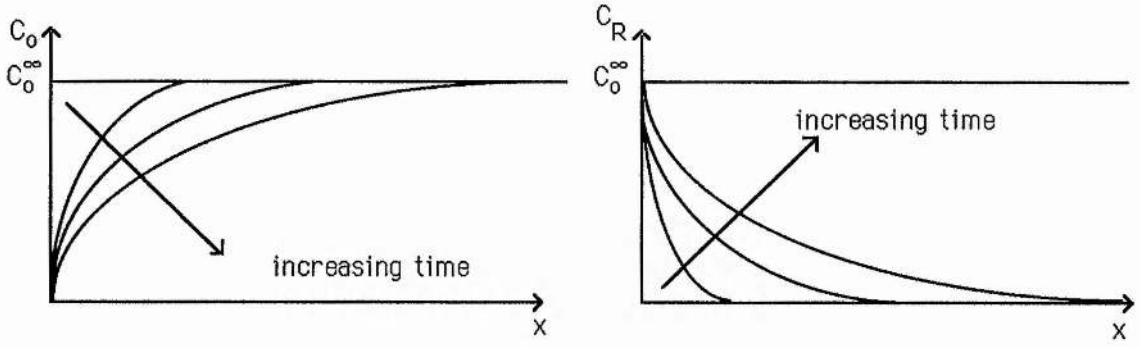

Figure 2-3 Concentration profiles for a potential step experiment in a system initially containing **O** but no **R**.

Since the current is directly proportional to the concentration gradient, it can be seen that it will decrease with time. The rate of change of the concentration gradient with time is given by Fick's second law of diffusion.

$$\frac{\partial C_i(x,t)}{\partial t} = D\left(\frac{\partial^2 C_i(x,t)}{\partial x^2}\right) \qquad 2\text{ - xviii)}$$

The exact form of the current transient may be obtained by solving Fick's second law subject to the boundary conditions of the experiment. Namely :-

At $t = 0$ $\quad C_o = C_o^\infty$ $\quad$ for all x

At $t > 0$ $\quad C_o^\sigma = 0$ $\quad$ for $x = 0$

$\quad C_o = C_o^\infty$ $\quad$ for $x = \infty$

Solution of the equations using Laplace transform techniques[82] yields an expression for the current transient. This is known as the Cottrell equation.

$$I = \frac{-nFD^{1/2}C_O^\infty}{\pi^{1/2}t^{1/2}} \qquad 2\text{ - xix)}$$

This assumes however that mass transport is the rate determining step i.e. that the reaction is mass transport (diffusion) controlled.

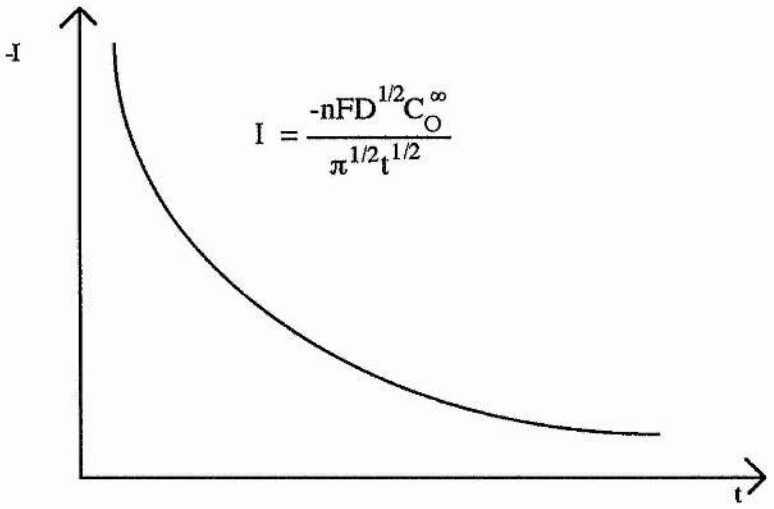

Figure 2-4 The current transient for a potential step experiment where the electrode reaction is diffusion controlled.

For a system under diffusion control, a graph of current against $t^{-1/2}$ should give a straight line through the origin. The diffusion coefficient may be determined from the gradient of the graph. A linear I versus $t^{-1/2}$ plot is often used as a test for diffusion control.

It should be noted that care needs to be taken when analysing data on very short time-scales for two reasons:-

a) There will be a current spike at $t \simeq 0$ due to the charging of the double layer.

b) The concentration gradients at $t = 0$ will be at their steepest and thus the rate of diffusion will be infinite. The reaction may therefore briefly become kinetically controlled.

2.7 Phase formation

2.7.1 *Introduction*

When the products of an electrode reaction are not soluble in solution, the current transient resulting from a potential step experiment may take a completely different form e.g formation of a new phase by electrodeposition of a metal. Phase formation is a multistep process requiring both nucleation of stable metal centres on the surface and their subsequent growth. The nucleation process requires a substantial overpotential. Once formed, however, the nuclei grow rapidly, the growth being proportional to their surface area. This often leads to a rising portion on the current transient in potential step experiments where a new phase is formed. Analysis of the transients over both short and long intervals can yield information on both the kinetics and mechanism of the nucleation and growth processes.

2.7.2 *Nucleation*

One of the first steps in the electrodeposition of a metal is the formation of nuclei of the new phase. It has been shown[82] that small centres with a high surface area to volume ratio are thermodynamically unstable and will tend to redissolve in the solution. A critical size must be achieved for a nucleus to be stable. This will only occur if a sufficient number of metal ad-atoms diffuse rapidly across the surface to form a cluster. The process is made more favourable by providing a large concentration of adsorbed metal ions i.e. by applying a large overpotential to the system.

The formation of stable nuclei follows first order kinetics. The number density of nuclei is given by the following expression:-

$$N(t) = N_0 \{ 1 - \exp(-At) \} \qquad 2 - xx)$$

where N_0 is the number of sites where nuclei can form and A is the rate constant for nucleation. The expression has two limiting forms :-

i) when $At >> 1$, $N(t) = N_0$

In this case all possible nuclei are created at the instant that the potential is applied. This is known as *instantaneous nucleation.*

ii) When $At << 1$, $N(t) = N_0At$

the number of nuclei increases with time . This is known as *progressive nucleation.*

Once the nuclei have been formed, they will continue to grow (providing that the conditions remain unchanged). Subsequent growth may be either two-dimensional, where only a monolayer may form without further nucleation, or three-dimensional, where growth occurs both parallel and perpendicular to the surface.The precise form of the current transient will depend on :-

a) whether the nucleation is instantaneous or progressive,
b) whether the growth is two-dimensional or three-dimensional,
c) the rate determining step e.g. incorporation of metal ad-atoms into the metal lattice or mass transport (diffusion) of metal ions to the electrode surface etc.

Each combination gives rise to a characteristic I-t transient, some of which are shown in Figures 2-5 and 2-6.

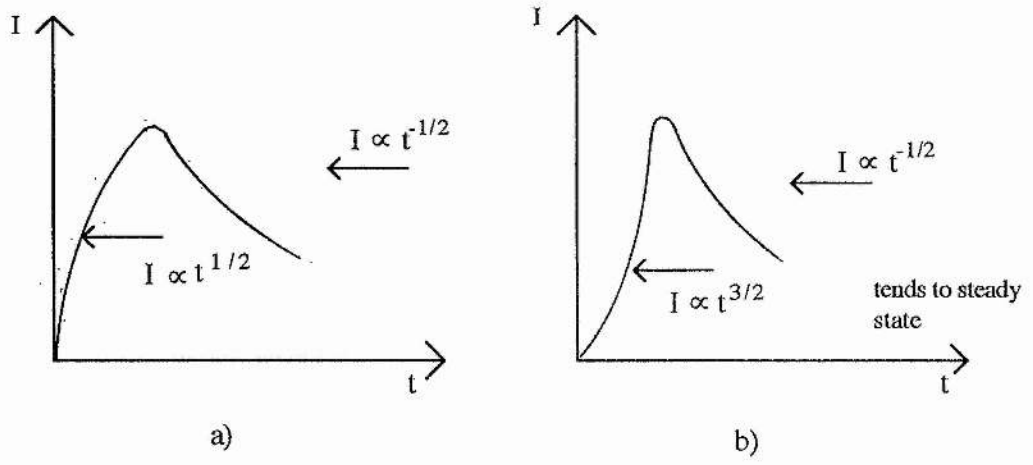

Figure 2-5 Three-dimensional diffusion controlled growth following a) Instantaneous nucleation and b) Progressive nucleation.

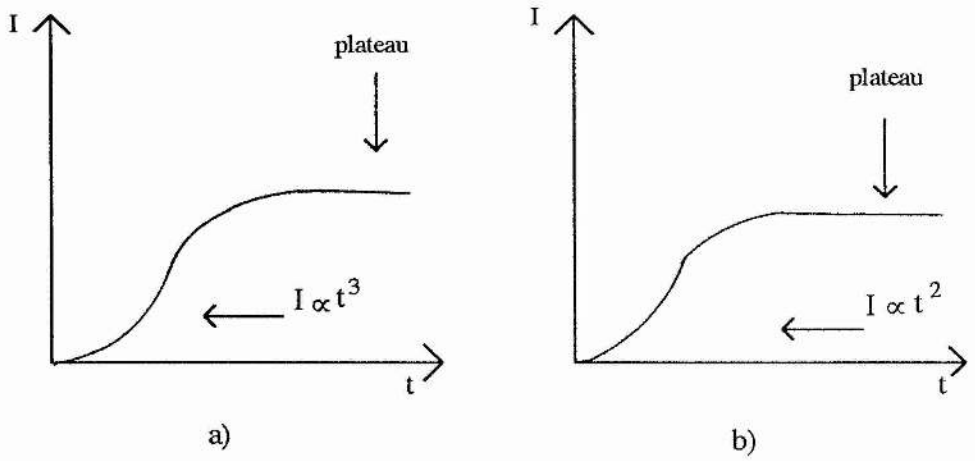

Figure 2-6 Three dimensional electron transfer controlled growth following a) Progressive nucleation and b) Instantaneous nucleation.

2.7.3 *Diffusion controlled growth*

Analytical expressions for the current transients can be obtained for simple geometries of solid growth centres e.g right circular cones and hemispheres[83]. Hills, Schiffrin and Thompson[84] have derived expressions for the current transients obtained for the nucleation and diffusion controlled growth of an isolated hemispherical centre.

$$I(t) = \frac{nF\pi (2DC^{\infty})^{3/2} M^{3/2}}{\rho^{1/2}} \left[1 - \exp\left(\frac{-nF\eta}{RT}\right) \right]^{3/2} t^{1/2} \qquad 2 - xxi)$$

where M is the relative atomic mass and ρ is the density.

There will be many nucleation centres formed on the substrate however, and over longer timescales, there will be interaction between their diffusion fields. This has been considered by Scharifker[85] and Bosco and Rangarajan[86].They obtained approximate expressions for the current transients for both instantaneous and progressive nucleation:-

$$I(t) = \frac{nFD^{1/2}C^{\infty}}{\pi^{1/2}t^{1/2}} \left[1 - \exp(-N_0 \pi k D t) \right] \qquad 2 - xxii)$$

for instantaneous nucleation where $k = (8\pi C^{\infty} M/\rho)^{1/2}$.

For progressive nucleation :-

$$I(t) = \frac{nFD^{1/2}C^{\infty}}{\pi^{1/2}t^{1/2}} \left[1 - \exp\left(\frac{A'\pi k D t^2}{2}\right) \right] \qquad 2 - xxiii)$$

where $k = 4/3(8\pi C^{\infty} M/\rho)1/2$ and A' is the rate constant for nucleation.

Over long time periods, these expressions approach the limiting form:-

$$I = \frac{nFD^{1/2}C^{\infty}}{\pi^{1/2}t^{1/2}} \qquad 2 - xxiv)$$

which may be recognised as the Cottrell equation for linear diffusion to a planar surface. It can be seen from figure 2-5 that diffusion controlled growth gives rise to a maximum in the current transient. Expressions for the maxima in each case may be obtained by differentiation of equations 2 - xxii and 2 - xxiii as follows.

For instantaneous nucleation:-

$$t_m = \frac{1.26}{N\pi kD}$$

$$I_m = 0.638nFDC^{\infty}k^{1/2}N_0^{1/2} \qquad 2 - xxv)$$

For progressive nucleation :-

$$t_m = \left(\frac{4.67}{AN_0\pi kD}\right)^{1/2}$$

$$I_m = 0.462nFD^{3/4}C^{\infty}k^{1/4}(AN_0)^{1/4} \qquad 2 - xxvi)$$

The product $I_m^2 t_m$ does not contain the quantities k, A or N and thus provides a diagnostic test for the type of nucleation.

$$I_m^2 t_m = 0.163\,(nFC^{\infty})^2 D \qquad 2 - xxvii)$$

(Instantaneous nucleation)

$$I_m^2 t_m = 0.260\,(nFC^{\infty})^2 D \qquad 2 - xxviii)$$

(Progressive nucleation)

2.8 Cyclic Voltammetry

2.8.1 *Introduction*

Cyclic voltammetry is one of the most versatile techniques available for the study of electroactive species and is often one of the first experiments to be performed in an electrochemical study of a system. The redox behaviour of a system may be quite rapidly probed over a wide potential range whilst the sweep rate dependence may indicate the presence of coupled chemical reactions. Several overviews of the theory and practice of cyclic voltammetry are available in the literature[87, 88, 89] whilst an in depth study of the theory is provided in the texts of The Southampton Electrochemistry Group [82] and Bard and Faulkner[90].

2.8.2 *The cyclic voltammetry experiment*

In the cyclic voltammetry experiment, the potential of the working electrode (controlled versus the reference electrode) is scanned linearly from one potential to a second 'switching' potential. After scanning this region where one or more electrode reactions take place, the scan is reversed and the redox behaviour of the products and / or intermediates formed in the forward scan are probed. Single or multiple cycles may be performed at a variety of scan rates (v) , the current being monitored as a function of the potential. The instrumentation typically required for the experiment is shown in figure 2-7

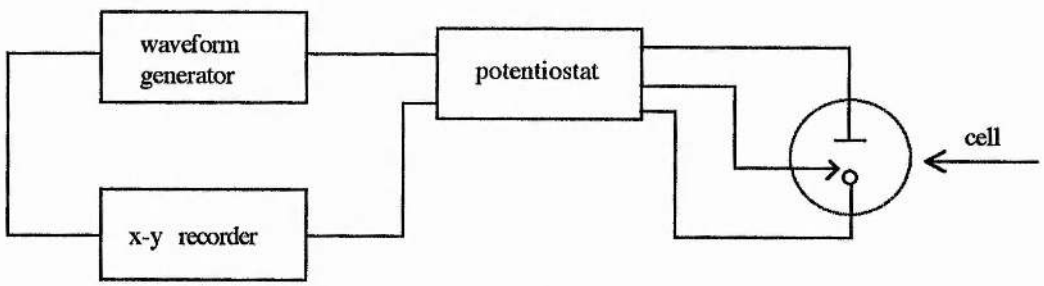

Figure 2-7 The instrumentation required for the cyclic voltammetry experiment.
(⊥ secondary electrode, ⎯o working electrode and → reference electrode)

For scan rates faster than 500 mV s^{-1}, it is necessary to replace the x-y recorder with a storage oscilloscope.

2.8.3 *Reversible reactions*

A reversible reaction is one where the rate of electron transfer is rapid compared to the rate of mass transport (diffusion) and both the products and the reactants are stable in solution. Figure 2-8 shows a typical cyclic voltammogram (CV) obtained for a reversible process.

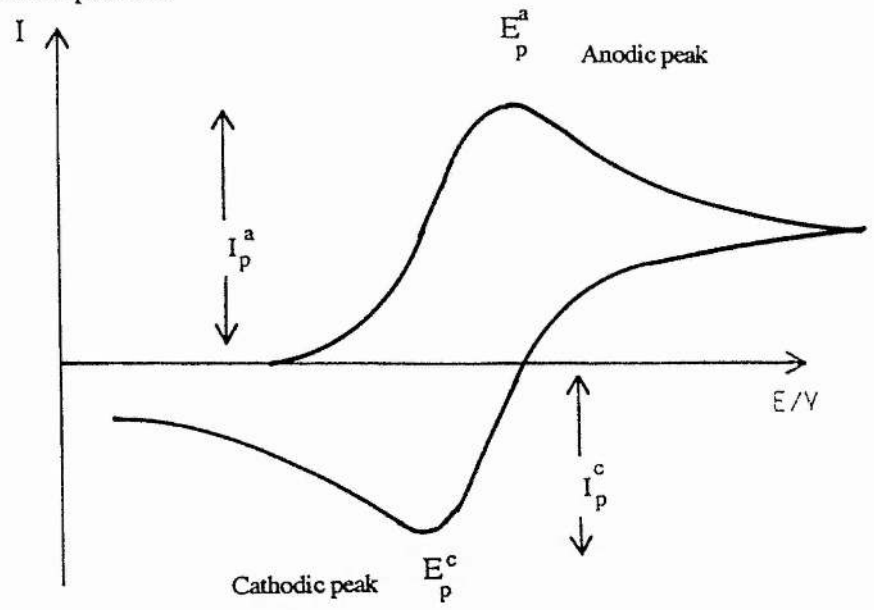

Figure 2-8 A typical cyclic voltammogram obtained for the reversible reaction

$$O + ne \rightleftharpoons R$$

The cathodic peak in the CV results from the competition between the rate of mass transport of species to the electrode and the rate of the electron transfer reaction. When the kinetics of electron transfer are fast, the concentrations of species **O** and **R** at the electrode are described by the Nernst equation (2 - i). The region close to the working electrode becomes depleted in **O** as it is swept to more negative potentials and a concentration gradient is set up. It was seen in section 2.5 that the current density at the electrode is given by :-

$$I = -nFD_O \left(\frac{\partial C_O(x)}{\partial x} \right)_{x=0} \qquad 2 - xxxi)$$

Eventually, the current becomes diffusion controlled ($I \propto t^{-1/2}$) and independent of the applied potential i.e the current decays with time.

As the sweep is reversed, reduction continues until the potential becomes sufficiently positive to cause oxidation of **R** as signalled by the anodic current. Once again, the magnitude of the current increases until the surface becomes depleted in **R** and the current becomes diffusion controlled. An anodic peak thus results.

The exact form of the cyclic voltammogram can be obtained by solution of Fick's second law for species **O** and **R** subject to the boundary conditions of the experiment. It can be shown that for linear diffusion to a planar electrode, the peak current for a reversible process is given by the Randles - Sevcik equation:-

$$|I_p| = 0.4463\, nF \left(\frac{nF}{RT}\right)^{1/2} C_x^{\infty} D^{1/2} \nu^{1/2} \qquad 2 - xxxii)$$

Thus one of the criteria for a reversible reaction is that a graph of I_p against $\nu^{1/2}$ should be linear and pass through the origin. It is also found that the peak positions E_p^A and E_p^C are independent of the scan rate ν for a reversible reaction.

2.8.4 *Irreversible systems*

When the kinetics of electron transfer are slow compared to mass transport, then it may not be possible to maintain a Nernstian equilibrium at the electrode surface for all sweep rates. A 'reversible' CV may be obtained for the slowest sweep rates. As the sweep rate is increased, the rate of mass transport approaches that for electron transfer and the peak separation is observed to increase. Furthermore, the peak height is slightly reduced compared to the completely reversible case. The exact form of the CV for the completely irreversible case may be obtained, as before, by solution of Fick's second law subject to the boundary conditions of the experiment i.e.

At $t = 0$ and $x = 0$, $C_O = C_O^{\infty}$ and $C_R = 0$

At $t > 0$ and $x = \infty$, $C_O = C_O^{\infty}$ and $C_R = 0$

At $t > 0$ and $x = 0$, $\frac{-I}{nF} = D_O \left(\frac{\partial C_O(x)}{\partial x} \right)_{x=0} = \vec{k} (C_O)_{x=0}$

Solution of the equations is slightly problematical due to the time dependence of the boundary conditions but is clearly described by Delahey[91] who obtained the following expression for the peak current density (I_p) :-

$$I_p = 0.282 \frac{\pi^{1/2} F^{3/2}}{(RT)^{1/2}} n(\alpha_C n_\alpha)^{1/2} D_O^{1/2} C_O^{1/2} \nu^{1/2} \qquad 2 - xxxiii)$$

where n_α is the number of electrons transferred up to and including the rate determining step. It can be seen that as for the reversible case, the peak height is proportional to $\nu^{1/2}$ but is is also proportional to $\alpha_C^{1/2}$. For a completely irreversible system, the reverse peak is absent from the CV. It should be emphasised however that the absence of such a peak does not necessarily imply an irreversible process but could be due to a fast chemical reaction following the electron transfer.

The dependence of peak position on the scan rate has been shown by Shain and Nicholson[92] to be of the following form :-

$$E_p^C = K - \frac{2.3RT}{2\alpha_C n_\alpha F} \log \nu \qquad 2 - xxxiv)$$

where :-

$$K = E_e^o - \frac{RT}{\alpha_C n_\alpha F} \left\{ 0.78 - \frac{2.3}{2} \log \left(\frac{\alpha_C n_\alpha F D_O}{(k_0^o)^2 RT} \right) \right\} \qquad 2 - xxxv)$$

Thus, as the sweep rate increases, the cathodic peak moves to more negative potentials. It should be noted that completely analogous reasoning may be applied to the position of the anodic peak which moves to more positive potentials with increasing sweep rate.

2.8.5 *Phase formation in cyclic voltammetry*

The plating and stripping of a material (e.g. a metal M) at an electrode gives rise to a characteristic CV of the form shown in figure 2-9. The processes occurring can be explained by reference to figure 2-9.

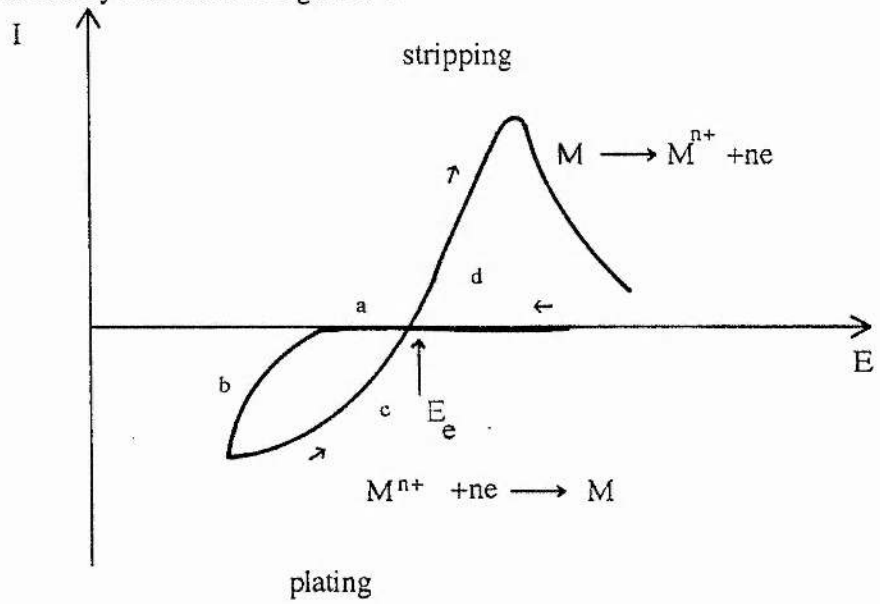

Figure 2-9 A CV obtained for the plating and stripping of a metal M on an inert cathode.

Upon sweeping cathodically (a) from the equilibrium potential, little current flows until a potential sufficient to cause nucleation has been applied. Upon reaching this potential, the magnitude of the current increases as deposition occurs (b). When the scan is reversed, the system is still at a potential where growth of the layer continues (c) and thus the magnitude of current in this region is greater than for the forward scan. This gives rise to the characteristic nucleation loop on all CV's where deposition occurs. Upon reaching a potential where oxidation can occur, the current rises rapidly

(d). Because the metal M is readily available on the surface of the electrode, the current does not become diffusion controlled. If the plating / stripping process is the only reaction occurring at the electrode, then the areas under the forward and reverse scans must be equal. (Cathodic charge = anodic charge). All the metal deposited on the forward scan is stripped on the reverse scan.

CHAPTER 3

THE THEORY OF AC IMPEDANCE MEASUREMENTS

3.1 Complex impedance plots

In an a.c. experiment, a small amplitude, sinusoidal voltage is applied across the cell and the sinusoidal current passing as a result of the perturbation is monitored. In general, two parameters are required to represent the current response. One is a measure of the opposition to the flow of charge (E_{max} / I_{max}) where E_{max} and I_{max} are the maximum values of the sinusoidal voltage and current repectively and is analogous to the resistance in DC theory. The other is the phase angle (θ) between the current and the voltage. These two parameters collectively describe the impedance, **Z** , of the system, which is a vector quantity. This may be represented as a point on a vector diagram.

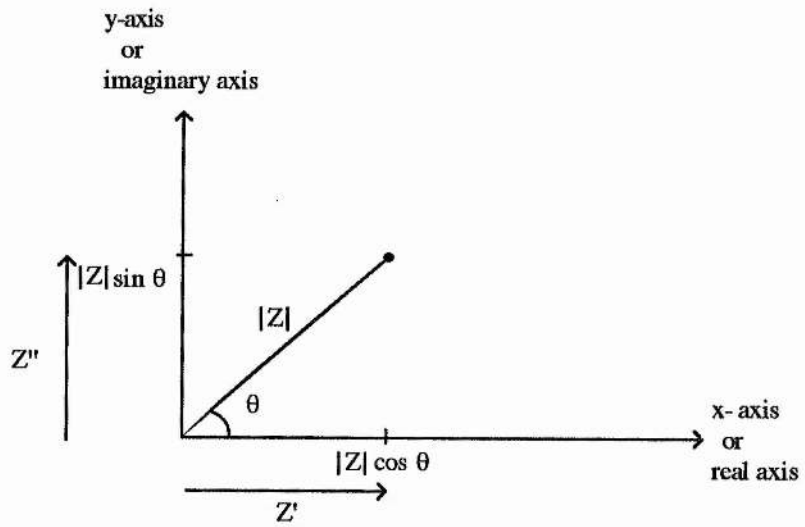

Figure 3-1 Representation of the impedance of a cell on a vector or Argand diagram.

The vector may thus be described in three ways:-

a) by its magnitude /**Z**/ and phase angle θ, b) by its component along the x-axis and y-axis (/**Z**/cos θ and /**Z**/sinθ respectively) or c) by a complex number $Z = Z' - j\,Z''$.

In the ac experiment, the impedance of the system, determined as a function of frequency, is plotted on an Argand diagram. Simple systems give characteristic impedance plots. These can be modelled by an equivalent circuit, e.g. constructed from resistors and capacitors, designed to reproduce the ac response of the cell under investigation. Subsequent analysis of the impedance plot often allows the impedances of the individual components in the equivalent circuit to be determined as well as giving an indication of the order in which they are connected. The equivalent circuit model can thus be used to determine the order and magnitude of the electrochemical processes occurring in the cell e.g. the double layer capacitance, C_{dl}, and the charge transfer resistance, R_{ct}. These parameters, once determined, can also yield kinetic information on the system.

3.1.1 *The resistor*

The magnitude of the impedance of a resistor is simply given by its resistance and is independant of frequency ($\theta = 0$) .

$$|\mathbf{Z}| = R$$

The complex impedance plot for a resistor is therefore a single point displaced a distance R along the real axis for all frequencies.

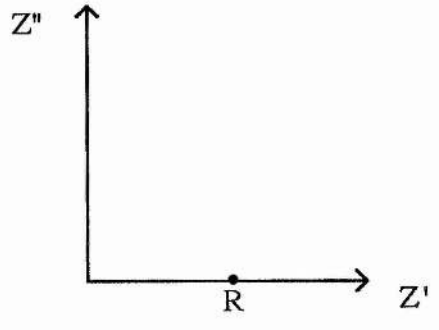

Figure 3.2 The complex impedance plot for a resistor

3.1.2 *The capacitor*

The capacitance, C, of a capacitor is given by the charge, q, stored per unit potential difference, E, across the plates.

$$C = q / E \qquad 3\text{-i})$$

Thus the current that passes through it is given by:-

$$I = \frac{dq}{dt}$$

$$= C\frac{dE}{dt} \qquad 3\text{-ii})$$

A sinusoidal voltage of amplitude E_{max} can be represented as:-

$$E = E_{max} \sin\omega t \qquad 3\text{-iii})$$

Thus:-

$$I = E_{max}\omega C \cos\omega t \qquad 3\text{-iv})$$

$$I = E_{max}\omega C \sin(\omega t+\pi/2) \qquad 3\text{-v})$$

(Where the angular frequency $\omega = 2\pi f$ and f is the signal frequency in Hz.)

Thus it can be seen that the voltage lags behind the current with phase angle $\theta = -\pi/2$.

The impedance of a capacitor (E / I) is therefore frequency dependent and will have a magnitude of $1/\omega C$.

$$\mathbf{Z} = -j / \omega C \qquad 3\text{-vi})$$

The complex impedance plot for a capacitor defines a vertical spike coincident with the imaginary axis, since there is no resistive component. (Note that it is common practise for electrochemists to plot negative imaginary impedances above the real axis)

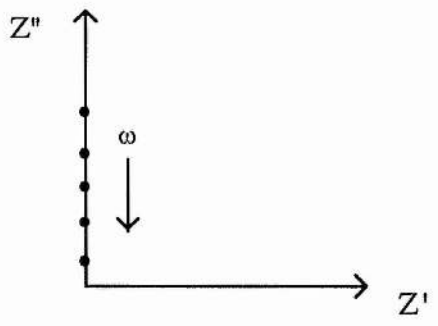

Figure 3-3 The complex impedance plot for a capacitor

3.2 Simple systems

The impedance of systems containing combinations of resistors and capacitors can be calculated if the impedances of the individual components are known. The total impedance of components connected in series is obtained by summation of the individual impedances:-

$$\mathbf{Z}_{tot} = \mathbf{Z}_1 + \mathbf{Z}_2 + ... \qquad 3\text{-vii})$$

The total impedance of components connected in parallel is found by summation of the individual reciprocal impedances:-

$$1/\mathbf{Z}_{tot} = 1/\mathbf{Z}_1 + 1/\mathbf{Z}_2 + ... \qquad 3\text{-viii})$$

The reciprocal of the impedance is also known as the admittance i.e $1/\mathbf{Z} = \mathbf{Y}$, which is additive for components in parallel.

$$\mathbf{Y}_{tot} = \mathbf{Y}_1 + \mathbf{Y}_2 + ... \qquad 3\text{-ix})$$

It is thus possible to predict the complex impedance plots that result from a variety of RC combinations.

3.2.1 *A resistor and capacitor in series*

For a resistor and capacitor connected in series:-

$$\mathbf{Z}_{tot} = R - j / \omega C \qquad 3\text{-x})$$

The complex impedance plot is therefore a vertical spike at a distance R along the real axis

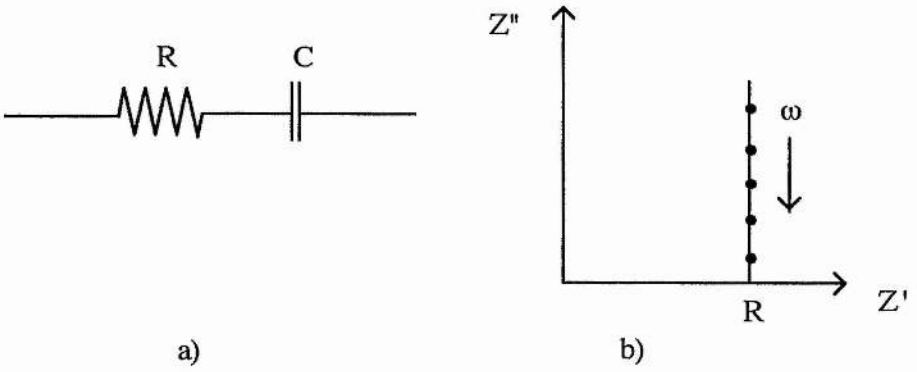

Figure 3-4 The equivalent circuit (a) and the complex impedance plot (b) for a series RC combination

3.2.2 *A resistor and capacitor in parallel*

The total admittance for a resistor and capacitor in parallel is found by summing the individual admittances.

$$\mathbf{Y}_{tot} = 1/R + j\omega C \qquad \text{3-xi)}$$

thus:-

$$\mathbf{Z}_{tot} = \frac{1}{1/R + j\omega C} \qquad \text{3-xii)}$$

Multiplying top and bottom by the complex conjugate ($1/R - j\omega C$) gives

$$\mathbf{Z}_{tot} = \frac{1/R - j\omega C}{1/R^2 + (\omega C)^2} \qquad \text{3-xiii)}$$

$$= \frac{R - j\omega CR^2}{1 + (\omega CR)^2}$$

$$= \frac{R}{1 + (\omega CR)^2} - \frac{j\omega CR^2}{1 + (\omega CR)^2} \qquad \text{3-xiv)}$$

$$= Z' - jZ''$$

If the scales of the real and imaginary axes are equal, then the equation defines a semicircle with diameter R.

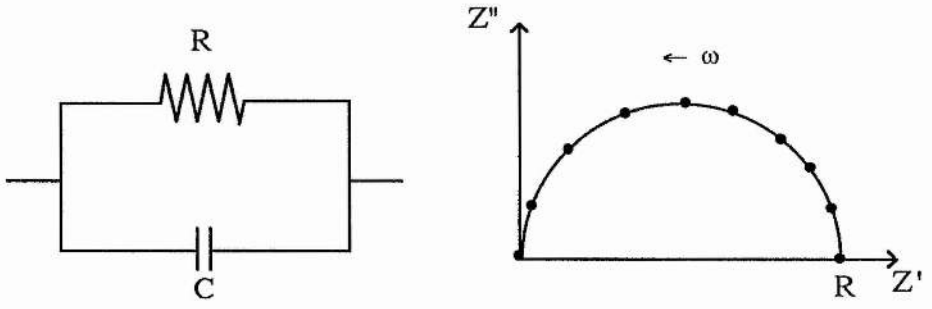

a) b)

Figure 3-5 The equivalent circuit (a) and complex impedance plot (b) for a parallel RC combination

At the maximum in the semicircle,

$$\frac{R}{1 + (\omega CR)^2} = \frac{\omega CR^2}{1 + (\omega CR)^2} \qquad 3\text{-xv})$$

Therefore :-

$$R = 1 / \omega_{max} C \qquad 3\text{-xvi})$$

It is thus possible to determine both R and C from the complex impedance plot.

3.3 Ac impedance measurements on polymer electrolytes

3.3.1 *Blocking electrodes*

In a system where there is no finite electrode reaction, the electrode is said to be blocking.The simplest real system consists of a two electrode cell containing a polymer electrolyte film between blocking electrodes where the cation and / or anion is mobile. Examples from this work include the systems :-

SS / $PEO_xCa(CF_3SO_3)_2$ / SS , SS / PEO_xNiI_2 / SS and Ni / $PEO_xCo(SCN)_2$ / Ni

(where SS represents a stainless steel electrode).

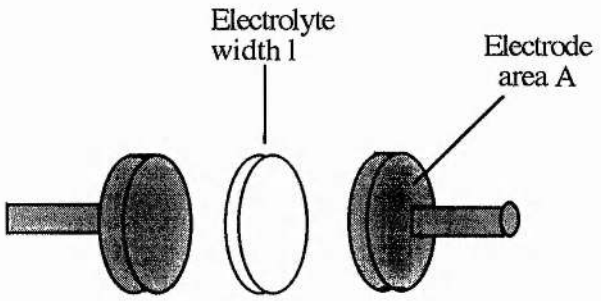

Figure 3-6 A two electrode cell

When the ac voltage is applied across the cell, the electrodes become alternately positively and negatively charged. This in turn induces migration of the ions back and forth in phase with the voltage . This migration of ions can be represented by a resistor R_b. The ions are alternately accumulated and depleted in the region of the the electrolyte near the electrodes, forming a layer of equal but opposite charge to that on each electrode. Each electrode / electrolyte interface thus behaves like a parallel plate capacitor and can be represented by a capacitance C_{dl}. This is usually referred to as the double layer capacitance.

The polymer itself also becomes polarised in the alternating field. This polarisation, which would occur even in the absence of the dissolved salt, can be represented by a capacitor C_b. The polarisation of the bulk polymer and migration of ions in the electrolyte can be considered to occur in parallel, thus the equivalent circuit modelling the system will contain the elements R_b and C_b in parallel. These are both in series with the electrode capacitance C_{dl}. In a symmetrical cell C_{dl} is usually deemed to represent the (identical) and combined response of both electrodes. the equivalent circuit for the system is thus given by figure 3-7:-

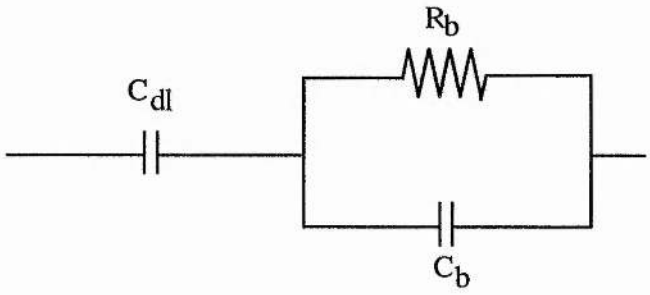

Figure 3-7 The equivalent circuit for a 2 electrode cell with blocking electrodes

It is a straightforward matter to determine the complex impedance plot that will arise from such a system. The total impedance is given by the sum of the impedance of C_{dl} ($-j / \omega C_{dl}$) and that for the parallel R_b C_b element (given by equation 3-iv).Thus:-

$$\mathbf{Z_{tot}} = \underbrace{\frac{R_b}{1 + (\omega R_b C_b)^2}}_{a} - j\underbrace{\left(\frac{\omega C_b R_b^2}{1 + (\omega R_b C_b)^2} \right)}_{b} + \underbrace{\frac{1}{\omega C_{dl}}}_{c} \qquad 3\text{-xvii)}$$

It is found typically that $C_{dl} \simeq 10^{-6}$ Fcm^{-2} whereas $C_b \simeq 10^{-12}$ Fcm^{-1}. Equation 3-xvii) can thus be simplified for certain frequency ranges (remembering that $\omega = 2\pi f$).

As $f \rightarrow \infty$:- $a \rightarrow 0$, $b \rightarrow 0$ and $c \rightarrow 0$

The complex impedance plot will thus intercept the origin.

When f (large) :- $c \ll (a + b)$

The contribution of the impedance of the electrode capacitance is negligible. The total impedance is therefore determined by the parallel R_b C_b combination. This gives rise to a semicircle, radius R_b, in the high frequency region.

When f (small) :- $a \rightarrow R_b$ $b \rightarrow 0$ and c(large)

The bulk capacitance makes a negligible contribution to the total impedance, which can thus simplified to a series R_b C_{dl} combination.This gives a vertical spike , a distance R_b along the real axis.

The complete complex impedance plot for the system is given in figure 3-8.

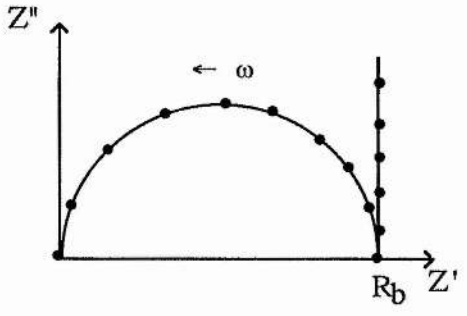

Figure 3-8 The complex impedance plot for a two electrode cell with blocking electrodes

The dielectric constant for the polymer electrolyte, ε, can be determined from the complex impedance plot if the cell constant (l / A) is known.

$$C_b = \frac{\varepsilon \varepsilon_0 A}{l} \qquad \text{3-xviii)}$$

Where ε_0 is the permittivity of a vacuum ($8.85 \times 10^{-14} F\,cm^{-1}$).

3.3.2 *Non blocking electrodes*

Consider first a two electrode system, consisting of an electrolyte between electrodes which are non blocking towards one of the mobile species. The response of the electrolyte to the applied voltage is identical to the one with blocking electrodes and can thus be represented by a parallel R_b C_b combination. This gives rise to a high frequency semicircle on the complex impedance plot. Alternate charging and discharging of the electrode / electrolyte interface results as before from the motion of ions in the field which do not undergo a reaction at the electrode. The electroactive species may also contribute to this process if the rate of the electrode reaction is slower than the rate of ionic conductivity. This is again represented by the electrode capacitance C_{dl}.

The kinetics of the electrode reaction will determine the flow of current across the interface. This impedance may be represented by the resistor R_e. If the kinetics of the electrode reaction are rapid then R_e will be small. Concommitantly, if the kinetics are slow R_e will be large and the behaviour of the system will approach that with blocking electrodes. Since these processes may be considered to occur in parallel, the equivalent circuit will contain an R_e C_{dl} combination. This gives rise to a semicircle of radius R_e at intermediate frequencies in the complex impedance plot.

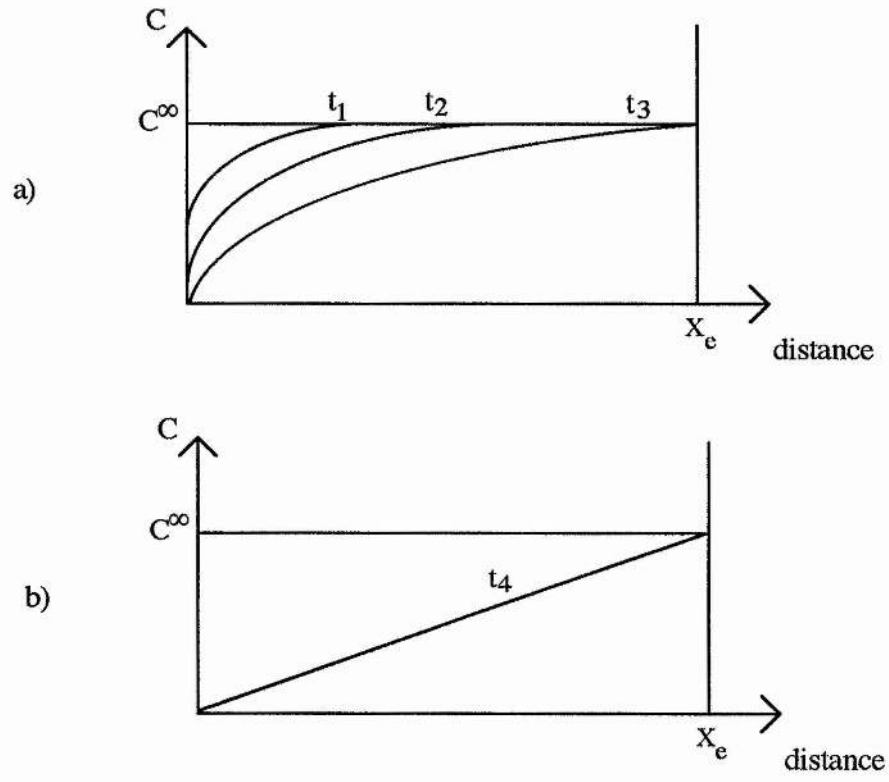

Figure 3-9 Concentration profiles for systems in the regime of a) semi-infinite diffusion and b) finite diffusion. (Where C^{∞} is the bulk concentration of the electroactive species, t_x the time and X_e the position of the second electrode.)

At very low frequencies, the amount of charge transferred in the electrode reaction is significant enough to produce concentration gradients within the electrolyte. The electroactive species is thus transported by diffusion as well as migration. On short timescales, the system is in the region where semi-infinite diffusion occurs (figure 3-9a), and, (assuming the electrode kinetics are relatively fast), the current passing through the electrode will be mass transport limited. The impedance of this process will be dependent on a variety of factors including the diffusion coefficient of the salt, D , temperature, T, electrode area A and concentration, C . It is commonly known as the Warburg impedance, Z_w:-

$$Z_w = \frac{RT}{n^2F^2 (2D)^{1/2} C} (\omega^{-1/2} - j\omega^{-1/2}) \qquad 3 - xix)$$

$$= A_w (\omega^{-1/2} - j\omega^{-1/2}) \qquad 3 - xx)$$

where n is the number of electrons transferred in the electrode reaction and A_w is the Warburg prefactor. It can be seen that the real and imaginary components of the Warburg impedance are equal. This gives rise to a line at 45° to the real axis at low frequencies. Over longer timescales, the system is still under mass transport control but a uniform concentration gradient is produced in the cell. This is the regime of finite diffusion (figure 3-9b). The current passed by the electrode becomes independent of frequency and the system exhibits behaviour approaching that for a dc experiment. Thus the ac impedance plot 'rolls over' and intercepts the real axis at the dc resistance of the cell. The overall impedance due to diffusion is often represented by Z_d which includes the Warburg term.

A Warburg impedance may also arise if the system contains a supporting electrolyte e.g. Ni / $PEO_{10LiClO_4}^{50NiI_2}$ / Ni . In this case, most of the current will be transported by the supporting electrolyte and transport of the electroactive species to the electrode will be by diffusion only. The diffusion coefficient in the Warburg expression (3-xix) will then be that for the electroactive species.

a)

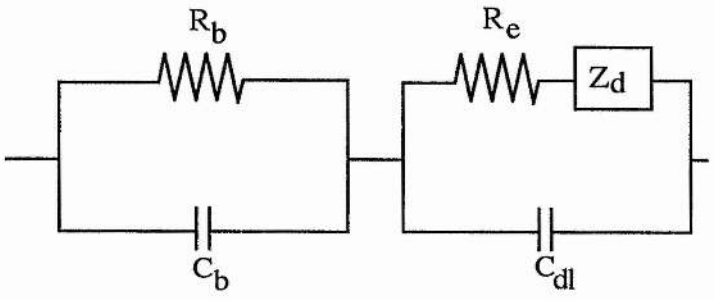

b)

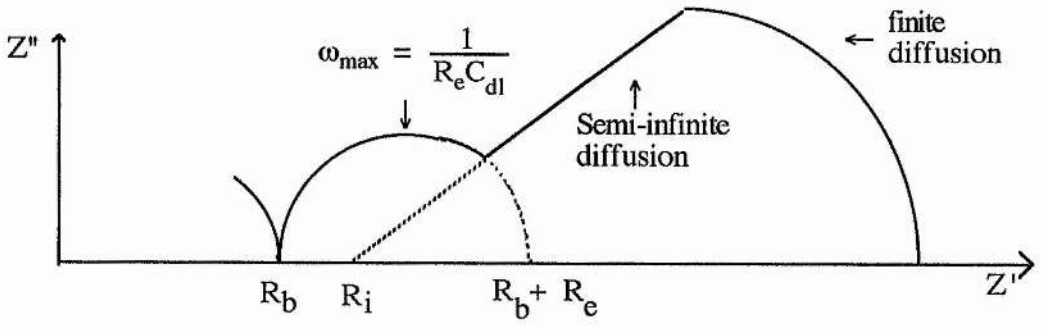

Figure 3-10 The equivalent circuit a) and complex impedance plot b) for a cell with non-blocking electrodes .

From figure 3-10 it is clear that the Warburg impedance will be given by :-

$$\mathbf{Z_W} = Z' - R_i + Z''j \qquad 3 - xxi)$$

where R_i is the intercept of the Warburg impedance with the real axis. Reference to equation 3 - xx) yields the real and imaginary components of the Warburg impedance as:-

$$Z'_W = A_W \omega^{-1/2} \qquad 3 - xxii)$$

$$Z''_W = A_W j\omega^{-1/2} \qquad 3 - xxiii)$$

The magnitude of the Warburg impedance is then given by:-

$$|\mathbf{Z_W}| = \sqrt{2}\, A_W \omega^{-1/2} \qquad 3 - xxiv)$$

A graph of $|\mathbf{Z_W}|$ against $\omega^{-1/2}$ will then have a gradient $m = \sqrt{2}\, A_w$ from which the diffusion coefficient may be calculated (figure 3-11).

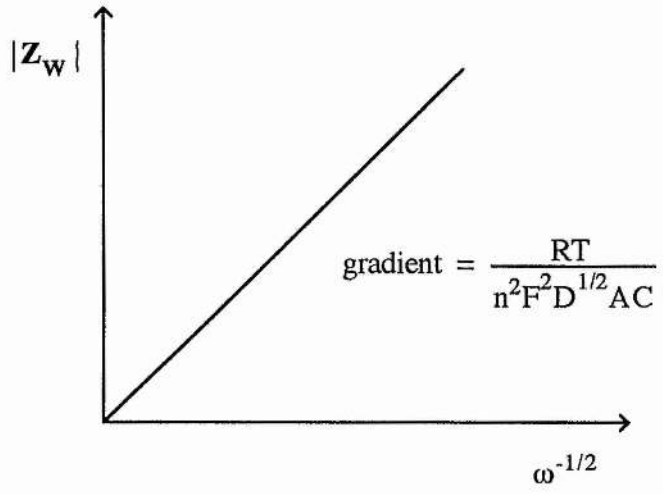

Figure 3-11 Calculation of the diffusion coefficient from ac impedance data

CHAPTER 4

EXPERIMENTAL

4.1 Preparation of polymer electrolytes

Unless otherwise stated, all manipulations were performed in an argon filled dry-box.

4.1.1 *Solvent Casting*

Known masses of PEO (B.D.H. M.W. $5x10^6$) were dissolved in anhydrous acetonitrile. Appropriate quantities of standard salt solutions in anhydrous acetonitrile ($LiClO_4$ and $LiCF_3SO_3$) or anhydrous ethanol ($Eu(CF_3SO_3)_3$) were added . The solutions were stirred for 24 hours to ensure homogeneity.

Films of the polymer electrolytes were obtained by casting from the solutions in Teflon formers. The formers, filled with solution, were placed in a gas tight chamber through which argon was continuously circulating over molecular sieves. After slow evaporation of the solvent (typically 4 days) , the formers with bases removed, were transferred to a drying tube and were heated under vacuum at 75°C for 4 days to remove residual solvent. Heating continued at 60°C for a further 4 days to obtain crystalline films.

The films obtained were typically between 0.1mm and 0.2mm thick and were stored in the dry-box.

4.1.2 *Cryogrinding / Hot Pressing*

A mixture of the salt, which had been pre-ground in a pestle and mortar, and PEO was transferred, under argon, to a large stainless steel test tube containing ball bearings.This was sealed with a rubber bung, transferred out of the dry-box and shaken in liquid nitrogen for 20 minutes. At these temperatures, the polymer becomes brittle and fractures under the impact of the ball bearings. An intimate mixture of the polymer and salt was thus produced. After grinding, the tube was left for

approximately 2 hours to return to room temperature, after which it was transferred to the dry-box. By altering the proportions of the salt and polymer, mixtures of a variety of compositions were produced.

A small sample (≈ 50 mg) of the cryoground mixture was pressed to 5 tons for 30 seconds between two Teflon discs in a 13mm pellet press.This was heated to 130 °C, under no applied pressure using a band heater and the temperature maintained for at least 3 hours. Upon cooling to 65°C , a pressure of 2 tons was applied. The sample was allowed to cool to room temperature overnight under the applied pressure.The films produced were typically between 0.1mm and 0.4mm thick.

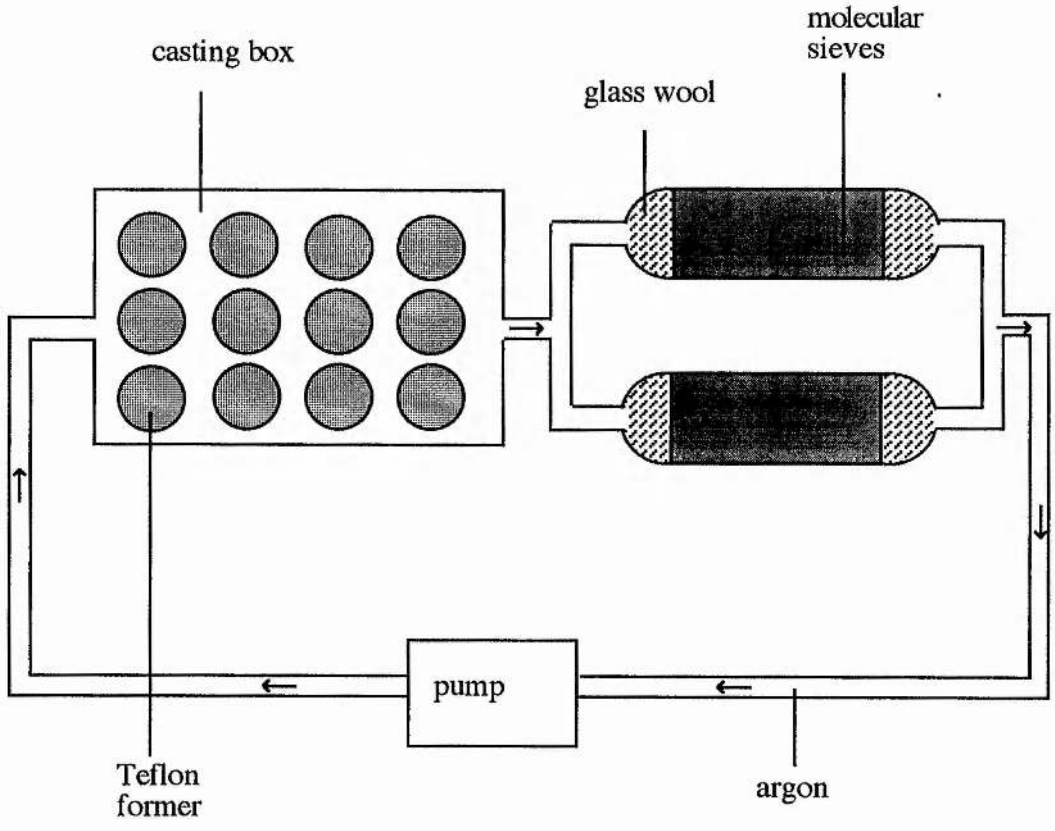

Figure 4-1 The solvent casting system

4.1.3 *A Comparison of the Solvent Casting and Hot pressing methods for Polymer Electrolyte Preparation.*

The ideal method of preparation would produce a homogeneous film of uniform thickness over a wide range of compositions.The sample should be anhydrous and completely free from all traces of solvent.

In many cases, the solvent casting method is capable of producing homogeneous samples for all but the most concentrated electrolytes. In this process, the components of the electrolyte are mixed microscopically in solution. As mentioned in section 1.2.7, the morphology of the final electrolyte depends on a variety of factors including the rate of solvent evaporation and the relative complexing abilities of the solvent and the polymer. In situations where the polymer competes efficiently for the salt, the formation of pre-cursor complexes means that little reordering is required to form the final complex. A highly crystalline polymer electrolyte results. Strongly coordinating solvents inhibit polymer-salt complex formation until the bulk of the solvent has been removed. This leads to polymer chain entanglement and a reduction in the long range order (and thus crystallinity) of the resulting electrolyte. Furthermore, complexes formed between the solvent and in particular highly charged cations often render it impossible to remove the last traces of solvent. This is found to be a particular problem, for example, in electrolytes containing magnesium salts[9].

Where anhydrous materials are used, the grinding/hot pressing method is capable of producing completely anhydrous and solvent free samples. Unlike the solvent casting method however, a microscopically intimate mixture of the components is not initially obtained. It is necessary to heat the samples above the melting point of the polymer to allow the salt to diffuse into it. If a crystalline complex is formed with a melting point greater than the preparation temperature, then this will serve to reduce the segmental motion of the polymer chains, some of which will be 'anchored' in the complex spherulites. This in turn will reduce the rate of diffusion of the salt into the polymer. It can thus be seen that in such cases the films formed by this method may not be completely homogeneous.

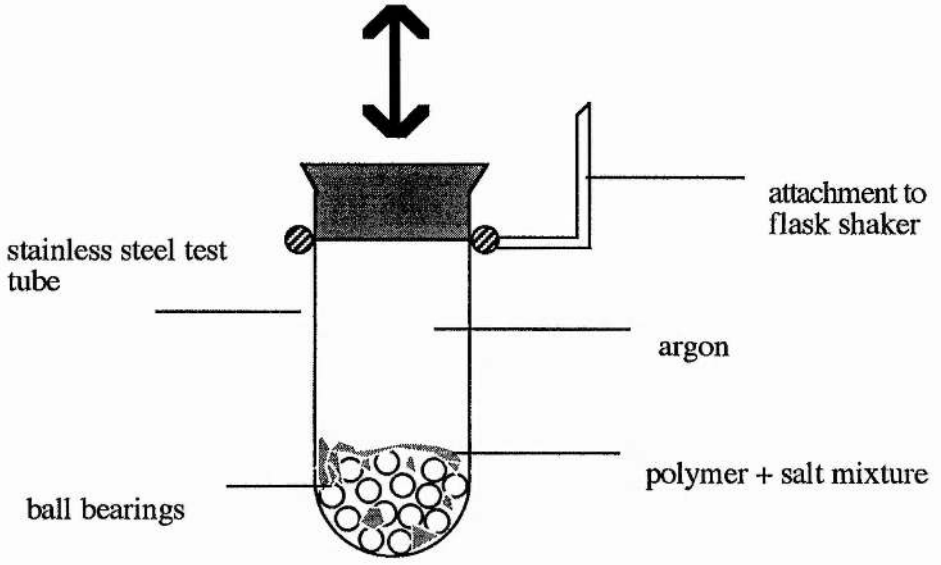

Figure 4-2 The apparatus for cryogrinding

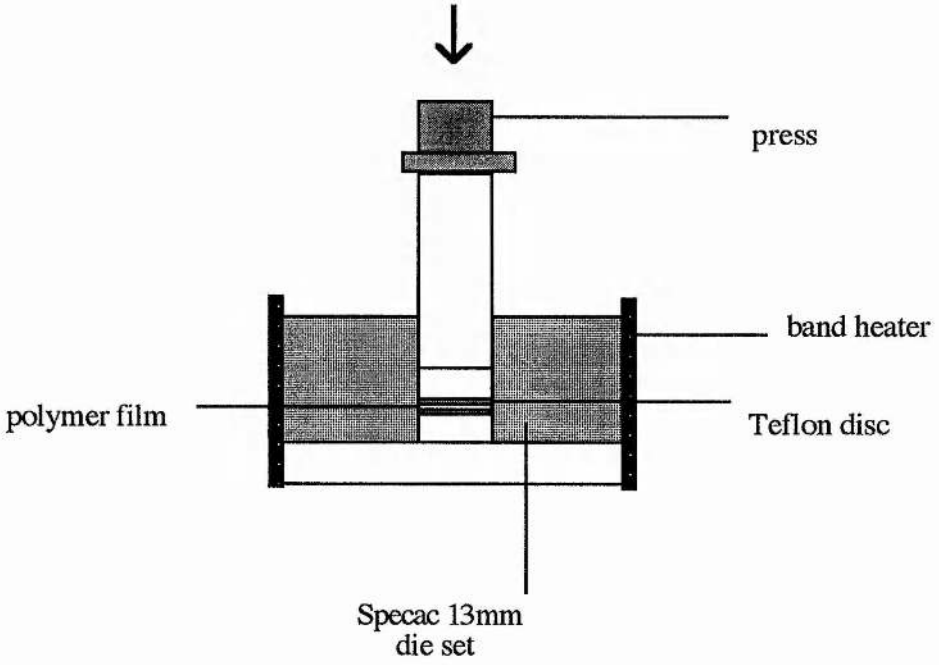

Figure 4-3 Apparatus for hot pressing

4.2 Preparation of salts

4.2.1 *Lithium Triflate and Calcium Triflate*

$$Li_2CO_3 + 2\,CF_3SO_3H \rightarrow 2\,LiCF_3SO_3 + H_2O + CO_2 \qquad 4\text{-i)}$$

$$CaCO_3 + 2\,CF_3SO_3H \rightarrow CaCF_3SO_3 + H_2O + CO_2 \qquad 4\text{-ii)}$$

Triflic acid (0.667 mol dm^{-3}) was slowly added to a suspension of the appropriate carbonate in distilled water ($^7Li_2CO_3$,AERE; $CaCO_3$,BDH). The solution was stirred (3hours $^7LiCF_3SO_3$;24 hours $Ca(CF_3SO_3)_2$),filtered through a fine sinter and the bulk water removed on a rotary evaporator to yield the hydrated salt. The anhydrous salt was obtained by heating under vacuum ($^7LiCF_3SO_3$, 150 °C, 24 hours; $CaCF_3SO_3$, 180 ^{0}C , 48 hours).

4.2.2 *Europium (III) Triflate*

$$Eu_2O_3 + 6CF_3SO_3H \rightarrow 2\,Eu(CF_3SO_3)_3 + 3H_2O \qquad 4\text{-iii)}$$

Triflic acid (0.667 mol dm^{-3}) was slowly added to a slight excess of the oxide Eu_2O_3 (Aldrich 99.9%) suspended in distilled water. The solution was stirred for 24 hours, filtered through a fine sinter and the bulk water removed on a rotary evaporator. The hydrated salt was recrystallized from acetonitrile and then dried at 150 °C for 48 hours.

4.2.3 *Europium(II) Triflate*

Routes to some europium(II) salts have been reported in the literature. The methods used by Cooley and Yost[93] and by McCoy[94] were adapted for the synthesis of europium(II)triflate. Reduction of europium(III)chloride was achieved using a Jones reductor[95] containing amalgamated zinc. The europium(II)chloride was then converted to the carbonate via the sulphate. Europium(II)carbonate was used in preference to the sulphate in the preparation of the triflate to avoid contamination of the final product with sulphate ions.

4.2.3.1 *Preparation of the Jones Reductor*

Amalgamated zinc containing approximately 1% of mercury was required. 235g of 20 mesh zinc covered with 1 mol dm^{-3} hydrochloric acid was stirred for 1 minute. 48cm^3 of 0.25 mol dm^{-3} mercury(II)chloride was added and the solution stirred rapidly for a further 3 minutes. The solution was decanted off and the zinc amalgam washed with distilled water containing a few drops of hydrochloric acid. The zinc amalgam was then transferred to a chromatography column (40 cm x 1.7 cm). Prior to use, the column was flushed with 200 cm^3 of 0.1 mol dm^{-3} hydrochloric acid.

4.2.3.2 *Preparation of Europium (II) Sulphate*

$$2Eu^{3+}_{(aq)} + Zn_{(s)} \rightarrow 2\,Eu^{2+}_{(aq)} + Zn^{2+}_{(aq)} \qquad 4\text{-iv})$$

$$Eu^{2+}_{(aq)} + SO_4{}^{2-}_{(aq)} \rightarrow EuSO_{4(s)} \qquad 4\text{-v})$$

A solution of europium(III)chloride was prepared by dissolution of 2.56g of Eu_2O_3 in 9.72 cm^3 of 6 mol dm^{-3} hydrochloric acid. This was made up to 250 cm^3 by the addition of distilled water and argon was bubbled through the solution to remove dissolved oxygen.

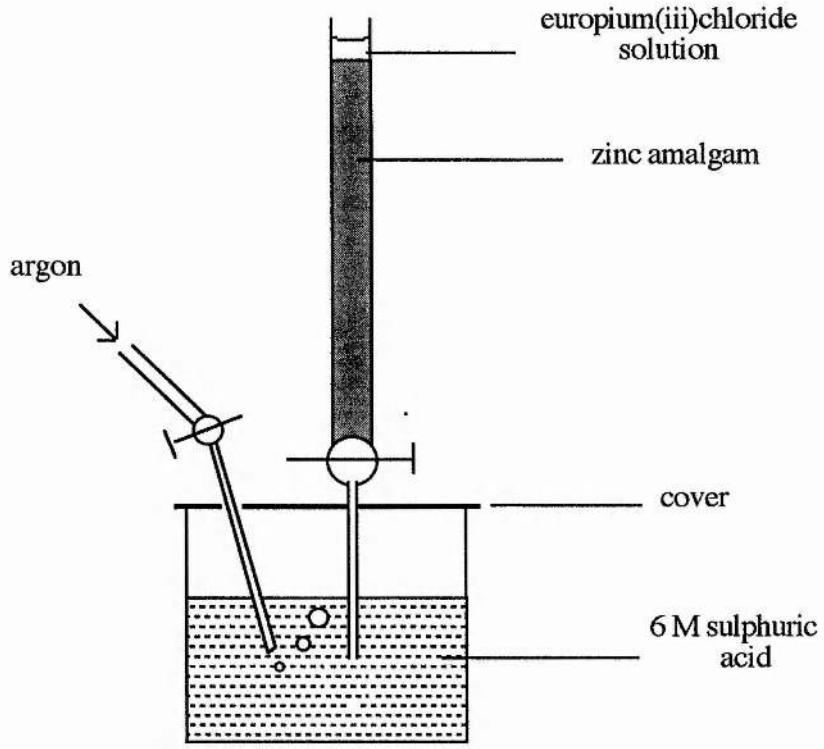

Figure 4-4 The Jones Reductor

The tip of the Jones Reductor was dipped into a 600 cm^3 beaker containing 60 cm^3 of 8 mol dm^{-3} sulphuric acid through which a stream of argon was passed. The europium(III)chloride solution was passed through the Jones Reductor at a rate of 1 cm^3 per minute followed by 150 cm^3 of 0.1 mol dm^{-3} hydrochloric acid. A white feathery precipitate of the α-modification of europium(II)sulphate was observed to form after about 40 minutes. The mixture was then heated to 80 ^oC (still under argon) whereupon , the precipitate became more dense (β- form) and settled to the bottom of the beaker. The β- form of europium(II)sulphate, unlike the α- form is only slightly soluble in sulphuric acid.

The mixture was cooled and filtered and the pink/white precipitate collected. This was washed with 0.1 mol dm^{-3} hydrochloric acid followed by a small quantiy of acidified methanol. The precipitate was dried by heating at 75 °C fo 8 hours .

4.2.3.3 *Preparation of Europium(II) Carbonate*

$$EuSO_4 + Na_2CO_3 \rightarrow Na_2SO_4 + EuCO_3 \qquad 4\text{-vi})$$

300 cm^3 of a solution containing 12.6g of $NaHCO_3$ and 10.8 g of NaOH in distilled water was boiled for 10 minutes to remove dissolved oxygen. The europium(ii)sulphate previoiusly prepared, was added to the solution, whereupon a fine yellow precipitate formed. The solution was boiled for a further 10 minutes and the precipitate collected by filtration through a fine sinter. The yellow europium(II)carbonate was dried at 75 °C for 24 hours and the composition of the resulting compound was confirmed by elemental analysis.

4.2.3.4 *Preparation of Europium(II) Triflate*

$$EuCO_3 + 2\ CF_3SO_3H \rightarrow Eu(CF_3SO_3)_2 + H_2O + CO_2 \qquad 4\text{-vii})$$

Triflic acid (degassed, 1.333 x 10^{-3} mol dm^{-3}) was added to a slight excess of $EuCO_3$ suspended in distilled water (also degassed) in an argon filled glove bag.The solution was stirred for 1 hour and filtered through a fine sinter. Bulk water was removed by gentle heating under vacuum to produce the white hydrated salt. This was dried by heating for 24 hours at 110 °C under vacuum after which the anhydrous salt was stored in the glove box.

4.3 Instrumentation

4.3.1 *Cell Design*

The body of the electrochemical cell was equally suited for use with 2 electrode cells and those requiring a third reference electrode. The Teflon body supported spring loaded stainless steel electrodes between which the polymer electrolyte discs and electrodes making up the cell were sandwiched.

Insertion of the cell into a gas tight, evacuable stainless steel container permitted subsequent removal from the glove box for electrical measurements. Contact between the cell and the equipment required for the electrical measurements was facilitated by means of electrical breakthroughs in the cylinder. Finally, cell temperature was monitored by a K-type thermocouple running through the cylinder.

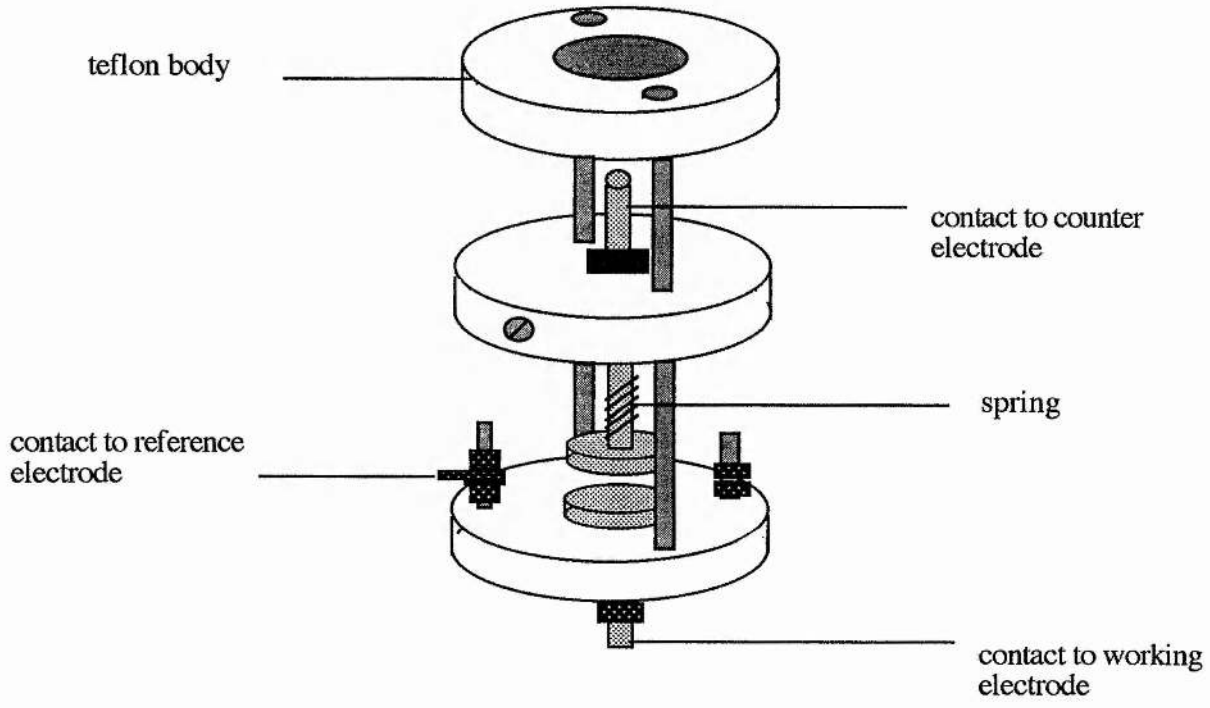

Figure 4-5 The cell design

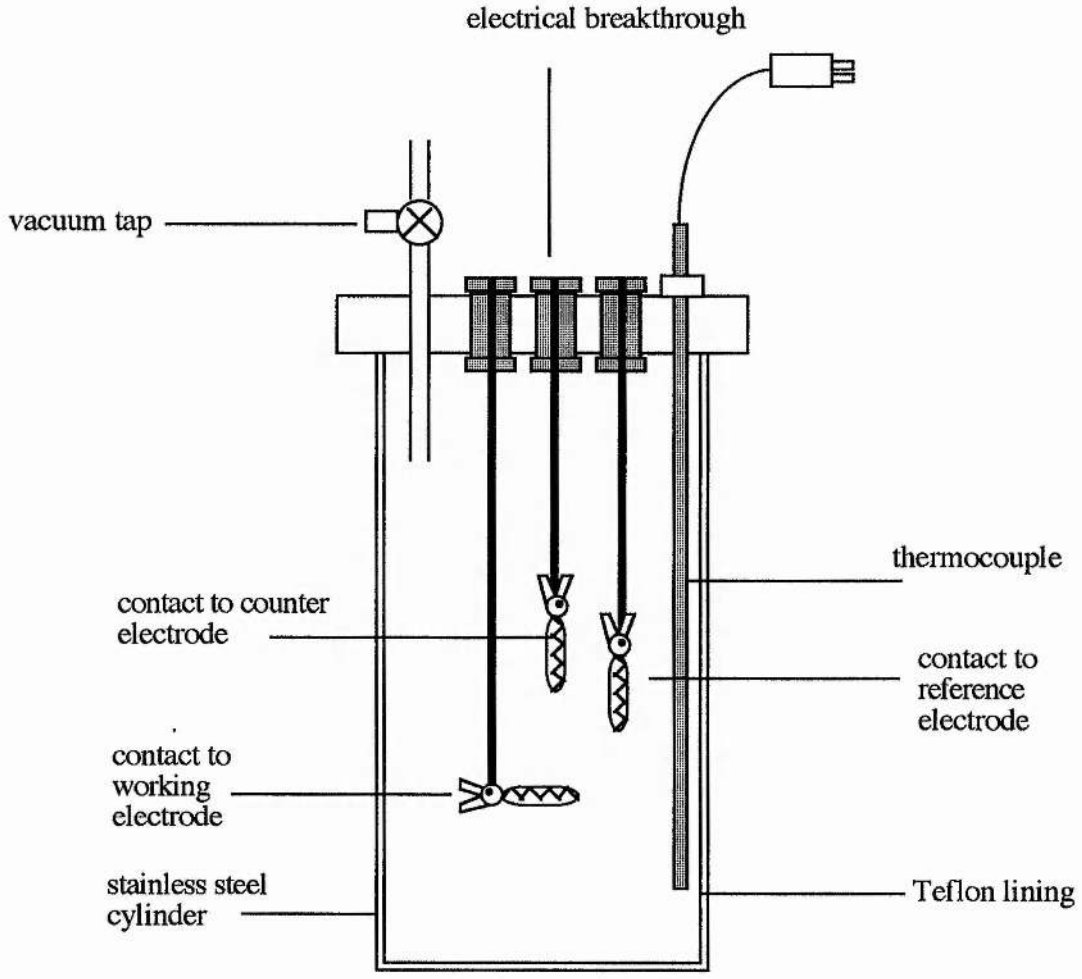

Figure 4-6 The stainless steel cylinder for removal of cells from the glove box

4.3.2 *Conductivity measurements*

AC conductivity measurements were performed using a Schlumberger 1250 or 1255 frequency response analyser (FRA) in conjunction with a 1286 electrochemical interface (ECI). The apparatus, under the control of a microcomputer , was driven by software written by Abrahams[96] and Gray[97]. Logarithmically decreasing sweeps, recorded typically from 100 kHz to 1 Hz ,were stored on floppy disks and used to produce complex impedance plots[98].

4.3.3 *Cyclic Voltammetry and Potential Step Experiments*

An Amel model 553 poteniostat, Hi Tek Instruments PPR1 waveform generator and Linseis x-y recorder were used to collect cyclic voltammograms. For potential step experiments, the x-y recorder was replaced with a J J Instruments y-t recorder.

4.3.4 *Differential Scanning Calorimetry*

All DSC scans were performed on a Perkin Elmer DSC7 differential scanning calorimeter, a 3700 data station and TAC 7/3 instrument controller. For subambient operation, a liquid nitrogen cooler was used. Hot pressed polymer electrolyte samples were sealed into small aluminium sample pans inside the glove box. A sealed empty pan acted as reference.

4.3.5 *Powder X-Ray Diffraction*

Powder X-ray diffraction data was collected on a Stoe STADI/P high resolution system equipped with a linear position sensitive detector covering ~ 6° in 2θ and employing Ge-monochromatised Cu-Kα_1 radiation. Data was collected in steps of 0.02° in 2θ. The system was equipped with a furnace for obtaining data at elevated temperatures.

CHAPTER 5

THE PEO : CALCIUM TRIFLATE SYSTEM

The aim of the investigation was to determine the phase diagram for the $PEO_xCa(CF_3SO_3)_2$ system by DSC and X-ray diffraction techniques. Conductivities for a range of compositions were measured as a function of temperature and interpreted in terms of the phase diagram.

5.1 Experimental

5.1.1 *Sample Preparation*

Cryoground mixtures of PEO and calcium triflate were made for a range of compositions $PEO_xCa(CF_3SO_3)_2$ (x = 4.0, 5.3, 6.0, 6.5, 8.0, 9.2, 10.1, 12.0, 20.5, 34.6, 50.4 and 103.7). Hot pressed discs were prepared for each composition as described in section 4.1.2.

5.1.2 *X-ray diffraction*

Cryoground mixtures of PEO and calcium triflate were sealed into 0.5mm Lindemann tubes in an argon filled dry-box. The samples were heated to ≈ 150°C for 4 days to facilitate dissolution of the salt in the polymer. Crystalline samples were obtained by annealing for a further 4 days before being run on the X-ray diffractometer. Use of a furnace attached to the diffractometer facilitated the acquisition of data at elevated temperatures.

5.1.3 *Differential Scanning Calorimetry*

DSC scans were recorded for each composition in order to determine the temperature at which phase changes occurred within the system. Heating and cooling cycles, typically in the range 0 to 350°C were run at 20°C per minute.

5.1.4 *Conductivity Measurements*

The conductivities of polymer electrolyte films $PEO_xCa(CF_3SO_3)_2$ (x = 5.3, 6.5, 12.0, 20.5 and 50.4) sandwiched between stainless steel electrodes, were determined by ac impedance techniques.

5.2 Results

5.2.1 *X-ray diffraction at room temperature*

Powder X-ray diffraction patterns recorded at room temperature over the whole composition range are shown in figures 5-1 and 5-2. It was observed that the diffraction patterns were composed of simple combinations of the patterns obtained for :-

a) pure crystalline PEO

b) pure calcium triflate

c) a crystalline complex formed between calcium triflate and PEO

The composition of the complex was determined as being very close to $PEO_6Ca(CF_3SO_3)_2$. Samples with a composition richer in salt ($x \leq 5.3$) gave diffraction patterns containing both salt and complex. Samples more dilute in salt ($x \geq 6.5$) gave patterns containing both PEO and complex. The most dilute compositions gave patterns similar to pure PEO. The diffraction patterns for $PEO_6Ca(CF_3SO_3)_2$ and $PEO_8Ca(CF_3SO_3)_2$ appeared to be very similar at first sight. A clearer understanding of the differences between the samples was obtained by studying their behaviour at elevated temperatures. This is discussed further in section 5.2.3. The diffraction patterns obtained for different samples of the same composition exhibited good reproducibility.

$PEO_xCa(CF_3SO_3)_2$	Diffraction patterns observed
x<6	Salt + Complex
x=6	Complex
x>6	Complex + PEO
x>>6	PEO

Table 5-1 A summary of the X-ray diffraction patterns observed at room temperature for different electrolyte compositions

The x-ray diffraction pattern for the crystalline complex was indexed and the lattice parameters determined. The system was observed to be orthorhombic with a = 10.6069Å, b = 12.4761Å and c = 16.8473Å. Details of the peak positions are given in appendix 3.

5.2.2 *Differential Scanning Calorimetry*

DSC is a powerful tool for establishing the temperature at which phase changes occur in polymeric systems. A survey of the literature in the field of polymer electrolytes indicates that no common practise has yet been adopted for reporting temperatures at which thermal events such as melting, dissolution and crystallisation occur. Many groups report the peak position of the thermal event whereas some report its onset. A few give no indication of the parameter which they are reporting. This can sometimes lead to confusion when trying to compare the results of different groups for similar systems.

In this thesis, both peak positions and onsets are reported. Where data is represented graphically, onsets have been used if at all possible. In situations where there are overlapping peaks, it is not always possible to determine the onset temperature. Many of the DSC spectra for the PEO:$Ca(CF_3SO_3)_2$ system fall into this category and for this reason, in this case, peak positions are used instead.

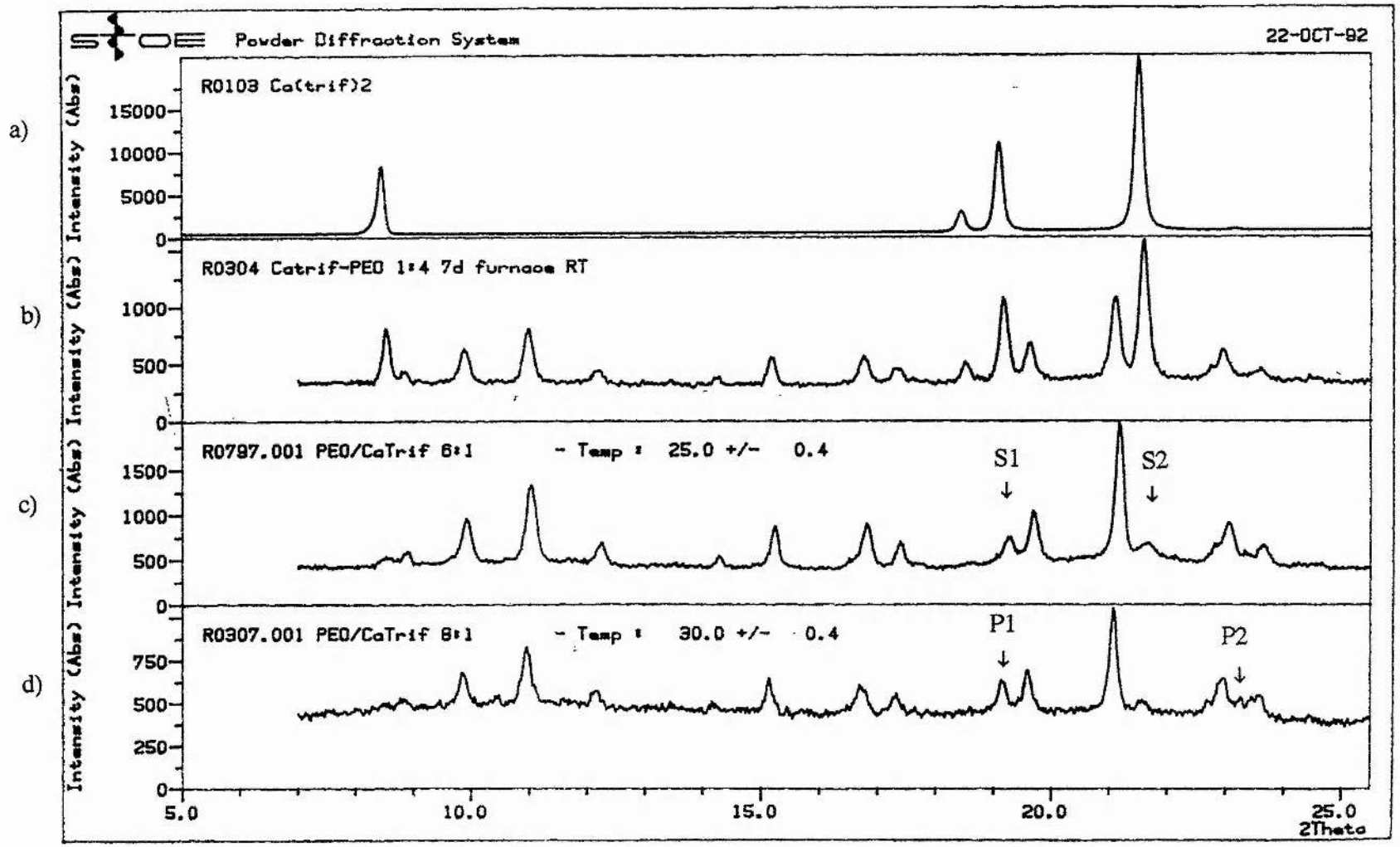

Figure 5-1 X-ray diffraction patterns for a) $Ca(CF_3SO_3)_2$, b) $PEO_4Ca(CF_3SO_3)_2$, c) $PEO_6Ca(CF_3SO_3)_2$ and d), $PEO_8Ca(CF_3SO_3)_2$

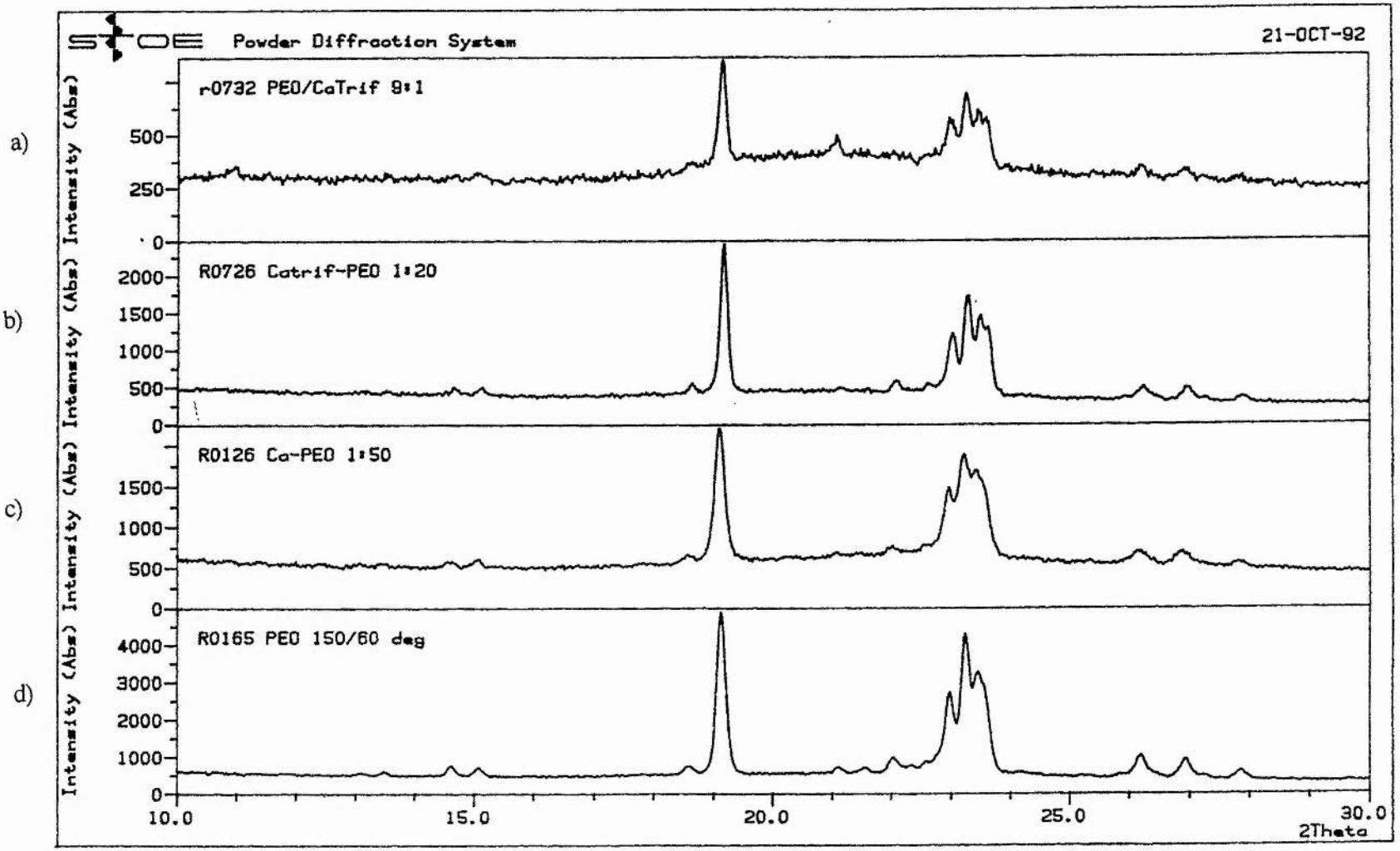

Figure 5-2 X-ray diffraction patterns for a) $PEO_{9.2}Ca(CF_3SO_3)_2$, b) $PEO_{20.5}Ca(CF_3SO_3)_2$, c) $PEO_{50.4}Ca(CF_3SO_3)_2$ and d) Pure PEO

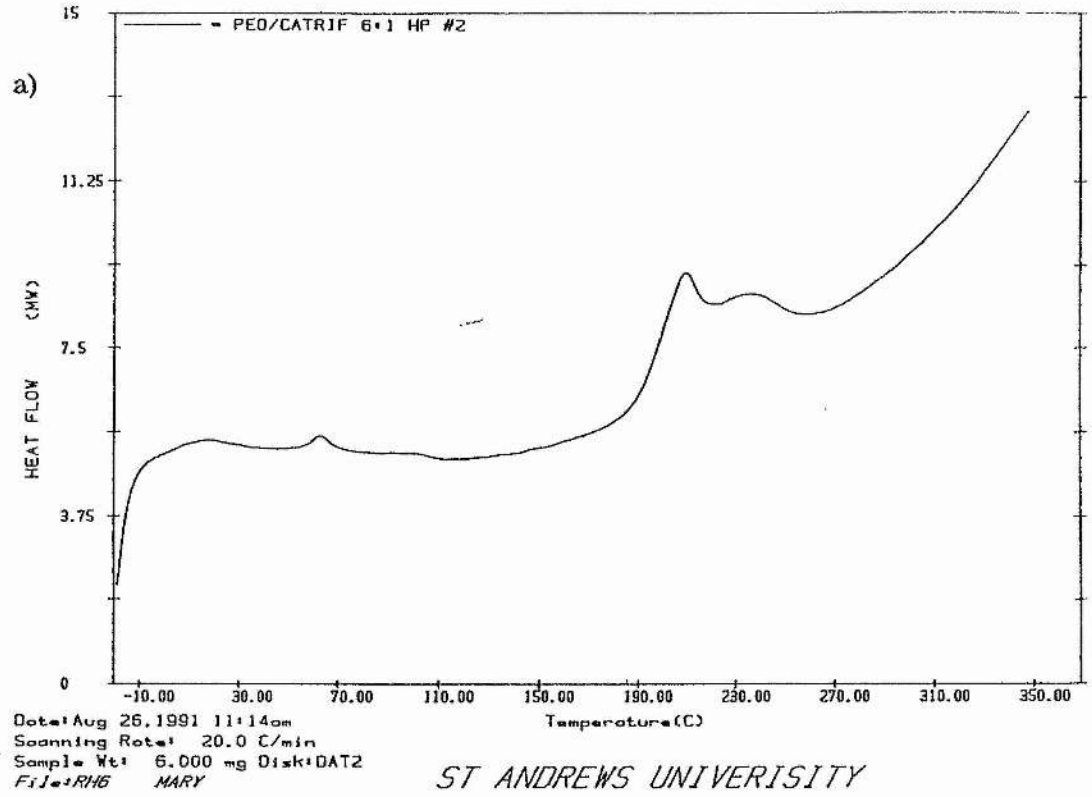

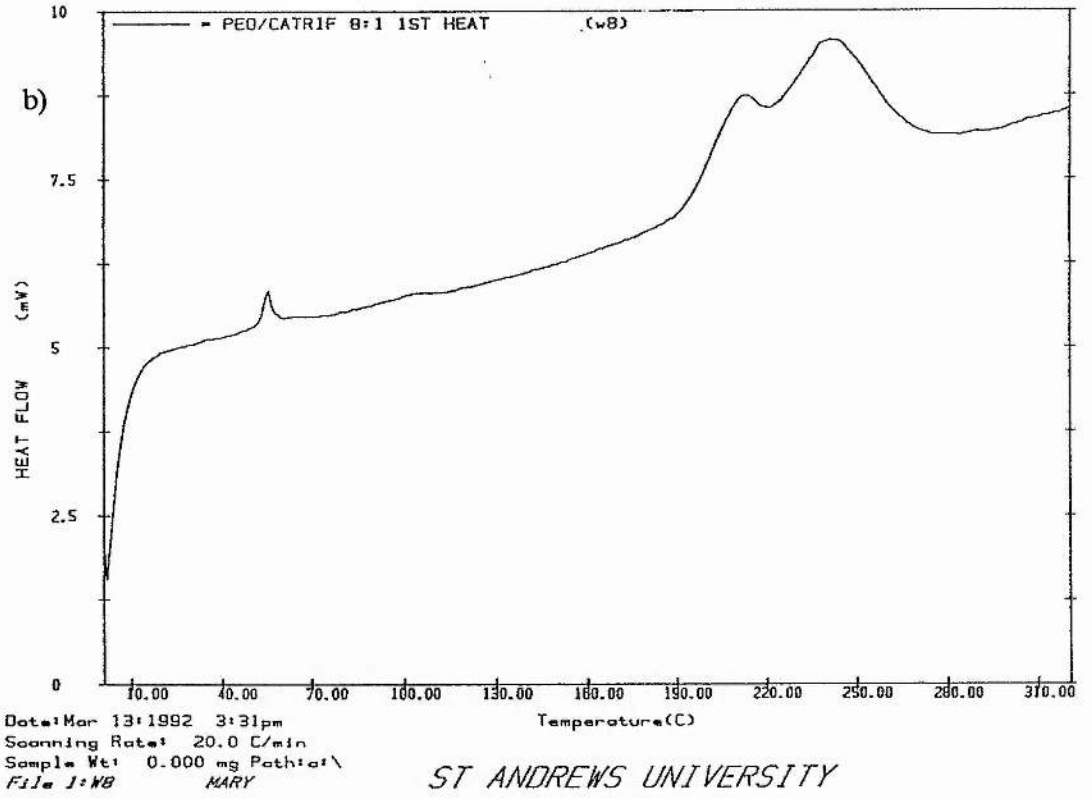

Figure 5-3 DSC trace for the first heating cycle a) $PEO_6Ca(CF_3SO_3)_2$ and b) $PEO_8Ca(CF_3SO_3)_2$

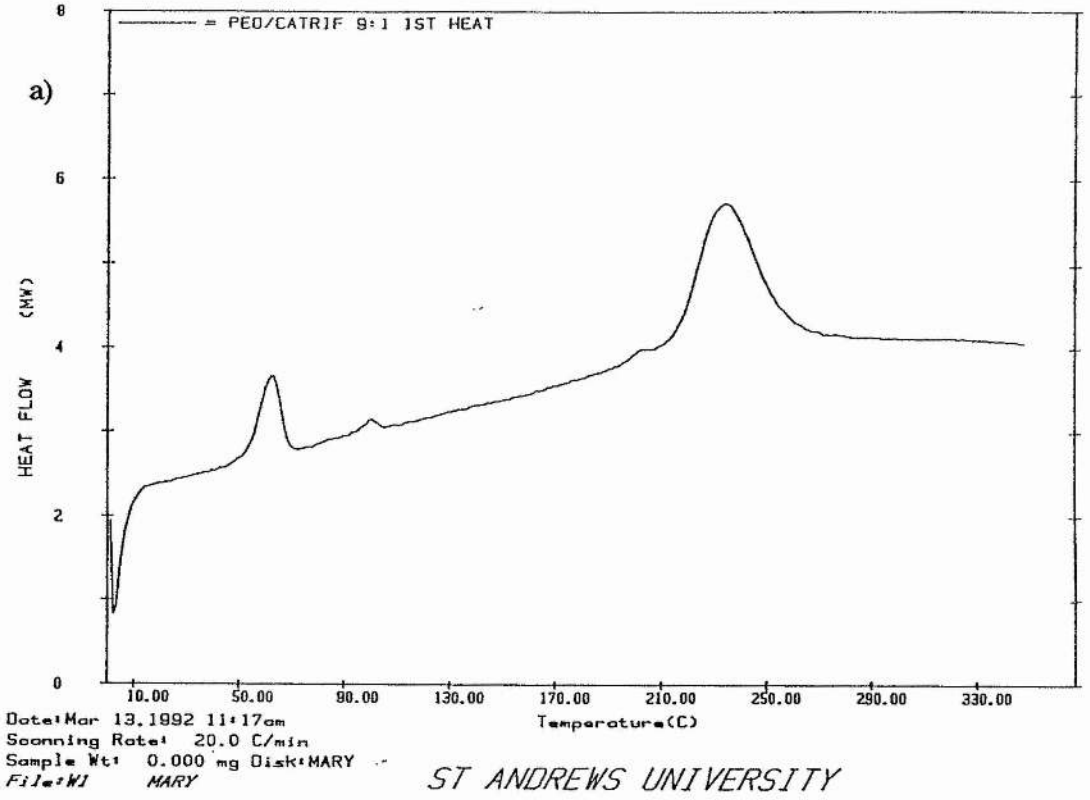

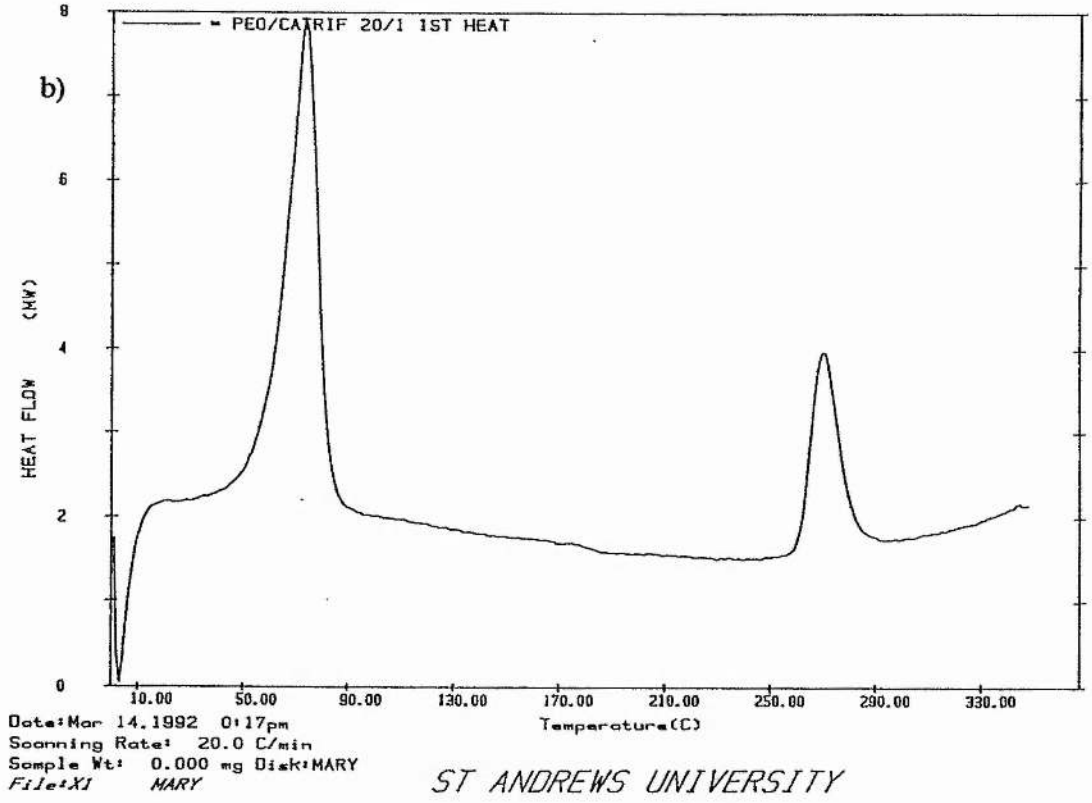

Figure 5-4 DSC trace for the first heating cycle a) $PEO_{9.2}Ca(CF_3SO_3)_2$ and b) $PEO_{20.5}Ca(CF_3SO_3)_2$

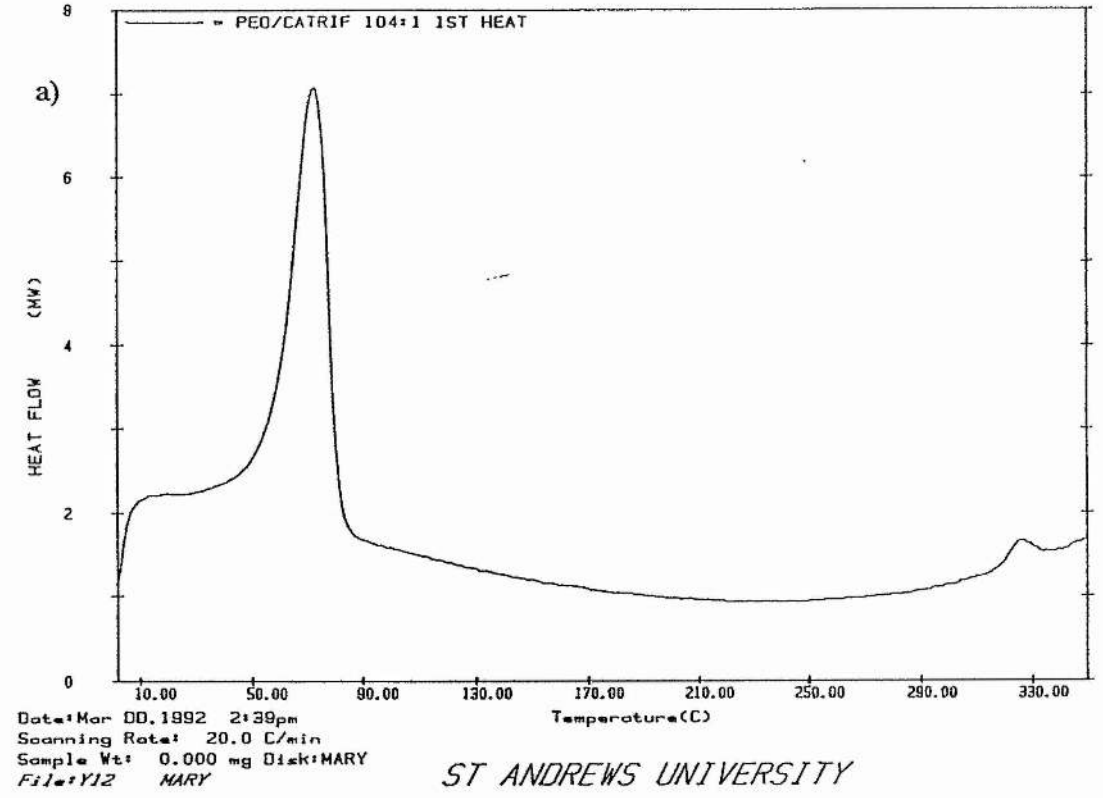

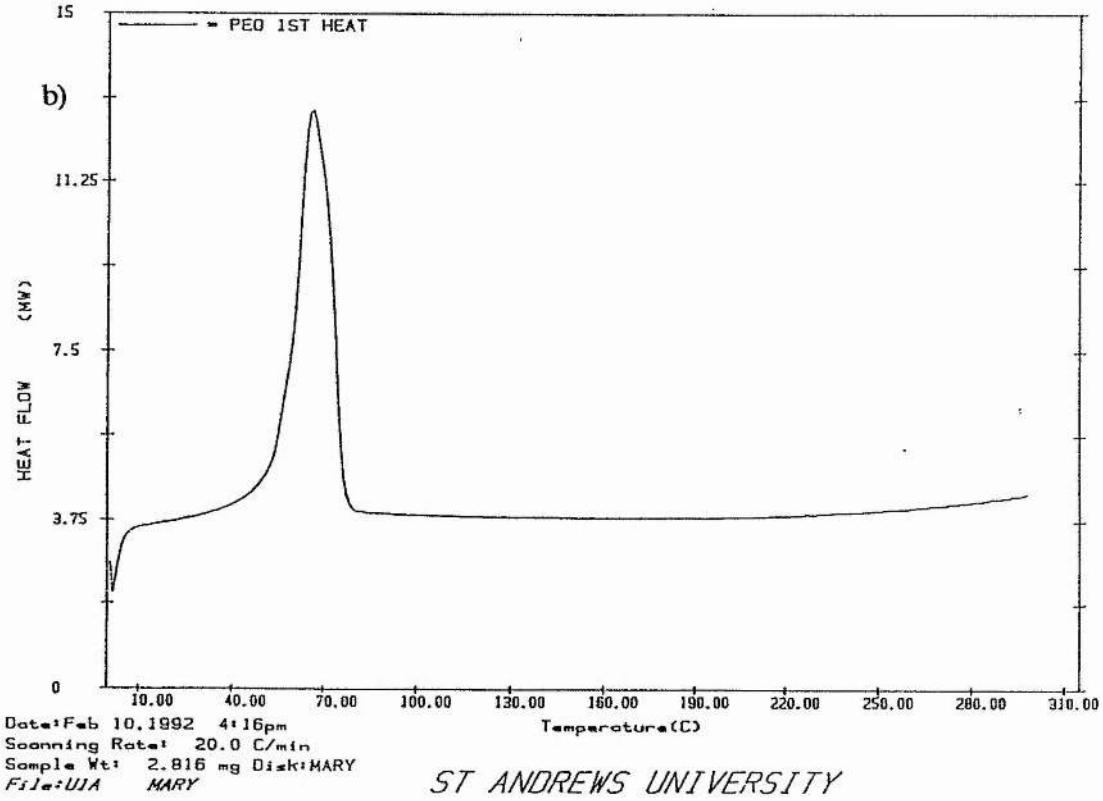

Figure 5-5 DSC trace for the first heating cycle a) $PEO_{104}Ca(CF_3SO_3)_2$ and b) PEO

5.2.2.1 *Differential Scanning Calorimetry - 1st heating cycle*

Some typical DSC traces obtained for the first heating cycle are shown in figures 5-3 to 5-5. For compositions richer in salt than $PEO_{9.2}Ca(CF_3SO_3)_2$, a double endotherm was observed in the region of 230°C. More dilute compositions gave only a single endotherm in this region, the peak shifting to higher temperature with decreasing salt concentration. For compositions more dilute in salt than $PEO_{6.5}Ca(CF_3SO_3)_2$ a single endotherm was observed in the region of 65°C. The magnitude of this endotherm appeared to increase with decreasing salt concentration. The DSC peak positions for the first heating cycles are shown as a function of composition in figure 5-6.

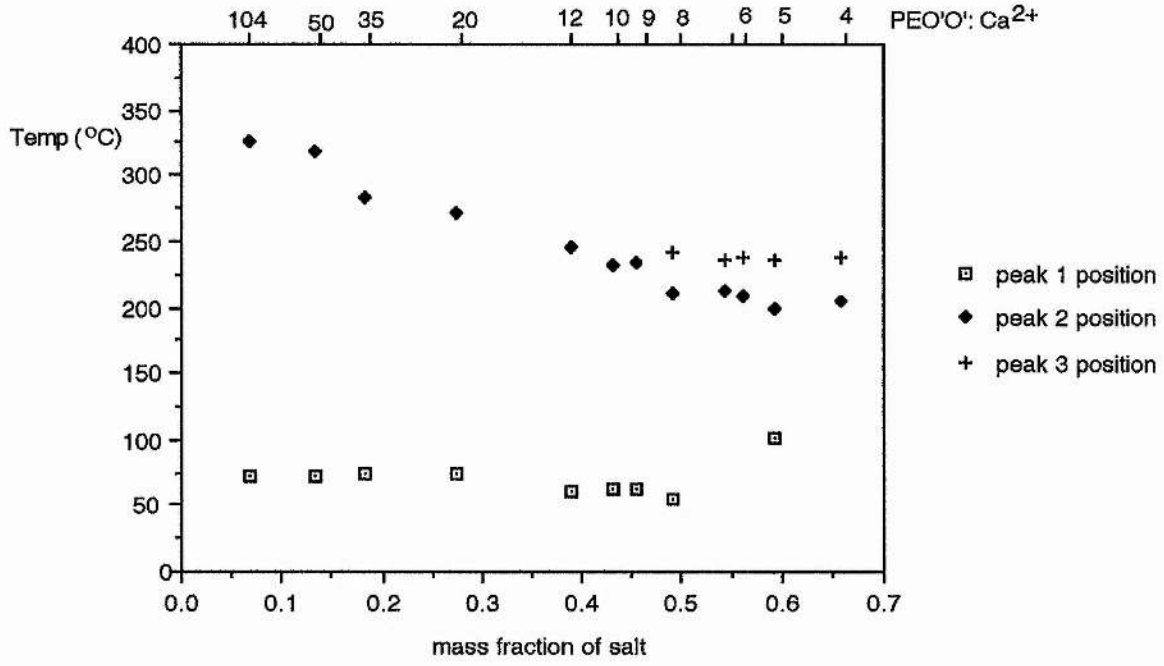

Figure 5-6 DSC peak positions versus composition for the first heating cycle

5.2.2.2 *Differential Scanning Calorimetry - 2nd and subsequent heating cycles*

On the second and subsequent heating cycles, the double endotherm, previously observed in the region of 230 °C was replaced by a single endotherm in the same region. For compositions slightly richer in PEO than the complex, the first endotherm (previously observed in the region of 65°C) was either absent or shifted to lower temperatures than observed on the first heating cycle. This is illustrated for $PEO_8Ca(CF_3SO_3)_2$ in figure 5-7.

Peak positions were found to be completely reproducible for the second and subsequent heating cycles. This is illustrated by figure 5-8 and comparison of the data in tables 5-2b and 5-2c.

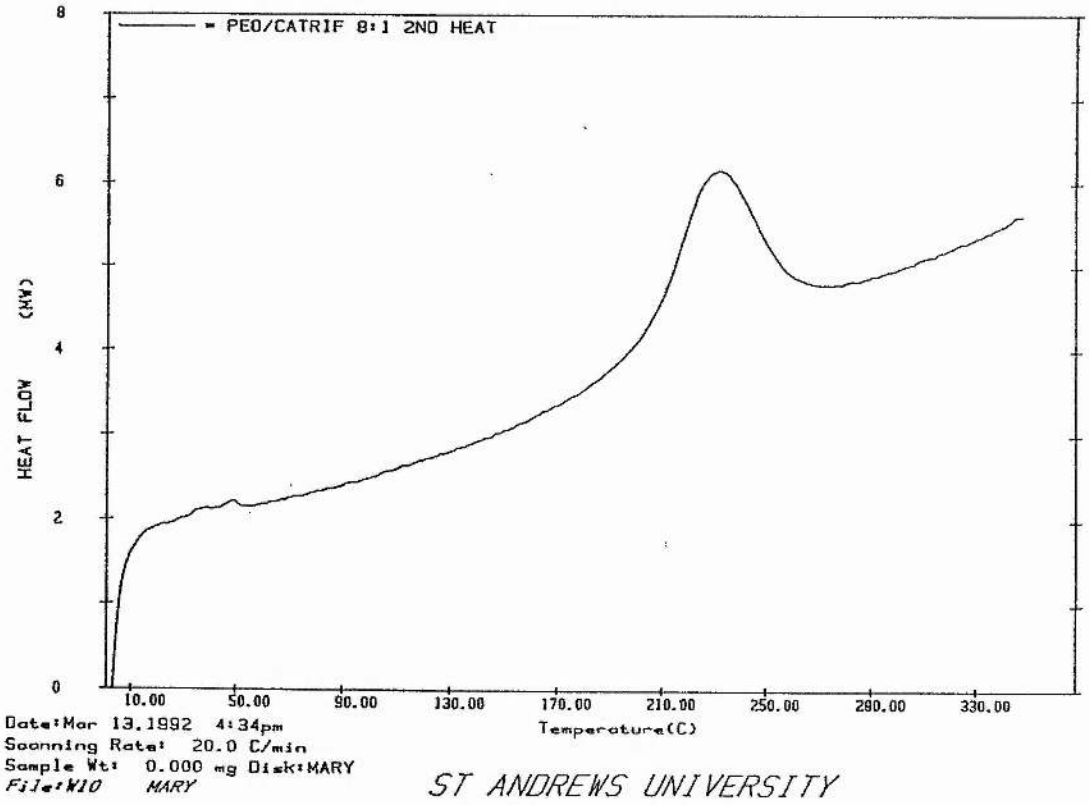

Figure 5-7 DSC spectrum for $PEO_8Ca(CF_3SO_3)_2$ - 2nd heating cycle

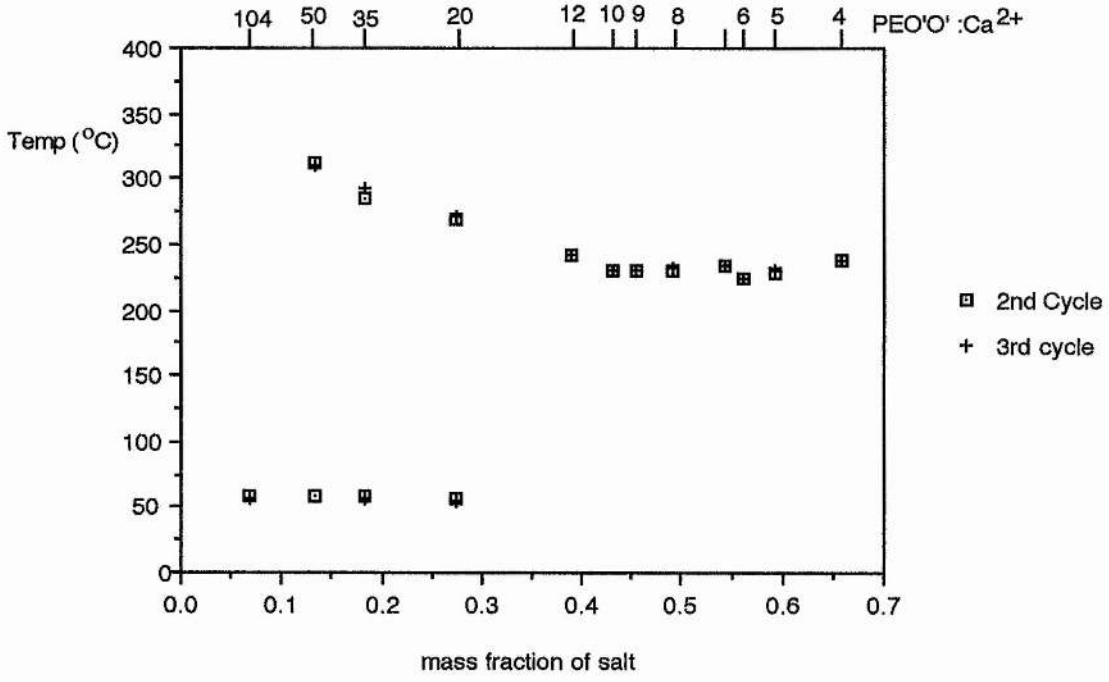

Figure 5-8 DSC peak positions versus composition for the second and third heating cycles

The DSC data for the first three heating cycles are summarised in table 5.2

x	Mass fraction of salt	peak 1 onset (C)	peak 1 position (C)	peak 2 onset (C)	peak 2 position (C)	peak 3 position (C)
4.0	0.658	-	-	187.3	205.5	238.6
5.3	0.592	86.7	100.7	183.9	199.5	235.2
6.0	0.562	-	-	185.2	208.4	239.0
6.5	0.542	-	-	200.7	212.5	236.2
8.0	0.490	52.6	55.6	193.0	211.3	242.3
9.2	0.455	53.5	62.6	214.8	234.3	-
10.1	0.432	51.0	61.7	220.7	232.2	-
12.0	0.390	51.8	60.9	235.0	246.3	-
20.5	0.273	59.6	73.6	261.6	270.5	-
34.6	0.182	60.4	73.8	276.4	283.8	-
50.4	0.132	59.3	72.9	303.1	317.3	-
103.7	0.069	57.2	72.5	318.6	325.4	-

Table 5-2a DSC data for the 1st heating cycle

x	Mass fraction of salt	peak 1 onset (C)	peak 1 position (C)	peak 2 onset (C)	peak 2 position (C)
4.0	0.658	-	-	186.1	238.6
5.3	0.592	-	-	131.0	228.0
6.0	0.562	-	-	184.8	224.8
6.5	0.542	-	-	179.9	234.1
8.0	0.490	-	-	203.3	229.8
9.2	0.455	-	-	212.4	229.4
10.1	0.432	-	-	216.4	230.5
12.0	0.390	-	-	233.1	242.4
20.5	0.273	49.4	57.5	260.7	268.8
34.6	0.182	51.2	59.1	272.6	285.8
50.4	0.132	52.9	59.5	311.1	311.4
103.7	0.069	51.5	58.4	-	-

Table 5-2b DSC data for the 2nd heating cycle

x	Mass fraction of salt	peak 1 onset (C)	peak 1 position (C)	peak 2 onset (C)	peak 2 position (C)
4.0	0.658	-	-	204.6	238.6
5.3	0.592	-	-	124.7	231.0
6.0	0.562	-	-	182.4	224.8
6.5	0.542	-	-	174.4	234.6
8.0	0.490	-	-	186.6	232.4
9.2	0.455	-	-	214.4	230.2
10.1	0.432	-	-	213.5	230.5
12.0	0.390	-	-	222.1	242.4
20.5	0.273	55.5	46.8	263.3	271.0
34.6	0.182	56.9	49.6	281.7	291.9
50.4	0.132	-	-	311.1	311.1
103.7	0.069	56.9	45.1	-	-

Table 5-2c DSC data for the 3rd heating cycle

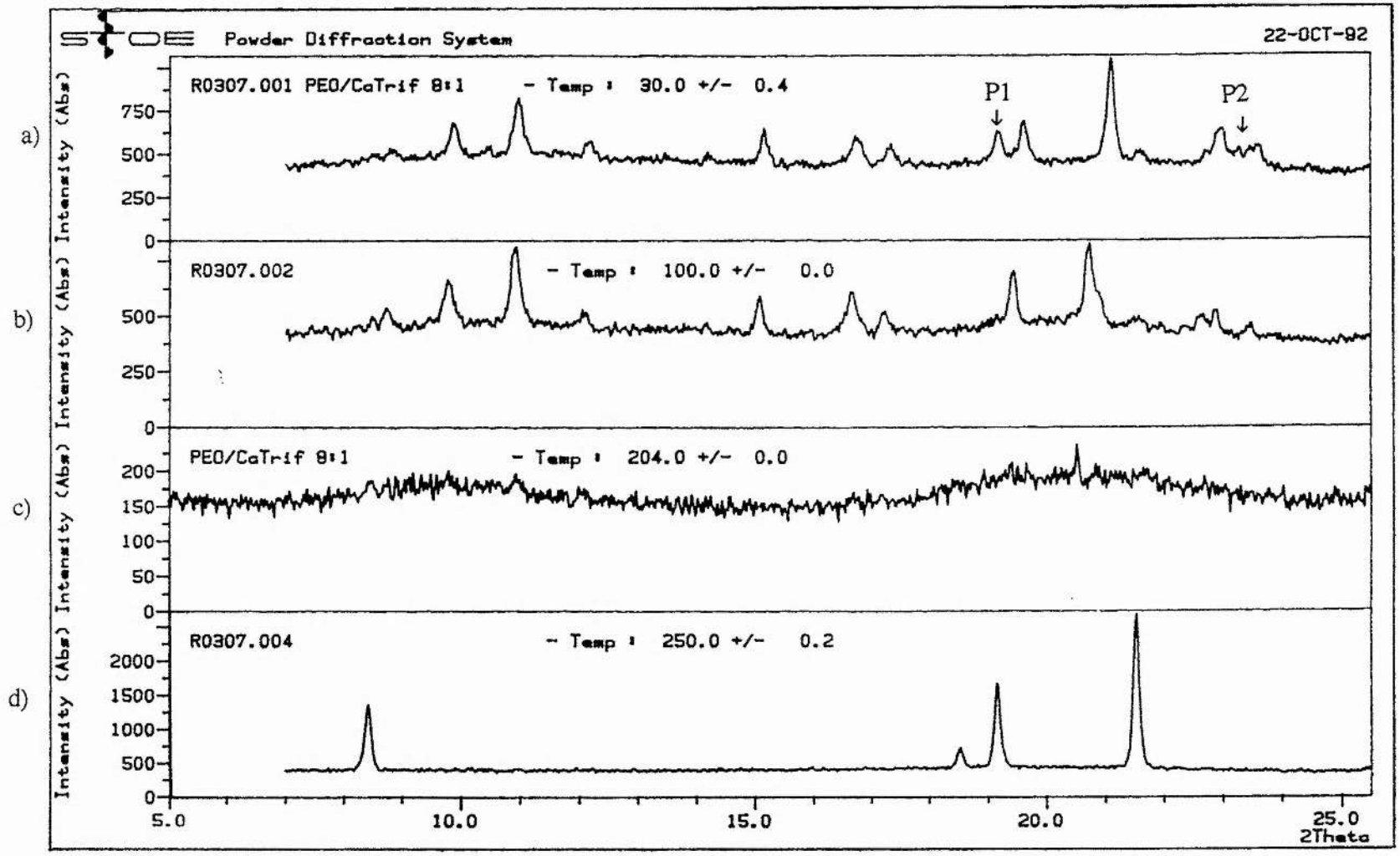

Figure 5-9 X-ray diffraction patterns for $PEO_8Ca(CF_3SO_3)_2$ heated to a) 30°C, b) 100°C, c) 204°C and d) 250°C

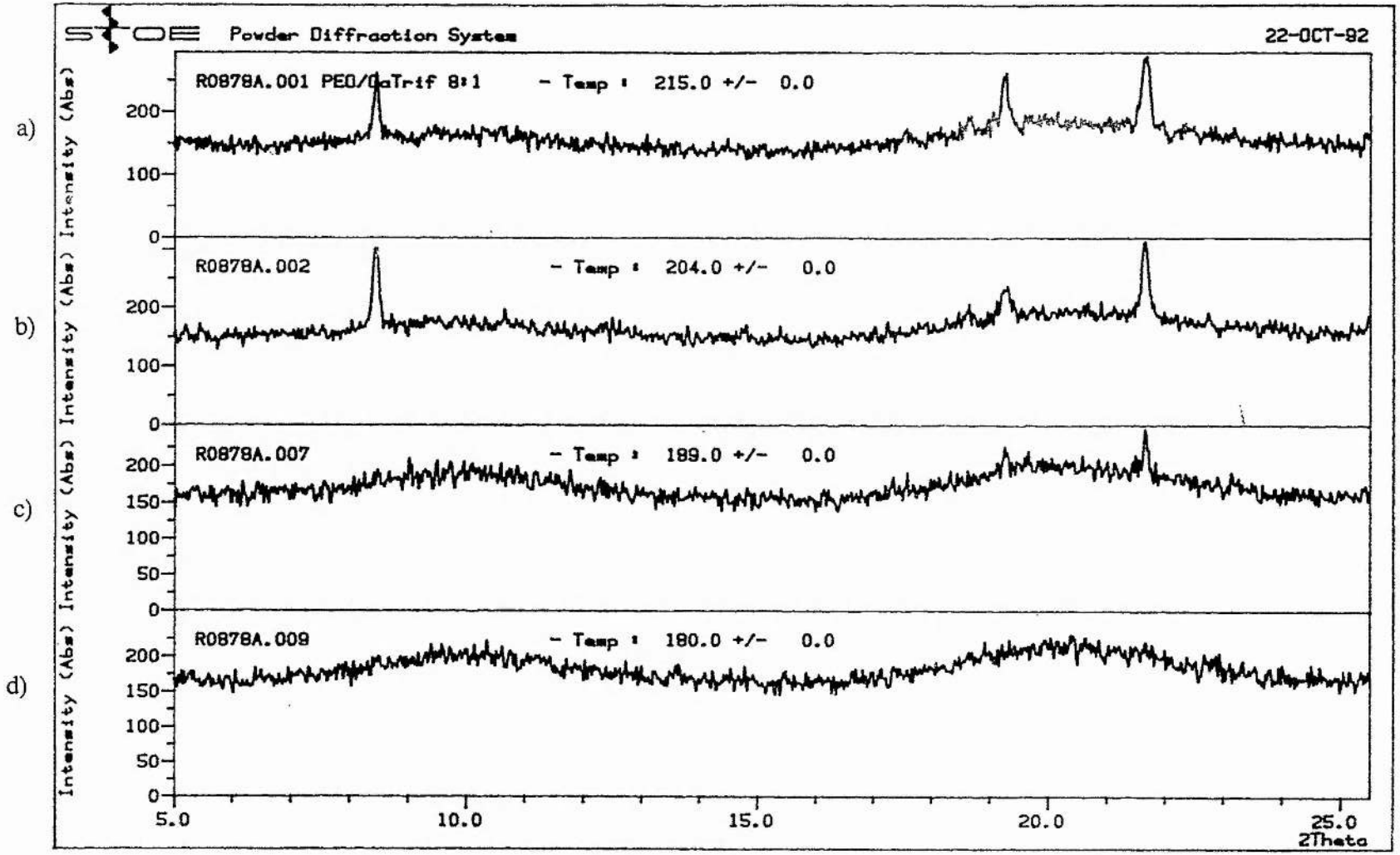

Figure 5-10 X-ray diffraction patterns for $PEO_8Ca(CF_3SO_3)_2$ cooled to a) 215°C, b) 204°C, c) 189°C and d) 180°C

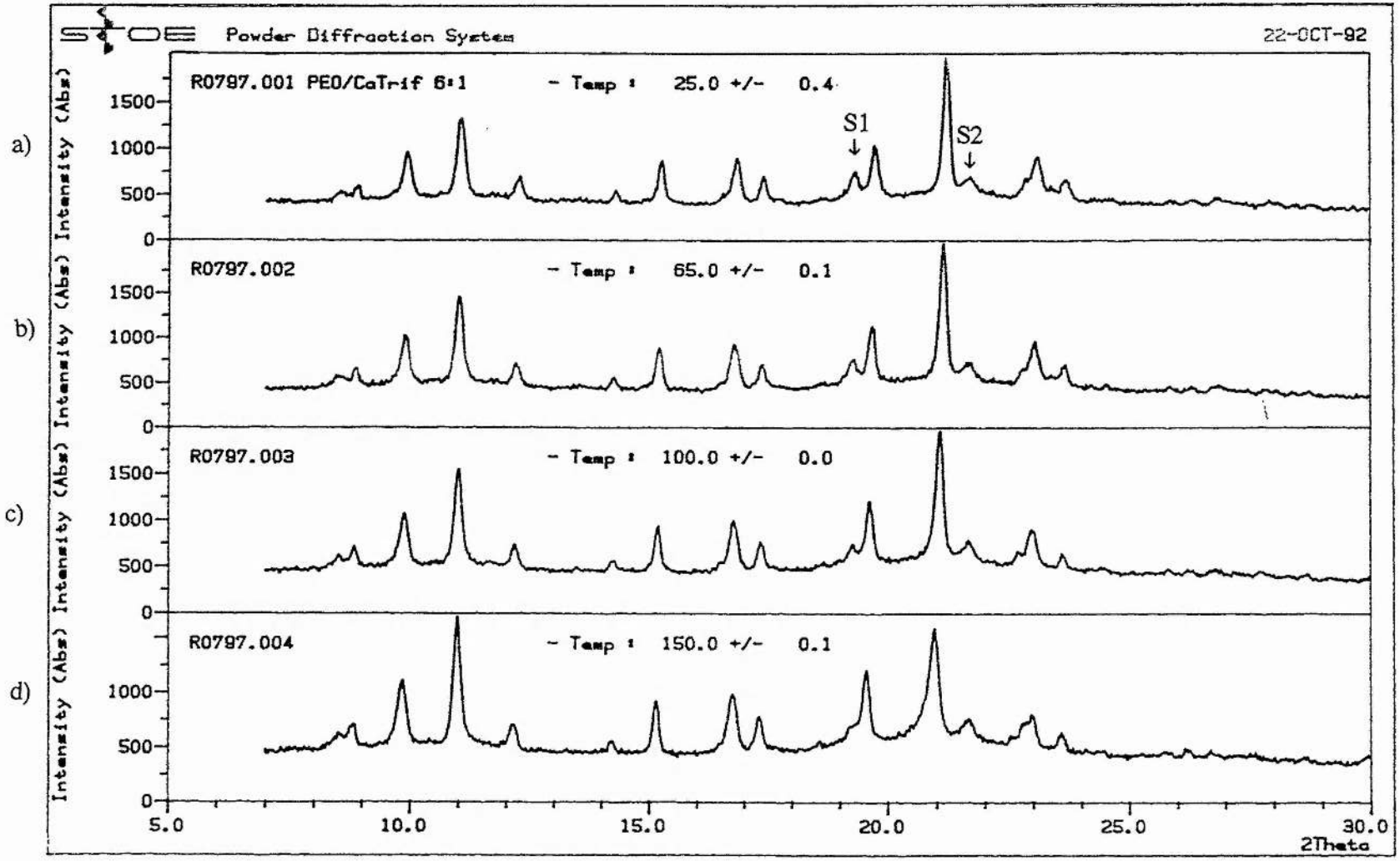

Figure 5-11 X-ray diffraction patterns for $PEO_6Ca(CF_3SO_3)_2$ heated to a) 25°C, b) 65°C, c) 100°C and d) 150°C

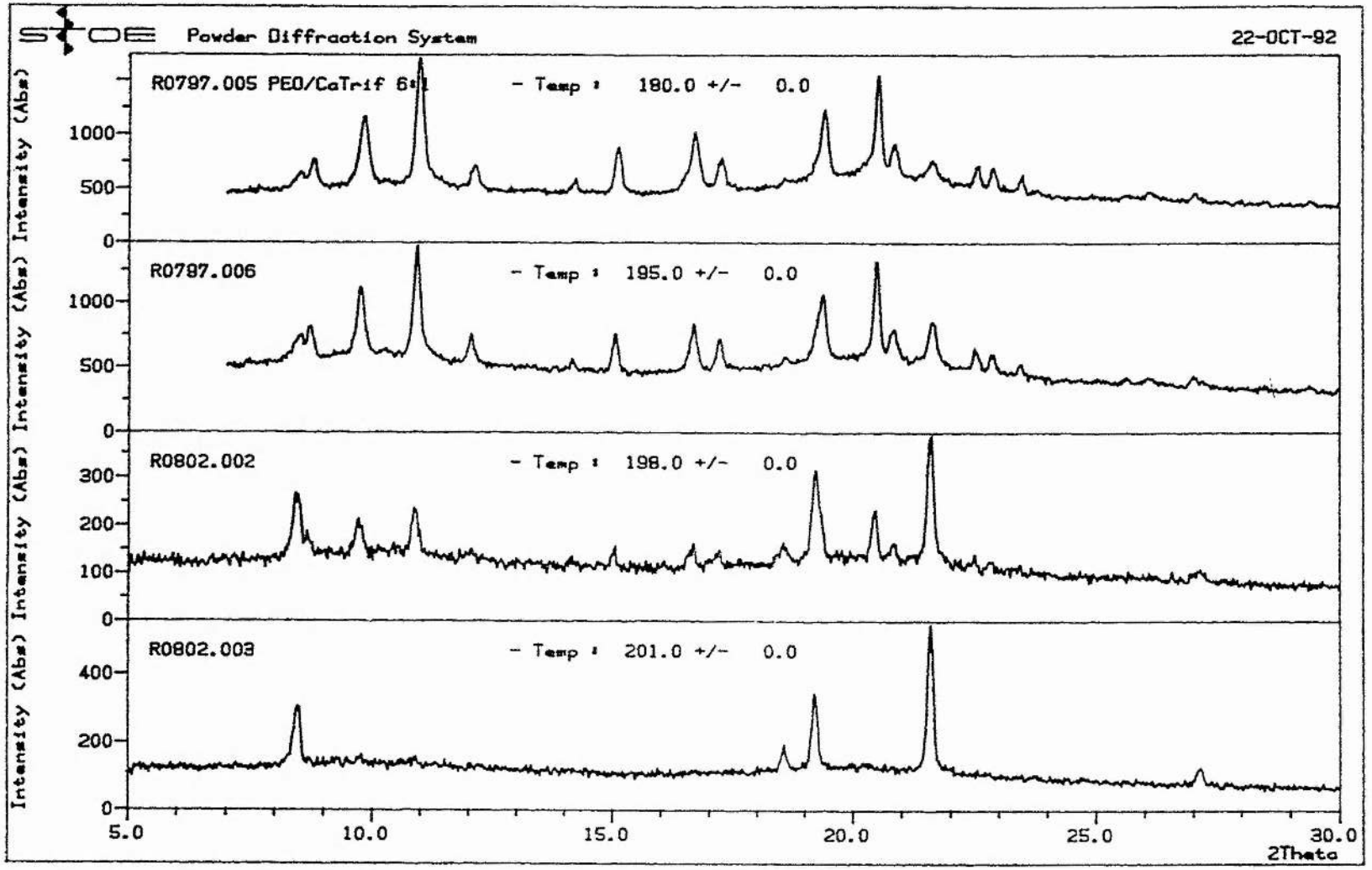

Figure 5-12 X-ray diffraction patterns for $PEO_6Ca(CF_3SO_3)_2$ heated to a) 180°C, b) 195°C, c) 198°C and d) 201°C

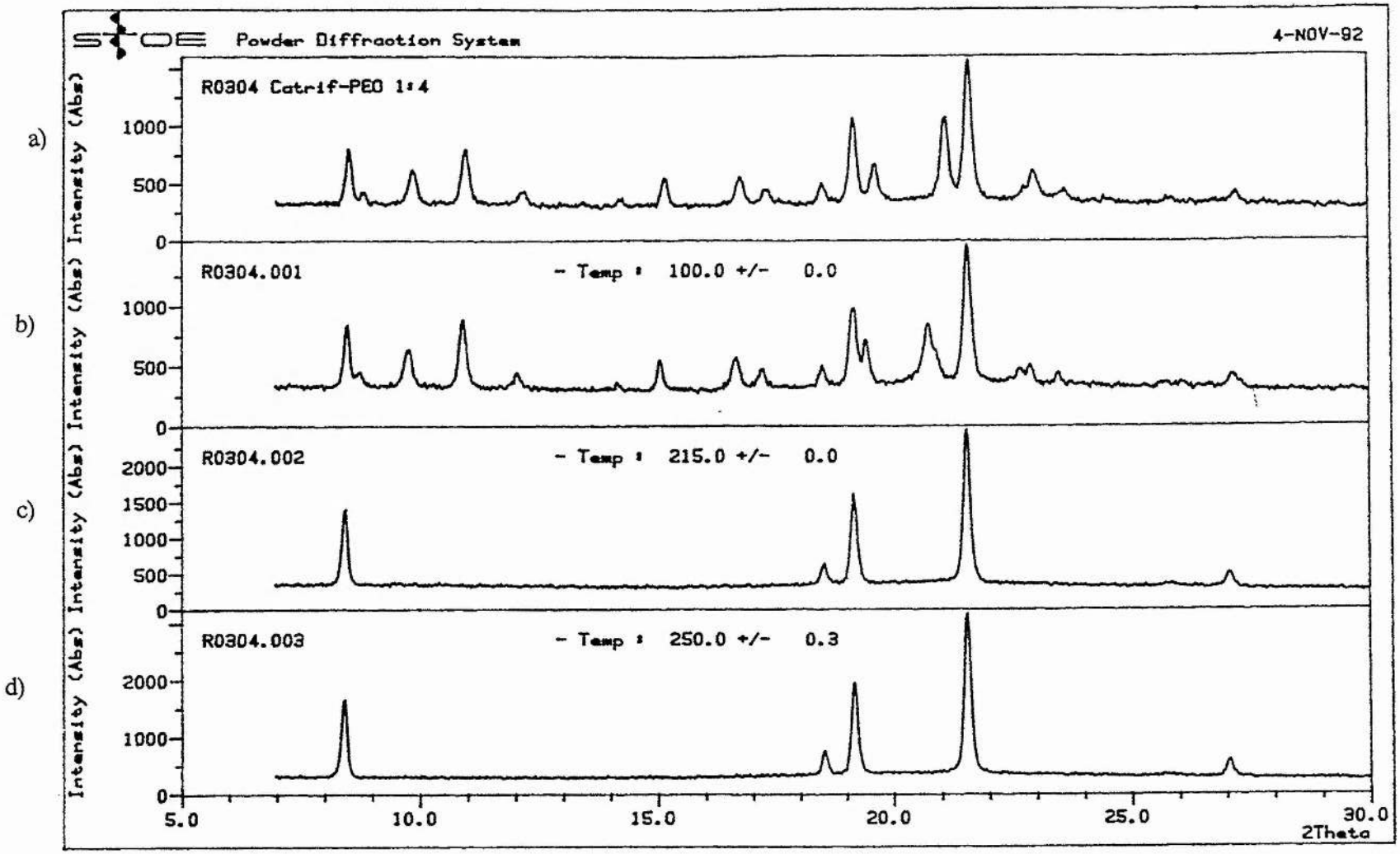

Figure 5-13 X-ray diffraction patterns for $PEO_4Ca(CF_3SO_3)_2$ at a) room temperature, b) 100°C, c) 215°C and d) 250°C

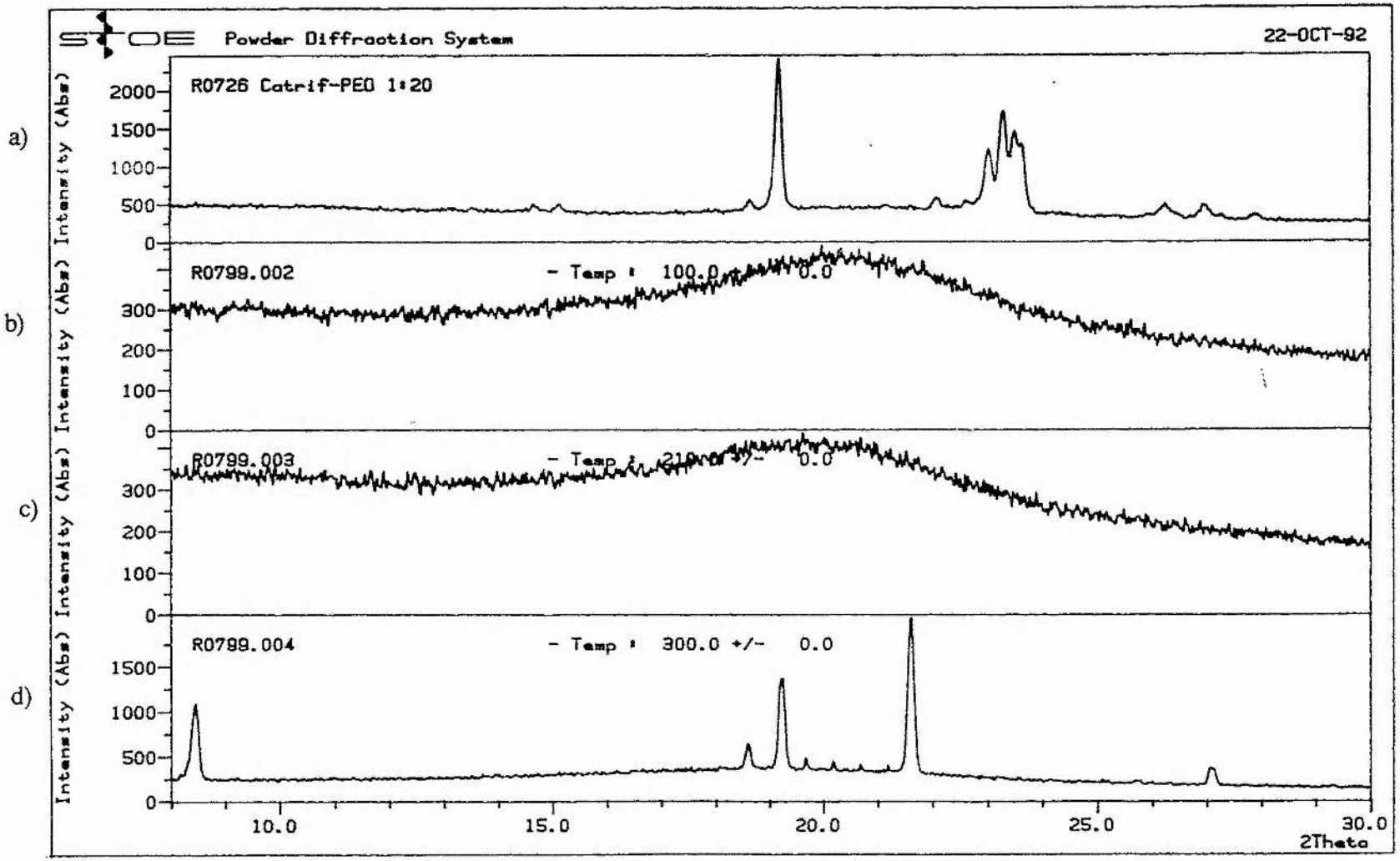

Figure 5-14 X-ray diffraction patterns obtained for $PEO_{20.5}Ca(CF_3SO_3)_2$ at a) room temperature, b) 100°C, c) 210°C and d) 300°C

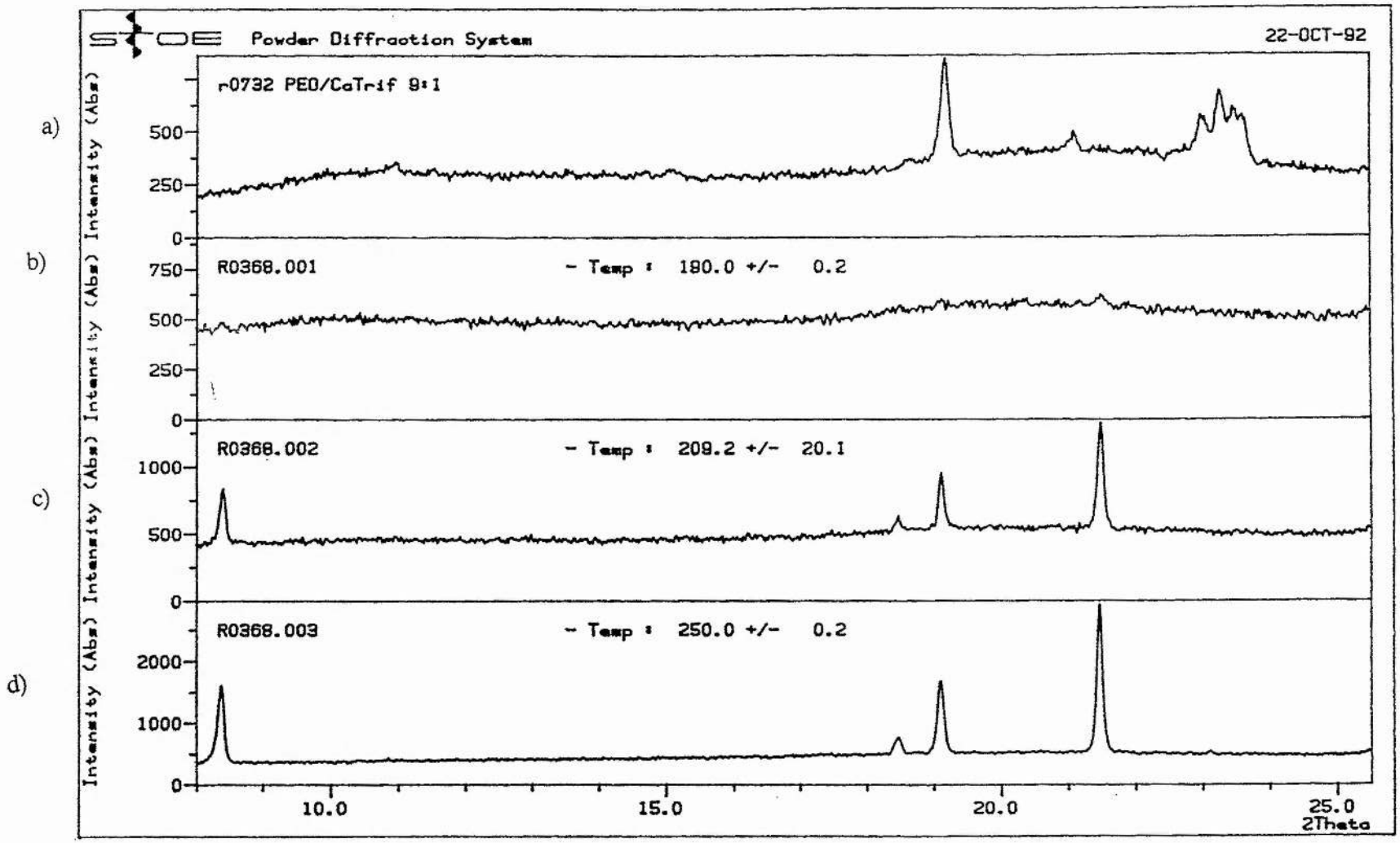

Figure 5-15 X-ray diffraction patterns obtained for $PEO_{9.2}Ca(CF_3SO_3)_2$ at a) room temperature, b) 190°C, c) 209 °C and 250°C

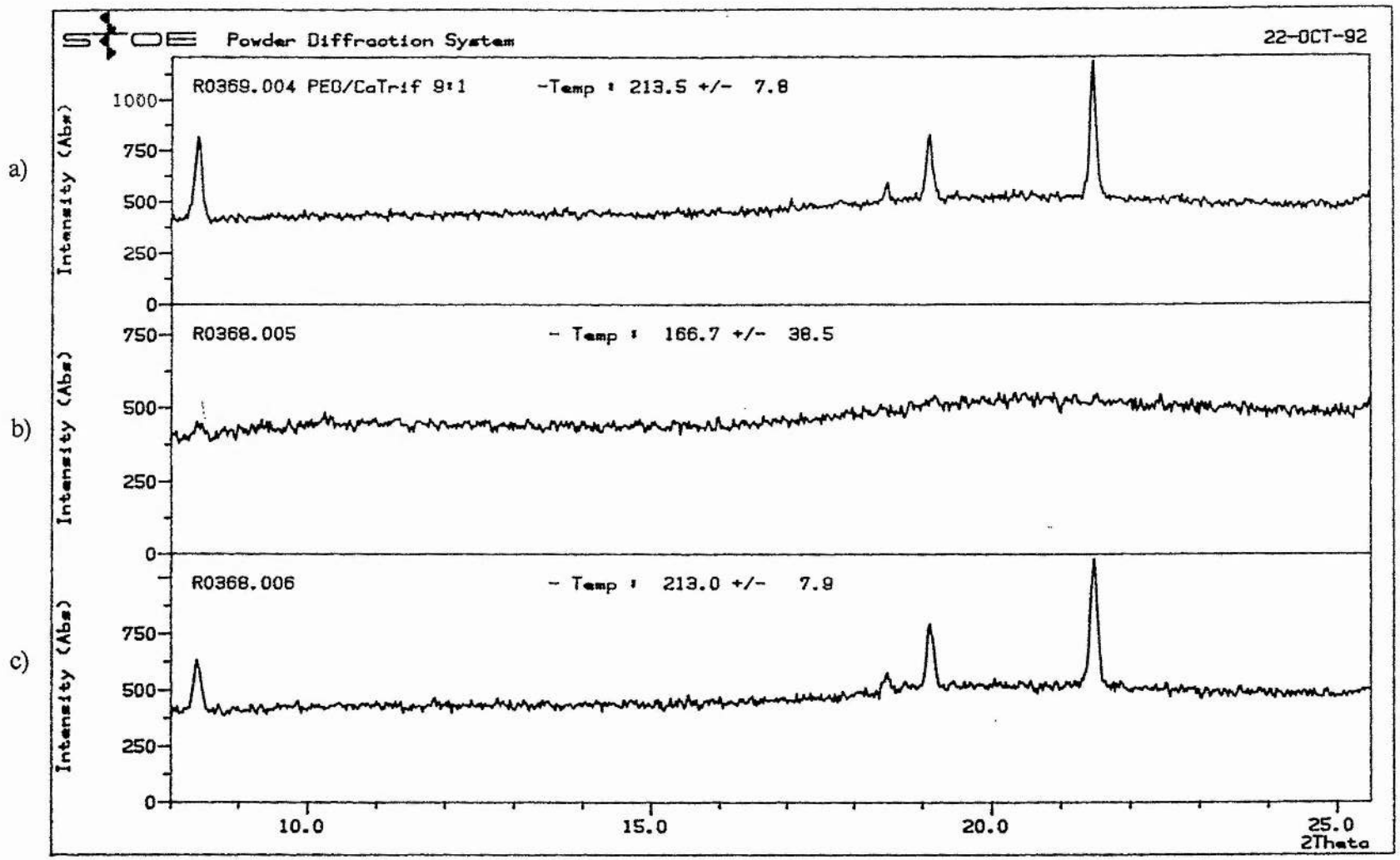

a)

b)

c)

Figure 5-15 (cont.) X-ray diffraction patterns obtained for $PEO_{9.2}Ca(CF_3SO)_3)_2$ at a) 213°C, b) 167°C and c) 213°C

5.2.3 *X-ray diffraction at elevated temperatures*

Powder X-ray diffraction patterns were recorded at temperatures either side of the thermal events indicated by DSC. Figure 5-9 shows some of the patterns obtained for $PEO_8Ca(CF_3SO_3)_2$. At room temperature, the pattern consisted of peaks due to the crystalline complex and PEO. At 100°C, the peaks due to the crystalline PEO had disappeared from the pattern but those due to the complex remained. As the temperature was further increased, the intensity of peaks due to the crystalline complex decreased and the sample became increasingly amorphous. Eventually, at 207°C, peaks due to the pure salt were detected. The intensity of these salt peaks increased with temperature.

Figure 5-10 shows some of the diffraction patterns obtained upon cooling the $PEO_8Ca(CF_3SO_3)_2$ sample. The salt gradually redissolved in the polymer until at 180°C a completely amorphous sample was obtained. The complex took several days to recrystallise completely from the sample. The peaks labelled P1 and P2 on figures 5-1d and 5-9a were ascribed to PEO since they were in the positions corresponding to the most intense PEO peaks (figure 5-2d) and then disappeared from the diffraction pattern upon heating.

The behaviour of the complex, $PEO_6Ca(CF_3SO_3)_2$, was somewhat different upon heating. The patterns obtained are shown in figures 5-11 and 5-12. At room temperature, the pattern consisted of peaks due to the crystalline complex. The pattern showed no significant change upon heating to 100°C due to the absence of uncomplexed PEO in the sample.

With increasing temperature, the peaks due to the complex shifted to slightly lower 2θ values as a result of thermal expansion of the complex and concommitant increase in the d spacings of the lattice. Above 180°C (the onset temperature for peak 2 in the DSC spectrum for $PEO_6Ca(CF_3SO_3)_2$), a peak at $2\theta = 20.8°$ appeared. There was also a change in the relative intensities of the group of peaks in the region $2\theta = 22.3$ -

23.5° on the 180°C diffractogram as compared to the room temperature diffractogram. Above 180°C, the intensity of the peaks due to the pure salt increased and those due to the crystalline complex gradually decreased in intensity. Eventually, at 201°C, the peaks due to the crystalline complex completely disappeared and those of the salt remained. The presence of peaks labelled S1 and S2 on figure 5-1c and 5-11 indicated that for this particular sample, small traces of salt were present. The position of S1 was identical to that of the PEO peak P1 in the 8:1 sample however, the intensity remained unchanged upon heating to 100°C. It was believed that peak S2 was coincident with a small complex peak since a peak in this position was also present in the 8:1 composition.

The behaviour of compositions richer in salt than $PEO_6Ca(CF_3SO_3)_2$ was identical to that for the crystalline complex with the exception that peaks due to the salt were present with significant intensities at all temperatures. This is illustrated for the $PEO_4Ca(CF_3SO_3)_2$ composition in figure 5-13.

For compositions more dilute in salt than $PEO_{9.2}Ca(CF_3SO_3)_2$, patterns were obtained at temperatures between the first and second endotherms that could possibly indicate the occurrence of a completely amorphous sample. At these compositions however, very little if any crystalline complex was detected at room temperature. It was therefore not possible to say with any certainty that the absence of observable complex peaks in the patterns was due to the absence of crystalline complex in the sample. It may simply have been present in insufficient quantities to be detected by the diffractometer. For all compositions, peaks due to the pure salt were obtained at the highest temperatures. This is illustrated for the $PEO_{20.5}Ca(CF_3SO_3)_2$ in figure 5-14.

The reversibility of the salt precipitation process is illustrated in figure 5-15 for a heating-cooling-reheating cycle of $PEO_{9.2}Ca(CF_3SO_3)_2$. This figure also illustrates the increase in salt peak intensity with increasing temperature.

5.2.4 *Conductivity Measurements*

The conductivities of polymer electrolyte films with compositions $PEO_xCa(CF_3SO_3)_2$ (where x = 5.3 6.5, 12.0, 20.5 and 50.4) were determined as a function of temperature, as illustrated in figures 5-16 to 5-21. All conductivities were significantly enhanced compared to the pure polymer. A 'knee' was observed in the Arrhenius plot for compositions where $x \geq 12.0$. This corresponded to the melting of uncomplexed PEO. The conductivity of $PEO_{5.3}Ca(CF_3SO_3)_2$ was only slightly enhanced compared to the pure polymer. The absence of uncomplexed PEO in the sample accounted for the absence of a 'knee' in the conductivity plot.

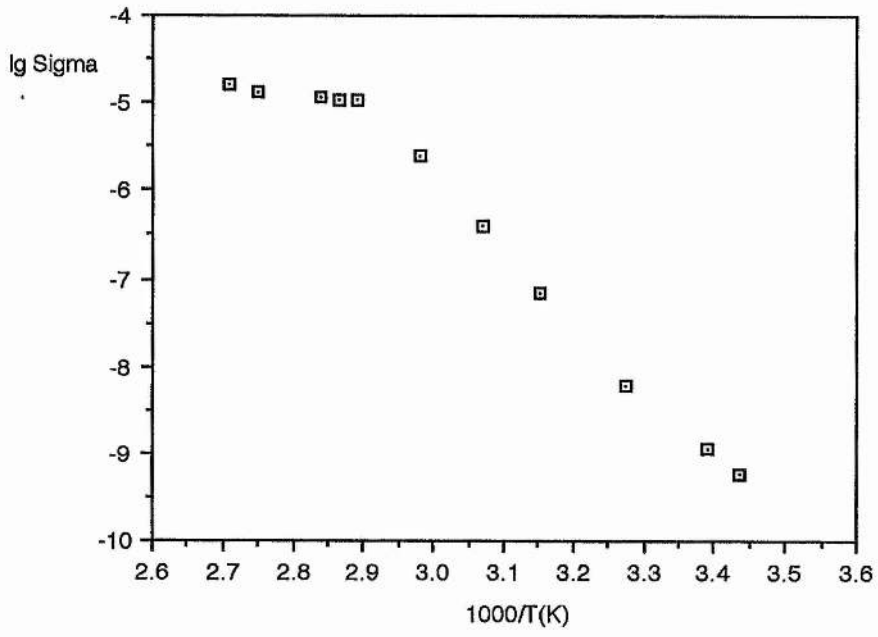

Figure 5-16 Conductivity of $PEO_{50.4}Ca(CF_3SO_3)_2$

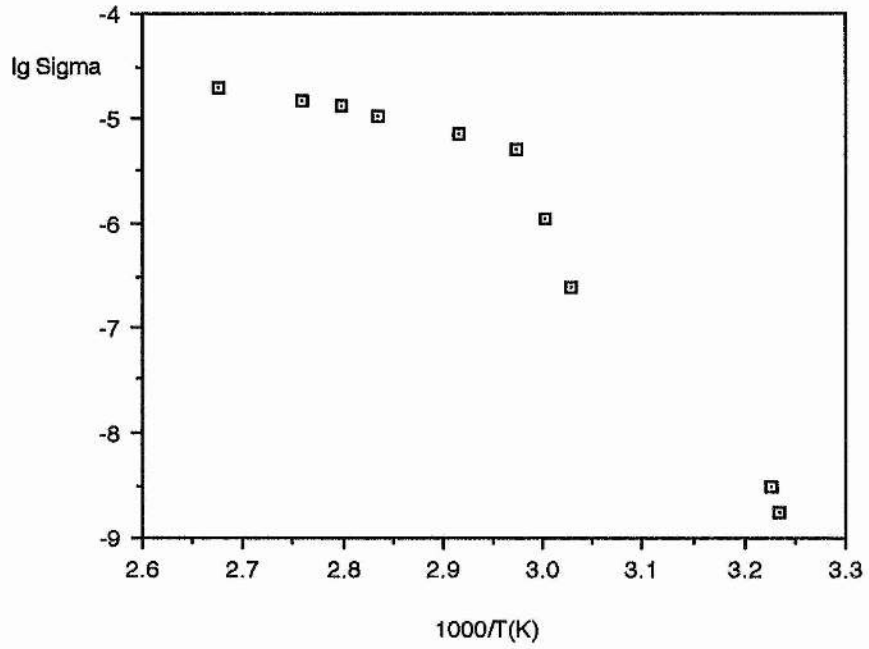

Figure 5-17 Conductivity of $PEO_{20.5}Ca(CF_3SO_3)_2$

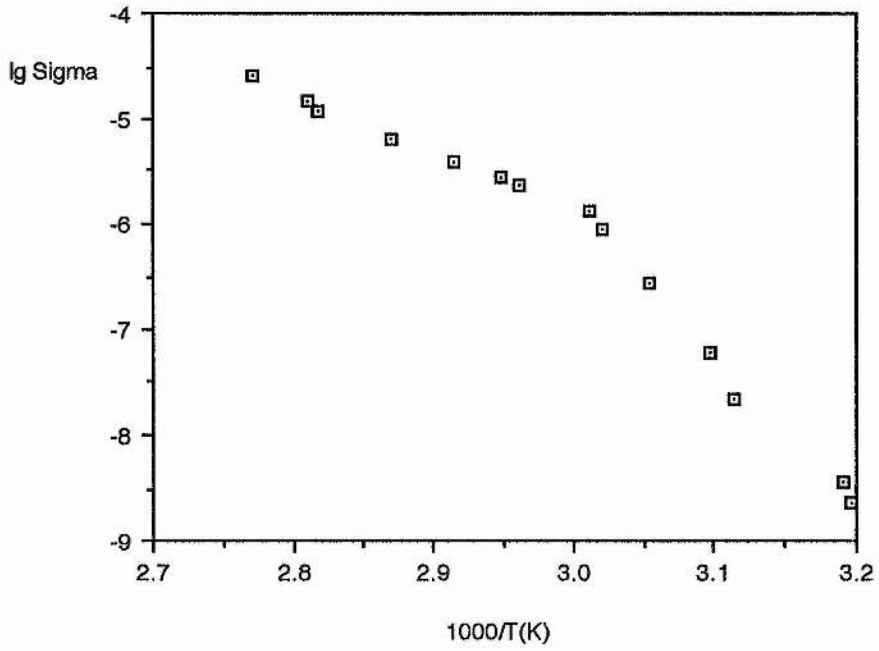

Figure 5-18 Conductivity of $PEO_{12.0}Ca(CF_3SO_3)_2$

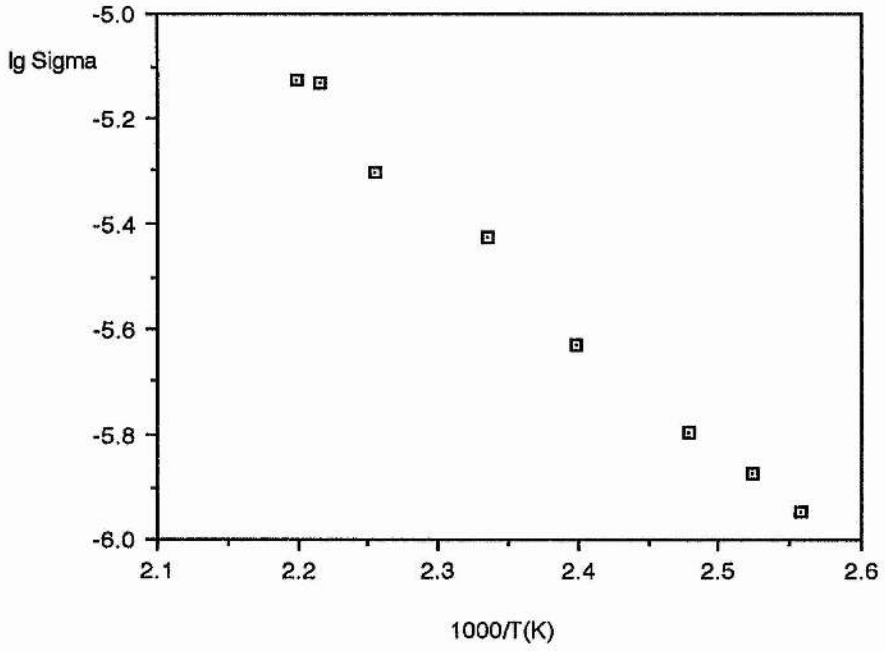

Figure 5-19 Conductivity of $PEO_{6.5}Ca(CF_3SO_3)_2$

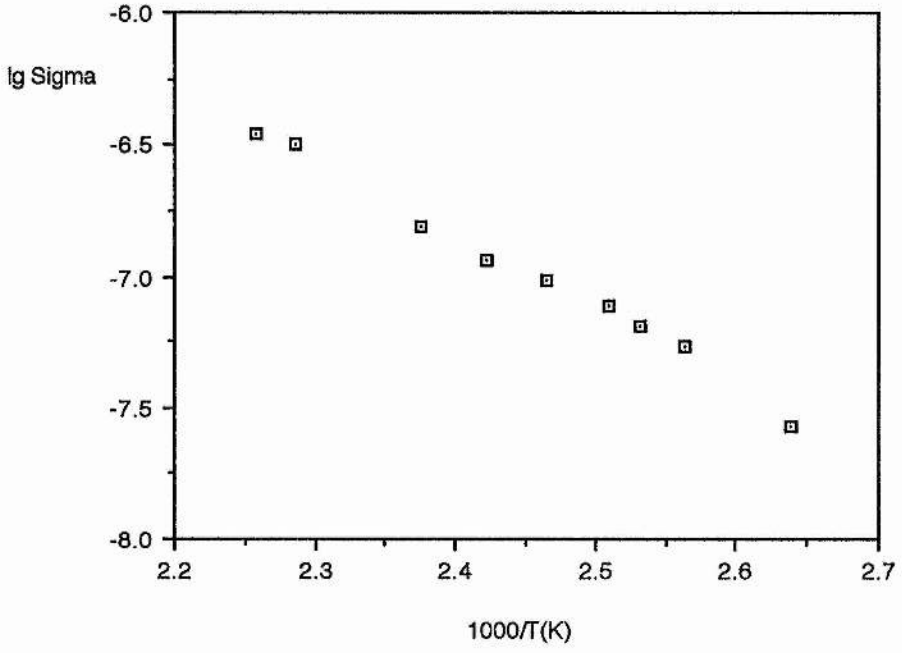

Figure 5-20 Conductivity of $PEO_{5.3}Ca(CF_3SO_3)_2$

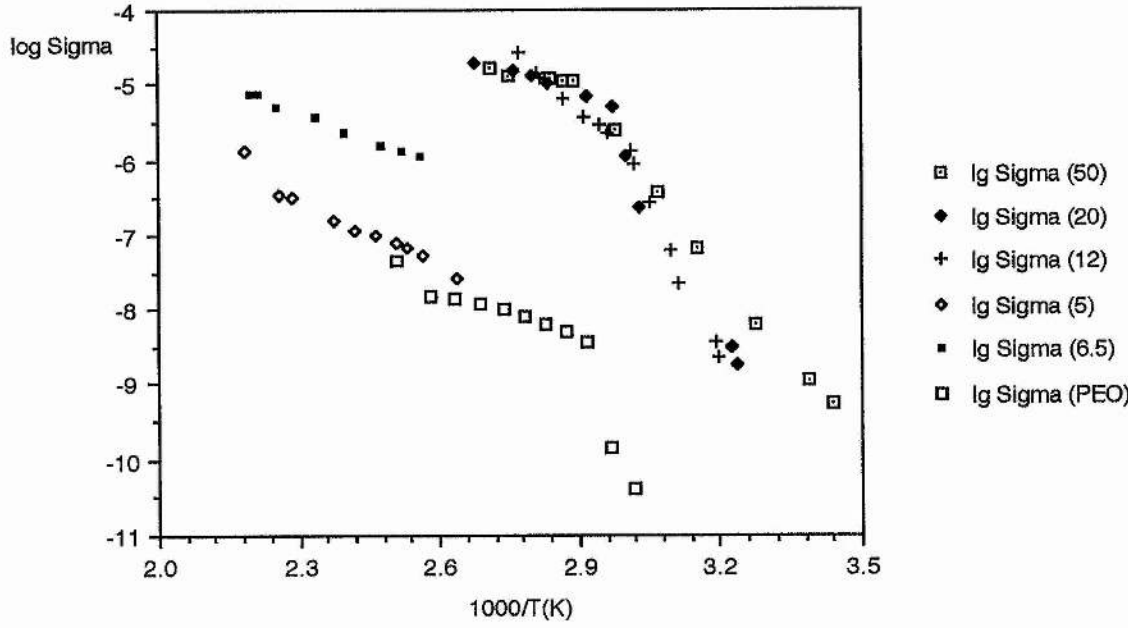

Figure 5-21 A comparison of the conductivities of the polymer electrolyte films $PEO_xCa(CF_3SO_3)_2$

5.3 Determination of the phase diagram for the PEO:$Ca(CF_3SO_3)_2$ system

Due to the complexity of the system, the proposed phase diagram has been presented at this stage in order that the reader can correlate each piece of evidence with the proposed model as it is presented.

5.3.1 *The Proposal*

The proposed phase diagram for the system is illustrated in figure 5-22.

(1) The first DSC endotherm, observed in the region of 60°C for compositions $PEO_xCa(CF_3SO_3)_2$ ($x > 6.5$), corresponds to the melting of uncomplexed PEO.

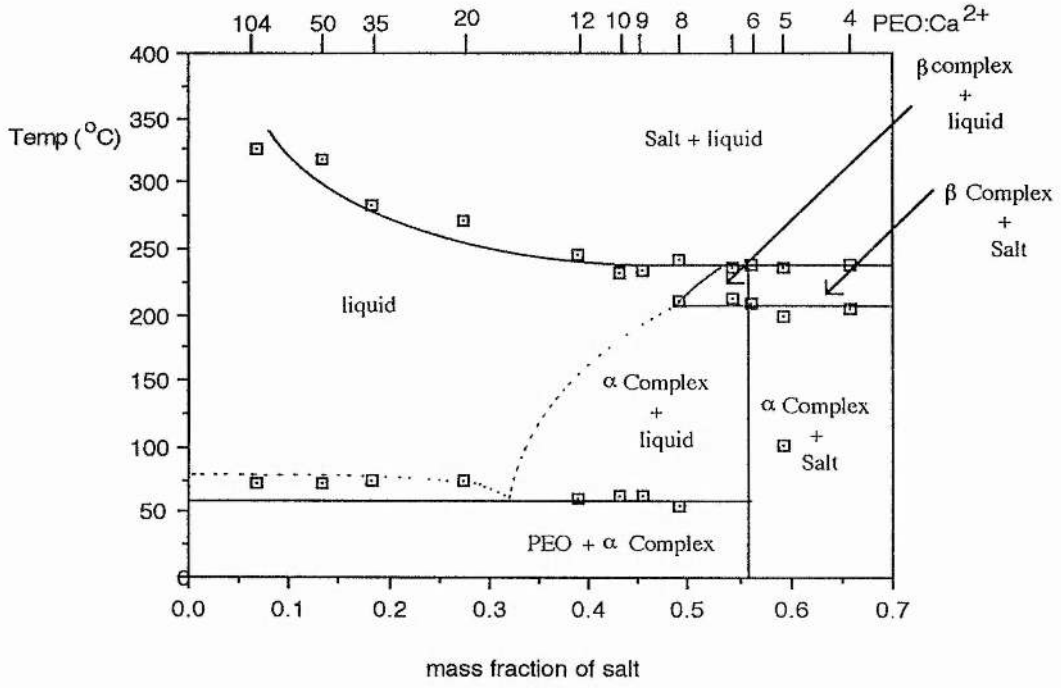

Figure 5-22 The proposed phase diagram for the PEO:$Ca(CF_3SO_3)_2$ system

(2) The second DSC endotherm, observed in the region of 200°C for compositions $x < 8$ corresponds to a phase transition between the two polymorphic forms of $PEO_6Ca(CF_3SO_3)_2$:-

$PEO_6Ca(CF_3SO_3)_{2\ (s)} \rightarrow PEO_6Ca(CF_3SO_3)_{2\ (s)}$

(α modification) (β modification)

(3) The second DSC endotherm observed for compositions $x \geq 8$ corresponds to the salt precipitation process:-

liquid $\rightarrow$ $PEO_{(l)}$ + $Ca(CF_3SO_3)_{2\ (s)}$

(4) The third DSC endotherm, observed in the region of 240°C for compositions $x < 8$, corresponds to the meritectic reaction:-

$PEO_6Ca(CF_3SO_3)_{2\ (s)} \rightarrow Ca(CF_3SO_3)_{2\ (s)}$ + liquid

(β modification)

(5) The reduction in solubility of the salt in PEO with increasing temperature is ascribed to the negative entropy of dissolution of the salt in the polymer.

5.3.2 *The rationale*

Examination of the data obtained by x-ray diffraction enabled the crystalline phases present at each temperature and composition to be determined. This in turn allowed the thermal events observed by DSC to be assigned to processes occurring in the PEO:$Ca(CF_3SO_3)_2$ system.

The data clearly indicated that the first DSC endotherm, observed in the region of 60°C for $PEO_xCa(CF_3SO_3)_2$ (x>6.5) could be assigned to the melting of crystalline PEO:-

$$PEO_{(s)} \longrightarrow PEO_{(l)} \qquad 5\text{-i)}$$

The high temperature endotherm (peak 2) observed for compositions where $x \geq 8$ was clearly the result of a salt precipitation process.

A good correlation was observed between the x-ray diffraction data and the DSC data. At 210°C, the $PEO_{20.5}Ca(CF_3SO_3)_2$ sample was completely amorphous (figure 5-14c), being below the onset temperature for DSC peak 2 (table 5-2a). At a similar temperature, salt was present in the x-ray diffraction pattern for the $PEO_{9.2}Ca(CF_3SO_3)_2$ sample. The onset temperature for DSC peak 2 was 214.8°C for this composition. Although this was slightly higher, it should be remembered that the onset temperature is defined as the intercept of the steepest tangent of the endotherm with the extrapolated baseline. Thus for a broad endotherm, the reaction may have occurred to a slight extent at temperatures just below this value.

The different behaviour of the diffraction patterns of the complex, $PEO_6Ca(CF_3SO_3)_2$ and the appearance of a third endotherm on the DSC spectrum, indicated that the process was more complicated at higher salt concentrations. In an attempt to rationalise the behaviour of the system, different composition regions were considered in turn.

The X-ray diffraction patterns obtained for $PEO_8Ca(CF_3SO_3)_2$, (figure 5-9), indicated that as the temperature was increased, the intensity of the peaks due to the crystalline complex decreased. It was postulated that this was due to the progressive dissolution of the complex in the amorphous region of the polymer. This process was assigned to the second DSC endotherm observed in the region of 200°C. At 204°C, the sample was almost completely amorphous and at temperatures greater than this, the salt started to precipitate from the amorphous sample. It thus appeared that the solubility of the salt decreased with increasing temperature. This was ascribed to a negative entropy of dissolution of the salt in the polymer and is justified as follows:-

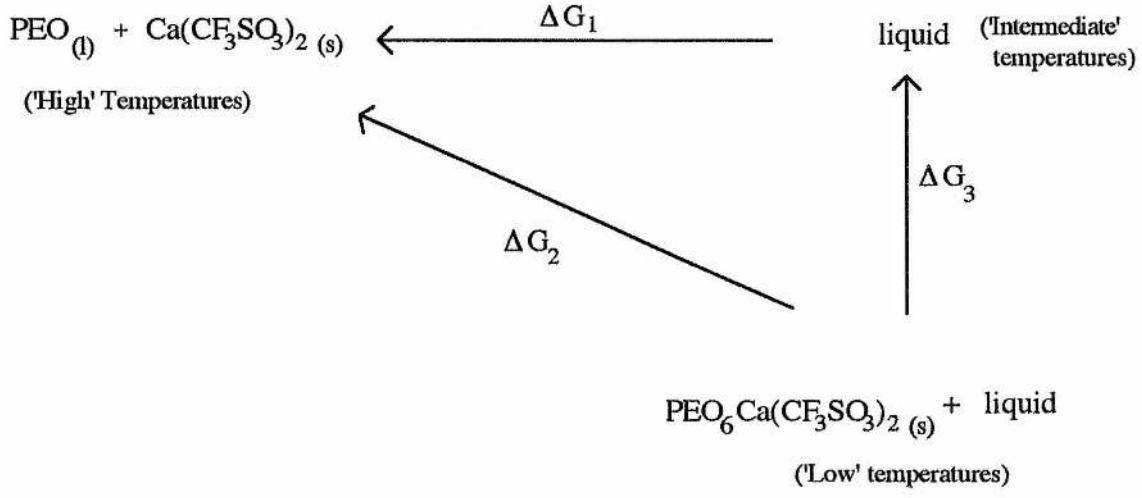

Figure 5-23 Simplified thermodynamic cycle for $PEO_8Ca(CF_3SO_3)_2$

Figure 5-23 shows a simplified thermodynamic cycle for $PEO_8Ca(CF_3SO_3)_2$ at temperatures in excess of the melting point of uncomplexed PEO. For a spontaneous change to occur in the system, the free energy change of the process ,(ΔG), must be negative. Thus :-

$$\Delta G < 0$$

and $$\Delta G = \Delta H - T\Delta S \qquad 5 - ii)$$

where ΔH and ΔS are the enthalpy and entropy changes for the process respectively. Differentiating 5-ii) with respect to temperature gives:-

$$\left(\frac{\partial \Delta G}{\partial T}\right)_P = -\Delta S \qquad 5\text{-iii)}$$

Reference to figure 5-23 indicates that ΔG_1, ΔG_2 and ΔG_3 all become more negative with increasing temperature. Thus,:-

$$\Delta S_1 > 0,\ \Delta S_2 > 0 \text{ and } \Delta S_3 > 0.$$

The enthalpy changes ΔH_3 and ΔH_1 are associated with the thermal events observed at $\approx$ 200°C and 240°C respectively. Both of these thermal events are endotherms and thus:-

$$\Delta H_3 > 0 \text{ and } \Delta H_1 > 0$$

If the approximation that $(\partial \Delta H_1 / \partial T)_p = 0$ is made, then the factor governing the precipitation of the salt from the liquid at high temperatures is the negative entropy of dissolution of the salt in the polymer. This can be rationalised by the fact that both inter- and intra- molecular coordination of the salt would reduce the segmental motion of the polymer. The magnitude of this effect is clearly greater than the loss of entropy of the ions upon formation of the salt lattice.

The implication of this phenomenon is that the solubility of the salt in the polymer decreases with increasing temperature. This would explain the upward trend of the second DSC endotherm with increasing PEO content.

For $PEO_6Ca(CF_3SO_3)_2$,unlike $PEO_8Ca(CF_3SO_3)_2$, the peaks due to the complex coexist with those due to the salt in the region of 180 - 195 °C, i.e. in the region between the two high temperature endotherms. Furthermore, the temperature at which the endotherms occurred appeared to be invariant for compositions $x < 8$. At the highest temperatures, as before, the only crystalline phase present was the pure salt. The upper DSC peak in this composition range (peak 3), could thus be assigned to the incongruent melting of the crystalline complex present.

$$PEO_6Ca(CF_3SO_3)_{2(s)} \rightarrow Ca(CF_3SO_3)_{2(s)} + \text{liquic}$$

(complex) 5 - iv)

Such a process is termed a meritectic reaction (and differs from a peritectic reaction in that it involves the rupture and formation of chemical bonds).

The phase rule[99] states that for a system in thermodynamic equilibrium:-

$$P + F = C + 2 \qquad 5 - v)$$

where P is the number of phases present,

F is the number of degrees of freedom and

C is the number of components in the system.

Since all experiments were carried out at atmospheric pressure and the system consisted of condensed phases only, the 'condensed' phase rule was invoked where

$$P + F = C + 1 \qquad 5\text{-vi)}$$

one degree of freedom having been surrendered.

For a two component system such as the PEO:$Ca(CF_3SO_3)_2$ system under investigation, this reduces to :-

$$P + F = 3 \qquad 5\text{-vii)}$$

The number of degrees of freedom available to the system may be 0, 1, or 2 depending on the number of phases present. The maximum number of degrees of freedom available to the system being two. These are normally assigned to temperature and composition.

It can be seen that for the situation where three phases are in equilibrium, i.e, during the meritectic reaction, the system retains no degrees of freedom. The temperature must therefore remain constant until one phase has been removed from the system. Some other process must also be occurring in the system below this temperature to account for the lower DSC endotherm (peak 2). The contancy of the temperature at which this endotherm occurs would again be explained by a process in which three phases were in equilibrium. The appearance of an additional peak at $2\theta = 20.8^o$ and the change in the relative intensities of the group of peaks in the region $2\theta = 22.3$ to 23.5^o as observed for $PEO_6Ca(CF_3SO_3)_2$ could possibly indicate the presence of another solid phase. The similarity of the pattern to that of the complex, $PEO_6Ca(CF_3SO_3)_2$, would suggest that the structure of this solid phase is only subtly different and has the same lattice parameters but a different space group. The DSC endotherm in the region of 200°C would then be assigned to a phase transition between the two polymorphic forms of $PEO_6Ca(CF_3SO_3)_2$:-

$$PEO_6Ca(CF_3SO_3)_{2\,(s)} \rightarrow PEO_6Ca(CF_3SO_3)_{2\,(s)}$$

(α modification) (β modification) 5 - viii)

where the α-modification is the form of the complex ususally present at room temperature. Reference to the DSC spectrum for $PEO_6Ca(CF_3SO_3)_2$ (figure 5-3a) indicates that the β-modification must melt incongruently since the alternative process:-

$$PEO_6Ca(CF_3SO_3)_{2\,(s)} \rightarrow \text{liquid} \rightarrow Ca(CF_3SO_3)_{2\,(s)} + \text{liquid}$$

(β-modification) 5-ix)

would give rise to three endotherms in the high temperature region of the DSC spectrum. Furthermore, the coexistance of the complex and salt rules out a transformation via an all amorphous phase.

At first sight, the increase in intensity of the salt peaks in the diffraction pattern for $PEO_6Ca(CF_3SO_3)_2$ between 180°C and 195°C might argue against this hypothesis. It is possible that the lower DSC endotherm could be ascribed to an upper limit of stability of $PEO_6Ca(CF_3SO_3)_2$, above which it breaks down into the salt and a crystalline complex of a different composition ($x > 6$). This proposition was ruled out due to the similarity of the diffraction patterns of the 'complex' either side of the thermal event. If a complex of a different composition were produced, a more radically different diffraction pattern would be expected. Furthermore, the variation of d-spacing with temperature exhibited a discontinuity in the region of 150 °C for 80% of the complex peaks studied. A typical example is illustrated in figure 5-24. If the complex remained unchanged, a continuous variation of d-spacing with temperature would be expected.

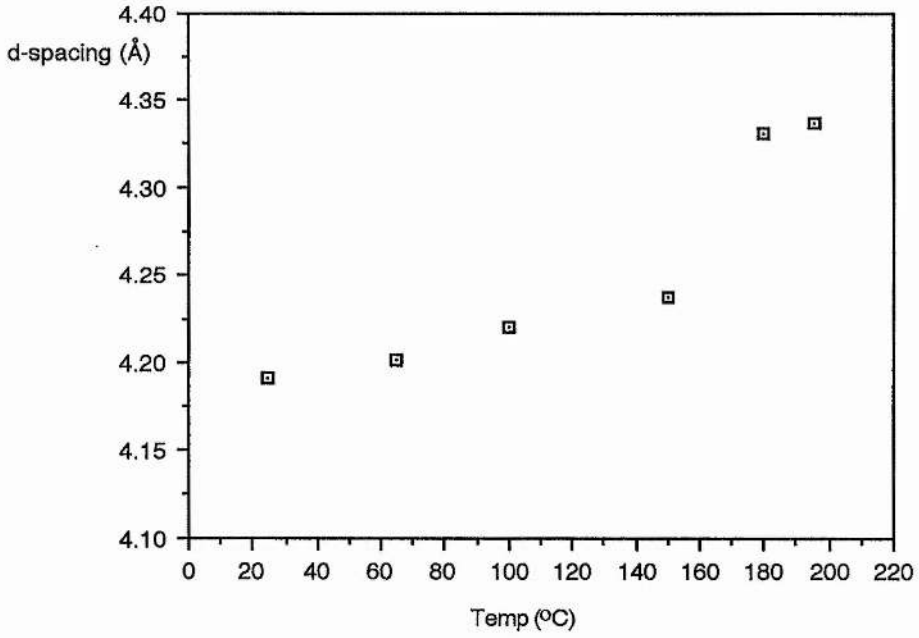

Figure 5-24 Variation of d-spacing with temperature for the complex peak observed at $2\theta = 21.18^{o}$ at 25 °C on the x-ray diffraction pattern for $PEO_6Ca(CF_3SO_3)_2$

The DSC endotherms in this region were fairly broad and it is likely that the onset for the upper endotherm is below 195°C. Thus at 195°C, incongruent melting of the β-modification of the complex may have been initiated. If the kinetics of the process are slow, then the coexistance of salt and complex in this region would be expected. The occurrence of only a single endotherm on the 2nd and subsequent heating cycles for compositions $x \leq 8$ is probably an indication that the system had been quenched upon cooling at this scan rate. The single endotherm observed was thus ascribed to the salt precipitation process.

The nature of the equilibrium between the α modification of the complex and the liquid phase for compositions $x > 8.0$ is difficult to ascertain. If the DSC assignments were made correctly for $PEO_8Ca(CF_3SO_3)_2$, then this indicates that for the process :-

$$PEO_6Ca(CF_3SO_3)_{2\,(s)} + \text{liquid} \xrightarrow{\Delta G_3} \text{liquid} \qquad 5 - x)$$

$\Delta H_3 > 0$ and $\Delta S_3 > 0$. Thus for the x = 8 composition at least, the solubility of the complex in the polymer increases with increasing temperature. It might be expected therefore that a simple eutectic sub-system would form for compositions where x > 8 consisting of the components PEO and $PEO_6Ca(CF_3SO_3)_2$. The absence of thermal events on the DSC spectra corresponding to the liquidus lines in this composition range would appear to argue against this proposition. The observation would however be explained if the complex in this region were amorphous, if there were slow dissolution kinetics or if it was present in insufficient quantities to be detected by DSC. For the latter case, a gradual reduction in the magnitude of the second endotherm would be expected upon proceeding to lower salt compositions. This was indeed observed between the x=6.5 and x =8 compositions. The presence of a eutectic in the region x > 8 is thus tenuously postulated.

5-4 Discussion of the conductivity results

The conductivities of the electrolytes $PEO_xCa(CF_3SO_3)_2$ (x = 50.4, 20.5 and 12.0) exhibited Arrhenius behaviour in all regions of the conductivity plots. The slope of the plots gave an indication of the activation energies for ionic conduction in these electrolytes. A change in the activation energy was observed in the region of 60°C corresponding to the melting of uncomplexed PEO and concommitant increase in the amorphous region of the polymer. Above 60°C, the segmental motion of the polymer increases dramatically. In terms of dynamic bond percolation theory, the complexion of open and closed bonds changes rapidly and the motion of ions is not limited by their renewal rate. In terms of free volume theory, there is an increase in the probability of voids greater than the critical volume becoming available to the ions. In short, above the melting point of uncomplexed PEO, motion of ions through the system becomes more facile.

The activation energies for conduction in this region increase upon going to more concentrated compositions. This is a reflection of the increased concentration of coordinated binding sites on the polymer, which in turn restricts the segmental motion of the polymer chains.

In light of the phase diagram illustrated in figure 5-22, it is clear that most of the polymer in the $PEO_{6.5}Ca(CF_3SO_3)_2$ sample was in the form of a crystalline complex up to $\simeq$240°C. It was only possible to obtain measurable conductivities for this sample in the temperature range 110 to 180°C under which conditions, the bulk of the electrolyte would have been crystalline. The motion of polymer chains in the (small) amorphous region of the electrolyte would be severely restricted, many polymer chains being 'anchored' to the crystalline regions. A single polymer chain may pass through more than one spherulite and/or the amorphous region of the electrolyte. This accounts for the reduced conductivity of the sample compared to the more dilute compositions.

The conductivity of the 5:1 composition was only slightly enhanced compared to the pure hot pressed polymer. Reference to the phase diagram indicates that the sample was almost completely crystalline throughout the temperature range of the conductivity exeperiment. The ionic conductivity of the sample was thus likely to result from the simple percolation of ions through the rigid lattice.

It would have been of interest to see how the conductivity of the $PEO_xCa(CF_3SO_3)_2$ electrolytes varied upon heating above the temperatures at which the phase changes occurred within the system. Unfortunately, this was outwith the range of the instrumentation.

CHAPTER 6

THE PEO:NICKEL IODIDE SYSTEM

The aim of the investigation was to characterise the properties of the polymer electrolyte system PEO_xNiI_2 as a function of composition and temperature. The composition and nature of the phases in the system were probed by DSC and X-ray diffraction techniques. Cyclic voltammetry, potential step and ac impedance techniques were used to probe the redox behaviour of the system. Due to the wide variety of procedures used, the experimental procedure, results and discussion of each technique is considered in turn.

6.1 Sample preparation

Cryoground mixtures of PEO and nickel iodide were prepared for a range of compositions PEO_xNiI_2 (x = 4.9, 8.0, 12.0, 20.2 and 50.6). Hot pressed discs were prepared for each composition according to the method described in section 4.1.2. For cyclic voltammetry, it was necessary to prepare polymer electrolyte films containing a supporting electrolyte as well as nickel iodide. Thus, discs of $PEO^{10\ LiClO_4}_{48.5\ NiI_2}$ were prepared. Hot pressed discs of $PEO_{9.9}LiClO_4$ were prepared for use with the lithium reference electrode in the cyclic voltammetry cell.

6.2 Differential scanning calorimetry

6.2.1 *Experimental*

DSC analysis was used to examine the thermal characteristics of the hot pressed films. Samples, sealed into DSC pans in an argon filled dry-box, were subjected to 0 to 300 °C heating cycles at a rate of 20 °C per minute.

6.2.2 *Results and discussion*

Two peaks were observed in the DSC spectra shown in figures 6-1 to 6-5. The first, a fairly sharp peak, was observed in the region of 65°C and was ascribed to the melting of uncomplexed PEO. The second peak observed in the region of 139.5 °C for $PEO_{4.9}NiI_2$, gradually shifted to higher temperatures with decreasing salt concentration. The results of the DSC peak area analyses are shown in table 6-1.

x	mass fraction of salt	Peak 1 position (°C)	Peak 1 onset (°C)	Peak 1 area Q1 (Jg^{-1})	Peak 2 position (°C)	Peak 2 onset (°C)	Peak 2 area Q2 (Jg^{-1})
4.9	0.592	60.9	54.2	8.7	139.5	125.6	11.8
8.0	0.470	63.7	55.1	28.9	148.3	136.6	13.1
12.0	0.572	70.5	55.4	80.4	152.1	141.1	18.1
20.2	0.260	69.1	56.9	85.4	166.9	161.2	15.8
50.6	0.123	60.9	60.9	-	184.1	177.9	-
∞	0.000	80.5	62.4	146.1	-	-	-
∞	0.000	77.2	68.9	114.8	-	-	-

Table 6-1 DSC data for PEO_xNiI_2

The DSC peak positions, recorded as a function of composition are shown in figure 6-7. Extrapolation of the latent heat of fusion of the uncomplexed PEO (Q1) to the composition axis (figure 6-8) suggests that this is absent from the system for compositions richer in salt than $PEO_{3.6}NiI_2$ .This would suggest that if a specific PEO:NiI_2 complex or solvate forms in the system, it has a composition in the region of $PEO_{3.6}NiI_2$. Furthermore, if the Ni^{2+} ion is situated inside the polymer helix, this is the composition expected for the case where there are two metal ions for every seven EO repeat units. It is clear however, that further data would need to be obtained to confirm this conclusion. In view of the x-ray diffraction data subsequently obtained, conclusions drawn from the DSC data were treated with caution.

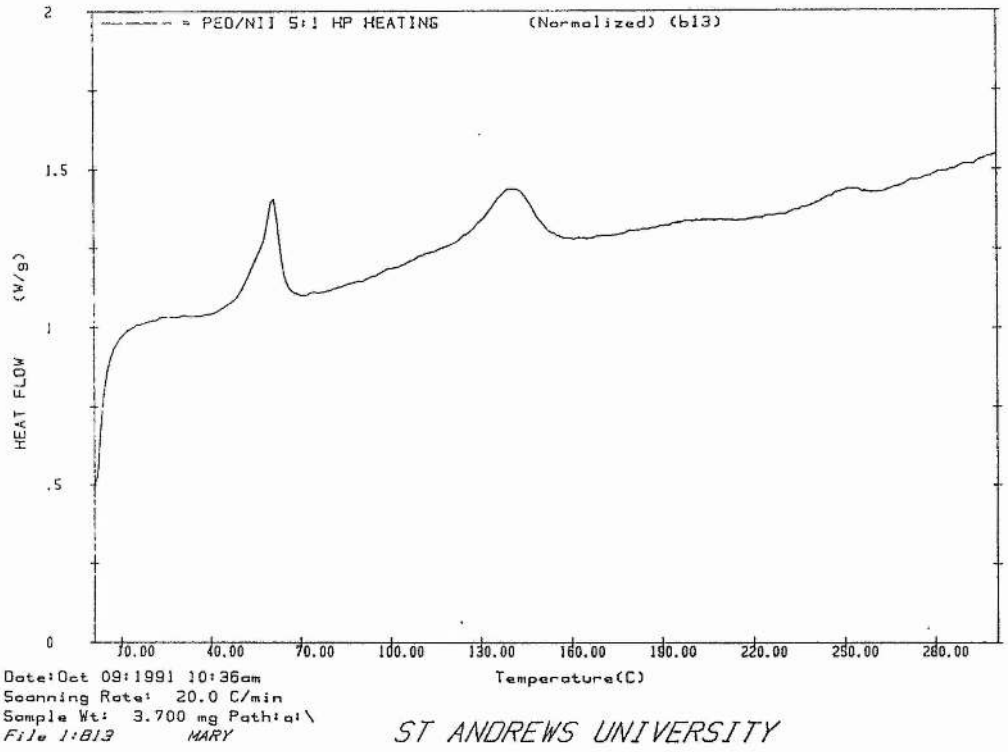

Figure 6-1 DSC spectrum for $PEO_{4.9}NiI_2$

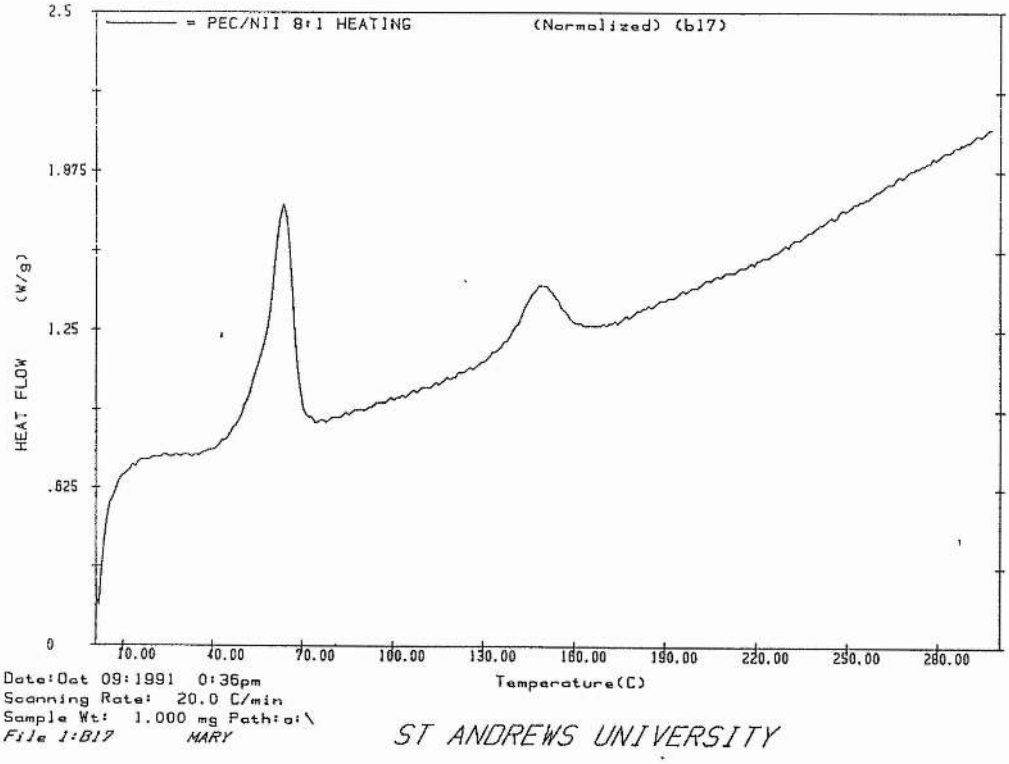

Figure 6-2 DSC spectrum for $PEO_{8.0}NiI_2$

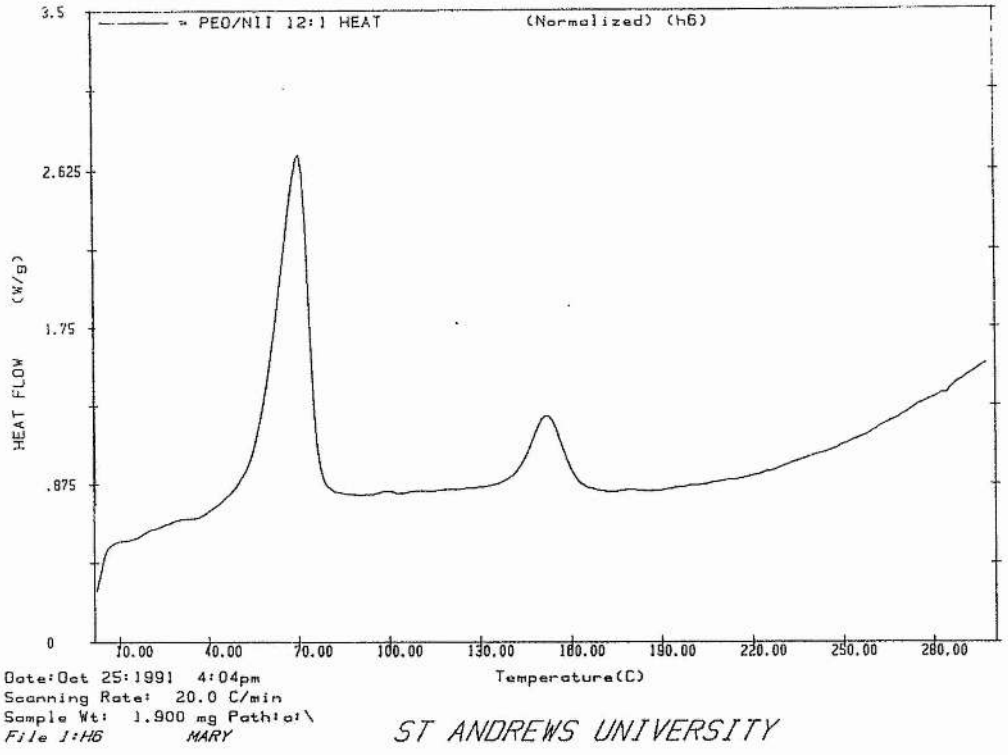

Figure 6-3 DSC spectrum for $PEO_{12.0}NiI_2$

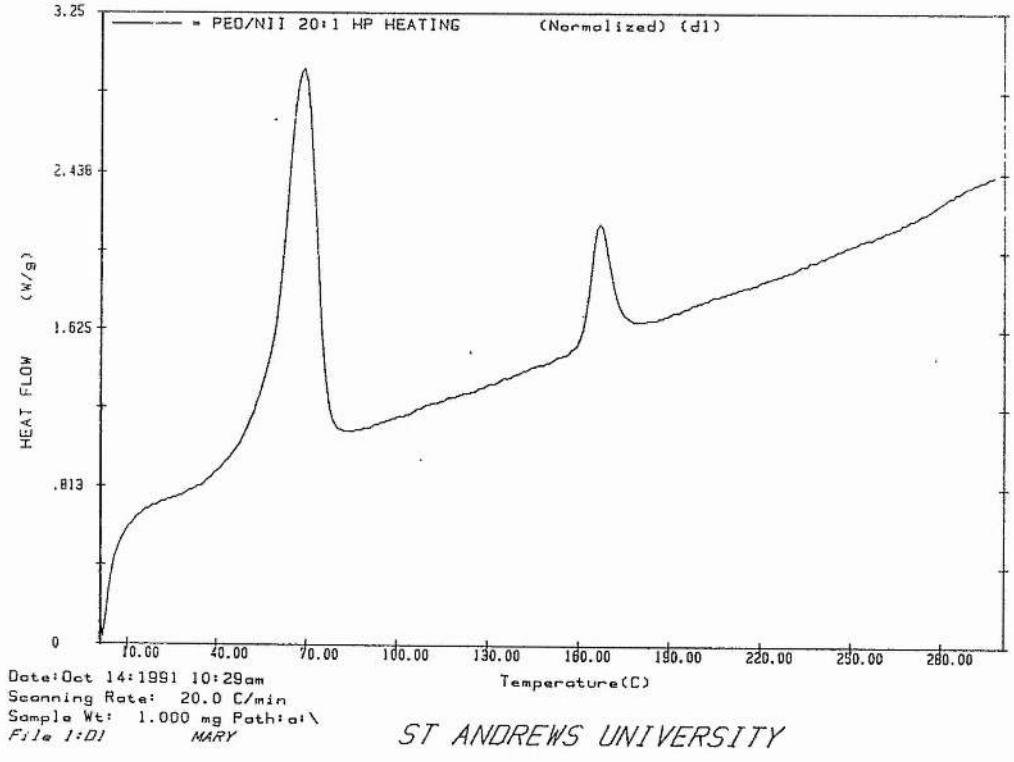

Figure 6-4 DSC spectrum for $PEO_{20.2}NiI_2$

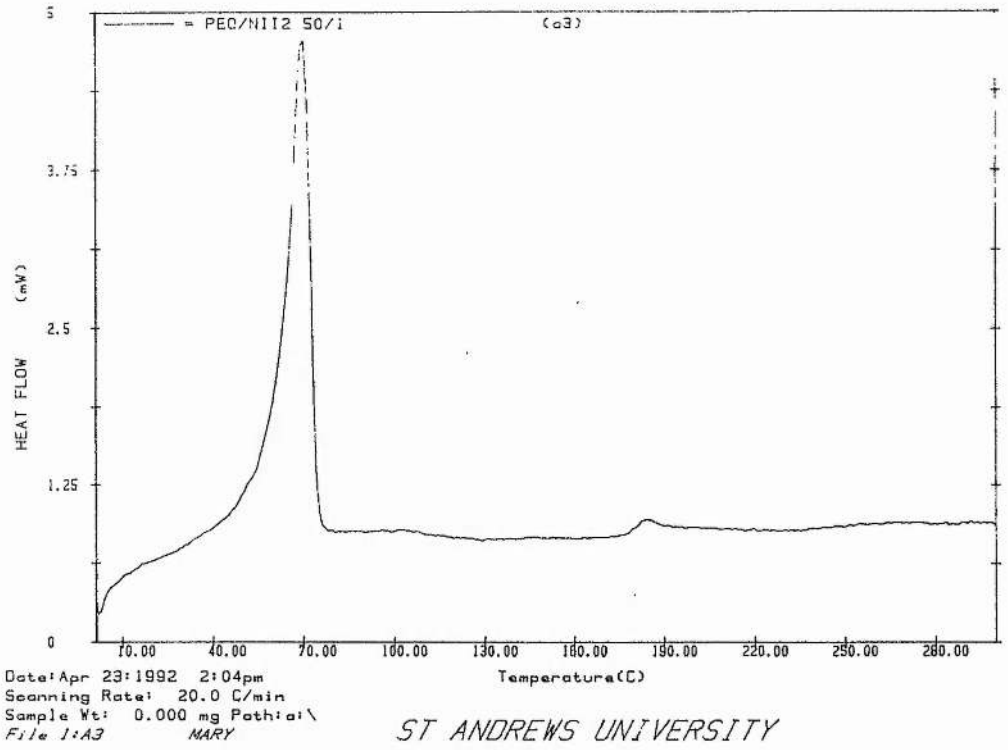

Figure 6-5 DSC spectrum for $PEO_{50.6}NiI_2$

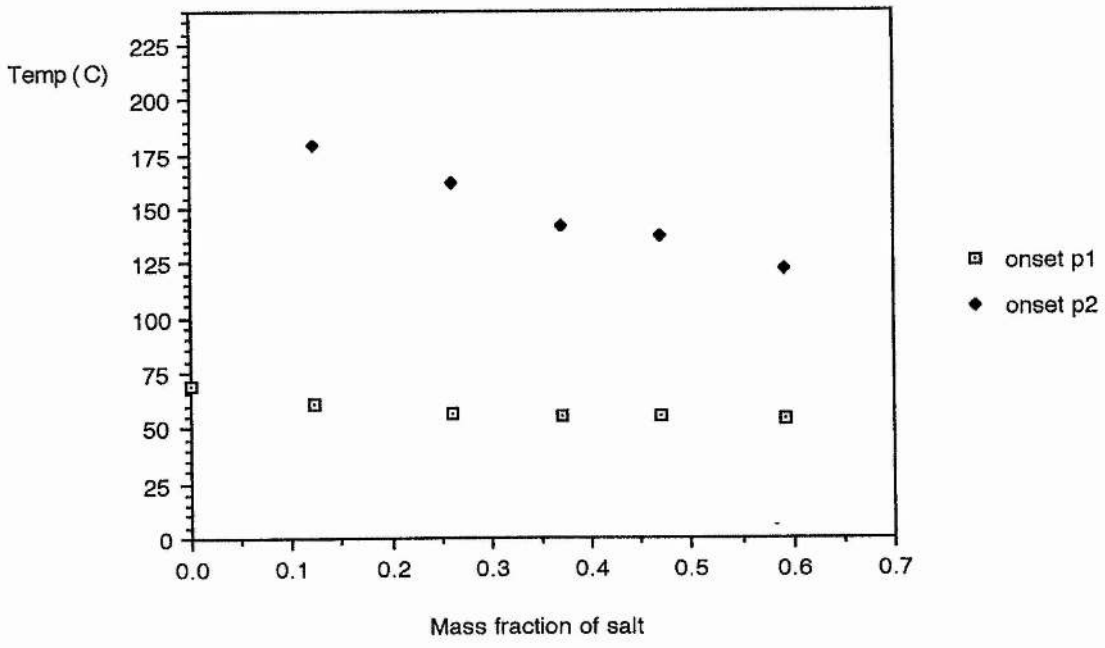

Figure 6-6 DSC peak onsets for PEO_xNiI_2

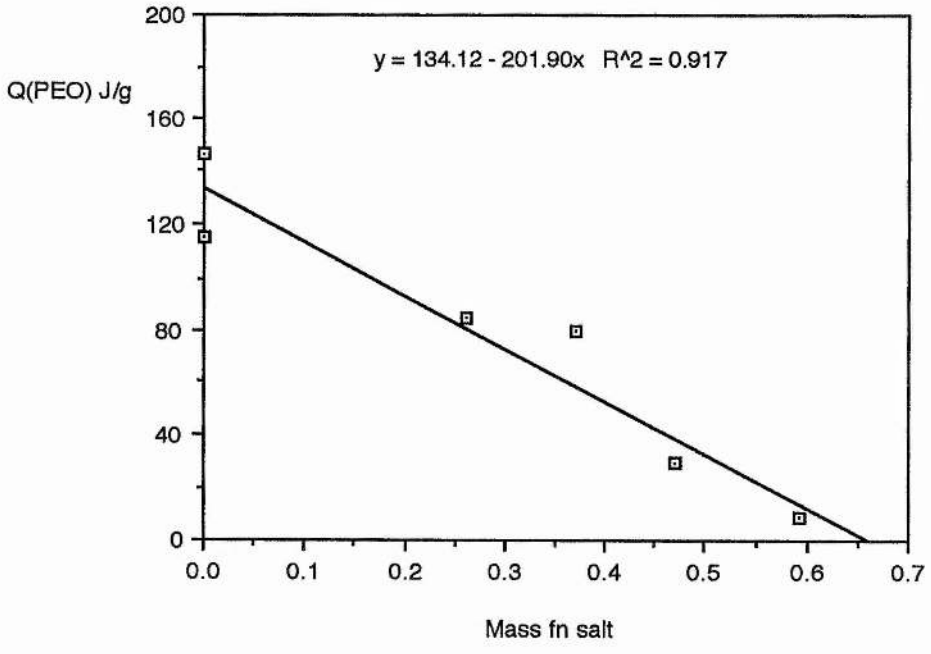

Figure 6-7 DSC peak 1 area (Q1) as a function of composition

6.3 X-ray diffraction

6.3.1 *Experimental*

Samples of the cryoground mixtures were sealed into 0.5mm Lindemann tubes in an argon filled drybox and were heated to ≈ 130°C fo 4 days. The samples were cooled slowly and allowed to stand for at least a week at room temperature before being run on the Stoe powder x-ray diffractometer.

6.3.2 *Results and discussion*

Some of the x-ray diffraction patterns obtained for the system are illustrated in figure 6-8. It was observed that even for the $PEO_{50.6}NiI_2$ sample, small peaks due to NiI_2 were observed suggesting that there had been incomplete dissolution of salt in the PEO. For compositions richer in salt than $PEO_{50.6}NiI_2$, peaks were observed that did

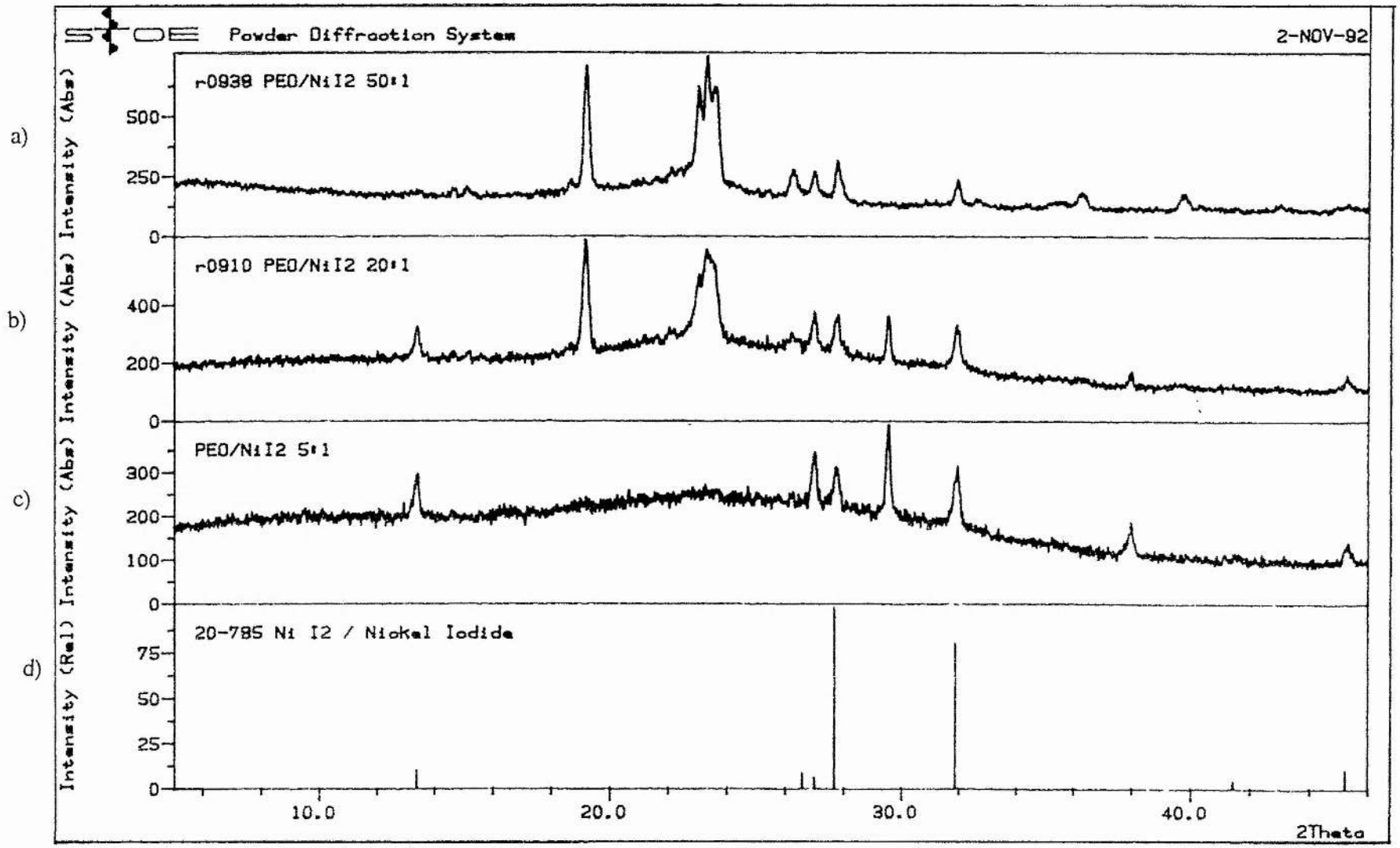

Figure 6-8 Powder x-ray diffraction patterns for the PEO_xNiI_2 system a) $PEO_{50.6}NiI_2$, b) $PEO_{20.2}NiI_2$, c) $PEO_{4.9}NiI_2$ and d) NiI_2

not correspond to either PEO or NiI_2. These were ascribed to the presence of a crystalline PEO:NiI_2 complex. Peaks due to PEO were absent from the $PEO_{4.9}NiI_2$ sample. The coexistance of NiI_2, complex and PEO in the 20:1 composition suggested that the components of the system had not reacted completely.

6.4 Conductivity measurements

6.4.1 *Experimental*

The conductivities of polymer electrolyte films sandwiched between stainless steel electrodes were determined by ac impedance techniques in the temperature range 40°C to 120 °C.

6.4.2 *Results and discussion*

The conductivities of films containing nickel iodide are shown in figures 6-9 to 6-14. They were observed to be significantly enhanced compared to the pure hot pressed polymer. For all compositions except $PEO_{4.9}NiI_2$, a 'knee' was observed in the region of 65°C corresponding to the melting of uncomplexed PEO and the subsequent increase in the amorphous component of the polymer responsible for ionic conduction. The Arrhenius plots above 65°C appeared to be virtually linear. Usually, amorphous polymer electrolytes exhibit curved Arrhenius plots where the system follows VTF behaviour [$\sigma = A \exp(-B/T-T_o)$, section 1.5.1]. The observed linearity for the PEO_xNiI_2 system may have been due to the restricted temperature range over which the data could be collected. Alternatively, it may have been a result of the presence of crystalline phases in the system. The reduction of segmental motion of the polymer chains may have served to reduce the ionic conductivity compared to an all amorphous system. Whatever the explanation however, similar behaviour has been observed for a variety of other systems as illustrated by the work of Yang et al[74]. The activation energies extracted for each composition in this temperature range were observed to be similar and are illustrated in table 6-2.

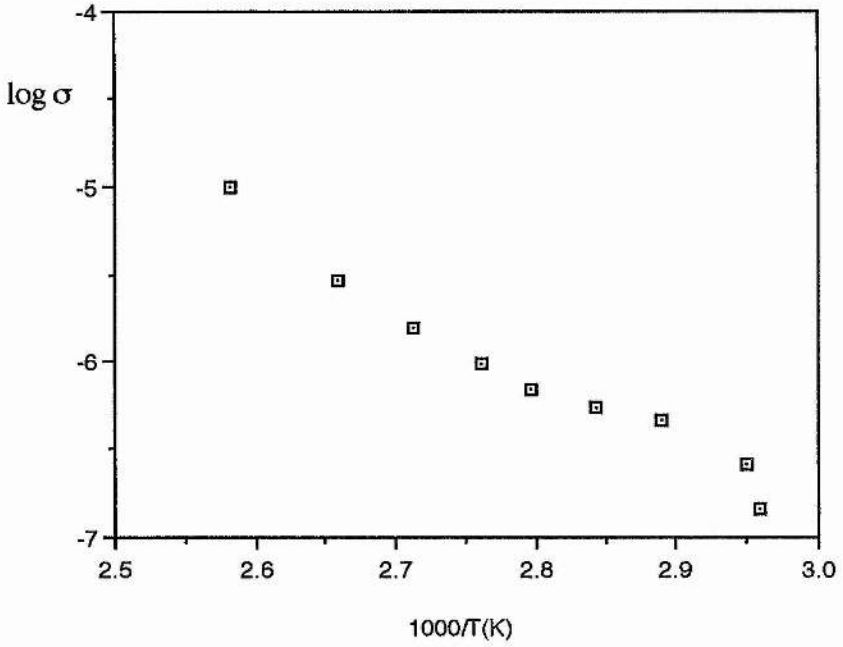

Figure 6-9 Conductivity of $PEO_{4.9}NiI_2$

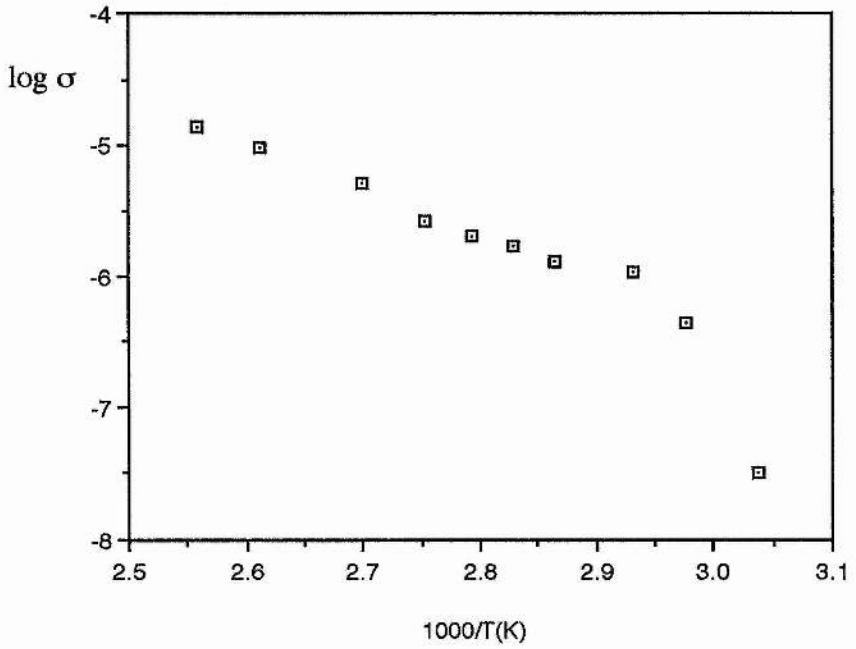

Figure 6-10 Conductivity of PEO_8NiI_2

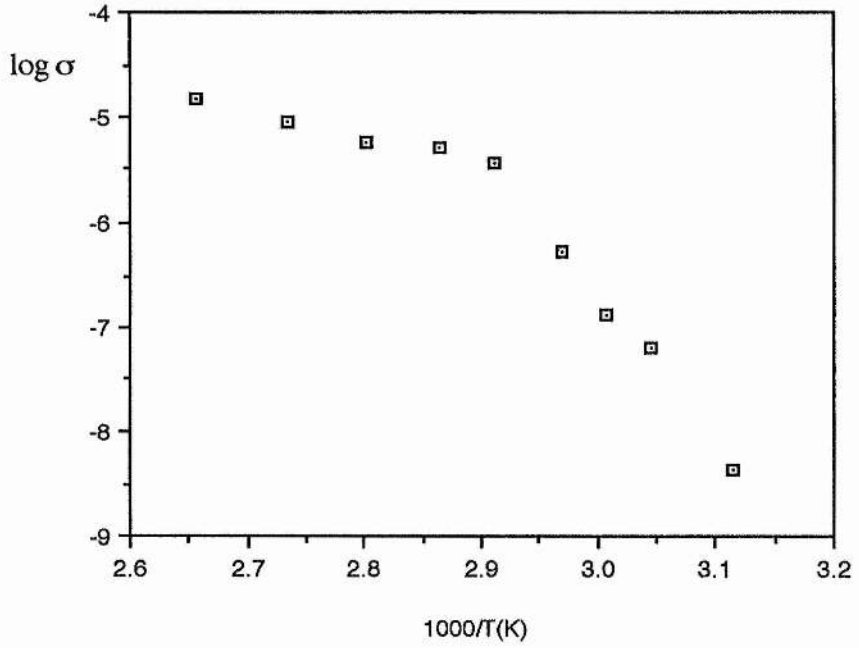

Figure 6-11 Conductivity of $PEO_{12}NiI_2$

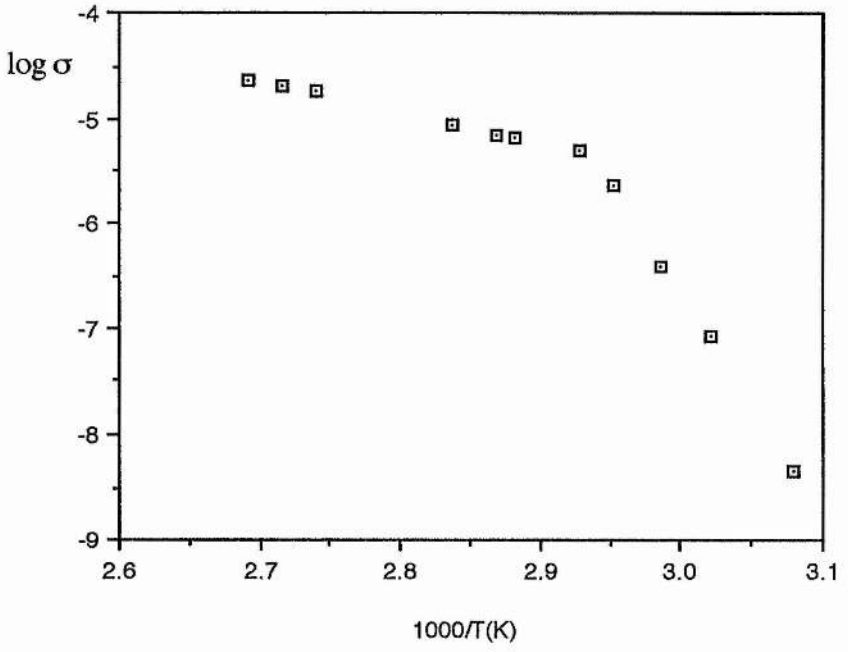

figur 6-12 Conductivity of $PEO_{20.2}NiI_2$

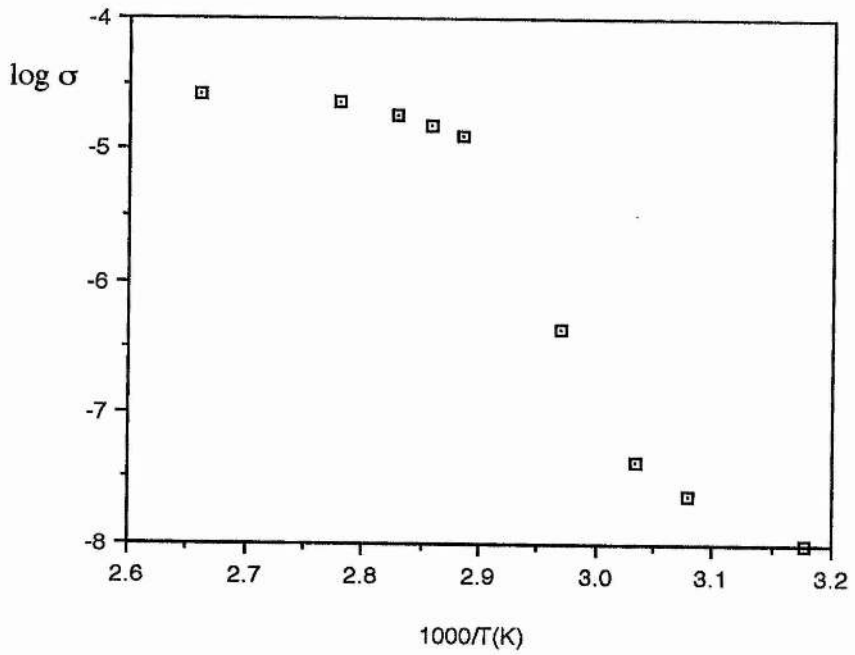

Figure 6-13 Conductivity of $PEO_{50.6}NiI_2$

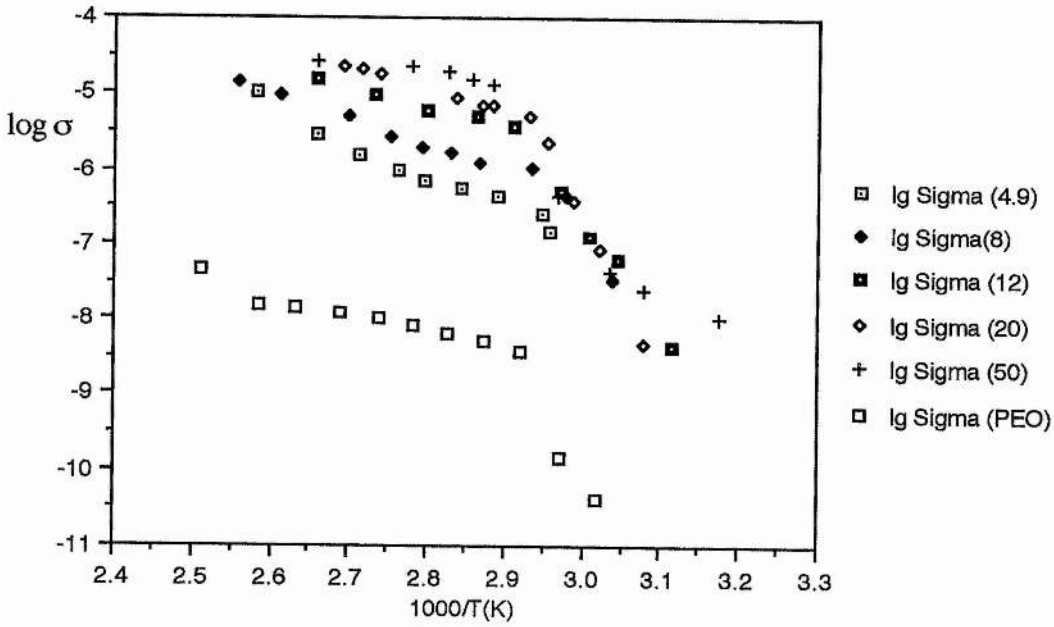

Figure 6-14 Comparison of the conductivitites of the PEO_xNiI_2 system

x	Activation energy (J mol^{-1})
4.9	3.52×10^4
8.0	2.67×10^4
12.0	1.94×10^4
20.2	2.30×10^4
50.6	2.08×10^4

Table 6-2 Activation energies for conduction of PEO_xNiI_2 above 65 °C

6.5 Cyclic voltammetry

6.5.1 *Experimental*

A three electrode cell of the form:-

$$Ni \,/\, PEO^{10\ LiClO_4}_{48.5\ NiI_2} \,/\, PEO_{9.9}LiClO_4 \,/\, Li \,/\, PEO_{9.9}LiClO_4 \,/\, Li$$

was prepared as illustrated in figure 6-15 and was heated to 86.0 °C under dynamic vacuum. A cyclic voltammogram was recorded at 50 mVs^{-1} in the 2.5V to 4.3V range measured with respect to the Li^+ / Li reference electrode. A 'blank' cell of the form:-

$$Ni \,/\, PEO_{9.9}LiClO_4 \,/\, PEO_{9.9}LiClO_4 \,/\, Li \,/\, PEO_{9.9}LiClO_4 \,/\, Li$$

was also prepared. The redox behaviour of this cell was probed under identical conditions in the region of 1.7V to 4.6V.

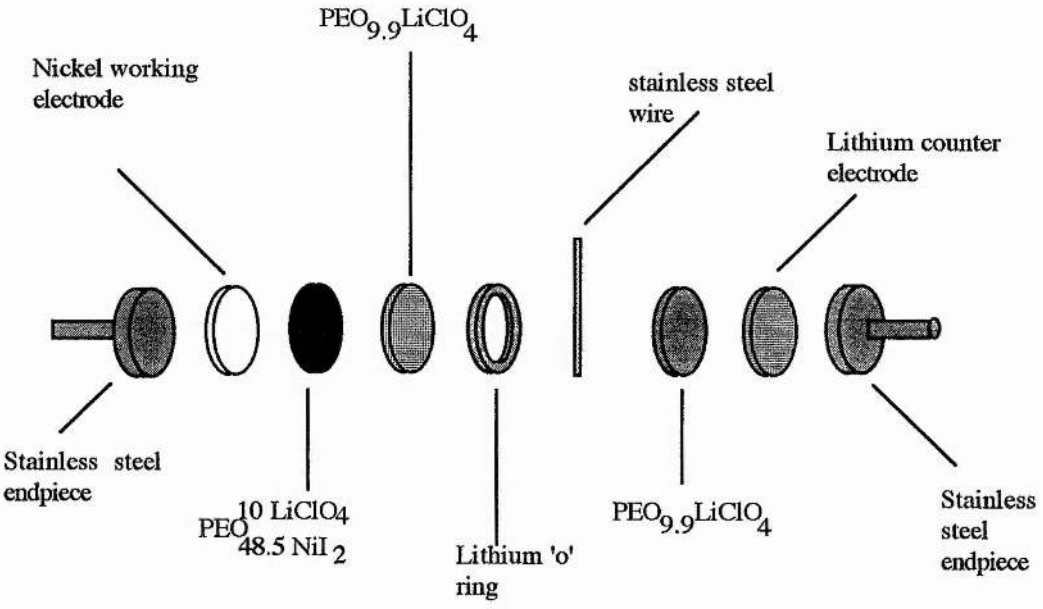

Figure 6-15 Cell construction for cyclic voltammetry

6.5.2 *Results and discussion*

The cyclic voltammograms obtained are shown in figures 6-16 and 6-17. No significant redox behaviour was observed in the blank system between 1.70V and 4.60V. Upon scanning cathodically in figure 6-17, nickel deposition occurred below ~ 2.8V. Stripping of nickel occurred on the anodic scan positive of 2.85V. The absence of a nucleation loop suggested that the overpotential for growth was approximately equal to the overpotential for nucleation. The data obtained from figure 6-17 was used to construct the Tafel plot of figure 6-18 in which lnI was plotted against the overpotential, η, (where $\eta = E - 2.840V$, E was the applied potential and 2.840V was the equilibrium potential measured with respect to the lithium reference electrode).

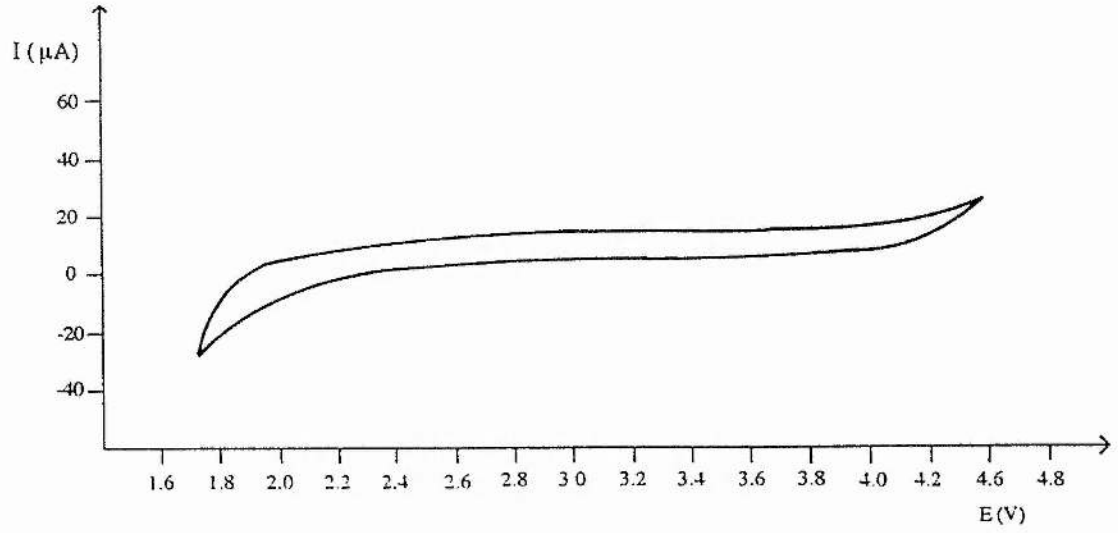

Figure 6-16 The cyclic voltammogram for the 'blank' system
Ni / $PEO_{9.9}LiClO_4$ / $PEO_{9.9}LiClO_4$ / Li / $PEO_{9.9}LiClO_4$ / Li (multicycled at 86.0 °C)

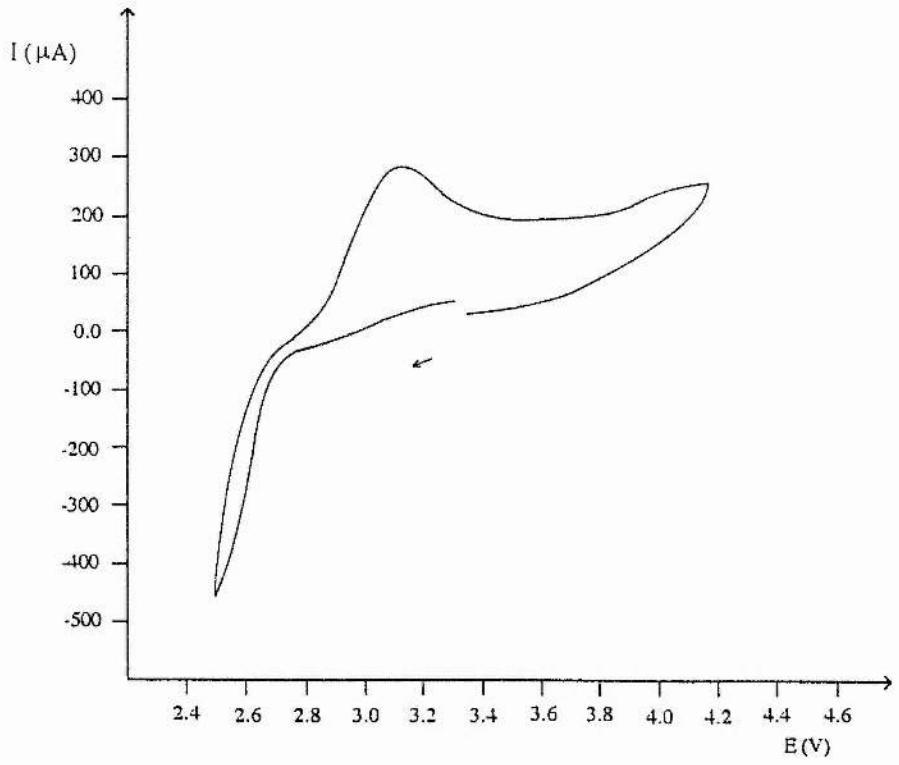

Figure 6-17 Cyclic voltammogram of the system containing nickel iodide
Ni / $PEO_{48.5\ NiI_2}^{10\ LiClO_4}$ / $PEO_{9.9}LiClO_4$ / Li / $PEO_{9.9}LiClO_4$ / Li at 86.0 °C

6.5.2.1 *Analysis of the Tafel plot*

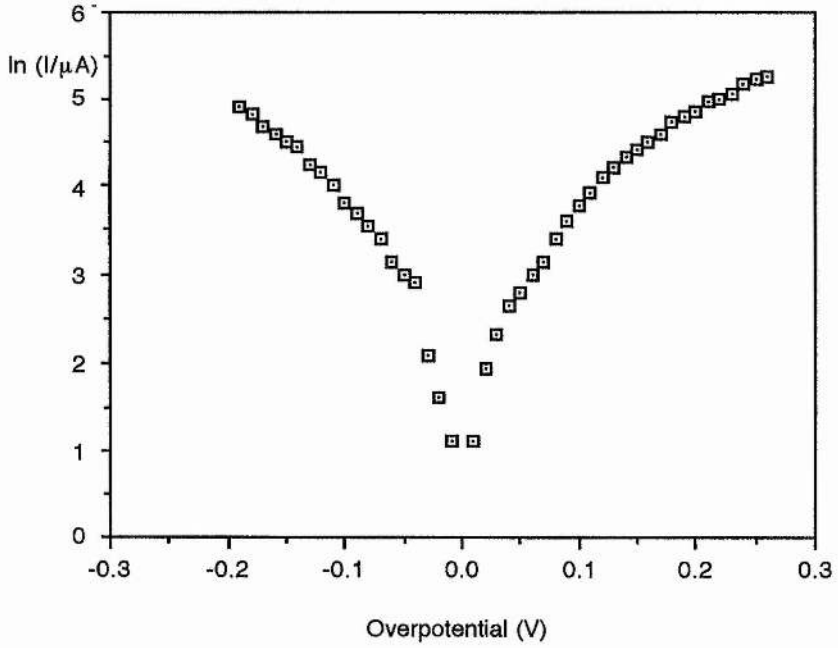

Figure 6-18 The Tafel plot

Analysis of the data for the cathodic process at large overpotentials enabled the transfer coefficient α_C to be determined (figure 6-19).

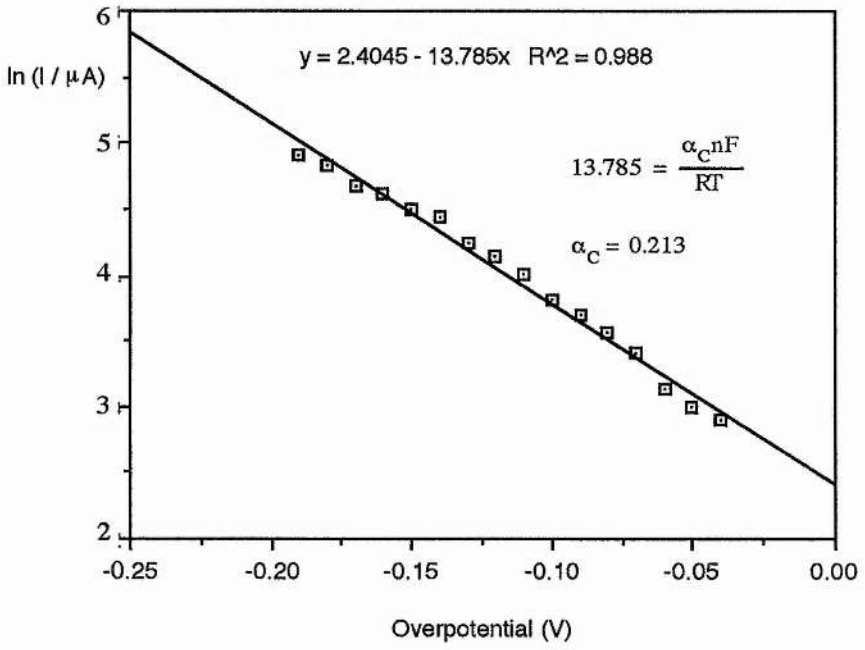

Figure 6-19 The Tafel slope for the cathodic process

The net current for the cathodic process at large overpotentials (η) was given by the following equation :-

$$\ln(I/\mu A) = 2.4045 - 13.785\eta \qquad 6\text{-iii)}$$

The slope of the Tafel plot for the anodic process was difficult to determine due to the curved nature of the plot at large overpotentials. The exchange current was obtained by substitution into equation 6-iii) at zero overpotential. Subsequent correction for the electrode area (0.905 cm^2) gave the exchange current density (equation 6-iv).

$$I_0 = \frac{\exp(2.4045)}{0.905} \qquad 6\text{-iv)}$$

$$\text{Thus } I_0 = 12.2\ \mu A cm^{-2}$$

6.5.2.2 *The heterogeneous rate constant*

The expression for the heterogeneous rate constant for electron transfer is given by the following equation :-

$$k^{\circ} = \frac{I_0}{nF(a^{\infty}_{Ni})^{\alpha_C}(a^{\infty}_{Ni^{2+}})^{1-\alpha_C}} \qquad 6\text{-v)}$$

where a^{∞}_{x} is the activity of species x.

The approximation was made that the activity of the Ni^{2+} ions in the bulk polymer was the same as their concentration i.e. $a^{\infty}_{Ni^{2+}} = C^{\infty}_{Ni^{2+}}$. For the system under investigation, the bulk concentration of nickel ions ($C^{\infty}_{Ni^{2+}}$)was determined as 3.328×10^{-4}mol dm^{-3}. The activity of solid nickel was taken as unity and the number of electrons involved in the electron transfer as 2. Substitution into equation 6-v gave:-

$$k^{\ominus} = 3.4 \times 10^{-8} \text{ cm s}^{-1} \qquad 6 - \text{vi})$$

X-ray diffraction data of the polymer electrolyte sample indicated the presence of small amounts of undissolved NiI_2 at room temperature. Even if the solubility of the salt increased with increasing temperature, at the temperature of the experiment, the presence of ion pairs, triples and higher multiples together with traces of the PEO:NiI_2 crystalline complex would serve to ensure that the approximation was not valid. For this reason it is likely that the value of $k^{\ominus}$ determined was an approximation. Qualitatively however, it was possible to deduce from the experiment that the kinetics of the redox reaction are slow. Biallozor et al[100] obtained a value for $k^{\ominus}$ of the order of 10^{-6} cm s^{-1} for $Ni(BF_4)_2$ in dimethyl sulphoxide. Despite the different experimental conditions, it appears that the kinetics of the redox reaction in the PEO:NiI_2 system are much slower.

6.5.2.3 *Summary of Tafel plot analysis*

The parameters characterising the system are summarised in table 6-3.

T (K)	359	I_o (μA cm^{-2})	12.2
n	2	$C^{\infty}_{Ni^{2+}}$ (mol cm^{-3})	3.328×10^{-4}
α_C	0.213	$k^{\ominus}$ (cms^{-1})	3.4×10^{-8}
A (cm^2)	0.905		

Table 6-3 Summary of the parameters describing the system.

6.5.2.4 *Ac impedance data*

Ac impedance data was taken from the cell used for cyclic voltammetry (Ni / $PEO_{48.5}^{10}\,NiI_2^{LiClO_4}$ / $PEO_{9.9}LiClO_4$ / Li / $PEO_{9.9}LiClO_4$ / Li). Data was collected in the frequency range 100kHz - 100mHz with a 3.00V dc bias (η = +0.160V). The complex impedance plot obtained is illustrated in figure 6-20.

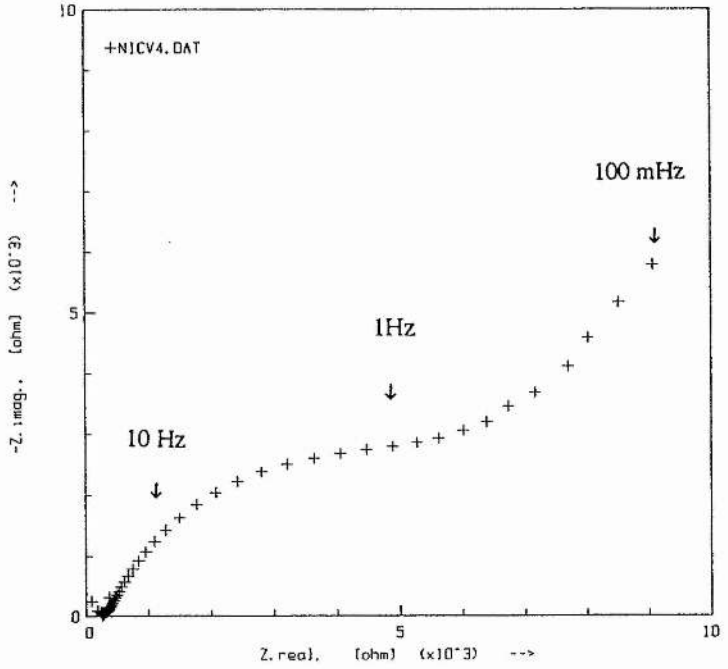

Figure 6-20 Complex impedance plot obtained for the cyclic voltammetry cell.

The high frequency intercept of the plot with the real axis corresponds to the bulk electrolyte resistance, R_b. The charge transfer resistance, R_{CT}, and the double layer capacitance, C_{dl}, were obtained from the semicircle in the complex impedance plot using the data fitting program[98]. The low frequency feature of the plot had the characteristics of a Warburg impedance. Data from this region of the impedance plot were used to to produce the graph illustrated in figure 6-21. The diffusion coefficient of the Ni(II) species in the system was determined by the method described in section 3.3.2.

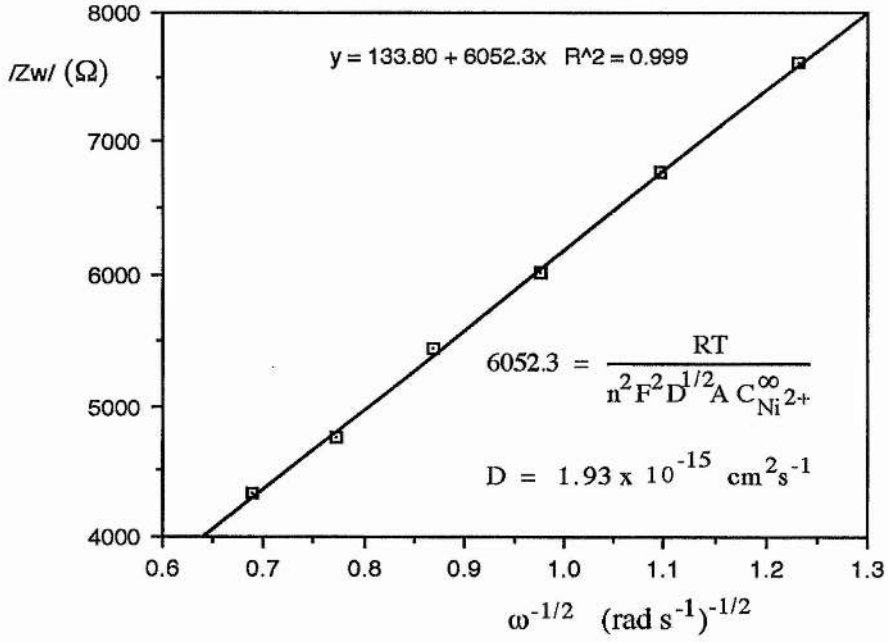

Figure 6-21 Calculation of the diffusion coefficient

Tha data illustrated in figure 6-21 exhibits excellent linearity suggesting that it can indeed be ascribed to a diffusional process. There was a possibility that the Warburg impedance could however be due to two dimensional diffusion of ad-atoms across the electrode surface prior to incorporation into the nickel lattice, rather than diffusion of nickel ions through the bulk. This was deemed less likely due to the highly defective nature of the polycrystalline electrode which was not highly polished. The mean free path of the ad-atoms to suitable incorporation sites would thus be very short. Also ad-atom formation would be unlikely to occur at the overpotential of the experiment (+0.16V)

The data obtained for the system by analysis of the ac impedance plot, corrected for electrode area, is summarised in table 6-4.

R_b (Ω cm^2)	2.95 x 10^2
R_{CT} (Ω cm^2)	7.21 x 10^3
C_{dl} (F cm^{-2})	2.44 x 10^{-5}
$D_{Ni(II)}$ (cm^2 s^{-1})	1.93 x 10^{-15}

Table 6-4 Data obtained by ac impedance analysis

The exchange current density was determined from the ac impedance data using equation 6-vii:-

$$I_o = \frac{RT}{nFR_{CT}} \qquad 6 - vii)$$

Substitution into this equation gave $I_o = 2.1$ μA cm^{-2}. This value was slightly lower than that obtained from the Tafel plot , however, both values of I_o, which agree to within an order of magnitude, indicate that the kinetics of the reaction are very slow.

6.5.3 *Conclusion*

The data obtained by cyclic voltammetry indicated that both the kinetics of the electron transfer and mass transport were slow. The mechanism for the reduction of Ni^{2+} is likely to be a highly complex multistep process, involving as it does more than one electron. Any one of a variety of steps could be the rate determining process e.g.

mass transport of the Ni(II) species to the electrode,

electron transfer,

ad-atom formation,

two dimensional diffusion of ad-atoms across the electrode surface,

incorporation of the ad-atoms into the lattice or

growth .

It is likely that the Ni^{2+} ion is strongly coordinated by the polymer. The acceptance of an electron by the solvated species will necessitate the reorganisation of the primary solvation sphere of the ion. This is likely to be a highly energetic process, involving as it does the cooperative motion of the high molecular weight polymer chains. Furthermore, the presence of crystalline phases in the system will serve to restrict the segmental motion of the polymer chains further increasing the solvent reorganisation energy.

If the metal ad-atoms were also partially solvated by the polymer, then two dimensional diffusion across the electrode surface would be inhibited by a similar mechanism. On the basis of this discussion, it would be expected that the kinetics of the electrode reaction would be slow for all redox processes of ions solvated by high molecular weight PEO based polymer electrolytes.

The magnitude of the diffusion coefficient for the Ni(II) species in the PEO_xNiI_2 system indicated that they were essentially immobile. Again, this is not unexpected for strongly coordinated ions in a system where segmental motion of polymer chains is severely inhibited by the presence of crystalline phases.

6.6 The potential step experiment

6.6.1 *Experimental*

The cell prepared for cyclic voltammetry, (Ni / $PEO^{10\ LiClO_4}_{48.5\ NiI_2}$ / $PEO_{9.9}LiClO_4$ / Li / $PEO_{9.9}LiClO_4$ / Li), was instantaneously stepped by - 270 mV from the open circuit voltage and the current recorded as a function of time.

6.6.2 *Results and discussion*

The current-time profile recorded in the potential step experiment is shown in figure 6-22.

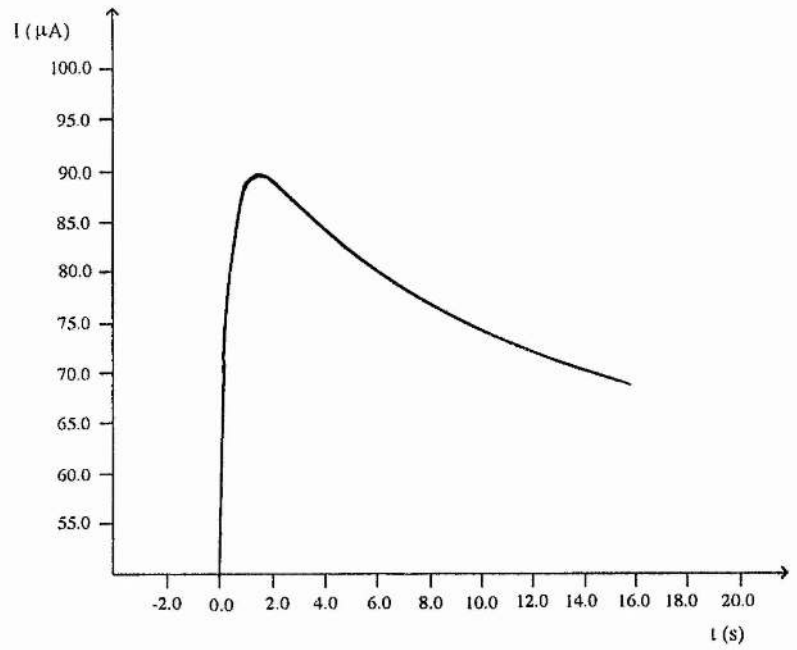

Figure 6-22 The current-time profile for the potential step experiment

Reference to figure 2-6 suggests that a maximum in the current-time profile is indicative of three-dimensional diffusion controlled growth. Further evidence in favour of this proposition is the $t^{-1/2}$ dependence of the current over long time scales as illustrated by figure 6-23.

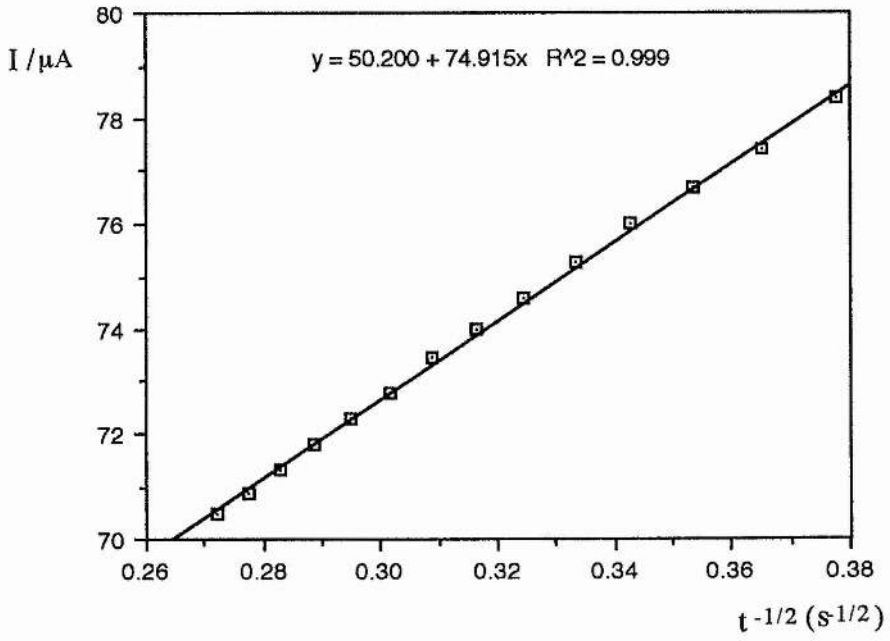

Figure 6-23 Current versus $t^{-1/2}$ (long timescales)

Over short timescales, the current is proportional to $t^{1/2}$ (figure 6-24) which is a characteristic of instantaneous nucleation.

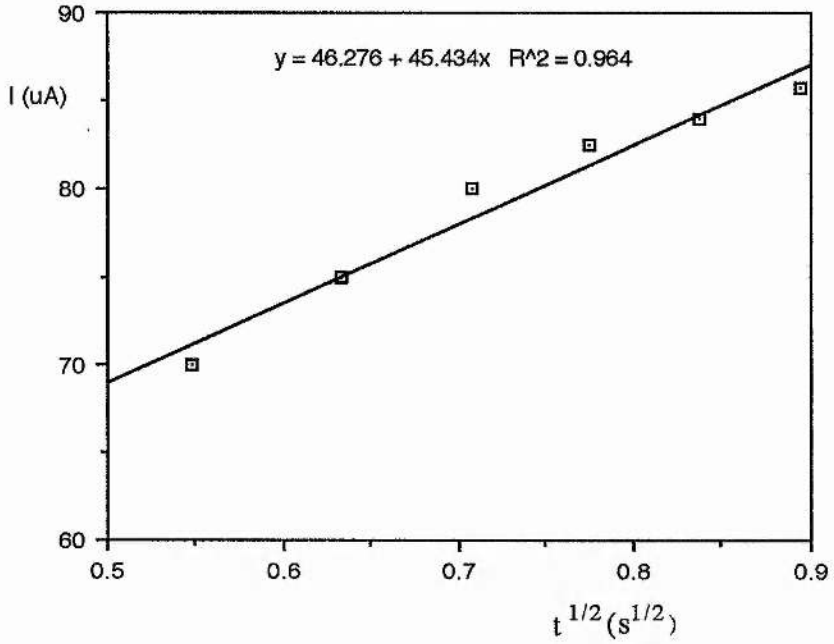

Figure 6-24 Current versus $t^{1/2}$ (short timescales)

Instantaneous nucleation rather than simple ad-atom formation was not unexpected under the conditions used in the experiment. At the relatively high overpotential used, fresh nucleation centres would be instantaneously formed on the polycrystalline surface and grow rapidly. Simple nickel ad-atom formation would only be expected on a defect free single crystal nickel surface at relatively low overpotentials.

6.6.2.1 *Calculation of the diffusion coefficient*

For diffusion controlled growth, the current obeys the Cottrell equation (2-xv). The diffusion coefficient for Ni(II) species can thus be determined from the gradient of figure 6-23 as shown in box 1.

BOX 1

gradient (m) = $nFD^{1/2}C_0^{\infty}/\pi^{1/2}$ $\quad$ $C = 3.328 \times 10^{-4}$ mol cm^{-3}

$n = 2$ $\quad$ $F = 9.648 \times 10^{4}$ C mol^{-1}

$D = 4.275 \times 10^{-12}$cm^{2}s^{-1} at 86° C

A further estimate for the diffusion coefficient is provided by equation 2-xxiii) in which it is related the time and current maxima as shown in box 2.

BOX 2

$$I_m^2 t_m = 0.163 (nFC_0^{\infty})^2 D$$

$I_m = 88.80\ \mu A$ $\quad$ $t_m = 1.55s$

$D = 1.82 \times 10^{-11}$cm^{2}s^{-1} at 86° C

The values for the diffusion coefficient determined in boxes 1 and 2 are in agreement to within an order of magnitude and further indicate that diffusion of Ni(II) species in the polymer electrolyte is slow. They were however several orders of magnitude larger than the value determined by ac impedance. The reason for this was unclear.

6.7 Dc polarisation experiments

6.7.1 *Experimental*

The method of Evans et al[64] was used to determine the cationic current fraction of polymer electrolyte films containing NiI_2. In each case, a film of $PEO_{20}NiI_2$ was sandwiched between nickel electrodes. A small dc polarisation potential (10 mV) was applied and the current monitored as a function of temperature. The current falls due to the establishment of a concentration gradient across the cell. This has the affect of reducing (and eventually stopping) the motion of the anions and also generates an emf in opposition to the applied potential thus reducing ion migration. In the steady state, the current is due simply to the net diffusion of species containing Ni^{2+} towards the cathode. The cationic current fraction, F_+, is the ratio of the initial (I^o) and steady state (I^s) currents. It differs from the transport number, t_+ , and the transference number, T_+, in that it contains a contribution from the current transported by the diffusion of neutral species. The method of Evans et al. also makes a correction for the polarisation of the electrodes in the experiment. This is particularly important for systems in which there is growth of a passive layer on the electrode during the experiment. Ac impedance data collected throughout the experiment enables the charge transfer resistance, R_{CT}, to be determined. The cationic current fraction is then given by :-

$$F_+ = \frac{I^s(\Delta V - I^o R^o_{CT})}{I^o(\Delta V - I^s R^s_{CT})} \qquad 6 - i)$$

where ΔV is the applied polarisation potential and R^o_{CT} and R^s_{CT} are the initial and steady state electrode resistances. Thus, R^o_{CT} and R^s_{CT} were determined from ac impedance measurements at the start and end of the experiment respectively. The initial current was given by:-

$$I^o = \Delta V (R^o_{CT} + R_b) \qquad 6 - ii)$$

where R_b is the bulk electrolyte resistance determined by ac impedance.

6.7.2 *Results*

6.7.2.1 *Untreated electrodes*

A cell was prepared containing a disc of $PEO_{20}NiI_2$ sandwiched between untreated nickel electrodes and heated to 100.4 °C under dynamic vacuum. The ac impedance plots obtained during the experiment are shown in figures 6-25 and 6-26.

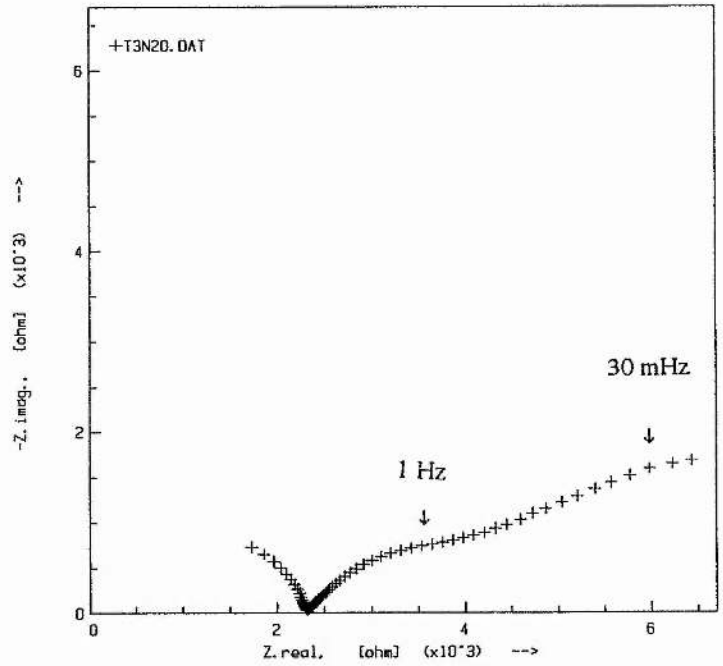

Figure 6-25 Ac impedance plot obtained at the start of experiment 6.7.2.1

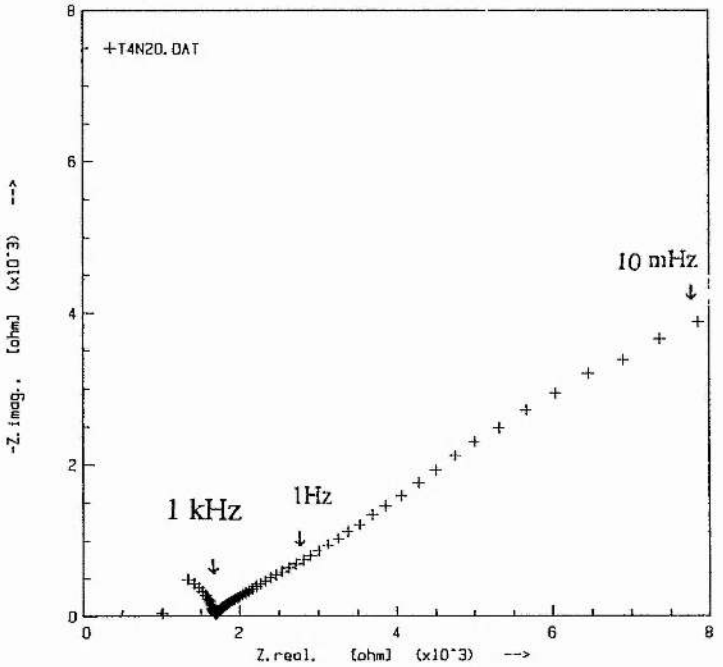

Figure 6-26 Ac impedance plot obtained at the end of experiment 6.7.2.1

The data obtained in experiment 6.7.2.1 is summarised are summarised in table 6-5.

$R^{o}_{CT}(\Omega)$	3.63×10^{3}	I^{s} (A)	6.70×10^{-8}
$R^{s}_{CT}(\Omega)$	1.54×10^{3}	ΔV (mV)	10.00
I^{o} (A)	1.68×10^{-6}	Rb (Ω)	2.32×10^{3}

Table 6-5 Data obtained from experiment 6.7.2.1

Substitution of the data into equation 6-i) gives a cation current fraction of $F_{+} = 0.016$.

6.7.2.2 *Polished electrodes (I)*

A fresh sample of $PEO_{20}NiI_2$ was sandwiched between polished nickel electrodes and was heated to 95.4 °C under dynamic vacuum. After recording an ac impedance plot, a potential of -270 mV was applied to the 'working' electrode for 30 seconds, followed by a similar pulse of + 270 mV. The process was repeated, followed by a final pulse at -270 mV. This was to ensure that a fresh coating of nickel was present on the surface of the electrodes. Following this procedure a second ac impedance plot was recorded and a dc polarisation potential of -10mV was applied to the system. The current was recorded as a function of time over a period of three days and the steady state current determined. Ac impedance data was collected (with a -10mV dc bias) at intervals throughout the experiment. The cationic current fraction was calculated by the method described in section 6.7.1.

The ac impedance plots obtained during the experiment are shown in figures 6-27 and 6-28. The data obtained are summarised in table 6-6.

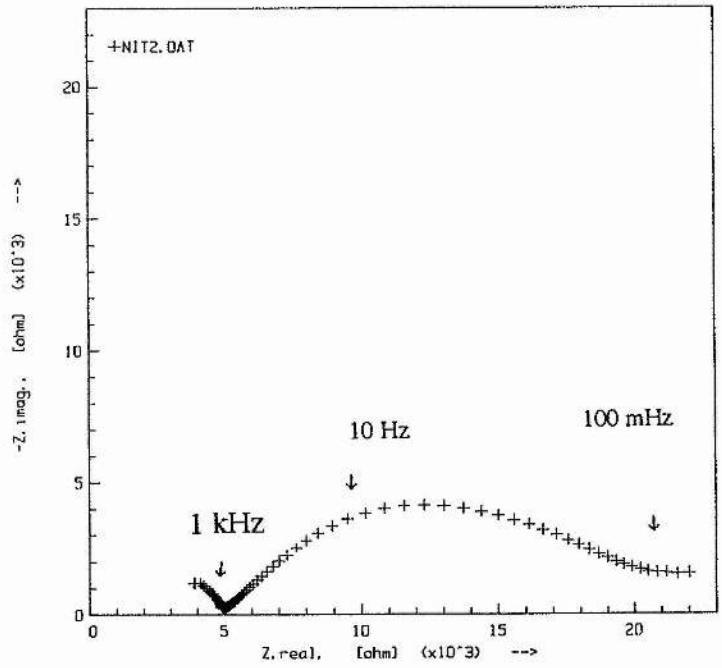

Figure 6-27 Ac impedance plot obtained at the start of experiment 6.7.2.2

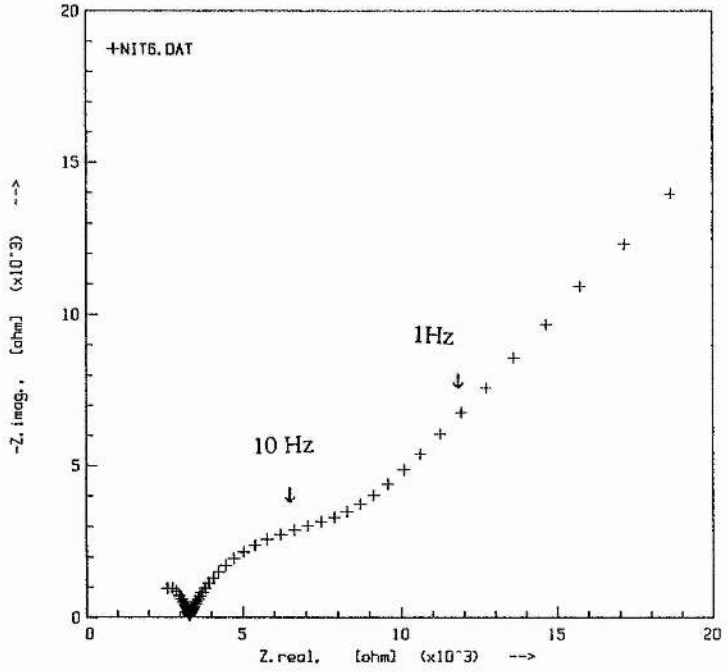

Figure 6-28 Ac impedance plot obtained at the end of experiment 6.7.2.2

$R^{o}_{CT}(\Omega)$	1.60×10^{4}	I^{s} (A)	1.40×10^{-7}
$R^{s}_{CT}(\Omega)$	9.36×10^{3}	ΔV (mV)	10.00
I^{o} (A)	4.75×10^{-7}	Rb (Ω)	5.04×10^{3}

Table 6-6 Data obtained from experiment 6.7.2.2

Substitution of the data into equation 6-i) gives a cation current fraction of $F_{+} = 0.082$.

6.7.2.3. *Polished electrodes (II)*

The cell from the previous section was allowed to stand at open circuit for 8 hours. A 10 mV dc polarisation potential was applied to the cell at 117.0 °C without further pre-treatment of the electrodes. Ac impedance data was collected throughout the experiment and the cationic current fraction determined as before.

The ac impedance plots obtained during the experiment are shown in figures 6-29 to 6-31. The data obtained are summarised in table 6-7.

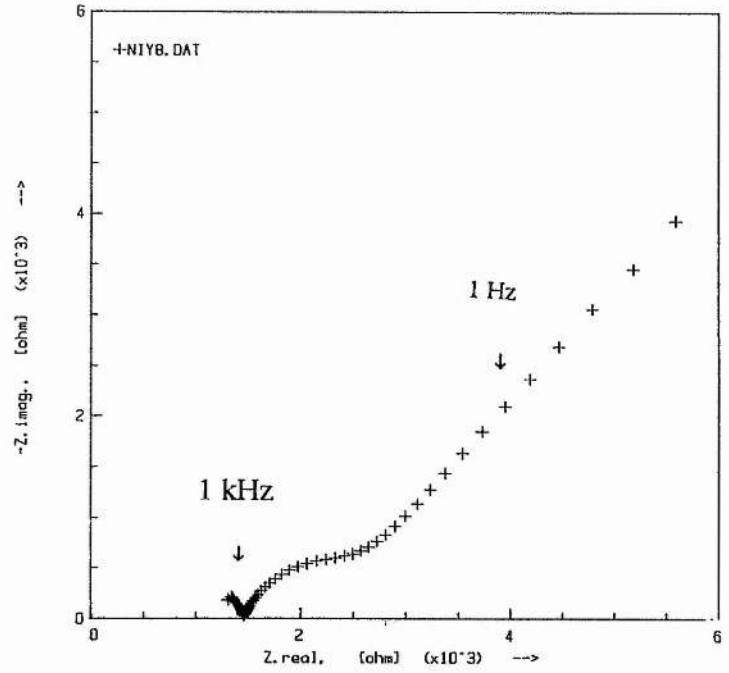

Figure 6-29 Ac impedance plot obtained at the start of experiment 6.7.2.3

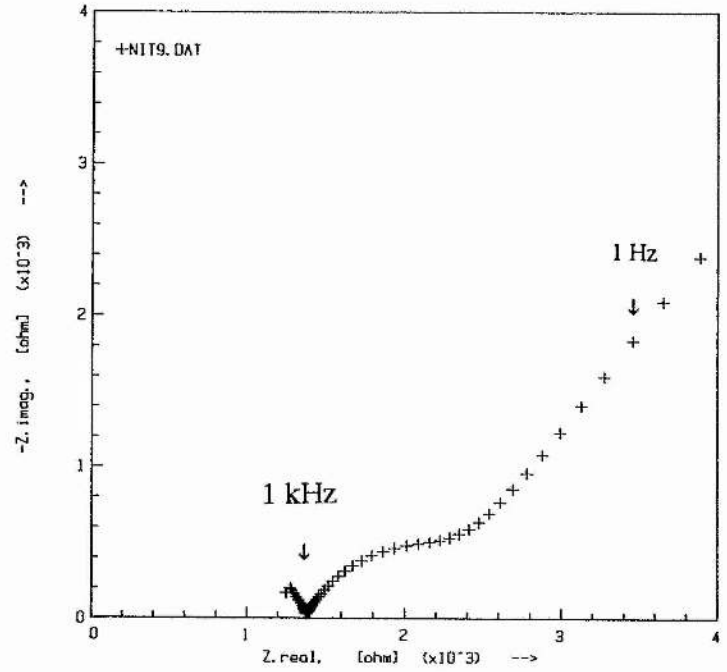

Figure 6-30 Ac impedance plot obtained during experiment 6.7.2.3

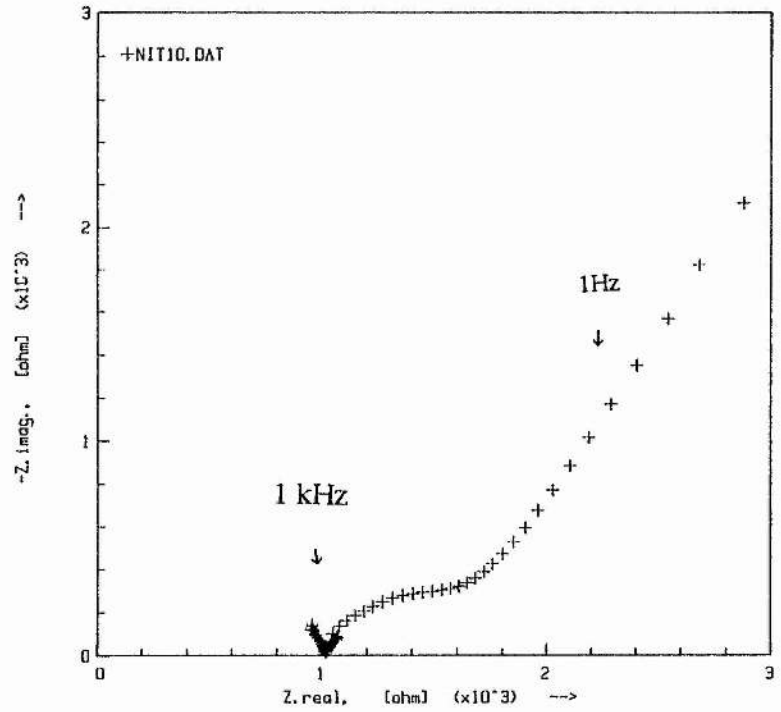

Figure 6-31 Ac impedance plot obtained at the end of experiment 6.7.2.3

$R^{o}_{CT}(\Omega)$	1.93×10^{3}	I^{s} (A)	2.58×10^{-7}
$R^{s}_{CT}(\Omega)$	1.01×10^{3}	ΔV (mV)	10.00
I^{o} (A)	2.94×10^{-6}	Rb (Ω)	1.47×10^{3}

Table 6-7 Data obtained from experiment 6.7.2.3

Substitution of the data into equation 6-i) gives a cationic current fraction of $F_+ = 0.039$.

6.7.3 *Summary of cationic current fraction data*

Expt.	Film	T (°C)	F_+
6.7.2.1	$PEO_{20}NiI_2$	100.4	0.016
6.7.2.2	$PEO_{20}NiI_2$	95.4	0.082
6.7.2.3	$PEO_{20}NiI_2$	117.0	0.039

Table 6-8 Summary of cationic current fraction data

It can be seen from the data that the values of F_+ were relatively unchanged by the different pre-treatment of the electrodes; in all cases, F_+ was less than 0.1. It was possible to conclude therefore that the films of $PEO_{20}NiI_2$ were principally anionic conductors and that the Ni(II) species were virtually immobile.

6.8 Conclusion

The following conclusions were drawn from the investigation of the PEO_xNiI_2 system:-

i) Ni(II) species are virtually immobile in the system as illustrated by:-

a) the extremely small magnitude of the diffusion coefficients determined, $D_{Ni(II)} \leq 1.82 \times 10^{-11}$ cm^2 s^{-1}.

b) the low values of the cationic current fraction ($F_+ < 0.1$)

ii) The electrode reaction kinetics for the redox process:-

$$Ni^{2+}_{(solv)} + 2e \rightleftharpoons Ni_{(s)}$$

are extremely slow as indicated by the low exchange current densities determined by ac impedance and cyclic voltammetry ($I_o \leq 12.2$ μA cm^{-2}).

iii) Deposition of nickel from the polymer electrolyte is characterised by instantaneous nucleation followed by three dimensional diffusion controlled growth.

iv) NiI_2 forms a crystalline complex with PEO as illustrated by DSC and powder x-ray diffraction.

v) The system is principally an anionic conductor, the conductivities of the PEO_xNiI_2 films being significantly enhanced compared to the pure hot pressed polymer.

CHAPTER 7

THE PEO:EUROPIUM TRIFLATE SYSTEM

The study of polymer electrolytes containing europium is of particular interest due to the availability of both the trivalent and divalent oxidation states. The aim of the current investigation was to probe the redox behaviour of the system using cyclic voltammetry and ac impedance techniques.

7.1 Experimental

7.1.1 *Characterisation of Europium salts*

The powder x-ray diffraction pattern of anhydrous $Eu(CF_3SO_3)_3$ prepared in section 4.2.2 consisted of a single sharp peak in the region of $2\theta = 8^o$ as illustrated in figure 7-1a. Upon exposure to moisture for 30 minutes, the sample gave the powder pattern illustrated in figure 7-1b. The observed reflections could be indexed on a powder pattern which was generated from single crystal[101] data for $Gd(CF_3SO_3)_3.9H_2O$ using the computer program LAZY-PULVERIX. This, together with the elemental analysis of the anhydrous salt confirmed that $Eu(CF_3SO_3)_3$ had indeed been prepared.

The elemental analysis of the europous triflate, $Eu(CF_3SO_3)_2$, prepared in section 4.2.3 indicated that the sample was deficient in carbon and contained small traces of hydrogen. It was therefore not possible to prepare polymer electrolytes containing both Eu^{3+} and Eu^{2+} as was initially envisaged.

7.1.2 *Preparation of samples*

For the cyclic voltammetry experiments, it was necessary to prepare polymer electrolytes containing both europium triflate and a supporting electrolyte. Films of compositions $PEO_{50\ Eu(CF_3SO_3)_3}^{10\ LiClO_4}$ and $PEO_{100\ Eu(CF_3SO_3)_3}^{20\ LiCF_3SO_3}$ were prepared by the solvent casting method (section 4.1.1). Films of $PEO_{20}LiCF_3SO_3$ and $PEO_{10}LiClO_4$ were also prepared by the same technique for use with the lithium reference electrode.

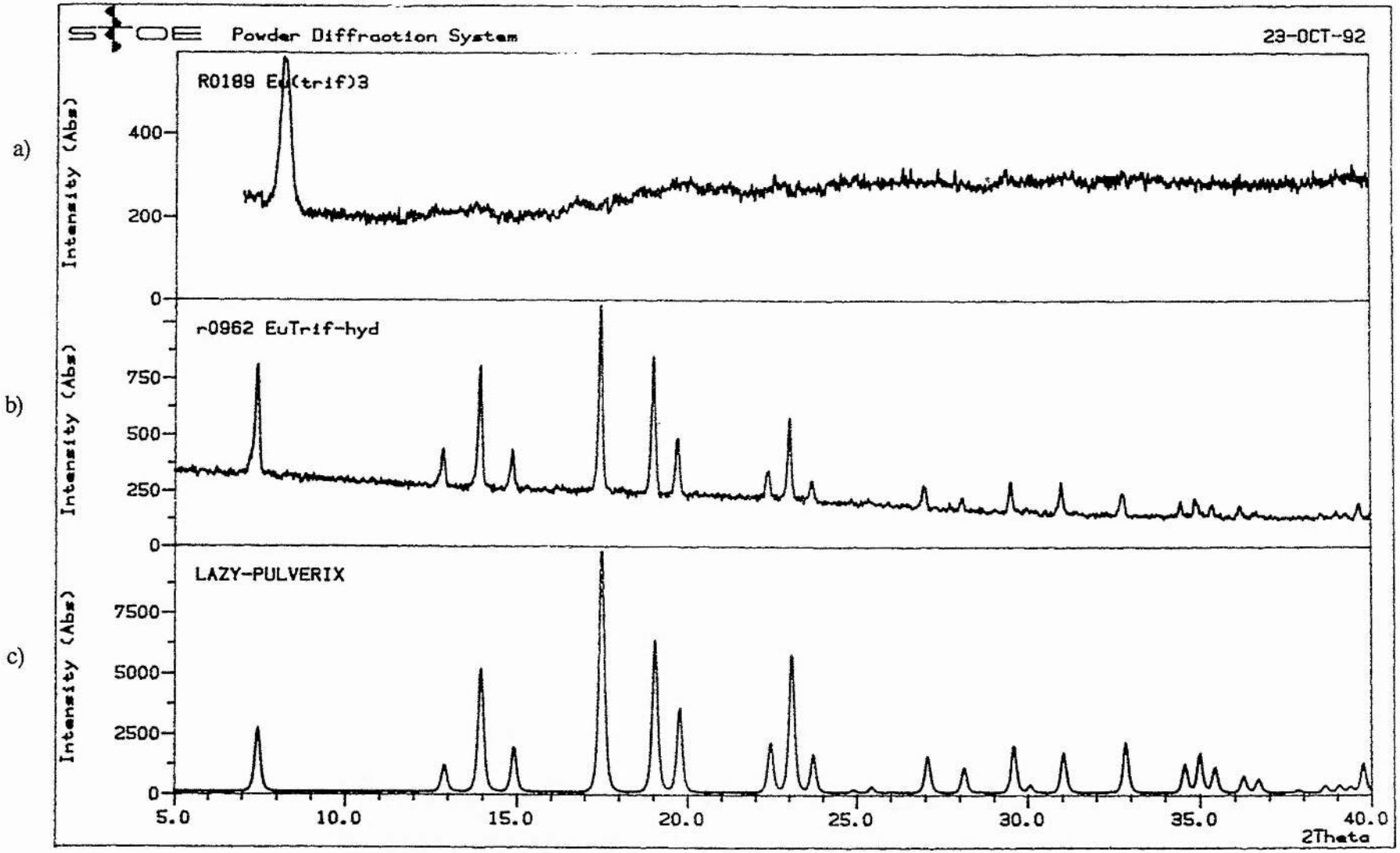

Figure 7-1 Powder x-ray diffraction patterns for $Eu(CF_3SO_3)_3$ a) anhydrous $Eu(CF_3SO_3)_3$, b) hydrated $Eu(CF_3SO_3)_3$, c) pattern generated by LAZY PULVERIX

7.1.3 *Cyclic Voltammetry*

Three electrode cells of the type illustrated in figure 7-2 were prepared in an argon filled drybox. Where $LiClO_4$ was used as a supporting electrolyte $PEO_{10}LiClO_4$ films were used with the lithium reference electrode and a $PEO^{10\ LiClO_4}_{50\ Eu(CF_3SO_3)_3}$ film was used in place of the $PEO^{20\ LiCF_3SO_3}_{100\ Eu(CF_3SO_3)_3}$ film. The cells were inserted into stainless steel cylinders (figure 4-6) before being removed from the drybox. Prior to all electrochemical measurements, the cells were heated under dynamic vacuum in a tube furnace and allowed to equilibriate for 1 hour at the required temperature.

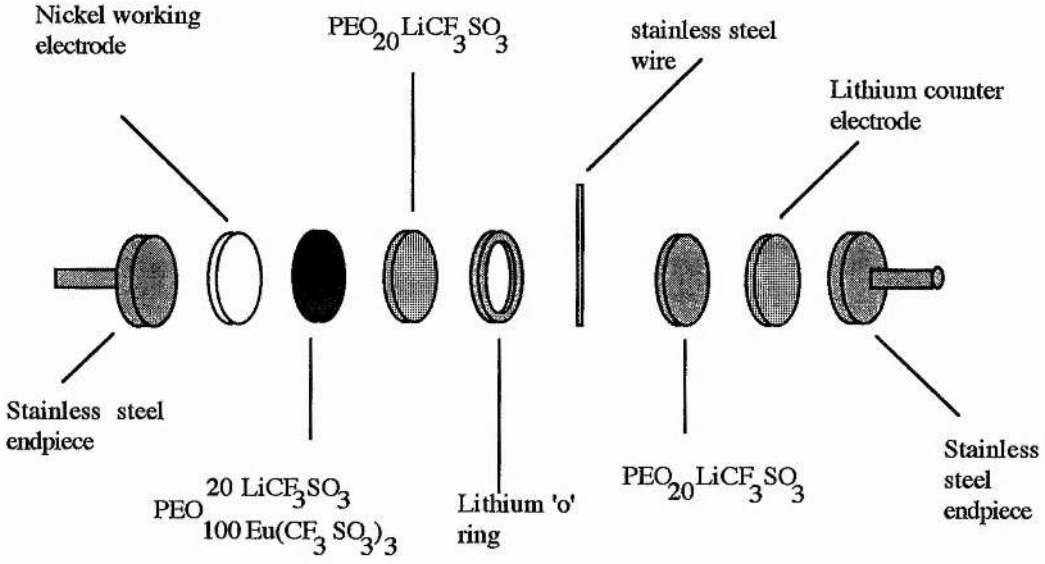

Figure 7-2 Three electrode cell used for cyclic voltammetry

7.1.4 *Ac impedance measurements*

Ac impedance data was collected from the cell used in section 7.1.3 for cyclic voltammetry.

7.2 Results

7.2.1 *Cyclic Voltammetry with $LiCF_3SO_3$ as a supporting electrolyte*

Cyclic voltammograms were obtained for a range of scan rates as illustrated in figure 7-3. The data obtained from the cyclic voltammograms is summarised in table 7-1.

Scan rate (mVs^{-1})	E_p^C (V)	E_p^A (V)	I_p^C (μA)	I_p^A (μA)	I_p^A/I_p^C
10	2.810	3.110	1.750	1.000	0.571
20	2.790	3.140	2.400	1.400	0.583
50	2.710	3.180	4.100	2.450	0.598
100	2.690	3.240	5.450	3.550	0.651
200	2.620	3.310	8.700	5.800	0.667
400	2.550	3.380	14.000	9.400	0.671

Table 7-1 Data obtained from cyclic voltammograms scanned between 2.55 and 3.55V at 75.4°C
(Potentials measured with respect to Li/Li^+ ($PEO_{20}LiCF_3SO_3$) reference electrode)

It was seen from figure 7-3 that the anodic peak current was smaller than the cathodic peak current for all scan rates. Furthermore, the ratio of the anodic to cathodic peak currents increased with increasing scan rate. It was also noted, that upon scanning anodically from the open circuit voltage, (3.089V), the anodic peak was absent on the first cycle. The variation of the peak positions, E_p^C and E_p^A, with the logarithm of the scan rate are illustrated in figures 7-4 and 7-5. E_p^C became more negative with increasing scan rate and E_p^A more positive. Reference to standard electrode potentials (7-i) indicated that the peaks observed in the cyclic voltammograms were in the region expected for the Eu^{3+}/Eu^{2+} couple determined with respect to a lithium reference electrode. (It should be noted that a discrepancy is expected due to the fact that the standard reference potentials refer to aqueous solutions whereas, the system under investigation has PEO as a solvent.)

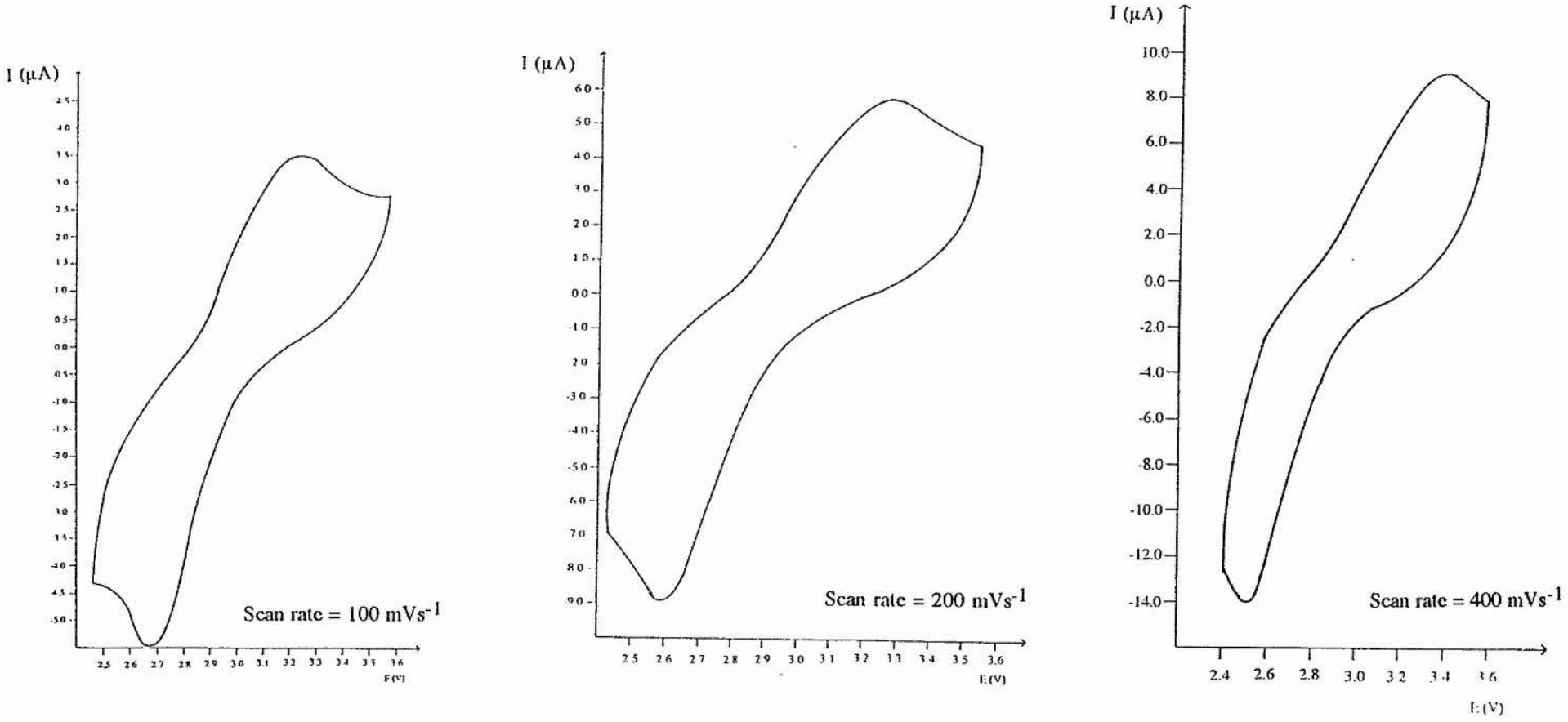

Figure 7-3 Cyclic voltammograms obtained for the cell Ni / $PEO^{20LiCF_3SO_3}_{100Eu(CF_3SO_3)_3}$ / $PEO_{20}LiCF_3SO_3$ / Li / $PEO_{20}LiCF_3SO_3$ / Li

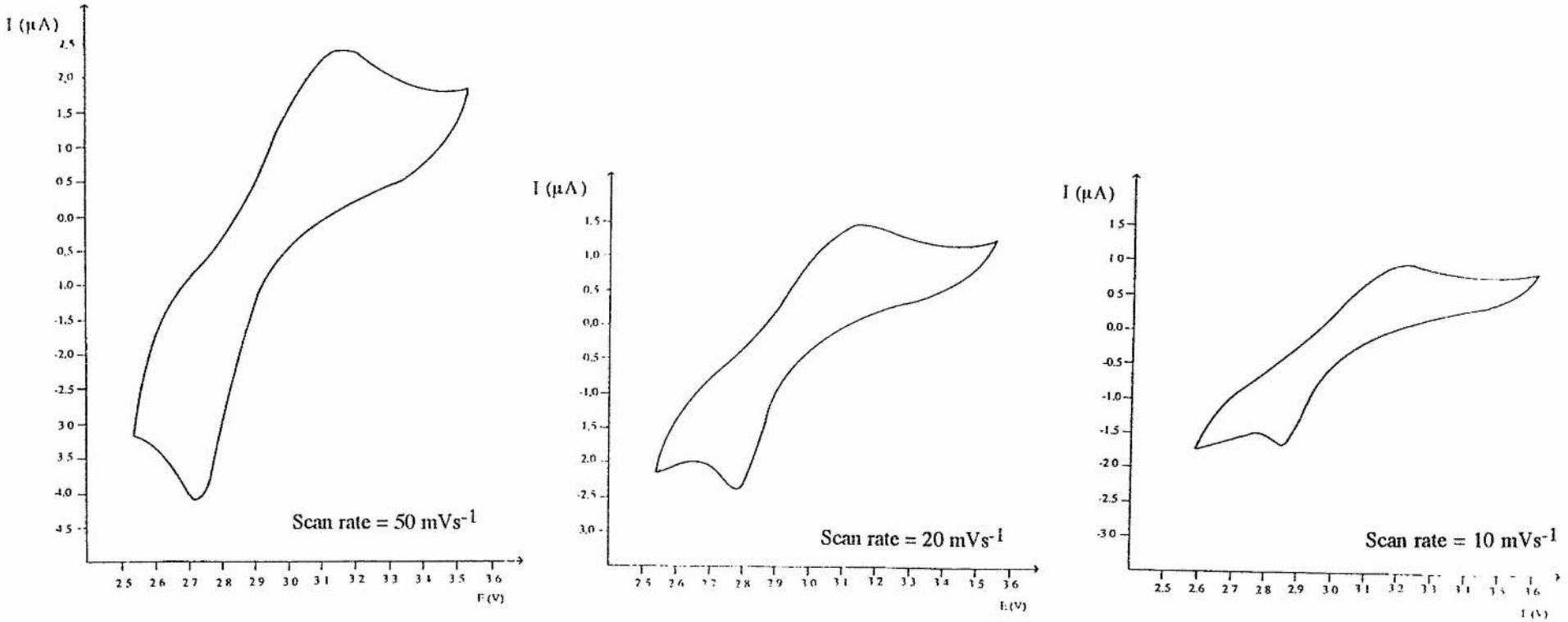

Figure 7-3 (cont.) Cyclic voltammograms obtained for the cell Ni / $PEO^{20LiCF_3SO_3}_{100Eu(CF_3SO_3)_3}$ / $PEO_{20}LiCF_3SO_3$ / Li / $PEO_{20}LiCF_3SO_3$ / Li

$$Eu^{3+} + e \rightleftharpoons Eu^{2+} \qquad E^{\ominus} = -0.360V$$

$$Li^{+} + e \rightleftharpoons Li \qquad E^{\ominus} = -3.040V \qquad 7 - i)$$

The cathodic peak was thus ascribed to the reduction of Eu^{3+} and the anodic peak was ascribed to the oxidation of Eu^{2+}.

Data from the cyclic voltammogram of figure 7-3 performed at $10mVs^{-1}$ was used to construct the Tafel plot of figure 7-6 using the method described in section 2.4. The transfer coefficients α_A and α_C were obtained from the gradients of the Tafel plot in the region of high overpotential as illustrated in figures 7-7 and 7-8. These in turn were used to calculate the exchange current density.

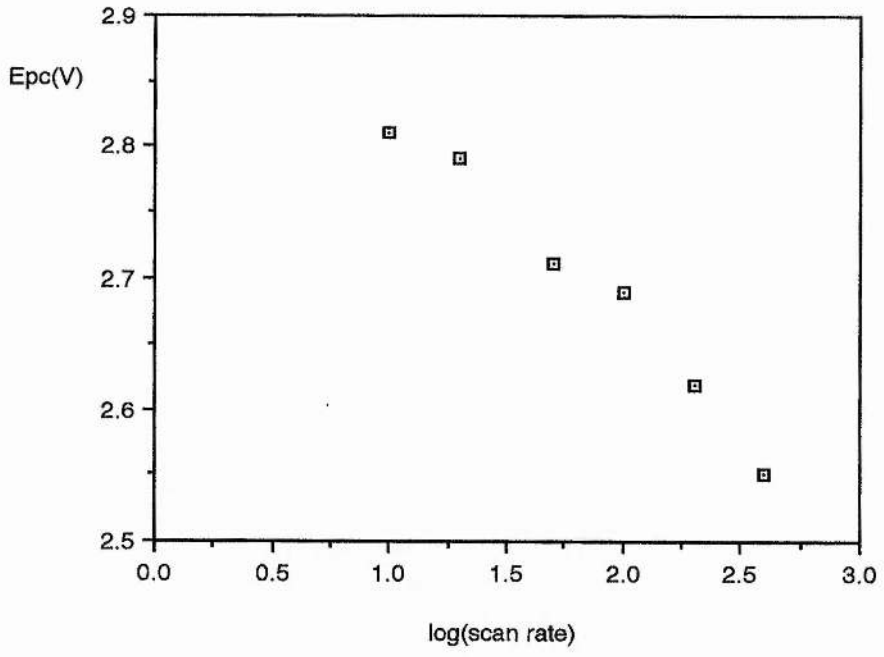

Figure 7-4 Variation of E_p^C with log(scan rate) for the cell

Ni / $PEO_{100Eu(CF_3SO_3)_2}^{20\,LiCF_3SO_3}$ / $PEO_{20}LiCF_3SO_3$ /Li / $PEO_{20}LiCF_3SO_3$ / Li

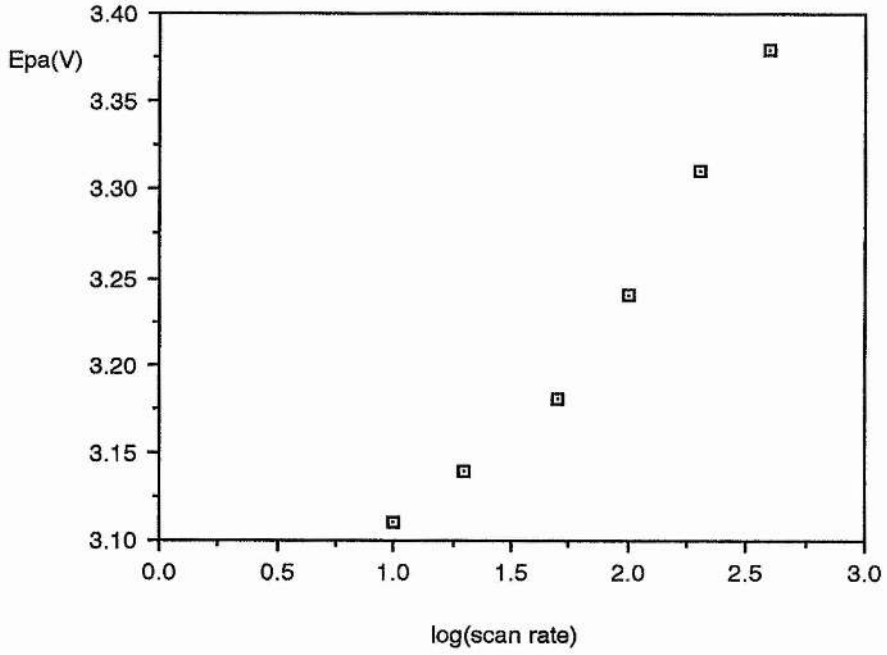

Figure 7-5 Variation of E_p^A with log(scan rate) for the cell

$$Ni / PEO_{100Eu(CF_3SO_3)_2}^{20\,LiCF_3SO_3} / PEO_{20}LiCF_3SO_3 / Li / PEO_{20}LiCF_3SO_3 / Li$$

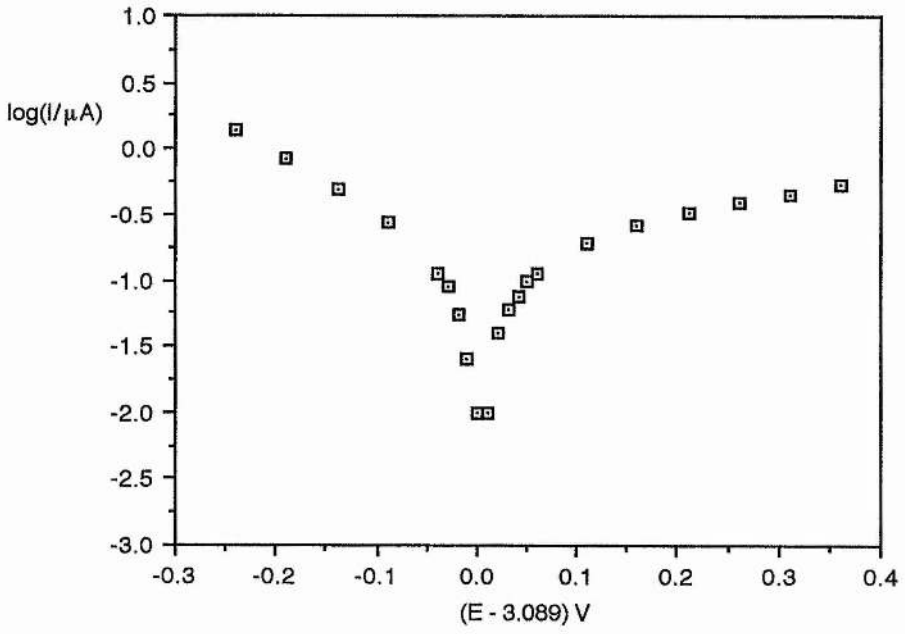

Figure 7-6 Tafel plot constructed from the data obtained from the cyclic voltammogram of figure 7-3 at 10 mVs^{-1}

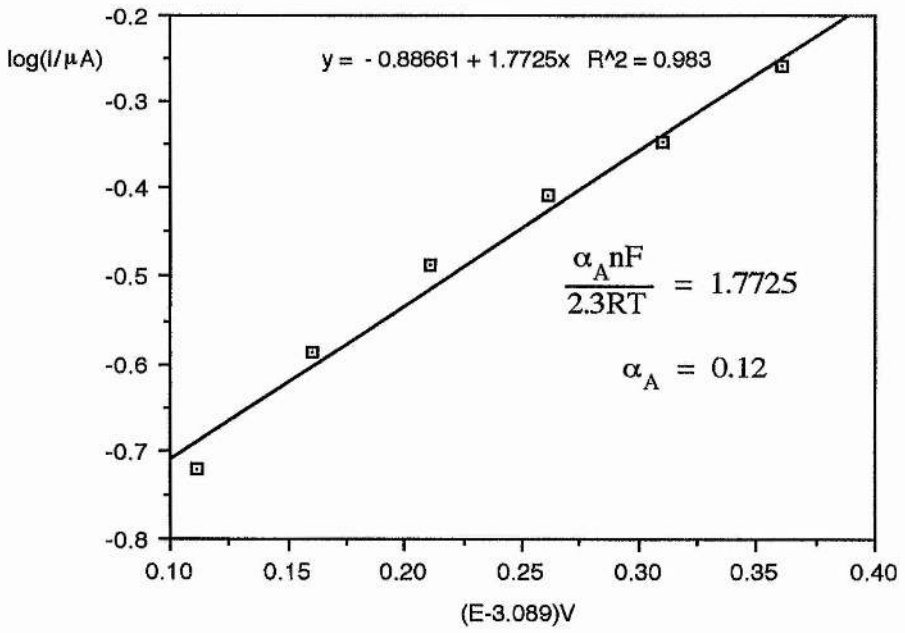

Figure 7-7 Determination of α_A

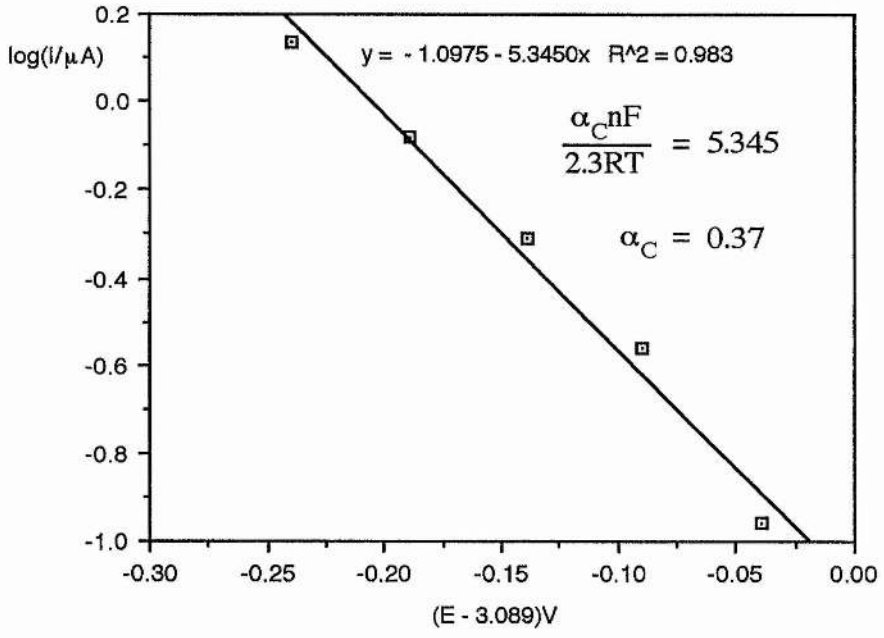

Figure 7-8 Determination of α_C

From figures 7-7 and 7-8 the exchange current density, (corrected for electrode area, A), was found to be given by $I_o = 0.12\ \mu A cm^{-2}$. The parameters determined for the cell in this section are summarised in table 7-2.

T (K)	348.4	α_A	0.12
A (cm^2)	0.885	α_C	0.37
$C_{Eu^{3+}}$ (mol cm^{-3})	1.882×10^{-4}	I_o ($\mu A\ cm^{-2}$)	0.12

Table 7-2 Parameters determined from cyclic voltammetry at 10 mVs^{-1} with $LiCF_3SO_3$ as supporting electrolyte

7.2.2 *Cyclic voltammetry with $LiClO_4$ as supporting electrolyte*

Cyclic voltammograms were obtained for a range of scan rates at 70.8°C of which the scan at 50 mVs^{-1} is illustrated in figure 7-9. The peaks were less well defined than those in the previous section and were therefore not subjected to a rigorous analysis.

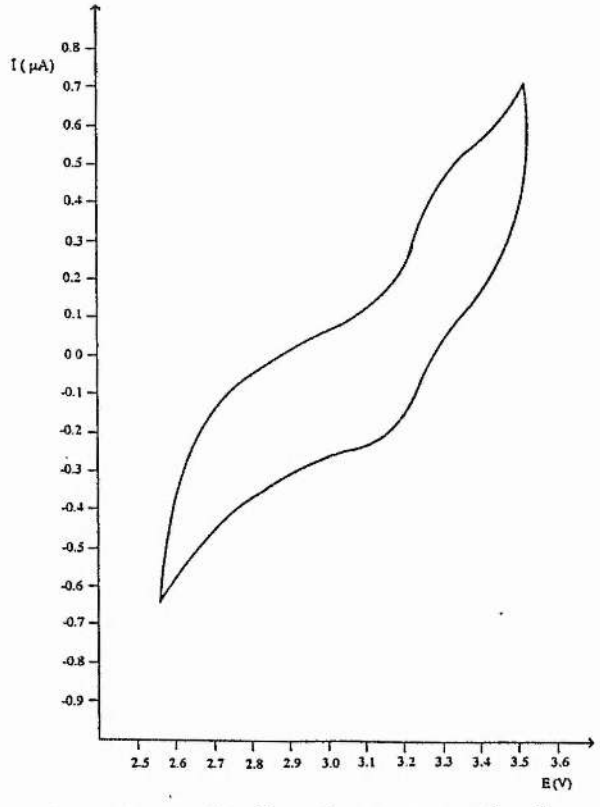

Figure 7- 9 Cyclic voltammogram for the cell

Ni / PEO $^{PEO_{10}LiClO_4}_{50Eu(CF_3SO_3)_2}$ / $PEO_{10}LiClO_4$ /Li / $PEO_{10}LiClO_4$ / Li

7.2.3 *Ac impedance measurements*

Ac impedance data was collected in the frequency range 100 kHz to 10 mHZ for the cell with $LiCF_3SO_3$ as supporting electrolyte (Ni / PEO $^{20\ LiCF_3SO_3}_{100Eu(CF_3SO_3)_2}$ / $PEO_{20}LiCF_3SO_3$ /Li / $PEO_{20}LiCF_3SO_3$ / Li). The data was collected with a dc bias of 2.98V [versus Li / $Li^+(PEO_{20}LiCF_3SO_3)$] corresponding to the potential midway between the oxidation and reduction peaks indicated by cyclic voltammetry. The data was used to construct the ac impedance plot illustrated in figure 7-10.

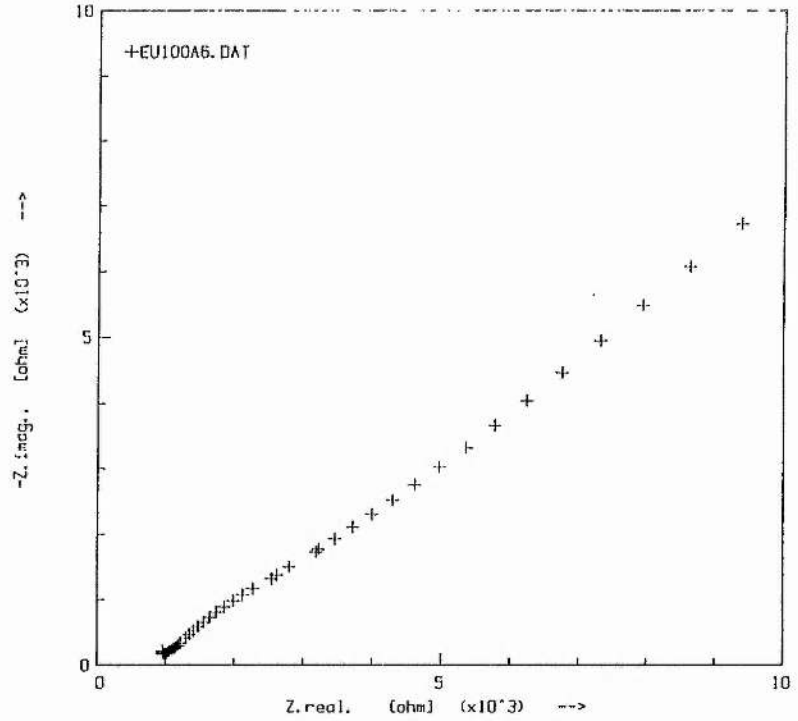

Figure 7-10 Ac impedance plot for the cell
Ni / PEO $^{20\ LiCF_3SO_3}_{100Eu(CF_3SO_3)_2}$ / $PEO_{20}LiCF_3SO_3$ /Li / $PEO_{20}LiCF_3SO_3$ / Li

It was not found to be possible to model the ac impedance data using any conventional equivalent circuit. The data in the intermediate / low frequency region of the plot fell onto a line at approximately 45° to the real axis. This was assigned to a Warburg impedance and suggested that the behaviour of the system was dominated by mass transport processes.

The data that fell in the region of the plot ascribed to the Warburg impedance were used to construct the graph illustrated in figure 7-11. In order to determine the diffusion coefficient by the method described in section 3.3.2, it was necessary to know the concentration of the diffusing species. It was assumed that the Warburg impedance could be ascribed to the diffusion of Eu^{3+} ions and that their concentration was simply equal to that of the dissolved salt. The validity and implications of this assumption are discussed in section 7.3. The parameters characterising the system are summarised in table 7-4.

T(K)	348.4	$R_i(\Omega)$	1.45×10^3
$C_{Eu^{3+}}$ (mol cm^{-3})	1.882×10^{-4}	$A(cm^2)$	0.885
$R_b(\Omega)$	1.01×10^3		

Table 7-4 Parameters characterising the ac impedance experiment

(Where $R_b(\Omega)$ was the bulk electrolyte resistance and $R_i(\Omega)$ was the high frequency intercept of the Warburg impedance with the real axis as illustrated in figure 3-10.)

The ac impedance data in the frequency range 10 to 80 Hz, which fell in the region of the plot ascribed to the Warburg impedance, were used to construct the graph illustrated in figure 7-11. The diffusion coefficient of the Eu^{3+} ions was determined by the method described in section 3.3.2.

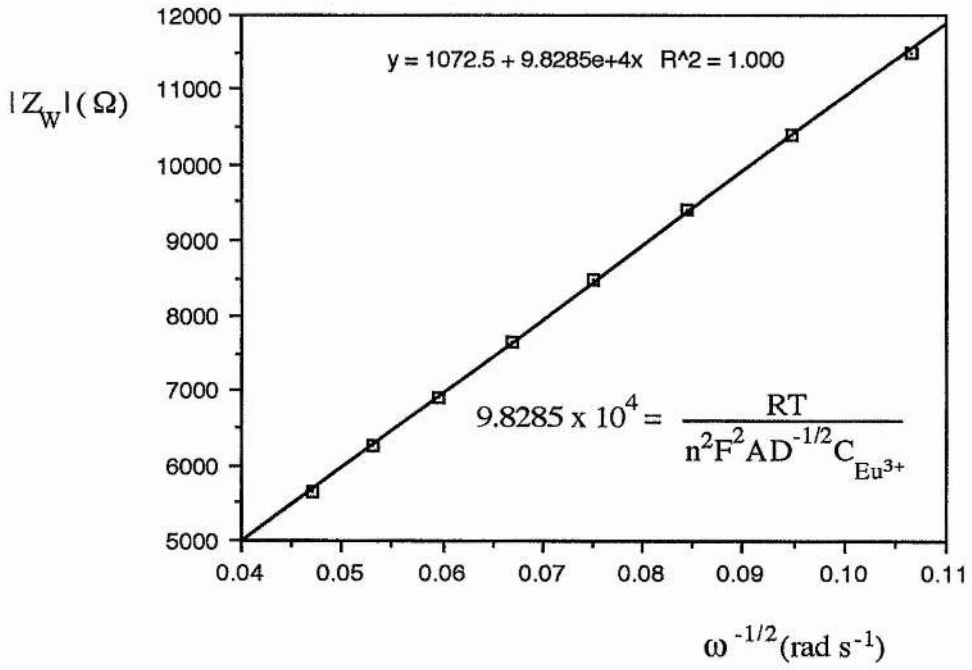

Figure 7-11 Calculation of the diffusion coefficient of the Eu^{3+} ions

The diffusion coefficient, D_{Eu3+}, for the europium ions in this system was determined as $D_{Eu3+} = 3.66 \times 10^{-16}\ cm^2 s^{-1}$.

7.3 Discussion

As mentioned in section 7.2.1, the positions of the peaks observed on the cyclic voltammograms were in the region expected for the Eu^{3+}/Eu^{2+} couple measured with respect to the Li^+/Li reference electrode. The most striking feature of the cyclic voltammograms however, was the reduced magnitude of the anodic peak (oxidation of Eu^{2+}) as compared with the cathodic peak (reduction of Eu^{3+}). This suggested that after electrochemical formation of Eu^{2+}, a following chemical step was removing it from the system. Further support of this hypothesis came from the fact that the ratio of the peak currents, (I_p^A / I_p^C), was less than unity and increased with increasing sweep

rate. i.e. at faster sweep rates, the anodic peak was larger due to the fact that more of the Eu^{2+} was oxidised before it had a chance to react. The reaction scheme for the system can be described as an ec mechanism in which an electron transfer step (e) is followed by a chemical step (c).

$$Eu^{3+} + e \rightleftharpoons Eu^{2+}$$
$$Eu^{2+} \rightleftharpoons C \qquad 7\text{-ii)}$$

Although it was not possible to postulate with any degree of certainty the nature of the chemical step, it was clear that the products, C, other than Eu^{3+} were not electrocative in the potential range of the experiment. The strongly reducing nature of the Eu^{2+} ion may enable it to scavenge any impurities present in the polymer or it may even have attacked the polymer itself.

In the light of the proposed ec mechanism for the reduction of the Eu^{3+} ions, the validity of determining the transfer coefficients from the Tafel plot figures 7-6 to 7-8 was called into question. At any given potential, the anodic current would be less than 'expected' due to the removal of Eu^{2+} from the system by the chemical step following electron transfer. For this reason, the slope of the Tafel plot, particularly in the region of high positive potentials would be reduced and the value of the transfer coefficient, α_A, determined in section 7.2.1 lower than the true value. For simple electron transfer reactions, the sum of the transfer coeficients , $\alpha_A + \alpha_C$, should equal unity. The departure from this behaviour in the Eu^{3+} / Eu^{2+} system was therefore a reflection of the complexity of the redox process.

The small exchange current density, 0.12 $\mu A cm^{-2}$, determined for the system (section 7.2.1), was indicative of slow kinetics for the electrode reaction. Optical microscopy experiments by Smith et al.[102] have suggested that $Eu(CF_3SO_3)_3$ forms a crystalline complex with PEO. In the temperature and composition range of the experiment however, it is unlikely that much of the Eu^{3+} present in the system was in

the form of a crystalline complex. It was probable that a PEO:$LiCF_3SO_3$ complex was present in significant proportions. This would have the affect of reducing the concentration of the supporting electrolyte in the amorphous regions of the polymer. The presence of these crystalline regions is likely to severely limit the segmental motion of the polymer chains in these amorphous regions, since some chains pass through both crystalline and amorphous regions.

In classical liquid electrolytes, the reorganisation of the primary solvation sphere upon electron transfer is often a relatively facile process for small solvent molecules. For the polymer electrolyte case, reorganisation of the polymer coordination sphere is likely to involve a significant amount of energy. This would give rise to a large activation energy for electron transfer and would thus severely limit the kinetics.

In section 7.2.3, it was assumed that the Warburg impedance dominating the ac impedance plot for the cell (Ni / PEO $^{20\ LiCF_3SO_3}_{100Eu(CF_3SO_3)_2}$ / $PEO_{20}LiCF_3SO_3$ /Li / $PEO_{20}LiCF_3SO_3$ / Li) could be ascribed to the diffusion of Eu^{3+} ions. It is likely however that several diffusional processes occur in the system :-

i) diffusion of Eu^{3+} ions towards and away from the electrode,

ii) diffusion of Eu^{2+} ions towards and away from the electrode,

iii) diffusion of the reactants involved in the chemical step towards the Eu^{2+} ions prior to the reaction and

iv) diffusion of the products of the chemical reaction away.

The behaviour of the system was clearly dominated by an extremely slow diffusional process. Of the first two steps, step i) is likely to be the slowest since the stronger interaction between the polymer and the hard Eu^{3+} ions is likely to render them more immobile than the less highly charged Eu^{2+} ions. If step iii) was the rate limiting step, then clearly the cyclic voltammograms would have exhibited more reversible behaviour than was illustrated in figure 7-3. Despite the unknown nature of the chemical step, it is likely that Eu^{3+} will be one of the products. This step will therefore

involve diffusion of Eu^{3+} ions as in step i). In conclusion, it can be seen that it is likely that the diffusional feature of the impedance plot can indeed be ascribed to the motion of Eu^{3+} ions and that the diffusion coefficient determined was indeed that for Eu^{3+}.

The diffusion coefficient determined appeared to indicate that mass transport of Eu^{3+} through the polymer was extremely slow. This is not unexpected due to the hard acid-hard base interaction between the Eu^{3+} ions and the ether oxygen atoms on the polymer. Strong coordination of the ion by the polymer would be expected to severely restrict the mobility of the ion through the polymer.

The presence of crystalline regions in the polymer would also inhibit the motion of ions by restricting the segmental motion of the polymer chains in the amorphous regions. Furthermore, the mean free path of the ions to the electrode would be greatly increased due to the tortuous routes taken to avoid these crystalline regions. These factors would all serve to reduce the determined value of the diffusion coefficient compared to the 'true' value in a completely amorphous system.

De Kreuk et al[103] determined $D_{Eu3+} = 8.5 \times 10^{-6}\ cm^2s^{-1}$ for a 10mM solution in 1M KCl. Despite the vastly different experimental conditions, the immobility of the Eu^{3+} ions in the PEO system, where $D_{Eu3+} \approx 3.66 \times 10^{-16}\ cm^2s^{-1}$ has been clearly demonstrated.

CHAPTER 8

THE PEO : COBALT THIOCYANATE SYSTEM

The aim of the investigation was to determine the conductivity of the polymer electrolyte system $PEO_xCo(SCN)_2$ as a function of temperature and composition and to correlate these findings with the thermal and structural data obtained by DSC and X-ray diffraction techniques.

8.1 Experimental

8.1.1 *Sample preparation*

Cryoground mixtures of PEO and cobalt thiocyanate were prepared for a range of compositions $PEO_xCo(SCN)_2$ (x = 4.0, 8.2, 12.1, 20.3, 48.7 and 210.0). Hot pressed discs were prepared for each composition as described in section 4.1.2.

8.1.2 *Differential Scanning Calorimetry*

DSC analysis was used to examine the thermal characteristics of the hot pressed films. Samples were sealed into DSC pans in an argon filled drybox and subjected to 0 - 250 °C heating cycles at a rate of 20 °C per minute. Fresh samples were subjected to -50 to +50 °C heating cycles performed at 20 °C per minute in order to determine the glass transition temperatures.

8.1.3 *Powder X-ray diffraction*

Due to the difficulty in packing the Lindemann tubes sufficiently, it was necessary to record x-ray diffraction data from hot pressed samples which were sandwiched between transparent x-ray tape to avoid ingress of moisture.

8.1.4 *Conductivity measurements*

The conductivities of polymer electrolyte films sandwiched between stainless steel electrodes were determined by ac impedance techniques in the temperature range 40 - 110 °C.

8.1.5 *UV-Visible Spectroscopy*

A sample of hot pressed $PEO_{210}Co(SCN)_2$ was sandwiched between quartz plates in a sealed cell holder. An absorption spectrum was obtained in the wavelength range 400 - 800 nm (12500 - 25000 cm^{-1}).

8.2 Results

8.2.1 *Differential Scanning Calorimetry*

Typical DSC traces obtained in the experiment are shown in figures 8-1 and 8-2 and the data summarised in table 8-1.

x	Mass fraction of salt	Tg(°C)	Peak 1 Onset (°C)	Peak 1 Position (°C)
4.0	0.499	24.4	No peak	No peak
8.2	0.327	8.5	51.4	60.4
12.1	0.247	5.7	54.2	64.3
20.3	0.164	-	53.3	68.2
48.7	0.076	3.9	61.1	75.2
∞	0.000	-60.0	62.5	80.5
∞	0.000	-60.0	68.9	77.2

Table 8-1 Thermal events observed by DSC in the $PEO_xCo(SCN)_2$ system

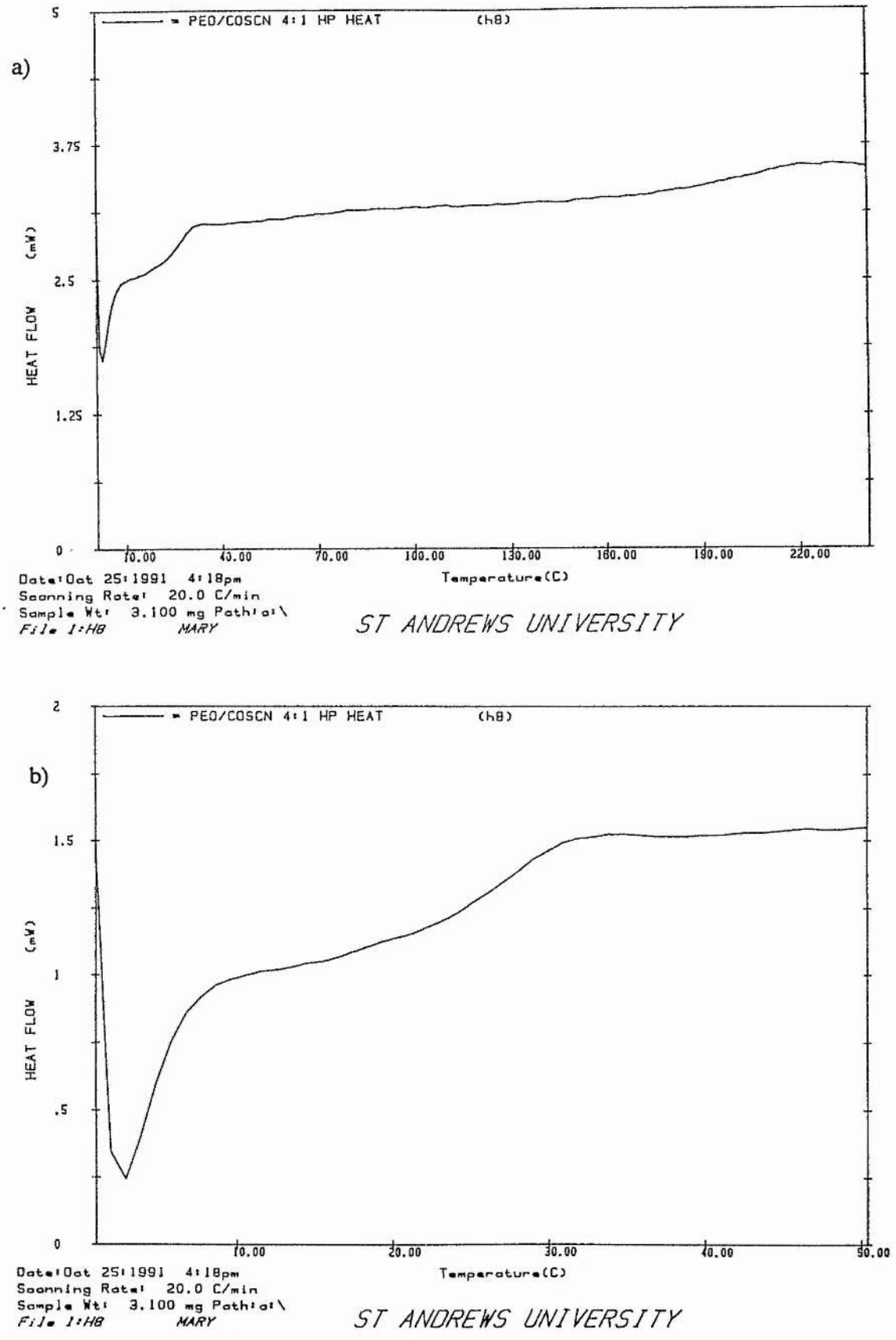

Figure 8-1 DSC spectra for $PEO_4Co(SCN)_2$

a) 0 to 250°C, b) -50 to 50°C

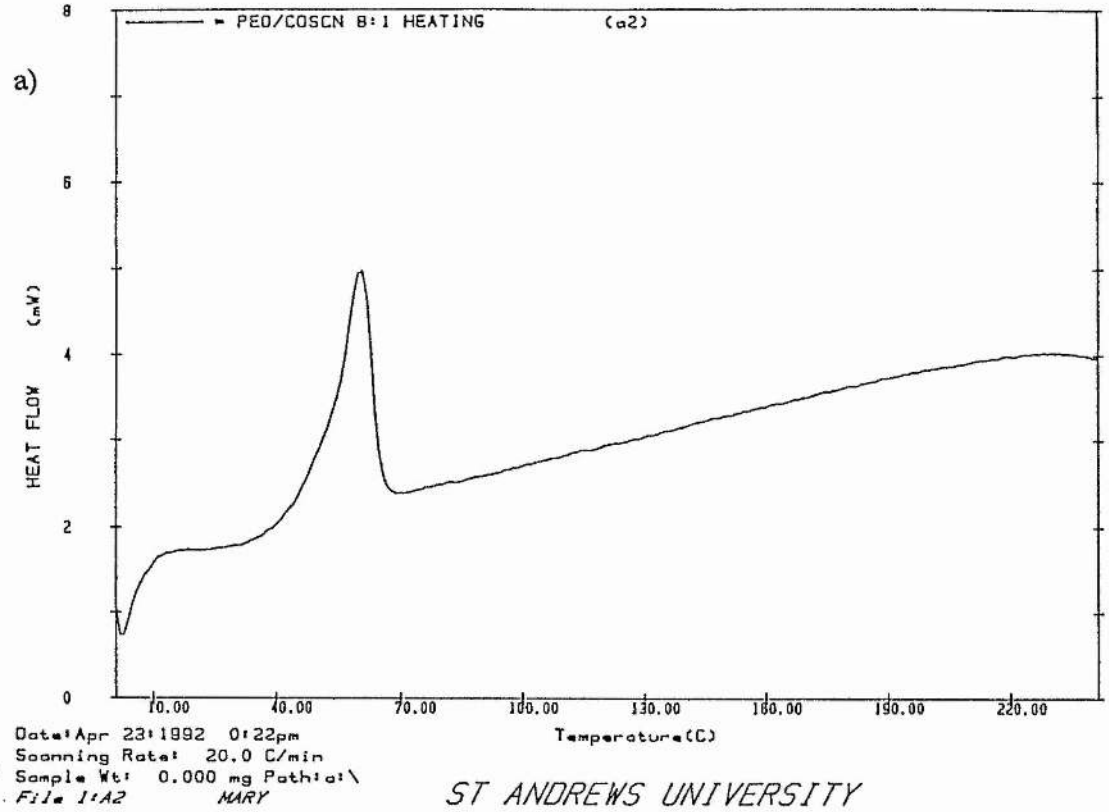

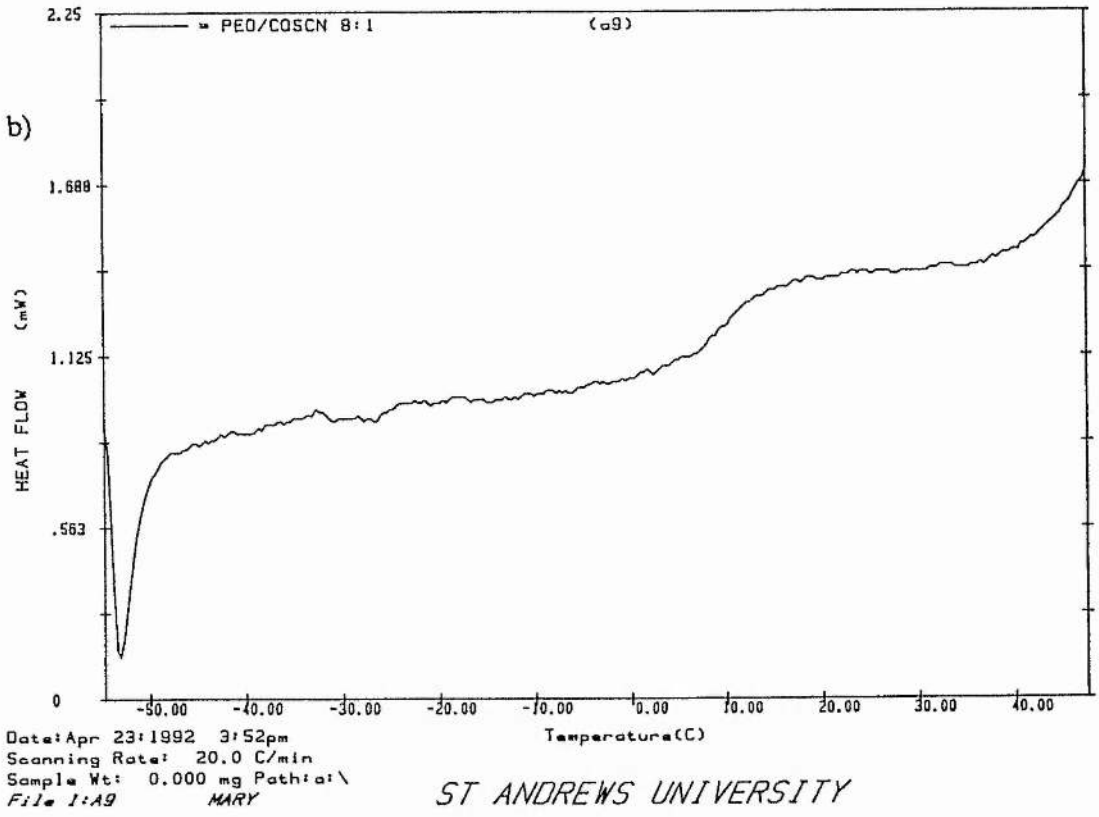

Figure 8-2 DSC spectra for $PEO_8Co(SCN)_2$
a) 0 to 250°C, b) -50 to 50°C

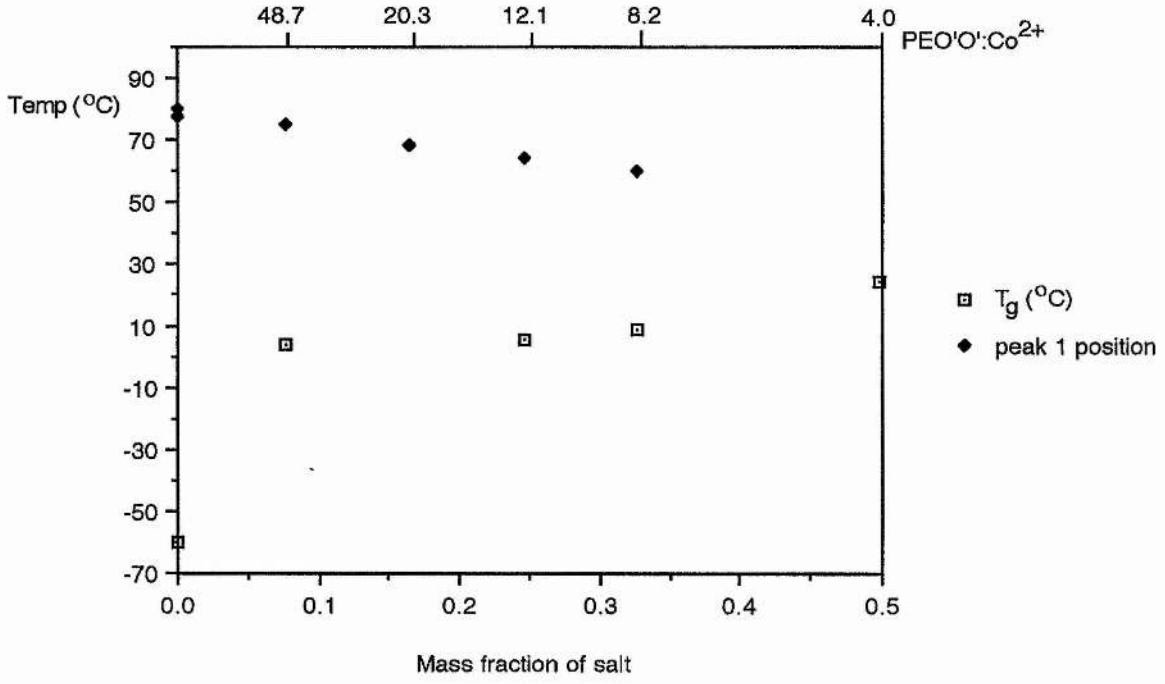

Figure 8-3 Thermal events observed for the $PEO_xCo(SCN)_2$ system

It was observed that the glass transition temperature (Tg) increased with increasing salt concentration. The thermal event in the region of 70 °C was ascribed to the melting of uncomplexed PEO.

8.2.2 *X-ray diffraction*

Some typical X-ray diffraction patterns recorded for the system are illustrated in figure 8-4. Crystalline PEO was observed for all compositions except $PEO_4Co(SCN)_2$. It was apparent, however, that the samples became increasingly amorphous with increasing salt content. Apart from the minute traces of cobalt thiocyanate observed in the pattern for $PEO_4Co(SCN)_2$, this composition was principally amorphous. There was no evidence for the presence of a polymer-salt crystalline complex.

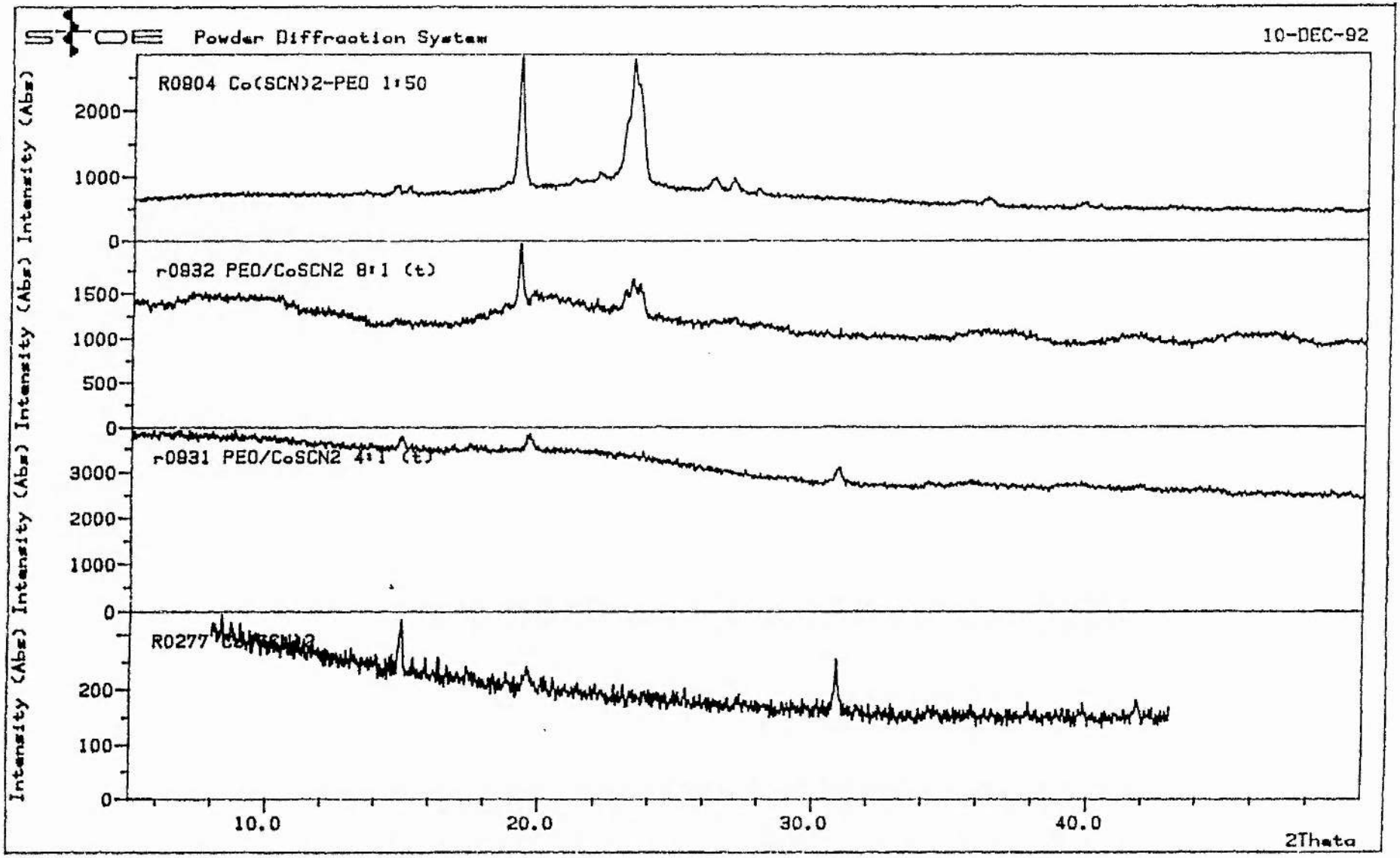

Figure 8-4 Powder x-ray diffraction patterns for the PEOxCo(SCN)$_2$ system, a) $PEO_{50}Co(SCN)_2$, b) $PEO_8Co(SCN)_2$ c) PEO, Co(SCN)$_2$ and d) Co(SCN)$_2$

8.2.3 *Conductivity measurements*

The variation of conductivity with temperature is illustrated for each composition in figures 8-5 - 8-10 together with a typical ac impedance plot. For all compositions containing uncomplexed PEO, a 'knee' was observed in the Arrhenius plots in the region of 60 °C. This corresponded to the melting temperature of uncomplexed PEO and concommitant increase in the amorphous component of the polymer electrolyte primarily responsible for ionic conductivity. The Arrhenius plots for these compositions above 60°C appeared to be linear.

Usually, amorphous polymers have curved Arrhenius plots exhibiting VTF behaviour in this temperature region. The observed linearity may be the result of the restricted temperature range over which the conductivity data could be collected. Alternatively, the linearity may have been a genuine feature of the system. This would be the case if, as is likely, an equilibrium exists between free ions and clusters. Prior to motion through the amorphous region of the polymer, it would be necessary for the ion to dissociate from the cluster. The associated enthalpy change would ensure that ionic conductivity was an activated process.

An activation energy was extracted from the data for these compositions above 60°C. This was observed to increase with increasing salt content as shown in figure 8-12. $PEO_4Co(SCN)_2$ exhibited VTF behaviour [$\sigma = A \exp(-B/T-T_0)$] over the whole temperature range where $A = -1.25$, $B = 1602\ K^{-1}$ and $T_0 = -25.9$ °C.

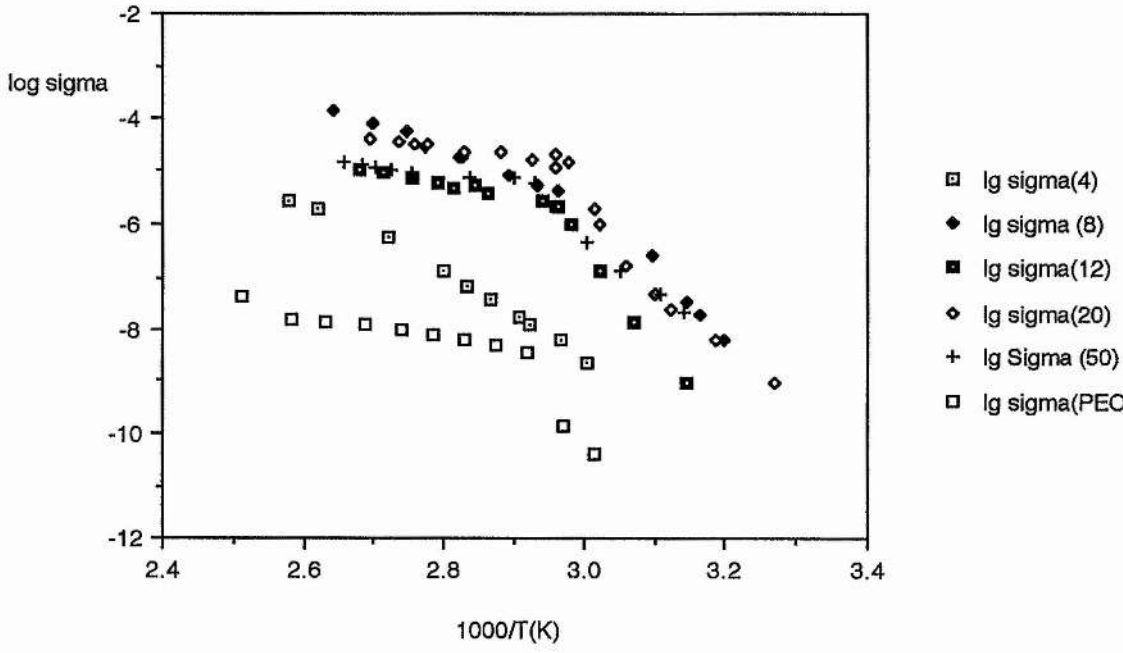

Figure 8 - 5 A comparison of the conductivities of the $PEO_xCo(SCN)_2$ system

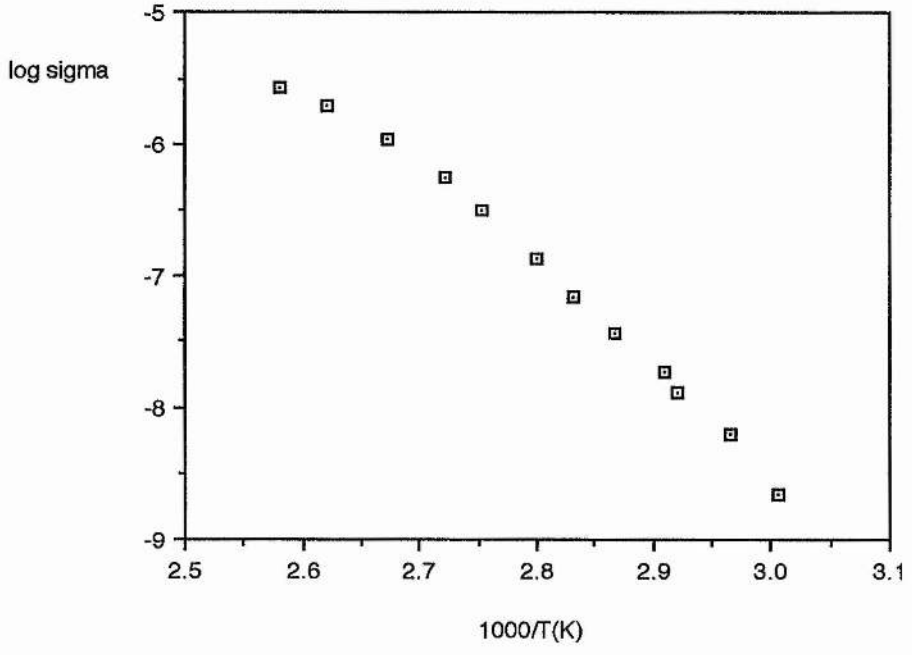

Figure 8-6 Conductivity of $PEO_4Co(SCN)_2$

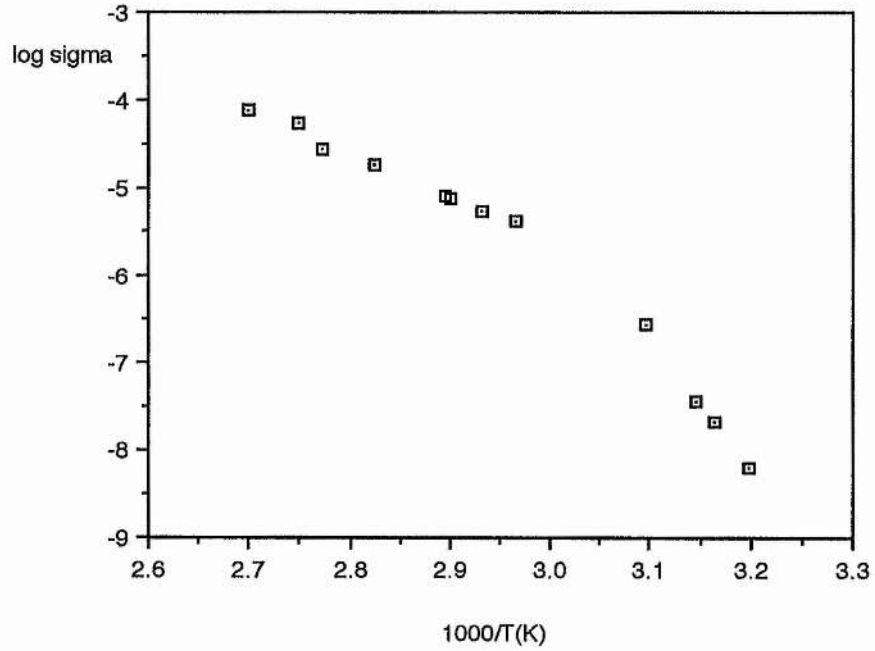

Figure 8-7 Conductivity of $PEO_8Co(SCN)_2$

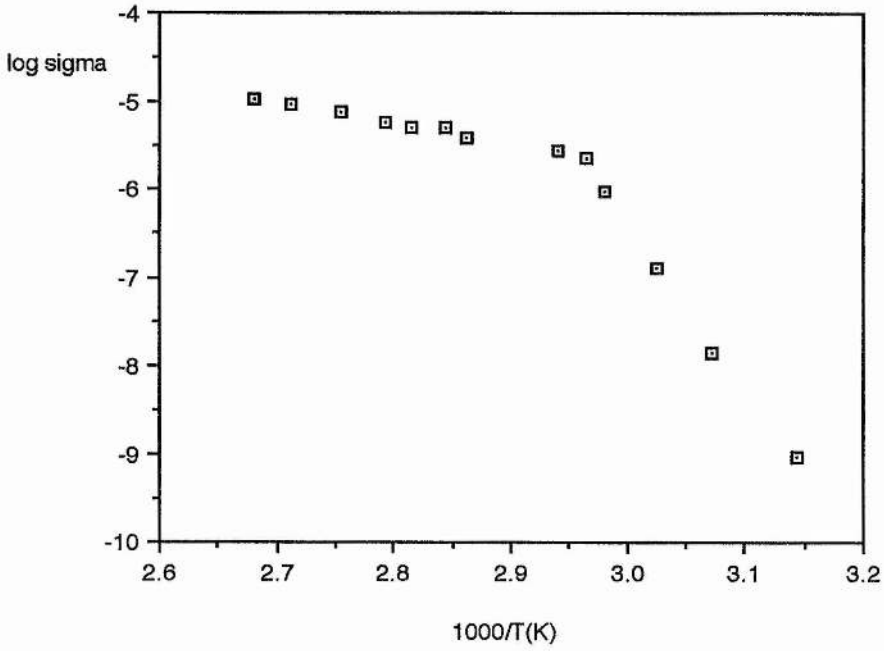

Figure 8-8 Conductivity of $PEO_{12}Co(SCN)_2$

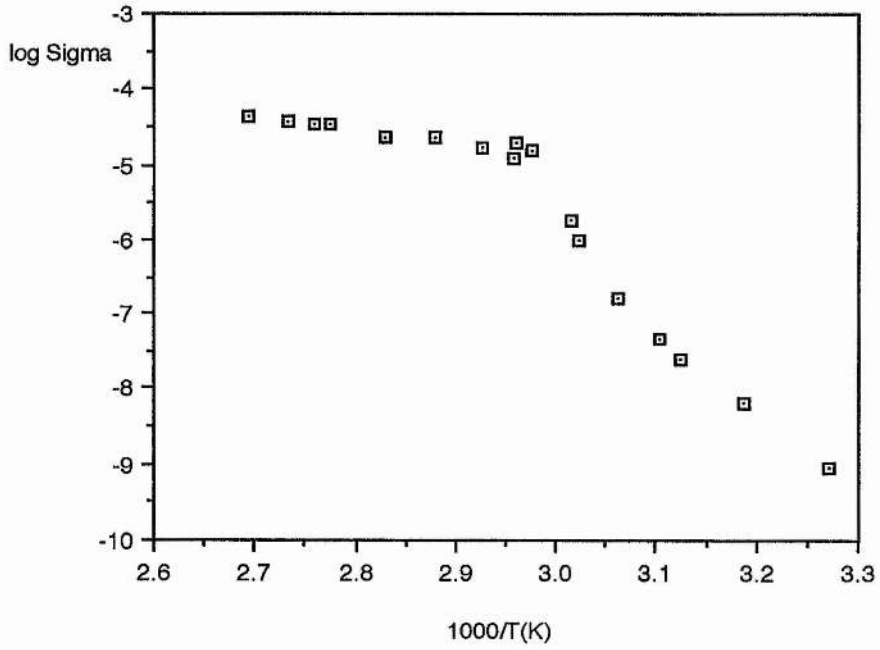

Figure 8-9 Conductivity of $PEO_{20}Co(SCN)_2$

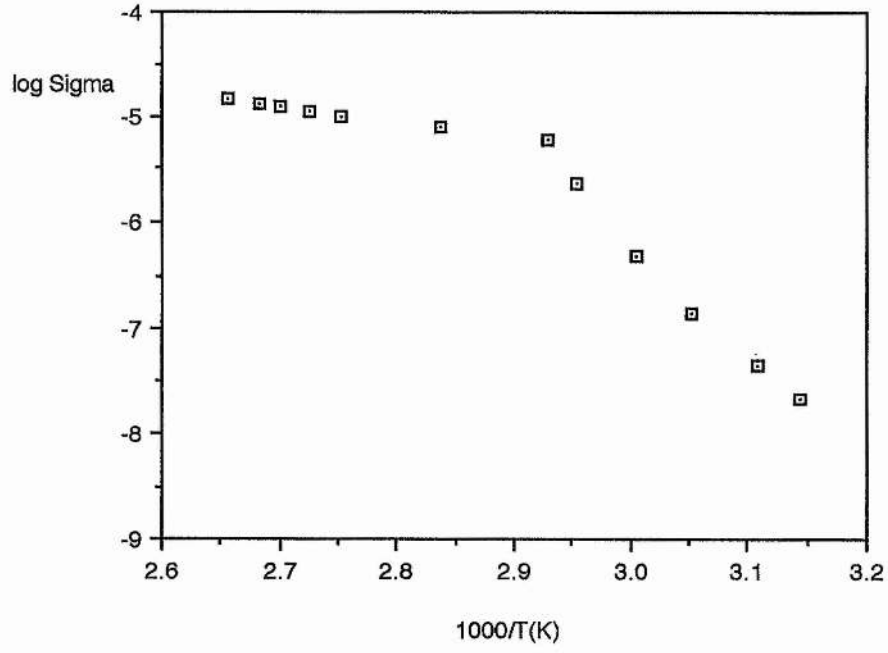

Figure 8 - 10 Conductivity of $PEO_{50}Co(SCN)_2$

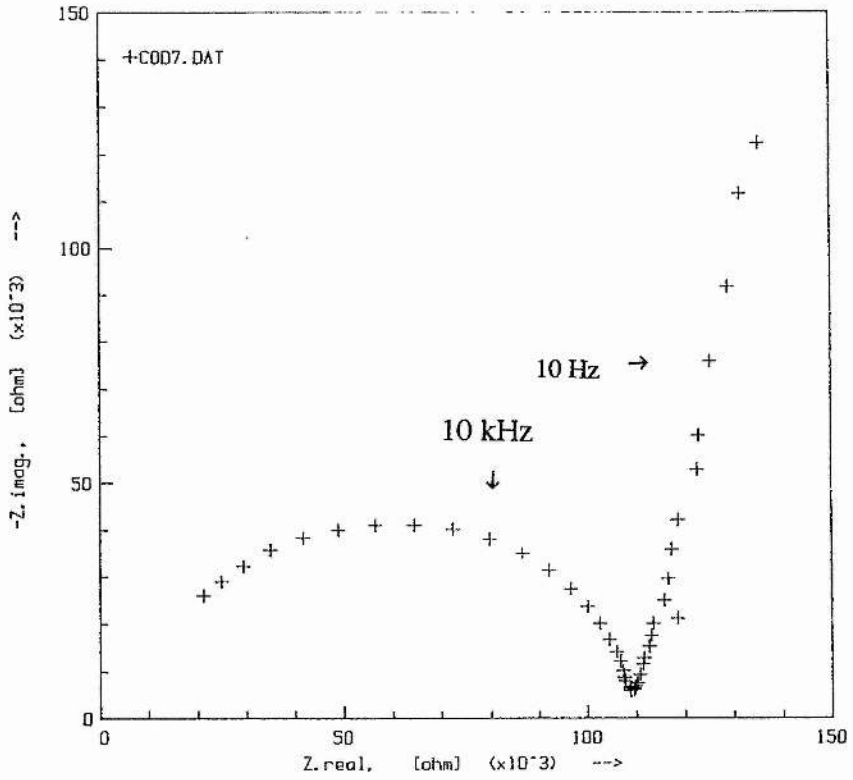

Figure 8 -11 Ac impedance plot for $PEO_4Co(SCN)_2$ at 90.4°C

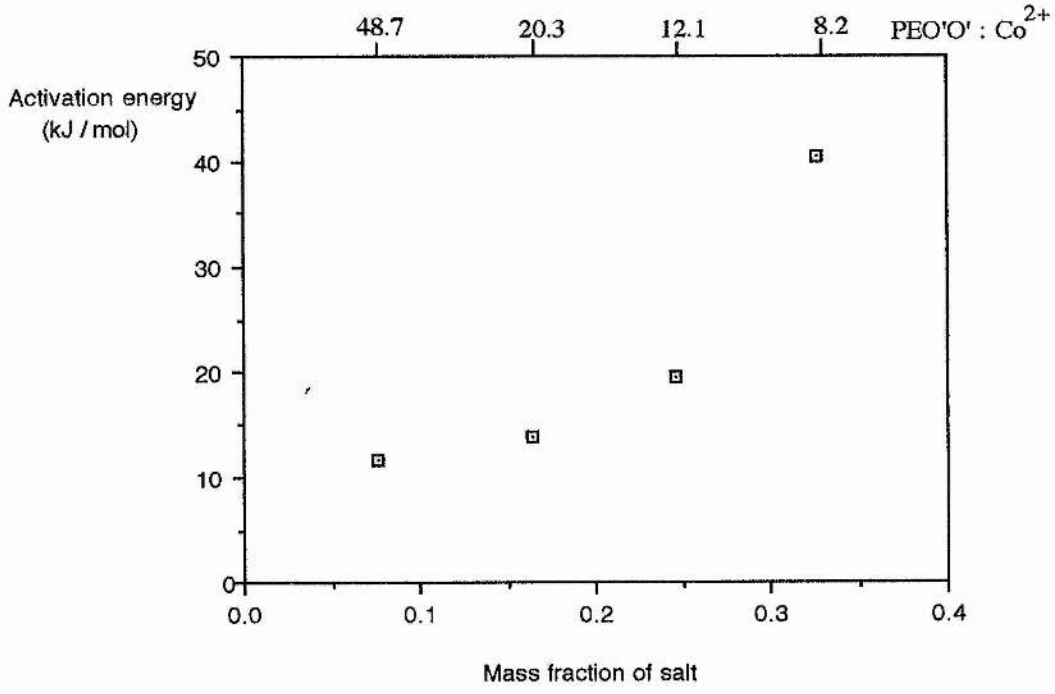

Figure 8-12 Activation energies for conduction above 60°C for the $PEO_xCo(SCN)_2$ system

8.2.4 *UV-Visible Spectroscopy*

The absorption spectrum obtained for $PEO_{210}Co(SCN)_2$ is shown in figure 8-13. It was clear that the intense blue colour of the hot pressed polymers could be ascribed to absorption in the region 550 - 700nm.

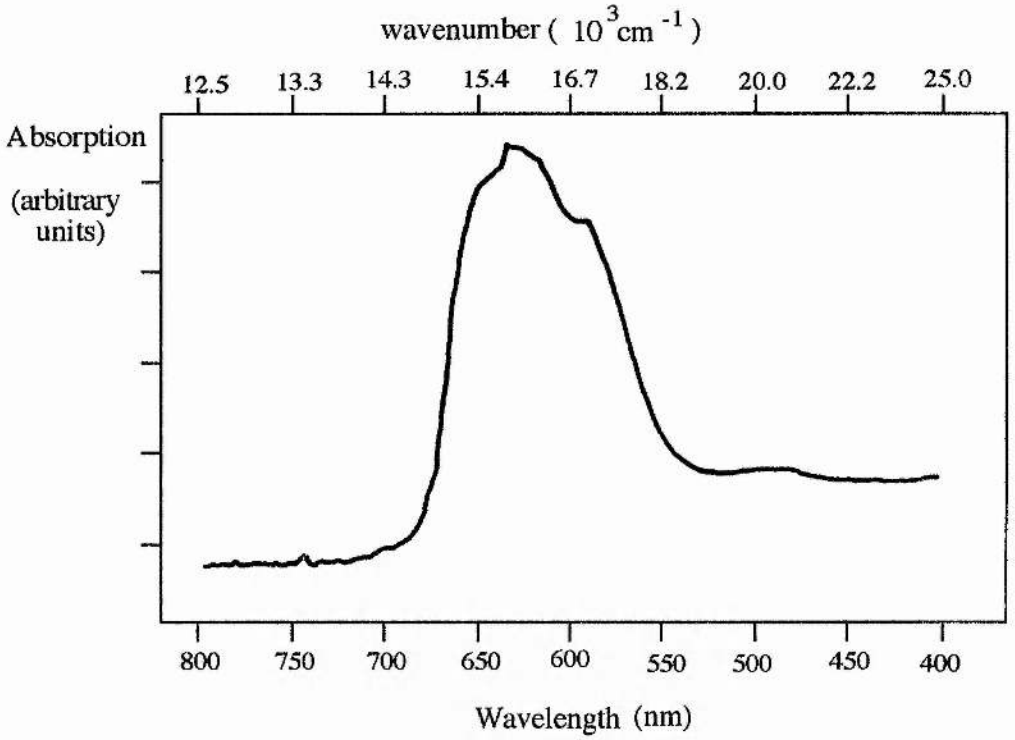

Figure 8 - 13 UV-Visible spectrum for $PEO_{210}Co(SCN)_2$

8.3 Discussion

The most common coordination geometries of d^7 ions, of which Co^{2+} is an example, are the octahedral and tetrahedral configurations. As a *general* rule, the octahedral complexes of high spin d^7 Co(II) are pink whereas the tetrahedral complexes are blue. Assignment of coordination geometries on the basis of colour alone must be treated with caution since exceptions to the rule have been observed. This is illustrated by the spectra for Co^{2+} in an octahedral (anhydrous $CoCl_2$) and tetrahedral environment ($CoCl_4^{2-}$) in figures 8-14 and 8-15 respectively, which show that both materials are blue. The Tanabe-Sugano diagram for d^7 ions is illustrated in figure 8-16.

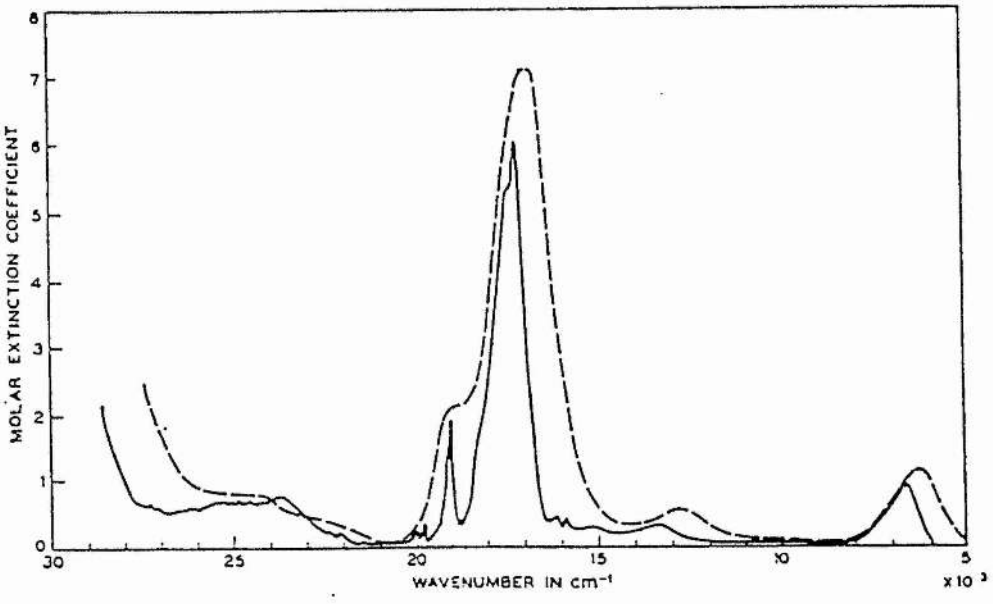

Figure 8-14 UV-visible spectrum for anhydrous $CoCl_2$[104]
(Broken curve = room temperature spectrum, solid curve = spectrum at 20K)

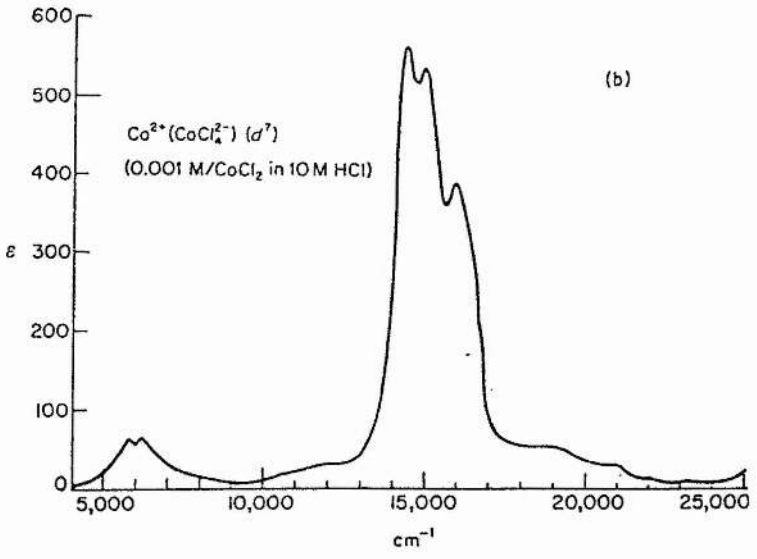

Figure 8-15 UV-visible spectrum for the $CoCl_4^{2-}$ complex[105]

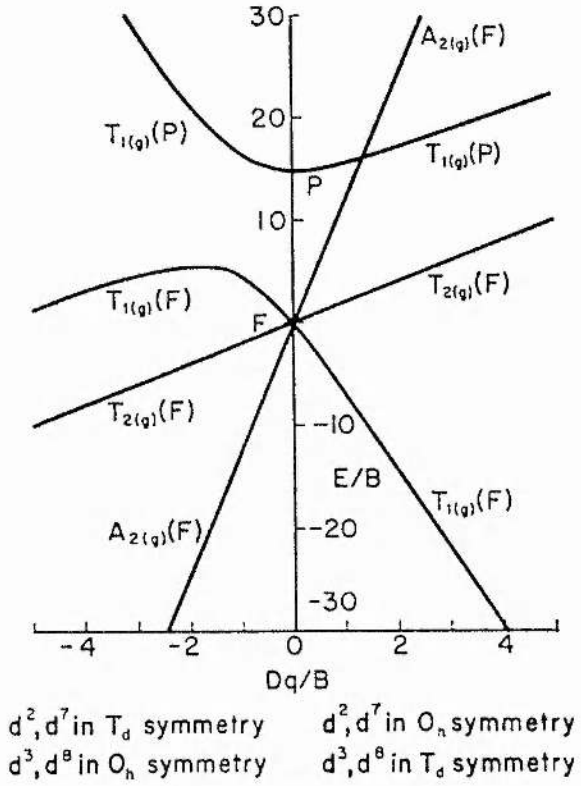

Figure 8-16 Tanabe-Sugano diagram for d^7 ions[105]

For tetrahedral complexes, three bands are expected in the spectrum.

ν_1	$^4A_2(F)$	→	$^4T_2(F)$	(I.R. region)
ν_2	$^4A_2(F)$	→	$^4T_1(F)$	(near I.R. region)
ν_3	$^4A_2(F)$	→	$^4T_1(P)$	(visible region)

[In the spectrum for the $CoCl_4^{2-}$complex, ν_1= 3500 cm^{-1}, ν_2 = 5800 cm^{-1} and ν_3 = 15000 cm^{-1}]

The envelopes of the bands are often complex. In particular, the visible band may be complicated by transitions to spin-forbidden doublet states. This fine structure is apparent on the spectrum for the $CoCl_4^{2-}$ complex.

For octahedral complexes, there are in general three bands observed in the UV-visible spectrum.

ν_1	$^4T_{1g}(F)$	→	$^4T_{2g}(F)$	(I.R. region)
ν_2	$^4T_{1g}(F)$	→	$^4A_{2g}(F)$	(visible region)
ν_3	$^4T_{1g}(F)$	→	$^4T_{1g}(P)$	(visible region)

[In the spectrum $CoCl_2$ $\nu_1 = 6600\ cm^{-1}$, $\nu_2 = 13300\ cm^{-1}$ and $\nu_3 = 17250\ cm^{-1}$]
The transition to the $^4A_{2g}(F)$ state is usually very weak, often appearing as a shoulder on the ν_3 band. Again, the bands exhibit multiple structure, mainly as a result of transitions to the spin forbidden ^2G and ^2H states.

It can be seen that on the basis of the discussion so far, it is difficult to say unequivocally whether the coordination of the Co^{2+} ion in the polymer is octahedral or tetrahedral. The presence of the shoulder on the high frequency side of the visible band does however favour the suggestion of tetrahedral coordination. Similar work by Huq et al[106] for $PEO_{16}CoBr_2$ indicated that the cobalt ion was tetrahedrally coordinated in the 'dry' polymer. (There was a transition to octahedral coordination upon exposure to moisture due to the formation of the $[Co(H_2O)_6]^{2+}$ species.) A precedent has thus been set for the tetrahedral coordination of Co^{2+} in PEO based polymer electrolytes. In general the association of pink and blue with the octahedral and tetrahedral coordination geometries is observed to hold for oxygen environments. If the Co^{2+} ions are tetrahedrally coordinated, there is the possibility of deviation from tetrahedral symmetry due to the presence of both SCN^- and ether oxygen atoms in the primary coordination sphere. Lever[107] has commented that the pseudo-tetrahedral complexes, CoL_3X and CoL_2X_2 have wider band widths than the 1500 - 2500 cm^{-1} observed for CoL_4 species. The band width of the peak observed in the visible region of the $PEO_{210}Co(SCN)_2$ spectrum was of the order of 4000 cm^{-1} which could be indicative of low symmetry affects.

In conclusion, the spectrum suggests that Co^{2+} is tetrahedrally coordinated in the polymer. It is tentatively postulated that the primary coordination sphere contains both SCN^- and ether oxygen atoms although more data over a wider frequency range would need to be collected to confirm this hypothesis.

It is clear from the DSC data of figure 8-3 that the glass transition temperature of the system increased with increasing salt content. This would account for the concomitant increase in the activation energy for ionic conduction. The higher the Tg, the slower the segmental motion of the polymer at a given temperature and therefore the slower the rate of redistribution of free volume in the system. In terms of DBP theory, the the renewal time for the bonds to change from closed to open configurations would be longer, thus, motion of ions through the system becomes increasingly more difficult with the rise in salt content.

The elevation of the glass transition temperature of polyethers by the incorporation of metal salts is a well established phenomenon.[108, 109, 110] This has been ascribed to the reduced segmental motion of the polymer that accompanies coordination of the cation by the lone pairs of electrons on the ether oxygen atoms. In cases where the cation is coordinated by more than one ether oxygen, the coordination may be either intra-molecular or inter-molecular. In the latter case, the cations act to form (sometimes transient) crosslinks between the polymer chains. The relative importance of the two types of coordination depends on a variety of factors including:-

i) The size of the chelate ring that would result from an intra-molecular interaction.

ii) The ability of the polymer to adopt the conformations required to maximise polymer - salt interaction.

An increase in the salt concentration however results in an increase in the concentration of binding sites involved in coordination. This gives rise to a concommitant increase in the 'stiffness' and Tg of the polymer which is irrespective of the mode of coordination. The variation of Tg with composition often exhibits sigmoidal behaviour[110] as illustrated in figure 8-17.

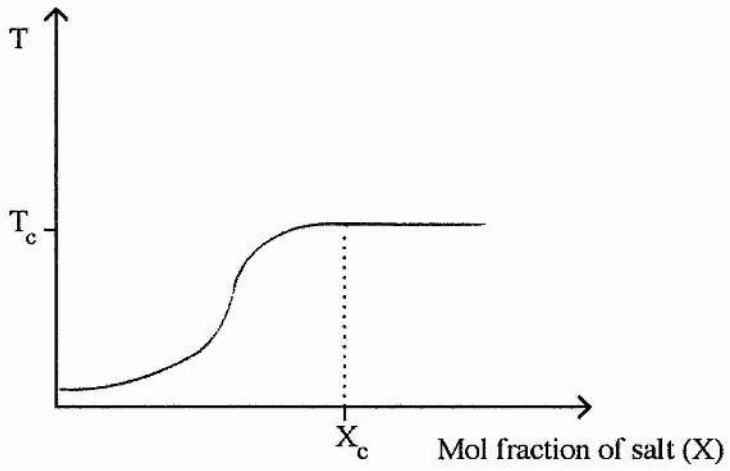

Figure 8-17 Sigmoidal variation of Tg with mol fraction of salt

The Tg rises with increasing salt concentration up to a certain limit (X_c,T_c),whereupon a plateau is reached. This corresponds to the composition at which the polymer becomes saturated with the salt i.e. the maximum number of binding sites on the polymer are occupied. At compositions greater than the critical composition, the 'excess' salt acts as a filler rather than coordinating with the polymer. It therefore has little affect on the Tg.

The presence of $Co(SCN)_2$ dissolved in the polymer had the affect of increasing the Tg by between 60 - 90°C over that of the pure polymer in the composition range investigated. It appeared as if a plateau in the Tg had been reached for compositions in the region $PEO_xCo(SCN)_2$ where $12 < x < 50$, since there was very little change in Tg in this range. Indeed, the presence of salt in the x-ray diffraction pattern for $PEO_4Co(SCN)_2$ suggested that the saturation limit of the salt in the polymer had been

reached by this composition. The further increase in Tg between the x = 8.2 and x = 4 compositions was therefore a deviation from the sigmoidal behaviour of the systems of James et al[110]. It should however be noted that the systems investigated by him were amorphous. The deviation could therefore result from complications due to the presence of crystalline PEO in the system at low salt concentrations.

The data appears to indicate that at the highest salt concentrations, segmental motion of the polymer is even more restricted. It may be the case that in this composition range, the anions take part in forming crosslinks between neighbouring polymer chains via bridging cobalt ions. This would serve to further 'stiffen' the system and could be acompanied by a change in the coordination geometry of the cobalt ions. The contribution of anions to crosslink formation is not without precedent as has been reported by Cameron and Ingram[111].

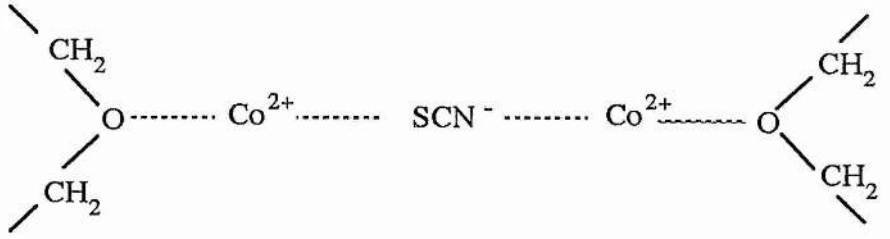

Figure 8-18 Contribution of anions to crosslinking

To investigate this hypothesis, it would be necessary to obtain UV-visible spectra for a variety of compositions. In particular, the fine structure of the bands would need to be carefully examined to obtain evidence for splitting due to low symmetry effects.

In light of the grossly elevated glass transition temperatures for the $PEO_xCo(SCN)_2$ system, It is likely that the absence of a crystalline $PEO:Co(SCN)_2$ complex is at least in part due to extremely slow crystallisation kinetics. The hot pressed films were left to crystallise at room temperature which even for the $PEO_{48.7}Co(SCN)_2$ film was only

15 - 20 °C above the Tg. The extremely slow polymer chain segmental motion at this temperature would ensure that long range order in the system would take an infinitely long time to achieve.

The ionic radius of the Co^{2+} ion is small enough, (0.78A), to be accomodated inside the polymer helix (see section 1.4). It is possible that the high charge density of the ion causes significant distortion of the helix. This may serve to inhibit its ability to pack in a regular manner and thus prevent crystallisation. Alternatively, the resulting distortion of the helix may make insertion of cations inside it an energetically unfavourable process. It may thus be the case that the cation forms random inter-molecular crosslinks and in such a situation, an amorphous material would be expected. As mentioned above, it is possible that the anions may also be involved in crosslinking which would give rise to a lower coordination symmetry for the Co^{2+} ion than if it were coordinated by the polymer alone.

CHAPTER 9

SUMMARY

The aim of the present chapter is to bring together the results of the different systems studied in this work in an attempt to see and understand any underlying trends of behaviour for PEO based systems containing multivalent ions.

The conductivities for the systems studied were observed to be of similar magnitudes for similar compositions. This is illustrated in figure 9-1 for films with an ether oxygen : cation composition of 12:1.

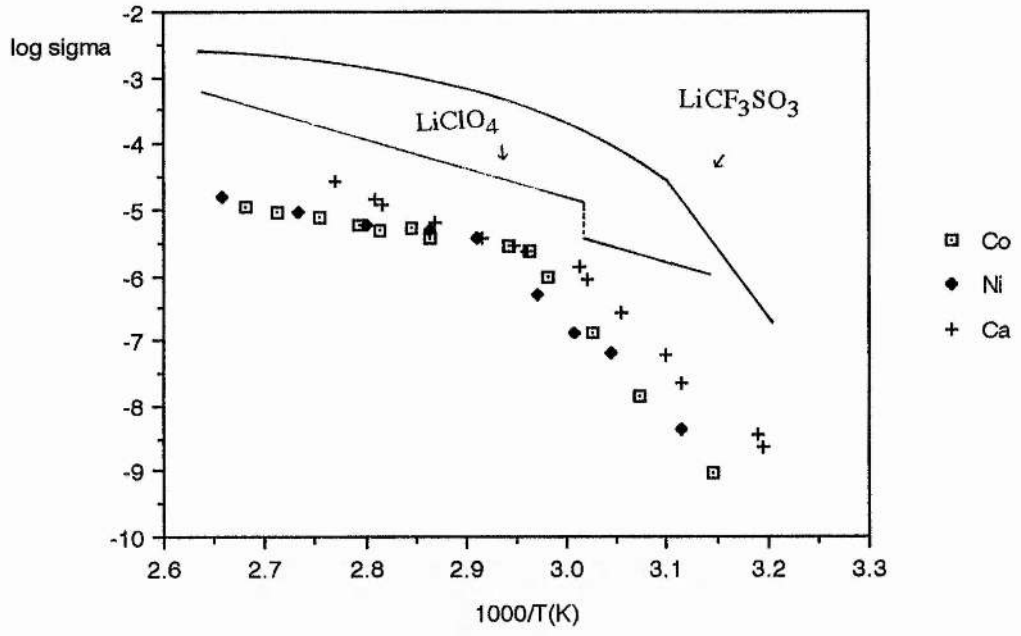

Figure 9-1 Comparison of conductivities of monovalent and divalent polymer electrolyte systems (PEO O :M = 12:1)

For all systems, the conductivities were significantly enhanced compared to the pure hot pressed polymer. They were however less enhanced than for systems containing monovalent ions. The conductivities of the PEO_8LiClO_4 and $PEO_8LiCF_3SO_3$

electrolytes shown in figure 9-1 were obtained for solvent cast polymer electrolyte films. Gray[10] has commented that films prepared by the hot pressing method often have conductivities enhanced by a factor of 10 over their solvent cast counterparts.

Evidence obtained from the $PEO_xEu(CF_3SO_3)_3$ and PEO_xNiI_2 systems indicates that the Eu(III) and Ni(II) containing species are highly immobile. This is not unexpected in light of the extremely hard nature of the cations. All of the multivalent ions studied are likely to have been tightly bound by the polymer and it would have been possible to predict that these systems would be principally anionic conductors. This was born out by the extremely slow transport of nickel containing species in the PEO_xNiI_2 system ($F_+<0.1$). The effective diffusion coefficients determined indicated that the Eu^{3+} containing species were even more immobile than the Ni(II) containing species in the polymer electrolyte ($D_{EuIII} = 3.66 \times 10^{-16}$ cm^2s^{-1}, $D_{Ni(II)} \leq 1.8 \times 10^{-11} cm^2s^{-1}$. This is to be expected in light of the fact that the former species have the greatest charge density.

The motion of ions through the polymer is facilitated by a high degree of segmental chain motion. This is greater at temperatures far in excess of the glass transition temperature. Factors affecting the Tg such as the degree of crosslinking in the polymer, will therefore affect the ionic conductivities. The glass transition temperatures for polymer films containing $Co(SCN)_2$ were grossly elevated compared to the pure polymer. It was postulated that there may have been an anionic contribution to crosslinking at high salt concentrations which may have been accompanied by an increase in the coordination number of the central cation. The contribution of anions to crosslinking in the polymer is not without precedent[111].

Of the polymer electrolyte systems studied in this work, the PEO:$Co(SCN)_2$ system was the only one in which there was not formation of a crystalline PEO:salt complex. The phenomenon was ascribed to the extremely slow crystallisation kinetics resulting from the high glass transition temperatures of the system. This appears to be a feature of polymer electrolyte systems containing Co^{2+} ions. Huq et al[4] reported the amorphous nature of the PEO_8CoBr_2 as compared to the analogously prepared

system, PEO_8NiBr_2, which was observed to have a Tg of -25 °C. James[110] et al determined the the glass transition temperatures of a variety of metal chlorides in low molecular weight amorphous PPO. They reported that $CoCl_2$ caused the greatest elevation in Tg of the systems studied. It thus appears that the *gross* elevation of the Tg in these systems must be ascribed to some property of the Co^{2+} ion rather than to any property of the anion (although the anions may make a contribution to the Tg elevation via the formation of crosslinks). The similarity of the Co^{2+} and Ni^{2+} ions (ionic radii Co^{2+} = 0.74Å and Ni^{2+} = 0.69Å) might suggest that the phenomenon is related to the electronic configuration of the central cation. Interestingly enough, among the systems investigated by James et al[110], $FeCl_3$ also caused a large elevation in Tg, however, for electrolytes containing 25 mol% of the salt, this was still some 60 °C below that for the system containing $CoCl_2$.

On the basis of the data obtained in this study alone, it was not possible to postulate with any certainty the reason for the gross elevation of Tg in systems containing Co^{2+} ions. It would be of interest to conduct a systematic study of the variation in glass transition temperatures for a wide range of transition metal salts in order to resolve the problem.

The electrochemical and redox studies of the $PEO_xEu(CF_3SO_3)_3$ and PEO_xNiI_2 systems indicated that both mass transport and the kinetics of the electrode reaction were slow. It was postulated that electron transfer may have been limited by reorganisation of the primary solvation sphere of the Ni or Eu species. This is likely to be a highly energetic process, involving as it does the cooperative motion of a high molecular weight polymer. Furthermore, if the nickel ad-atoms remain partially solvated by the polymer, then by the same argument, two dimensional diffusion across the electrode surface may have been inhibited. On the basis of this hypothesis, it is likely that the kinetics of electrode reaction should be slow for all redox processes containing multivalent ions in polymer electrolyte systems.

The salt precipitation process observed at high temperatures in the phase diagram of the PEO:$Ca(CF_3SO_3)_2$ system was ascribed to a negative entropy of dissolution of

the salt in the polymer. This results from the loss of conformational freedom of the polymer chains upon complexation with the cations. The appearance of salt at high temperatures has been observed in several systems (e.g. the PEO:NaSCN[49], PEO:KSCN[49] and PEO:NaI[10] systems).This, however, is the first reported case of a PEO based system in which salt precipitation occurs from the all amorphous / liquid phase and is therefore the only one in which there is evidence for a negative entropy of dissolution of the salt in the polymer. The temperature at which the process occurs depends on the relative magnitudes of the enthalpy and entropy terms, the solution becoming unstable when the positive entropy term more than compensates for the negative enthalpy term. [$\Delta G_{soln} = \Delta H_{soln} - T\Delta S_{soln}$]. For this reason, it will vary for each cation, anion and polymer host combination and will not be observed if the onset temperature for the process is above the decomposition temperature of the system.

The technique of variable temperature powder x-ray diffraction is ideally suited to the study of polymer electrolytes since it is possible to follow the appearance and disappearance of specific crystalline phases as a function of temperature and composition. For example, the $Ca(CF_3SO_3)_2$ phase could be identified specifically precipitating from the polymer. To the author's knowledge, this is the first application of such a technique in this field.

REFERENCES

(1) D.E.Fenton, J.M.Parker and P.V.Wright, *Polymer* 14, 589, (1973)

(2) M.B.Armand, J.M.Chabagno and J.Duclot, *2nd International Conference on Solid Electrolytes*, St. Andrews, Scotland, Sept 20-22 (1978)

(3) M.B.Armand, J.M.Chabagno, and M.J.Duclot, *Fast Ion Transport in Solids*, Ed. P.Vashista, J.Mundy, G.K.Shenoy, North Holland and New York (1978)

(4) R.Huq and G.C.Farrington, *Solid State Ionics*, 28-30, 990,(1988)

(5) S.Schantz, M.Sandberg and M.Kakihana, *Solid State Ionics*, 40-41, 645, (1990)

(6) B.L.Papke, M.A.Ratner and D.F.Shriver, *Physical Chemistry of Solids*, 42(6), 493, (1981)

(7) S.Schantz, J.Sandahl, L.Borjesson, L.M.Torell and J.L. Stevens, *Solid State Ionics* 28-30, 1047, (1988)

(8) G.Peterson, P.Jacobson and L.M.Torell, *Electrochimica Acta*, 37(9), 1495 (1992)

(9) J.Shi, *PhD Thesis*, Centre for Electrochemical and Materials Science,St.Andrews University, (1992)

(10) F.M.Gray, *Solid Polymer Electrolytes - Fundamentals and Applications*, VCH Publishers inc., New York (1991)

(11) B.L.Papke, M.A.Ratner and D.F.Shriver, *J.Electrochem Soc*, 129(8), 1694, (1982)

(12) P.V.Wright, Polymer, 30, 1179, (1989)

(13) *Polymer Electrolyte Reviews II*, Ed. J.R.MacCallum and C.A.Vincent, Elsevier Applied Science, London and New York (1989)

(14) D.F Shriver, B.L.Papke, M.A.Ratner, R.Dupon and T.Wang, *Solid State Ionics*, 5 ,83, (1981)

(15) P.G.Bruce, F Krok, J.Nowinski, F.M.Gray and C.A.Vincent, *Solid State Ionics*, 27 ,81,(1988)

(16) R.G.Pearson, *J.American Chem.Soc.*, 85 ,3543,(1963)

(17) J.E.Mark, *Macromolecules*, 11(4), 627,(1978)

(18) M.Watanabe, M.Rikukawa, K.Sanui and N.Ogata, *Macromolecules*, 19, 188, (1986)

(19) C.K.Chiang, G.T.Davis, C.A.Harding and T.Takahashi, *Macromolecules*, 18, 825 (1985)

(20) C.K.Chiang, G.T.Davis,C.A.Harding and T.Takahashi, *Solid State Ionics*, 18&19, 321,(1986)

(21) C.S.Harris, D.F.Shriver, M.A.Ratner, *Macromolecules*, 19, 987, (1986)

(22) T.Takahashi, G.T.Davis, C.K.Chiang and C.A.Harding, *Solid State Ionics*, 18 &19, 321,(1986)

(23) S.Clancy, L.A.Ochrymowycz, *Macromolecules*, 19, 606, (1986)

(24) R.J.Neat, A.Hooper, M.D.Glasse and R.G.Linford in *The Proceedings of the 6th Riso International Symposium on Metallurgy & Materials Science*, Ed.F.W.Poulson, N.Hessel Andersen, K.Clausen, S.Skaarup and O.T.Sorensen, Roskilde, (1984)

(25) R.J.Neat, M.D,Glasse, R.G.Linford and A.Hooper, *Solid State Ionics*, 18&19, 1088, (1986)

(26) D.R.Payne and P.V.Wright, *Polymer*, 23, 690, (1982)

(27) A.Wendsjo and H.Yang in the *2nd International Symposium on Polymer Electrolytes*, Ed. B.Scrosati, Elsevier Applied Science, London & New York (1990)

(28) R.Huq and G.C.Farrington, *J.Electrochem Soc.* 135(2), 524,(1988)

(29) C.C.Lee and P.V.Wright, *Polymer*, 23, 681, (1982)

(30) Y.Chatani and S. Okamura, *Polymer*, 28, 1815, (1987)

(31) Y. Chatani, T.Takayanagi and A.Honma, *Polymer*, 31, 2238, (1990)

(32) T.Hibma, *Solid State Ionics*, 9&10, 1101, (1983)

(33) H.Tadokoro, Y.Chatani, T.Yoshihara, S.Tahara and S.Murahashi, *Die Makromolekulaire Chemie*, 73, 109,(1964)

(34) Y.Takahashi, I.Sumita, H.Tadokoro, *J.Polymer Sci.*, 11, 2113, (1973)

(35) Y.Takahashi and H.Tadokoro, *Macromolecules*, 6(5), 672,(1973)

(36) J.M.Parker, P.V.Wright and C.C.Lee, *Polymer*, 22, 1305, (1981)

(37) D.F.Shriver, B.L.Papke, M.A.Ratner, R.Dupon, T.Wong and M.Brodwin, *Solid State Ionics*, 5, 83, (1981)

(38) B.L.Papke, M.A.Ratner and D.F.Shriver, *J.Electrochem.Soc.*, 129(7), 1434, (1982)

(39) P.Lightfoot, M.Mehta and P.G.Bruce, *J. Materials. Chem.*, 2(4), 379, (1992)

(40) C.Berthier, W.Gorecki, M.Minier, M.B.Armand, J.M.Chabagno and P.Rigaud, *Solid State Ionics*, 11, 91, (1983)

(41) C.A.Vincent, Progress in Solid State Chemistry, 17, 145,(1987)

(42) Y.L.Lee and B.Crist, *J.Applied Physics*, 60(8), 2683, (1986)

(43) W.Gorecki, R.Andreani, C.Berthier, M.B.Armand, M.Mali, J.Ross and D.Brinkmann, *Solid State Ionics*, 18&19, 295, (1986)

(44) M.Minier, C.Berthier, W.Gorecki, *J.Physique*, 45, 739, (1984)

(45) J.E.Weston and B.C.H.Steele, *Solid State Ionics*, 2, (1981)

(46) P.R.Sorensen and T.Jacobsen, *Polymer Bulletin*, 9, 47, (1983)

(47) C.D.Robitaille and D.Fateux, *J.Electrochem.Soc.*, 133(2), 315,(1986)

(48) S.M.Zahurak, M.C.Kaplan, E.A.Rietman, D.W.Murphy and R.J.Cava, *Macromolecules*, 21, 654, (1988)

(49) C.Robitaille, S.Marques, D.Boils and J.Prud'homme, *Macromolecules*, 20(2), 3023, (1987)

(50) S.Besner, A.Vallee, and J.Prud'homme, *Polymer Prepr.*, 30(1), 4067, (1989)

(51) D.Fateux, M.D.Lupien and C.Robitaille, *J.Electrochem.Soc.*,134, 2761, (1986)

(52) V.C.Z.Bermudez, J.Morgado, T.M.A.Abrantes and L.Alcacer in *2nd International Symposium on Polymer Electrolytes*, Ed. B.Scrosati, Elsevier Applied Science, London and New York, (1990)

(53) S.Passerini, R.Curini and B.Scrosati, *Applied Physics A*, 49, 425, (1989)

(54) M.Smith in E.C. Brite-Euram Project, Report October 1991- March 1992

(55) G.S.Fulcher, *J.American Chem.Soc.*, 8, 3339, (1925)

(56) M.L.Williams, R.F.Landel and J.O.Ferry, *J.American Chem.Soc.*, 77, 3701, (1955)

(57) M.H.Cohen and D.Turnbull, *J.Chemical Physics*, 31(5), 1164, (1959)

(58) J.H.Gibbs and E.A. DiMarzio, *J.Chemical Physics*, 28(3), 373, (1958)

(59) G.Adam and J.H.Gibbs, *J.Chemical Physics*, 43(1), 139, (1965)

(60) B.L.Papke, M.A.Ratner and D.F.Shriver, *J.Electrochem.Soc.*, 129, 1694, (1982)

(61) S.D.Druger, M.A.Ratner and A.Nitzan, *Solid State Ionics*, 9&10, 1115,(1983)

(62) *Polymer Electrolyte Reviews I*, Ed. J.R.MacCallum and C.A.Vincent, Elsevier Applied Science, London and New York (1987)

(63) M.Leveque, J.F.LeNest, A.Gandini and H.Cheradame, *J.Power Sources*, 14, 23, (1986)

(64) J.Evans, C.A.Vincent and P.G.Bruce, *Polymer*, 28, 2324, (1987)

(65) A.Bouridah, F.Dalard, D.Deroo, and M.B.Armand, *Solid State Ionics*, 18&19, 287, (1986)

(66) J.E.Weston and B.C.H.Steele, *Solid State Ionics*, 7, 81, (1982)

(67) P.Ferloni, G.Chiodelli, A.Magistris and M.Sanesi, *Solid State Ionics*, 18&19, 265, (1986)

(68) M.Leveque, J.F.LeNest, A Gandini and H.Cheradame, *Makromolekulaire Chemie Rapid Communications*, 4, 497, (1983)

(69) L.L.Yang, A.R.McGhie and G.C.Farrington, *J.Electrochem.Soc*, 133(7), 1381, (1986)

(70) F.M.Gray, C.A.Vincent, P.G.Bruce and J.L.Nowinski, in *2nd International Symposium on Polymer Electrolytes*, Ed. B.Scrosati, Elsevier Applied Science, London and New York, (1990)

(71) T.M.A.Abrantes, L.J.Alcacer and C.A.C.Sequeira, *Solid State Ionics*, *18&19*, 315, (1986)

(72) M.H.Sheldon, M.D.Glasse, R.J.Latham, R.G.Linford, H.Yang and G.C.Farrington, in *Extended abstracts of the 1st International Symposium on Polymer Electrolytes*, St.Andrews, (1987), pp 30.1 - 30.4

(73) M.H.Sheldon, M.D.Glasse, R.J.Latham, R.G.Linford, H.Yang and G.C.Farrington in reference 72

(74) L.L.Yang, R.Huq, G.C.Farrington and G.Chiodelli, *Solid State Ionics*, 18&19, 291, (1986)

(75) R.Huq, G.Chiodelli, P.Ferloni, A.Magistris and G.C.Farrington, *J.Electrochem.Soc.*, 134(2), 364, (1987)

(76) W.I.Archer and R.D.Armstrong, *Electrochimica Acta*, 26, 167, (1981)

(77) D.Fateux, *Solid State Ionics*, 17, 133, (1985)

(78) M.B.Armand, *Solid State Ionics*, 9&10, 745, (1983)

(79) F.Bonino, B.Scrosati, A Selvaggi , J.Evans and C.A.Vincent, *J.Power Sources*, 18, 75, (1986)

(80) M.B.Armand in reference 54

(81) L.L.Yang and G.C.Farrington, *J.Electrochem.Soc.*, 139(6), 1645,(1992)

(82) *Instrumental Methods in Electrochemistry*, Southampton Electrochemistry Group, Ellis Horwood, (1990)

(83) R.D.Armstrong, M.Fleischmann and H.R.Thirsk, J *Electroanal.Chem. 11*, 208,(1966)

(84) G.J.Hills, D.J.Schiffrin and J.Thompson, *Electrochimica Acta*, 19, 657, (1974)

(85) B.R.Scharifker and G.J.Hills, *Electrochimica Acta*, 28, 879, (1983)

(86) E.Bosco and S.K.Rangarajan, *J.Electroanal. Chem.*, 134, 213, (1982)

(87) D.H.Evans, K.M.O'Connell, R.A.Petersen and M.J.Kelly, *J.Chem. Ed.*, 60(4), 290, (1983)

(88) G.A.Mabbott, *J.Chem.Ed.*, 60(9), 697, (1983)

(89) P.T.Kissinger and W.R.Heinemann, *J.Chem.Ed.*, 60(9), 702, (1983)

(90) A.J.Bard and L.R.Faulkner, *Electrochemical Methods - Fundamentals and Applications*, J.Wiley, (1980)

(91) P.Delahay, *J.American Chem.Soc.*, 75, 1191, (1953)

(92) R.S.Nicholson and I. Shain, *Analytical Chem.*, 36(4), 707, (1964)

(93) R.A.Cooley and D.M.Yost, *Inorg.Synth.*, 2, 69, (1940)

(94) H.N.McCoy, *J.American Chem.Soc.*, 57, 1577, (1936)

(95) H.W.Stone and D.N.Hume, *Indust. and Eng. Chem. (Anal. Edn.)*, 11(11), 598,(1939)

(96) I. Abrahams, Heriot-Watt University, Personal communication

(97) F.M.Gray, St.Andrews University, Personal communication

(98) B.A.Boukamp, *Equivalent Circuit Program*, Univerity of Twente, (1988)

(99) S.T.Bowden, *The Phase Rule and Phase Relations*, Macmillan and Co. Ltd., London, (1990)

(100) S.Biallozor, A.Lisowska-Oleksiak and M.Lieder, *Electrochim. Acta*, 29(2), 283, (1984)

(101) J.McB.Harrowfield, D.L.Kepert, J.M.Patrick and A.H.White, *Aus. J.Chem*, 36, 483, (1983)

(102) M.Smith in E.C. Brit-Euram Project, Annual Report October 1990-September 1991

(103) C.W. DeKreuk, M.Sluyters-Rehbackand J.H.Sluyters, *J.Electroanal. Chem.* 28, 391, (1970)

(104) J.Ferguson, D.L.Wood and K Knox, *J.Chem. Phys.* 29(4), 881, (1963)

(105) B.N.Figgis, *Introduction to Ligand Fields*, Interscience Publishers (John Wiley and Sons), New York, London and Sydney, (1966)

(106) R.Huq, M.A.Saltzberg and G.C.Farrington, *J.Electrochem. Soc.*, 136(5), 1260, (1989)

(107) A.B.P.Lever, *Inorganic electronic spectroscopy, Studies in physical and theoretical chemistry* 33, 2nd Edition, Elsevier (1984)

(108) J.F.Le Nest, A.Gandini and H.Cheradame, *Br. Polymer Journal*, 20, 253, (1982)

(109) R.E.Wetton, D.B.James and W.Whiting, *J.Polymer Sci. (Polymer Letters)*, 14, 186, (1976)

(110) D.B.James, R.E.Wetton and D.S.Brown, *Polymer*, 20,187, (1979)

(111) G.G.Cameron and M.D.Ingram in reference 13

APPENDIX 1

THE STRUCTURE OF THE POLYETHYLENE OXIDE : SODIUM PERCHLORATE COMPLEX PEO_3NaClO_4 FROM POWDER X-RAY DIFFRACTION DATA

Structure of the Poly(ethylene oxide)–Sodium Perchlorate Complex PEO_3–$NaClO_4$ from Powder X-Ray Diffraction Data

Philip Lightfoot,* Mary Anne Mehta and Peter G. Bruce
Centre for Electrochemical and Materials Sciences, Department of Chemistry, University of St Andrews, St Andrews, Fife KY16 9ST, UK

The crystal structure of the poly(ethylene oxide)–sodium perchlorate complex has been refined by the Rietveld method, using soft chemical constraints, from powder X-ray diffraction data. PEO_3–$NaClO_4$ crystallises in the monoclinic system, space group $P2_1/a$, $a=18.319(1)$ Å, $b=8.3459(6)$ Å, $c=8.5784(7)$ Å, $\beta=123.14(1)^\circ$, $Z=4$. The complex is isomorphous with the PEO_3–NaI complex, and is composed of a helical polymer chain wrapped around the alkali-metal cation. Perchlorate ions associate with the Na^+ ions in a zig-zag manner, resulting in five-fold co-ordination around the Na^+, comprising three oxygens from the polymer chain and one each from the surrounding perchlorate ions. This is the first example of the full structural characterisation of a polymer electrolyte complex by powder diffraction methods, and demonstrates that this should become a powerful technique in the understanding of the structure–property relationships of these materials.

Keywords: *Powder diffraction; Rietveld analysis; Polymer electrolyte; Chemical constraint*

Salts such as $LiCF_3SO_3$, $LiClO_4$ and $NaClO_4$ may be dissolved in high-molecular-weight poly(ethylene oxide), $(CH_2CH_2O)_n$, to yield solid electrolytes.[1] These materials are under extensive investigation because of their possible application in high-energy-density batteries, fuel cells and electrochromic display devices. Both crystalline and amorphous phases may be formed. While ionic conductivity is confined to the amorphous phases, structural information on the crystalline phases is of considerable importance, both in terms of developing a complete understanding of the nature of the polymer–salt systems in general and because such structural information gives insight into the nature of the structural units present in the amorphous phases.

Very little structural work has so far been reported on any of these crystalline complexes. Indeed, only three complete structure determinations of poly(ethylene oxide) (PEO)–salt complexes have been presented: PEO_3–NaI, PEO_3–NaSCN and PEO–NaSCN, by Chatani and co-workers.[2,3] In addition, information on the structure of a PEO_4–KSCN complex, but only in two dimensions, is available.[4]

A common characteristic of the structures studied so far is the presence of the PEO chain itself in helical conformation, similar to that found in the structure of pure PEO.[5] The disposition of the ionic portion of the complex relative to this chain does, however, vary. In the NaI and NaSCN (3:1) complexes the Na^+ is clearly held within the helix, being co-ordinated by the ether oxygens and counter anions, the latter of which are external to the polymer chains. However, in the KSCN complex and the NaSCN (1:1) complex, the K^+ and Na^+ ions are reported to be external to the helix.

The studies which have been reported were all carried out by single-crystal methods applied to stretched, oriented fibres of the complexes. The lack of structural studies to date is in part owing to the difficulty of preparing stretched fibres and to the inferior quality of the X-ray data when compared with that obtained from more conventional molecular crystals. Furthermore, the structure of the complex may be modified by preparation in the form of stretched fibres. We are therefore using high-resolution powder X-ray diffraction data to carry out our structural studies.

Powder diffraction methods are not confined to establishing the size and shape of the unit cell. Provided a basic starting model for the crystal structure is known, the Rietveld[6] method allows this model to be refined by analysing the intensities of the powder data until a complete solution of the structure is obtained. This is now a well established method of structure refinement. Recently, the technique has been extended to allow the determination of crystal structures without a starting model.[7,8] Such *ab initio* determinations promise to be of considerable value in the future. However, in this paper we report the structure refinement of the crystalline PEO_3–$NaClO_4$ complex, which is isomorphous with the corresponding NaI complex. This is the first example of the use of powder diffraction and the Rietveld method in the characterisation of a polymer–salt complex.

Experimental

Synthesis

Unless otherwise stated, all manipulations were performed in an argon-filled dry box. $NaClO_4$ (Aldrich 99+%) was first dried at 180 °C for 8 h under vacuum then thoroughly ground in a pestle and mortar. PEO (BDH, $M=5\times10^6$) was dried at 50 °C for 48 h and an appropriate quantity mixed with the $NaClO_4$. The mixture was transferred to a stainless-steel ball mill, removed from the glove box and ground at liquid-nitrogen temperatures for 20 min using the technique developed by Gray *et al.*[9] After returning the mixture to room temperature, it was transferred back into the glove box and sealed into a 0.5 mm glass capillary. This was heated at 150 °C for 4 days to promote reaction of the polymer and salt, then annealed at 60 °C for a further 4 days.

X-Ray Diffraction

Powder X-ray diffraction data were collected on a Stoe STADI/P high-resolution system equipped with a linear position-sensitive detector covering *ca.* 6° in 2θ, and employing Ge-monochromatised Cu-$K\alpha_1$ radiation. The sample was mounted in the 0.5 mm diameter capillary, and data collected in the range $5^\circ<2\theta<80^\circ$ in steps of 0.02°. The raw data were corrected with a polynomial background function using the GENIE program.[10]

Structure Determination

Careful inspection of the data suggested that a small amount of $NaClO_4$ was present as an impurity, and two peaks were therefore omitted from the data prior to pattern indexing. The powder pattern was then indexed using the program TREOR,[11] which successfully indexed the first 20 peaks with a monoclinic cell of dimensions $a_1 = 8.586$ Å, $b_1 = 8.355$ Å, $c_1 = 16.943$ Å, $\beta = 115.0°$, figure-of-merit[12] = 16.3. This cell is related to that reported by Hibma,[4] being half the volume, with $a_1 \approx c_H/2$, $b_1 \approx b_H$, $c_1 \approx a_H$. On inspection it became apparent that our cell was similar to that of the PEO_3–NaI complex. In order to proceed with the structure determination, this cell was transformed as follows: $a_2 = a_1 + c_1$, $b_2 = b_1$, $c_2 = a_1$, producing the cell $a_2 = 18.322$ Å, $b_2 = 8.355$ Å, $c_2 = 8.586$ Å, $\beta = 123.1°$. This is the more conventional setting of a cell corresponding to that of Chatani and Okamura for the PEO_3–NaI complex, which had c as the unique axis.[2] Systematic absences for this cell defined the space group as $P2_1/a$. Starting parameters for the Rietveld refinement were taken from Chatani and Okamura,[2] with Cl replacing I initially. Rietveld analysis was carried out using the GSAS suite,[13] employing a pseudo-Voigt peak shape. The refined data range was $10° < 2\theta < 70°$, covering 3000 data points, and including 490 reflections. $NaClO_4$ was included as a second phase of fixed structural parameters throughout the refinement. Owing to the complexity of the structure, and the limited quantity of data, soft chemical constraints were used throughout to define the polymer chain, such that C—O = 1.44(1) Å, C—C = 1.57(1) Å, C—C—O = 109°. Additionally, the conformation of the chain was constrained such that all C—C bonds were *gauche* and all C—O bonds *trans*, resulting in a $(t_2gt_2gt_2g)_2$ pattern as in the PEO_3–NaI complex. This is the expected, and most stable conformation for an unstretched PEO chain.[14] We note that the use of chemical constraints in the refinement of polymer structures from oriented fibre data has also been reported.[15] After refinement of this partially determined structure, it was possible to locate the missing O atoms of the ClO_4^- group from successive difference Fourier maps. The fact that clear peaks were present at appropriate distances from the Cl and Na atoms indicates that the proposed model is a unique solution. However, it was still found necessary to use soft constraints on the Cl—O [1.44(1) Å] and O—Cl—O angles (109°) to give the best possible refinement. Finally, temperature factors were refined such that all the chain atoms were equivalent and all the atoms of the ionic portion of the complex were equivalent. Owing to the limited quality and quantity of data and the complexity of the structure, it was felt that refinement of a less constrained set of temperature factors would not be physically reasonable. Hydrogen atoms were not located. A smooth refinement was then achieved, converging to the agreement factors $R_{wp} = 6.9\%$, $\chi^2 = 1.95$, for 65 refined parameters. The final refined Rietveld fit to the X-ray data is good and is shown in Fig. 1.

Results and Discussion

Final refined atomic parameters are given in Table 1, and selected bond distances in Table 2. Plots of the structure along both b and c are given in Fig. 2 and 3, respectively. The arrangement of the polymeric chain and ionic component is essentially the same as that in the PEO_3–NaI complex,[2] with ClO_4^- substituting for I^-. As in that case, the Na^+ ions are located within the helices. The resultant Na^+ ion co-ordination is best described as five-fold, though it does not correspond to any regular high-symmetry co-ordination. The co-ordinating atoms comprise three polymer oxygens and two perchlorate oxygens (Fig. 4), all within the accepted range

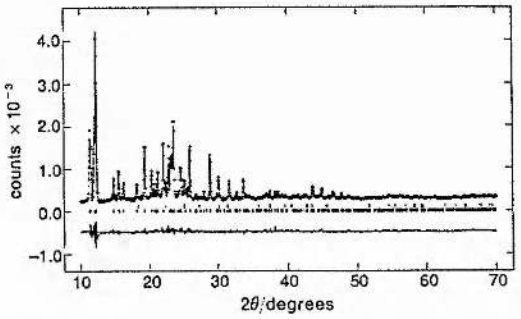

Fig. 1 Final observed (top), calculated (middle) and difference (bottom) profiles for the Rietveld refinement of PEO_3–$NaClO_4$. Reflection positions are marked

Table 1 Refined atomic parameters for PEO_3–$NaClO_4$, space group $P2_1$, a, $a = 18.319(1)$ Å, $b = 8.3459(6)$ Å, $c = 8.5784(7)$ Å, $\beta = 123.14(1)°$

atom	x	y	z	U(iso)/Å^2
Cl	0.1292(8)	0.1852(13)	0.0260(17)	0.19(1)
Na	0.285(1)	0.427(2)	0.110(2)	0.19(1)
O(1)	0.298(1)	0.537(2)	0.369(2)	0.023(3)
C(1)	0.271(1)	0.699(2)	0.362(2)	0.023(3)
C(2)	0.168(1)	0.701(2)	0.204(3)	0.023(3)
O(2)	0.159(1)	0.692(2)	0.028(2)	0.023(3)
C(3)	0.073(1)	0.660(3)	−0.122(3)	0.023(3)
C(4)	0.070(1)	0.654(2)	−0.311(2)	0.023(3)
O(3)	0.085(1)	0.810(2)	−0.350(2)	0.023(3)
C(5)	0.097(1)	0.821(2)	−0.499(2)	0.023(3)
C(6)	0.116(1)	1.006(2)	−0.512(3)	0.023(3)
O(4)	0.894(1)	0.736(3)	0.866(3)	0.19(1)
O(5)	0.210(1)	0.098(3)	0.140(3)	0.19(1)
O(6)	0.639(1)	0.200(3)	0.913(3)	0.19(1)
O(7)	0.933(1)	0.927(3)	0.083(3)	0.19(1)

Table 2 Selected bond lengths (Å) and angles (degrees)

Cl—O(4)	1.37(2)	Na—O(1)	2.29(2)
Cl—O(5)	1.45(2)	Na—O(2)	2.76(2)
Cl—O(6)	1.44(2)	Na—O(2′)	2.98(2)
Cl—O(7)	1.38(2)	Na—O(3)	2.34(2)
		Na—O(5)	2.62(2)
		Na—O(6)	2.49(2)
O(1)—C(1)	1.43(1)	C(6)—O(1)—C(1)	114(1)
C(1)—C(2)	1.61(1)	O(1)—C(1)—C(2)	105(1)
C(2)—O(2)	1.43(1)	C(1)—C(2)—O(2)	107(1)
O(2)—C(3)	1.42(1)	C(2)—O(2)—C(3)	113(1)
C(3)—C(4)	1.60(1)	O(2)—C(3)—C(4)	109(1)
C(4)—O(3)	1.41(1)	C(3)—C(4)—O(3)	108(1)
O(3)—C(5)	1.41(1)	C(4)—O(3)—C(5)	114(1)
C(5)—C(6)	1.60(1)	O(3)—C(5)—C(6)	106(1)
C(6)—O(1^i)[a]	1.39(1)	C(5)—C(6)—O(1^i)	108(1)
torsion angles[b]			
O1—C1—C2—O2	75		
C1—C2—O2—C3	−168		
C2—O2—C3—C4	−179		
O2—C3—C4—O3	69		
C3—C4—O3—C5	−171		
C4—O3—C5—C6	178		
O3—C5—C6—O1^i	−76		
C5—C6—O1^i—C1^i	174		
C6—O1^i—C1^i—C2^i	170		

[a] Symmetry operator: (i) $1/2-x$, $1/2+y$, $-z$. [b] A positive rotation is clockwise from atom 1 when viewed from atom 3 to atom 2.

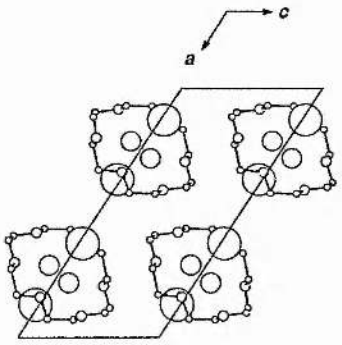

Fig. 2 View of the PEO_3–$NaClO_4$ structure along *b*. Large circles, ClO_4^-; medium circles Na^+, smaller circles O, C

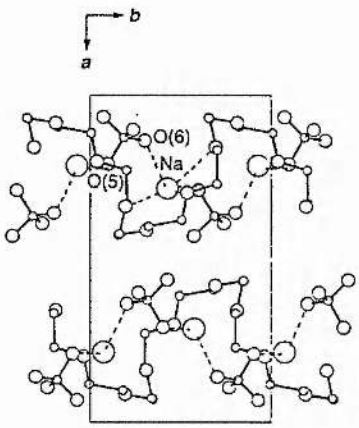

Fig. 3 View of the PEO_3–$NaClO_4$ structure along *c*. Dashed lines indicate the connectivity of neighbouring ionic species. Na^+, O(5) and O(6) are labelled (see text)

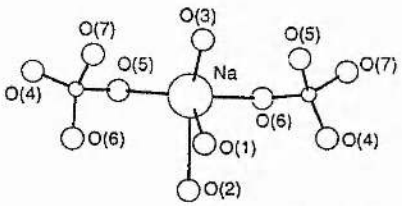

Fig. 4 Na^+ ion co-ordination in PEO_3–$NaClO_4$

2.2–2.8 Å, the next-nearest neighbour being O(2) at 2.98 Å. Bond lengths within the ClO_4^- group may reflect the co-ordination of the oxygens to Na^+, *i.e.* the Cl—O(5)/O(6) bonds appear relatively long owing to their co-ordination to Na^+. Each ClO_4^- group donates an O(5) to one Na^+ ion and an O(6) to an adjacent Na^+ ion, giving a continuous network along the *b* axis (Fig. 3). The perchlorate ions bridge Na^+ within a chain; there is no evidence of either ClO_4^- or Na^+ ions acting as crosslinks between neighbouring helices.

The quality of the profile fit and the refined interatomic distances preclude any gross error in the proposed model (for example an alternative conformation of the PEO chain). The relatively high thermal parameter for the ionic component is not unexpected, and probably reflects some degree of static–rotational disorder in the ClO_4^- group. It is well known that the cations are tightly bound to the ether oxygens of the polymer chains whereas the anions interact only weakly with the chains. Under these circumstances, a range of orientations of similar energy are likely to be available to the ClO_4^- groups. In such a case some disorder is to be expected.

The replacement of I^- ions by ClO_4^- groups has resulted in an expansion of the unit cell. The helix is more stretched along its axis than is the case for the iodide structure. Furthermore, neighbouring chains are further apart. There is evidence that in amorphous polymer electrolytes the majority of the current is carried by the anions.[16] If this is so and if, in addition, the presence of ClO_4^- ions provides a less dense structure in the amorphous phase, this may explain the relatively high ionic conductivities normally associated with perchlorate-based systems.

The authors are grateful to SERC for support. P.G.B. thanks the Royal Society for the provision of a Pickering Research Fellowship.

References

1 M. Armand and M. Gauthier, in *High Conductivity Solid Ion Conductors*, ed. T. Takahashi, World Scientific, Singapore, 1989.
2 Y. Chatani and S. Okamura, *Polymer*, 1987, **28**, 1815.
3 Y. Chatani, Y. Fujii, T. Takayanagi and A. Honma, *Polymer*, 1990, **31**, 2238.
4 T. Hibma, *Solid State Ionics*, 1983, **9/10**, 1101.
5 Y. Takahashi and H. Tadoroko, *Macromolecules*, 1973, **6**, 672.
6 H. M. Rietveld, *J. Appl. Crystallogr.*, 1969, **2**, 65.
7 P. Lightfoot, C. Glidewell and P. G. Bruce, *J. Mater. Chem.*, 1992, **2**, 361.
8 A. K. Cheetham and A. P. Wilkinson, *J. Phys. Chem. Solids*, 1991, **52**, 1199.
9 F. M. Gray, J. R. Maccallum and C. A. Vincent, *Patent appl.* 8619049, 5 8 86.
10 W. I. F. David, M. W. Johnson, K. J. Knowles, C. M. Moreton-Smith, G. D. Crosbie, E. P. Campbell, S. P. Graham and J. S. Lyall, *Rutherford-Appleton Laboratory Report No.* RAL-86-102, 1986.
11 P-E. Werner, *Z. Kristallogr.*, 1964, **120**, 375.
12 P. M. de Wolff, *J. Appl. Crystallogr.*, 1968, **1**, 108.
13 A. C. Larson and R. B. Von Dreele, *Los Alamos Laboratory National Laboratory Report No.* LA-UR-86-748, 1987.
14 C. A. Vincent, *Prog. Solid State Chem.*, 1987, **17**, 145.
15 S. Arnott and A. J. Wonacott, *Polymer*, 1966, **7**, 157.
16 P. G. Bruce, M. T. Hardgrave and C. A. Vincent, *Solid State Ionics*, in the press.

Paper 1/06183F; *Received 9th December*, 1991

APPENDIX 2

MATERIALS

The follwing appendix gives details of the materials used and where relevant, the drying process. Where drying under vacuum is indicated, a rotary oil pump was used capable of achieving a vacuum of typically 0.01 mm of mercury.

Acetonitrile	Aldrich Chemical Company, anhydrous 99+%, dried over molecular sieves
Calcium carbonate	BDH, 98%
Calcium triflate	Prepared in section 4.2.2, dried at 180 °C for 8 hours under vacuum
Cobalt thiocyanate	dried at 90 °C for 4 days under vacuum
Europium oxide	Aldrich Chemical Company, 99.9%
Europium triflate	Prepared in section 4.2.2, dried at 150 °C for 48 hours under vacuum
Ethanol	Aldrich Chemical Company, anhydrous, dried over molecular sieves
Hydrochloric acid	Fisons specified laboratory reagent
Lithium carbonate	AEA Technology, Harwell
Lithium perchlorate	Aldrich Chemical Company, A.C.S. reagent, dried at 200 °C for 8 hours under vacuum
Lithium triflate	Aldrich Chemical Company, dried at 150 °C for 48 hours under vacuum
Mercury(II) chloride	Aldrich Chemical Company, 99+% A.C.S reagent
Nickel Iodide	BDH laboratory reagent, dried at 100 °C for 4 days under vacuum

Polyethylene oxide	BDH, Molecular weight $5x10^6$, dried at 50 °C for 48 hours days under vacuum
Sodium hydrogen-carbonate	Aldrich Chemical Company, 99.7+% A.C.S reagent
Sodium hydroxide	Aldrich Chemical Company, 97+% A.C.S. reagent
Sodium perchlorate	Aldrich Chemical Company, 99+%, dried at 200 °C for 8 hours days under vacuum
Sulphuric acid	Fisons specified laboratory reagent
Triflic acid	Aldrich Chemical Company, 98+%
Zinc	Aldrich Chemical Company, A.C.S. reagent, 20 mesh

APPENDIX 3

POWDER X-RAY DIFFRACTION DATA FOR $PEO_6(CaCF_3SO_3)_2$

The following appendix gives details of the indexed powder x-ray diffraction pattern for the $PEO_6Ca(CF_3SO_3)_2$ crystalline complex. The author is indebted to Dr. Philip Lightfoot for indexing the pattern illustrated in figure A3-1.

A3-1 Powder x-ray diffraction data

Wavelength = 1.54056 Å

Crystal system = Orthorhombic

Lattice parameters:- a = 10.6069 Å, b = 12.4761 Å and c = 16.8473 Å

Volume 2229.45 $Å^3$

N	H	K	L	obs (2θ°)	calc (2θ°)	delta (°)	d(obs) (Å)	d(calc) (Å)
1	0	1	1	8.809	8.812	-0.0031	10.0297	10.0262
2	1	0	1	9.852	9.846	0.0063	8.9703	8.9761
3	1	1	0	10.954	10.939	0.0146	8.0704	8.0811
4	1	1	1	12.166	12.137	0.0293	7.2687	7.2863
5	0	2	0	14.161	14.186	-0.0253	6.2492	6.2381
6	0	2	1	15.127	15.133	-0.0060	5.8522	5.8499
7	2	0	0	16.672	16.703	-0.0302	5.3130	5.3034
8	1	2	1	17.288	17.297	-0.0088	5.1251	5.1225
9	1	2	2	19.584	19.570	0.0138	4.5292	4.5324
10	0	0	4	21.055	21.076	-0.0204	4.2159	4.2118
11	1	0	4	22.705	22.697	0.0084	3.9131	3.9145
12	1	2	3	22.893	22.879	0.0145	3.8814	3.8838
13	1	3	1	23.538	23.558	-0.0199	3.7765	3.7734
14	2	2	2	24.435	24.413	0.0226	3.6398	3.6431
15	3	0	1	25.734	25.725	0.0090	3.4591	3.4603
16	3	1	0	26.160	26.175	-0.0151	3.4036	3.4017
17	3	1	1	26.709	26.713	-0.0037	3.3348	3.3344
18	0	2	5	30.145	30.119	0.0255	2.9622	2.9646
19	0	1	6	32.662	32.662	-0.0006	2.7394	2.7394
20	2	4	1	33.742	33.731	0.0108	2.6541	2.6549
21	0	3	5	34.237	34.222	0.0151	2.6169	2.6180

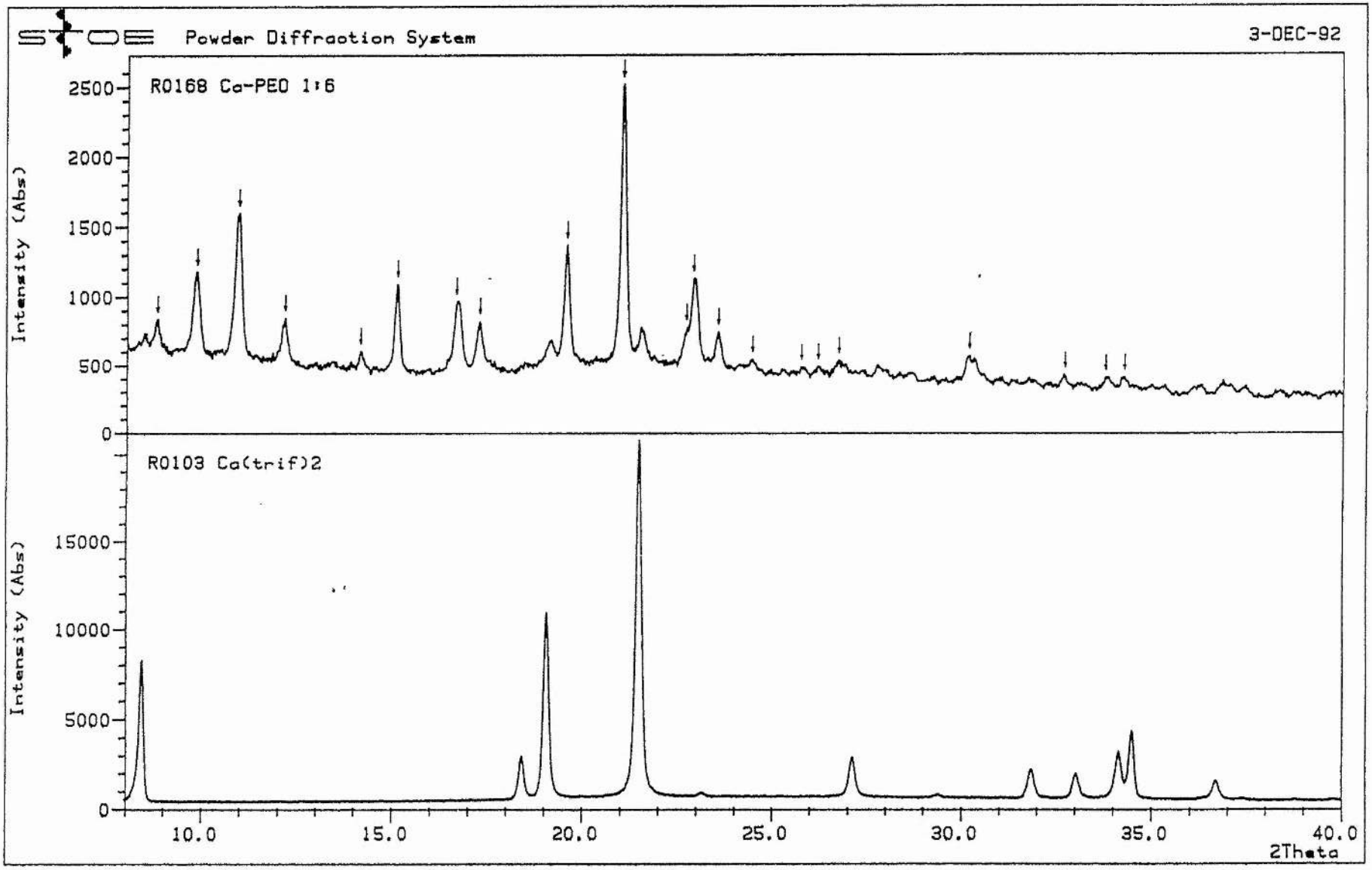

Figure A3-1 Peaks indexed in the powder x-ray diffraction pattern of the $PEO_6Ca(CF_3SO_3)_2$ complex